technische universität
dortmund

Universitätsmedizin Essen
Universitätsklinikum
Klinik und Poliklinik für Strahlentherapie

Dissertation for the attainment
of the academic degree Dr. rer. nat.

Brachytherapy meets X-rays

A novel concept to treat ophthalmic tumours

presented by
Henning Manke
born 23.02.1993 in Kempen, Germany

AG Albrecht
Faculty of Physics
TU Dortmund University

Dortmund, August 2023

Der Fakultät Physik der Technischen Universität Dortmund zur Erlangung des akademischen Grades eines Doktors der Naturwissenschaften vorgelegte Dissertation.

Betreuer: Prof. Dr. Bernhard Spaan und Prof. Dr. Johannes Albrecht

Erstgutachter: Prof. Dr. Johannes Albrecht
Zweitgutachter: Jun.-Prof. Dr. Armin Lühr

Vorsitzender der Prüfungskomission: Prof. Dr. Heinrich Päs
Vertretung der wissenschaftlichen Mitarbeitenden: Dr. Anton Savitsky

Datum des Einreichens der Dissertation: 17. August 2023
Datum der mündlichen Prüfung: 3. November 2023

Abstract

Intraocular tumours are a life-threatening risk. Smaller tumours can be treated with ^{106}Ru applicators. Meanwhile, more prominent tumours get treated with ^{125}I applicators, which results in a higher risk of side effects, or proton therapy, which is only available at a limited number of specialised centres and may lead to toxic tumour syndrome. Therefore, a novel combined therapy concept is presented and analysed in this thesis. The idea combines the use of ^{106}Ru applicators and external beam radiotherapy performed with soft X-rays. With the confocal irradiation technique and the utilisation of the ^{106}Ru applicator as a beam-stop for the X-ray beams, healthy tissue is spared from high dosages to reduce the risk of side effects. The combined therapy concept can be implemented in hospitals with relatively low costs and resembles a novel bulb-preserving modality for large intraocular tumours.
As the first steps to this therapy concept, measurements are performed with a novel solid phantom with three different detector types to assess the absorption of the X-rays in the ^{106}Ru applicator. Additionally, the clinical benefit is investigated with a novel software workflow, in which 3D models are created using patient data from the University Hospital Essen in Germany. The modalities are simulated with these 3D models. Dose-volume histograms are presented to evaluate the combined therapy concept and to compare it to stand-alone brachytherapy.

Zusammenfassung

Intraokulare Tumoren stellen ein lebensbedrohliches Risiko dar. Kleinere Tumoren können mit ^{106}Ru-Applikatoren behandelt werden. Größere Tumoren werden dagegen entweder mit ^{125}I-Applikatoren behandelt, was ein höheres Risiko von Nebenwirkungen mit sich bringt, oder mit Protonen bestrahlt, was nur an wenigen spezialisierten Zentren möglich ist. Darüber hinaus birgt die Protonentherapie das Risiko, dass das Tumorgewebe ischämisch wird. In dieser Arbeit wird ein neuartiges kombiniertes Therapiekonzept vorgestellt und analysiert. Das Konzept kombiniert den Einsatz von ^{106}Ru-Applikatoren und externer Strahlentherapie in Form von niederenergetischen Röntgenstrahlen. Mit der konfokalen Bestrahlungstechnik und der Verwendung des ^{106}Ru-Applikators als Absorber für die Röntgenstrahlen kann gesundes Gewebe geschont werden, um das Risiko von Nebenwirkungen zu minimieren. Es kann relativ kostengünstig in Kliniken implementiert werden und stellt eine neue bulbuserhaltende Modalität für große intraokulare Tumoren dar.
Als erste Schritte zu diesem Therapiekonzept werden Messungen und deren Ergebnisse vorgestellt, die mit einem neuen Festkörperphantom und drei verschiedenen Detektortypen durchgeführt wurden, um die Absorption der Röntgenstrahlen in einem ^{106}Ru-Applikator zu bewerten. Zusätzlich wird der medizinisch-physikalische Nutzen untersucht. Mit einem neuartigen Software-Workflow werden 3D-Modelle mit anonymen Patientendaten aus dem Universitätsklinikum Essen erstellt und die Strahlentherapie simuliert. Dosis-Volumen-Histogramme werden ausgewertet, um das kombinierte Therapiekonzept zu bewerten und mit der alleinigen Brachytherapie zu vergleichen.

Contents

List of abbreviations

General

AEP	Azimuthal Equidistant Projection
CBS	Command Based Scorer
COB	A ^{106}Ru-applicator model with a notch to be positioned close to the optic nerve
COMS	The Collaborative Ocular Melanoma Study, COMS-applicators is used as a synonym for ^{125}I-applicators
DDC	Depth Dose Curve
DVH	Dose-Volume Histogram
EBRT	External Beam Radiation Therapy
GPS	General Particle Source
LET	Linear Energy Transfer
MC	Monte Carlo
OAR	Organ At Risk
PEN	PolyEthylene Naphthalate
PWLR	Plastic Water® Low Range, distributed by Sun Nuclear GmbH, Norderstedt, Germany
SD	Sensitive Detector
STL	Standard Triangle Language or Standard Tessellation Language
TTS	Toxic Tumour Syndrome

Companies

BEBIG	Eckert & Ziegler BEBIG GmbH, Berlin, Germany.
Oraya	Formerly Oraya Therapeutics Newark, California, USA. Now Carl Zeiss Meditec AG, Jena, Germany.
UKE	University Hospital Essen, Essen, Germany.
Universal Robots	Universal Robots (Germany) GmbH, München, Germany.
WOmed	Wolf Medizintechnik GmbH, St. Gangloff, Germany - a subsidiary of BEBIG Medical GmbH, Berlin, Germany.

Software

FilmQA Pro	Ashland Inc., FilmQA pro™ software v.7. `https://www.ashland.com/industries/medical/filmqa-pro-software`
Fusion360	Autodesk® Fusion 360®. `www.autodesk.de/products/fusion-360`.
Geant4	Geant4, free software published and maintained by the Geant4 Collaboration. `https://geant4.web.cern.ch`
Inventor	Autodesk® Inventor®. `www.autodesk.de/products/inventor/`.
MS Excel	Microsoft® Excel®.
SpekCalc	SpekCalc, developed by Gavin Poludniowski and Phil Evans at The Institute of Cancer Research, London, UK. `http://spekcalc.weebly.com`
VBA	Microsoft® Visual Basic® for Applications.

1 Introduction

Eye tumours are life-threatening if left untreated due to possible metastasis to other organs, such as the liver, lungs and bones [1]. Until the 1950s, the only available treatment was enucleation, which is the removal of the entire eye. Nowadays, there are many different bulb-preserving modalities with a tumour control rate of more than 90 % in experienced centres [2]. The two most common modalities are proton therapy and brachytherapy. The latter is performed most often with either ^{125}I or ^{106}Ru applicators. To date, there is no general therapy concept across clinics due to the locally available options and different perceptions of the indications and contraindications of the modalities. At the UKE[1], approximately 22 % of the patients are treated with a primary enucleation because no available bulb-preserving treatment option is indicated [3].

Stereotactic radiosurgery with high-energy X-rays is reported to have relatively low eye retention rates [4–6].

Proton therapy has the advantage of an extremely steep fall-off in the dose profile after the main energy deposition in the so-called Bragg peak. However, in most cases, the treatment plan consists of one entry field, resulting in a relatively high dose in healthy tissue in front of the tumour [7–9]. In addition, the safety margins sometimes include the optic nerve, which may result in severe side effects [10, 11]. Because of the fact, that only approximately twenty of these centres treat ophthalmic tumours [12], not all patients with large tumours can benefit from this therapy.

Brachytherapy with ^{125}I applicators is most often performed with the so-called COMS[2] applicators, which consist of a metal carrier with ^{125}I seeds that emit low-energy photons. Because of their dose profile, COMS applicators are generally indicated for tumours with a height of up to 10 mm [14]. Due to the range of the photons, organs at risk may suffer from high dose values, which can result in an unwanted loss of vision or other side effects [2].

^{106}Ru applicators are based on a silver calotte with a layer of radioactive Ruthenium inside. The decay chain includes ^{106}Rh, the therapeutically important beta emitter with a maximum energy of 3.5 MeV [15], which results in a steeper dose gradient compared to COMS applicators. Therefore, the treatment with ^{106}Ru applicators does not expose

[1] University Hospital Essen, Essen, Germany.
[2] Named after the Collaborative Ocular Melanoma Study, see Ref. [13].

healthy tissue as much as ^{125}I brachytherapy but is limited to a maximum tumour height of 7 mm [16, 17].

Due to these limitations, a bulb-preserving modality for large intraocular tumours, which can be implemented at many clinics, becomes necessary.

The therapy concept presented in this thesis aims to extend the existing modalities to maximise the fraction of bulb-preserving treatments. The idea combines brachytherapy with ^{106}Ru applicators with simultaneously performed External Beam Radiation Therapy (EBRT) comprising soft X-rays. The ^{106}Ru applicator irradiates especially the tumour base, while the confocal irradiation with X-ray beams provides a dose boost in the other tumour parts, such as the tumour apex. Additionally, as the concept includes that the X-ray therapy takes place during the application time of the brachytherapy source, the silver plaque may resemble a target which absorbs most of the X-rays and can therefore be classified as a beam-stop. Thus, healthy tissue located behind the plaque is shielded from dose exposure. Furthermore, the therapy concept uses insensitive parts of the eye, the so-called pars plana, as entry spots to spare organs at risk in the anterior part of the eye. Confocal irradiation additionally reduces the dose in healthy tissue to minimise the risk of side effects. Due to the additional dose by the EBRT, the overall application time of the ^{106}Ru applicator is reduced.

In this thesis, the fundamental idea of the combined therapy concept and the first considerations on the clinical realisation are described. It presents measurements performed with a conventional X-ray therapy unit and a novel solid phantom. A detailed description of the phantom and the underlying considerations are given. The phantom can be used with three different detector types: a soft X-ray chamber, radiochromic films and self-made scintillation detectors. In addition, the improvements in the production process of the scintillation detectors are shown. With the data obtained within those measurements, the utilisation of the ^{106}Ru applicator as a beam-stop for the X-rays is evaluated.

Furthermore, the methods presented in this thesis include a novel software which enables the computation of 3D eye models from fundus photos. It considers the distortions in the fundus photo due to its projection type. It also allows the user to retrospectively evaluate a brachytherapy treatment with a ^{106}Ru applicator by displaying dose profiles in organs at risk and the tumour. This is the first software to compute dose profiles regarding ophthalmic brachytherapy, based not only on treatment plans but also on the actual position of the ^{106}Ru applicator during its application time, which can be derived from the fundus photo. A variant of this software was already used for a retrospective study on dose-effect curves [18, 19].

A workflow is developed and described to evaluate the physical medical benefit of the combined therapy concept. It comprises the patient-specific data obtained from the previously described software, a 3D modelling software and Monte Carlo (MC) simulations. The workflow enables to obtain Dose-Volume Histograms (DVHs) of the combined therapy concept or standalone brachytherapy for both artificially modelled and authentic

cases. By implementing the patient data into a generic eye model, a patient-specific model is created. It is exported to the MC simulation, which includes the brachytherapy with a ^{106}Ru applicator and 16 X-ray beams. The combination of these modalities is optimised so that the combined therapy concept provides the best possible tumour coverage while sparing healthy tissue. A set of six cases, consisting of three authentic and three modified cases with highly prominent tumours, are simulated. The novel therapy concept is evaluated with the obtained dose profiles of the combined therapy concept compared to standalone brachytherapy.

This thesis begins with an introduction to the treatment of ophthalmic tumours and the associated basics of particle and medical physics. It is followed by the presentation of the combined therapy concept and its fundamental ideas in chapter 3. Afterwards, the general methods of this thesis are described. Chapter 5 continues with the description of the new phantom, the improved production process for scintillation detectors and furthermore presents and evaluates the measurement results. In chapter 6, the software to compute 3D eye models to enable retrospective treatment analysis is presented. It is followed by the presentation of the simulation and optimisation workflow to obtain DVHs of different cases and an evaluation of the benefit of the novel therapy concept. In chapter 8, comprehensive descriptions and considerations for the clinical implementation of the novel concept are described. The thesis closes with a summary and discussion of all methods and results, giving an outlook on future improvements and ideas regarding the combined therapy concept.

2 Treatment of ophthalmic tumours

This chapter provides an overview of fundamental principles aimed at facilitating a deeper comprehension of the analysis of the combined therapy concept presented in this thesis. Therefore, the chapter starts with the anatomy of the human eye and an introduction regarding intraocular tumours. The treatment options and their indications are presented in section 2.3 followed by the issue of highly prominent tumours. Section 2.5 introduces the basics of X-ray therapy. The chapter ends with an overview of the interactions of particles with matter and biological tissue.

2.1 The anatomy of the human eye

A healthy eye with the essential compartments is presented in figure 2.1a. The outer white skin that mainly contains connective tissue is called the sclera. The choroid, with many blood vessels, is located between the sclera and the retina, the innermost layer. The retina contains many sensory cells and neurons. The electric signals produced by those cells are transported via the optic nerve to the brain. The papilla represents the intraocular part of the optic nerve, in which no sensory cells are located. Also, the blood vessels, reaching the cells through the choroid, enter the eye close to the papilla [20–22].

Regarding the refractive power of the visual system, the cornea with a high refractive index and its curvature contributes the most. The lens is not only necessary due to its refractive index, but moreover, it allows accommodation. The pars plana resembles the area where the retina and choroid merge. It is considered to have few vessels. In surgery, the pars plana is often used as an access point to reach structures in the eye globe [20–22].

2.2 Intraocular tumours

The two most common types of intraocular tumours are retinoblastomas and uveal melanomas, which are depictured in figure 2.1b. An incidence of 1.3 to 8.6 cases per million per year in Europe is reported [23].

Usually, retinoblastomas are detected in childhood with a mean age at initial diagnosis of 18 months. With the so-called Brückner test, the patient is tested for pupillary

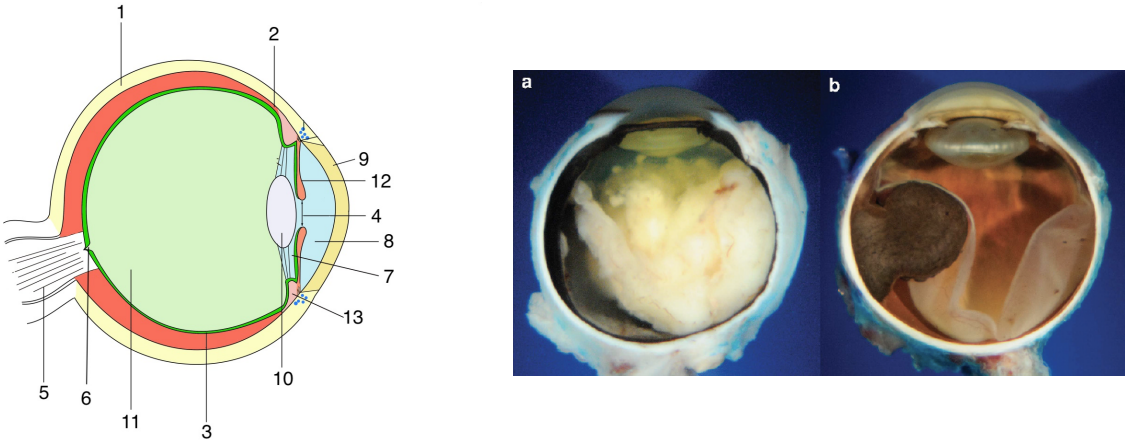

a) b)

Figure 2.1: a) A depiction of the cross-section of the human eye with the following structures: 1) sclera, 2) choroid, 3) retina, 4) pupil, 5) optic nerve, 6) papilla, 7) posterior chamber, 8) anterior chamber, 9) cornea, 10) lens, 11) vitreous body, 12) iris, 13) ciliary body. The illustration is reproduced from Ref. [24]. b) Histology of the two most common intraocular tumours, Retinoblastoma (left) and uveal melanoma (right). The figure is extracted from Ref. [25].

reflex, which may lead to the detection of leukokoria and retinoblastoma. While the Brückner test mostly finds tumours in an advanced stage, earlier staged tumours are whitish, flat tumours on the retina, which may even occur multifocal or bilateral in case of genetic predisposition. Retinoblastomas are either sorted by using the international classification of retinoblastoma or the tumour node metastasis classification [26].

The diagnosis of uveal melanomas typically occurs in the sixth decade of life or later [26, 27]. The initial symptoms are highly correlated with the location of the tumour in the eye. Peripheral tumours are often found due to lens displacement, secondary glaucoma or visual field defects, which occur in advanced tumour stages. However, the tumour may grow for months or years until detected. 33 % of the patient patients are asymptomatic at the time of initial detection [27]. Tumours near the optic nerve get recognised earlier because of the loss of sight, which often occurs due to the proximity to the macula [26]. 90 % of the uveal melanomas are located in the choroid, 6 % in the ciliary body and 4 % in the iris [28].

2.3 Treatment options and their indications

After diagnosis, the precise localisation and determination of the size are crucial to the therapy concept. Therefore, an ultrasound measurement and, in rare cases, a magnetic resonance tomography is performed. The height of the tumour, which describes the distance between the tumour base and apex, is measured in addition to the dimensions of the tumour base [29]. Some clinics also use 3D scans with ultrasound [30].

As with most tumours, many treatment options exist for ophthalmic tumours. The best option is chosen due to indications and contraindications. Next to systemic or local chemotherapy, cryotherapy, laser coagulation and resection, several radiation therapy modalities are considered, described in the following sections. If all eye-preserving therapies are contraindicated or fail, the eye must be removed entirely. This process is called enucleation. The primary target of all modalities is to remove or destroy tumour tissue to prevent further growth, while the secondary target is to spare as much healthy tissue as possible to minimise side effects.

The most established eye-preserving modalities for uveal melanoma are radiotherapy and surgical resection. For the two main irradiation techniques, brachytherapy and proton therapy, clinics often report a 5-year local tumour control rate of over 90 % [2, 11, 31–34].

All therapies have in common that the visual prognosis and complication rates depend on several variables, such as the location and size of the tumour and the applied dose, which is described more comprehensively in Ref. [35, 36]. Unfortunately, there is a lack of published randomised clinical studies which compare different irradiation techniques [26].

For brachytherapy, only few studies on the correlation of side effects and deposited dose in the corresponding structures exist. In addition, the studies are based on the treatment plan [37–39]. As the position uncertainty of the surgeon leads to high uncertainties for dose values in organs at risk (OARs), such correlations must be used with caution. Studies regarding conventional fractionated X-ray therapy present critical dose values for OARs, which should not be exceeded. To obtain a maximum risk of 3 to 7 % for radiation-induced optic neuropathy, the optic nerve must not be treated with more than a maximum dose of 55 to 60 Gy [40, 41]. Furthermore, the applied dose to the retina must not exceed the limit of a maximum dose of 50 Gy, as this increases the risk of blindness to at least 1 % [40, 41]. Additionally, for the same dose threshold, the risk of retinopathy is at least 44 % [42]. On the one hand, brachytherapy can not fall below this critical dose value because of the close distance between parts of the retina and the ^{106}Ru applicator. On the other hand, the tumour itself leads to partial vision loss itself. The deposited dose in the lens should be less than 5 Gy to avoid the risk of opacification [41, 43]. In the case of opacification, the lens may get surgically exchanged. This is an often performed procedure in ophthalmology.

2.3.1 Surgical resection

Different variations of resection all aim to conserve the eye and vision while removing threats of metastatic spread. The technical difficulties and concerns of surgical mistakes that lead to metastatic spreads are overcome in advanced centres [44]. Remnants of tumour tissue are locally treated with an endolaser. Surgical resection is often used to reduce tumour volume, as the volume is highly correlated to the Toxic Tumour Syndrome (TTS). This therapy is often combined with other modalities [33, 45, 46].

2.3.2 CyberKnife

Some clinics also report using stereotactic radiosurgery [4–6, 47, 48]. However, the reported eye retention rates vary from 70.3 % to 91.6 % [4–6]. Accordingly, it is lower than for brachytherapy and proton therapy, possibly due to the relatively low mean dose prescribed to the tumour volume. For example, in Ref. [4] the tumour was irradiated with 29 Gy.

2.3.3 Proton therapy

Another established modality to treat intraocular tumours is proton therapy. As this modality needs large gear, the modality is restricted to specialised centres, of which there are currently 108 worldwide [49]. However, only 20 centres treat ophthalmic tumours [12] because special equipment is needed. A typical setup for this therapy is shown in figure 2.2a.

Proton therapy uses the benefit of the Bragg peak in the dose profile, which is visualised in figure 2.2b. Its advantage lies in the steep distal fall-off after the maximum dose is reached at a certain distance, which can be calculated using the primary energy of the protons. By choosing a set of different energies, the bragg peak is spread out through the target volume [50–53].

The dose is typically applied in 4 to 5 fractions with a total of 56 to 70 Gy for uveal melanoma and 6 fractions with a total of 31.6 Gy for retinoblastoma [53]. These dose values include the relative biological effectiveness of protons which is usually assumed to be 1.1 [53, 55]. The eye position while therapy is maintained with the patient looking at a visual target. The therapy is interrupted if the staff observes too much movement on the live camera image. A safety margin of 2.0 to 2.5 mm is applied to the primary target volume resulting from the uncertainties of the therapy. If the precision of the measurements is very accurate and the patient is highly cooperative, safety margins may be reduced to prevent side effects of high dose in the optic nerve and fovea. Otherwise, tumours near the optic nerve may only be treated while the safety margin extends into the optical nerve or other important organs at risk [50–53].

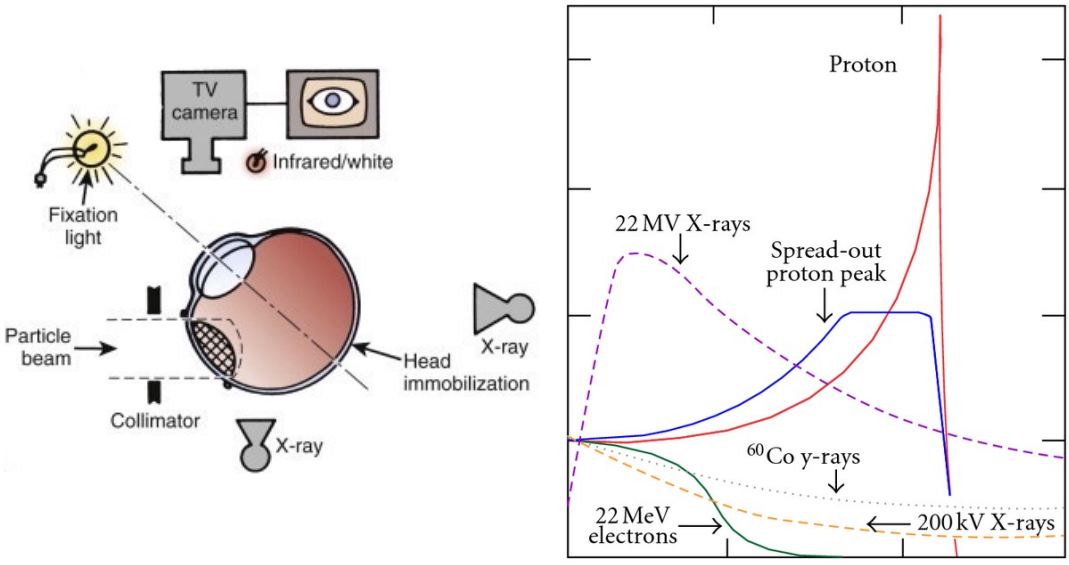

a) b)

Figure 2.2: a) Schematic of proton therapy obtained from Ref. [51]. b) Depth dose curves of a proton beam in direct comparison to other radiation qualities. The plot is acquired from Ref. [54].

2.3.4 Brachytherapy

Since the 1930s, brachytherapy has been used to treat intraocular tumours [14]. With the application of a radioactive source as close as possible to the tumour, the malignant tissue is destroyed by the radiation and the resulting deposited dose. Nowadays, the two most common types are ruthenium-106 and iodine-125 applicators, which are displayed in figure 2.3. In the past and rarely today, other nuclides, e.g. strontium-90, palladium-103, cobalt-60 and caesium-131, have been used. The encapsulated radio nuclide emits beta and/or gamma particles.

Under general or local anaesthesia, the applicator is sutured to the eye. Localisation of the tumour and positioning of the applicator is done by indirect ophthalmoscopy and transillumination. Since 2022, the manufacturer of the ruthenium applicators BEBIG[3] also provides the so-called Damato Templates as a positioning aid [56, 57]. According to Ref. [58], some clinics use intraoperative or postoperative ultrasound to check the position of the applicator.

[3]Eckert & Ziegler BEBIG GmbH, Berlin, Germany.

Figure 2.3: Presentation of various applicators for ophthalmic brachytherapy. 1 to 3: ^{106}Ru applicators of different type. Number 2 has a cutout for the optic nerve. 4 to 6: Compartments of a COMS applicator: the silicone carrier (4), the iodine seeds (5) and the calotte (6). The picture is obtained from Ref. [59].

COMS applicators

The COMS applicator is the most widely used type of ^{125}I applicators [14]. The compartments of a COMS applicator comprise a golden calotte and a silicone carrier into which iodine seeds are inserted, as shown in figure 2.3. ^{125}I decays with a half-life of approximately 60 d [15] by electron capture into an excited state of tellurium-125. During this decay, photons with a maximum energy of 35.5 keV are emitted [15]. COMS applicators are the most common brachytherapy method for ophthalmic tumours in North America due to the early standardised methods and a 12-year study that showed both the benefits and relatively high tumour control rates for this eye-preserving therapy in comparison to enucleation [14]. The 2D dose profile and Depth Dose Curves (DDCs) are shown in figure 2.4. Due to the dose gradient COMS applicators are mostly used for maximum tumour heights of 10 mm [14].

Ruthenium-106 applicators

Due to several studies, e.g. Ref. [31, 60–62], ^{106}Ru applicators are the common brachytherapy source to treat ophthalmic tumours in Europe. Figure 2.3 displays three of many different models. One of them has a cutout which allows the applicator to be positioned very close to the optic nerve. The plaque consists of a silver calotte in which the radioactive isotope is deposited on a thin gold foil. ^{106}Ru is a beta emitting isotope with a half-life of 371.5 d and a maximum energy for the e^- of 39.4 keV. While these electrons have no therapeutic use, the follow-up isotope ^{106}Rh decays by emitting e^- with a maximum energy of 3.5 MeV and a half-life of 30.1 s. The decay of ^{106}Rh partially leads to an excited state of ^{106}Pd. The two most probable energies are 512 keV and 622 keV [15]. The concave side resembles a 0.1 mm thick exit window for the electrons, while the back of 0.9 mm silver absorbs most of the particles [63]. A ^{106}Ru applicator dose profile is presented in figure 2.4. At 5 mm distance approximately 20 % of the dose rate remains.

The dose rate of an active ^{106}Ru applicator is usually in the range of 7.2 to 12.0 Gy/h at the concave surface [14, 32, 64–66].

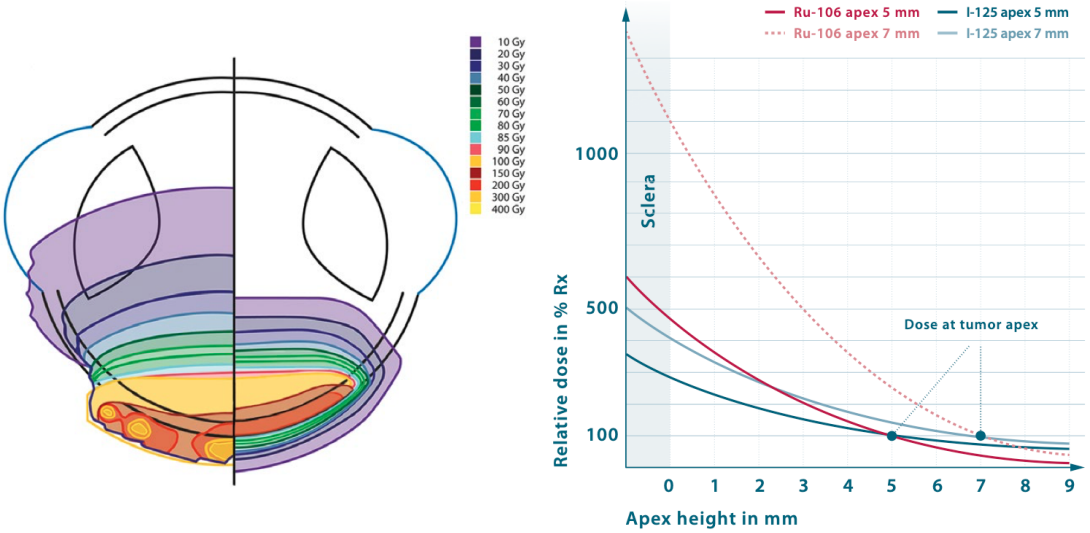

a) b)

Figure 2.4: The dose profiles of the two most common brachytherapies for intraocular tumours: COMS- and ^{106}Ru applicators. a) The two-dimensional dose profile of a COMS applicator is shown on the left in comparison to the dose profile of a ^{106}Ru applicator on the right. b) The depth dose curves, normalised to 100 % at 5 and 7 mm. Both figures are acquired from Ref. [65].

Dose concept: Unlike many other radiation therapies, there is no generally accepted dose prescription when working with ^{106}Ru applicators. There is no generalised explicit dose prescription in literature but only an overview of current practices. The American Brachytherapy Society - Ophthalmic Oncology Task Force advises that the dose prescription point is the tumour apex, the point of maximal thickness. Furthermore, the isodose line of the prescribed dose should enclose the entire target volume [14]. The European Society for Radiotherapy & Oncology recommends a dose of 100 Gy at the tumour apex [64].

Many publications state a prescribed dose of 100 Gy at the tumour apex, which is mainly based on empiric data [38, 61, 67–71]. Meanwhile, some groups report higher values of up to 150 Gy [32, 39, 72, 73]. The increased dose is justified with higher tumour regression rates and small changes regarding side effect rates [32]. Another concept is published in Ref. [74], in which the tumour height was not taken into account, but the dose profile was adjusted to 85 Gy in 5 mm distance to the plaque. A similar concept with 100 Gy in 5 mm was used in Ref. [33], but precedent transscleral tumour resection has been performed in this particular study.

The UKE published their dose prescription concept and their considerations leading to it [16]. This concept takes many different uncertainties into account and recommends a minimum dose of 130 Gy at the apex and a dose range of 700 to 1500 Gy for the sclera contact dose. This is the dose in 0.5 mm distance to the ^{106}Ru applicator on its central axis. Of course, individual cases might be treated differently in close communication with the patient. The type of ^{106}Ru applicator is mainly chosen due to the tumour dimensions. If the tumour is close to the optic nerve, a ^{106}Ru applicator with an appropriate notch is used. However, a hospital may not always have every type of ^{106}Ru applicator available for economic reasons. This might result in the decision to apply the next bigger type of ^{106}Ru applicator. In addition, bigger ^{106}Ru applicators are indicated for tumours with small tumour base area but large apex height due to the depth dose curve of the different models. This results in larger irradiated parts of the eye which are not yet affected by the tumour.

In general, medical physicists calculate the time of application by all given parameters, including the tumour dimensions, the activity of the chosen applicator and the corresponding depth dose curve. Many clinics, including the UKE, use their self-written software for treatment planning. These programs are often based on Microsoft Excel® and Visual Basics® for Applications. The 'Plaque Simulator'[4] is a published planning software with no official medical product certification often used to extend the treatment planning.

Because of the steep depth dose gradient of the electrons and the dose prescription, each applicator model has a maximal treatable tumour height. Simulations showed that tumours with a height of up to 5 mm are generally treatable [77]. Accurate knowledge of the tumour dimensions and precise positioning is needed for larger tumours to ensure correct irradiation [77]. Brachytherapy with ^{106}Ru applicators is performed with tumours measuring up to 7 mm in height, as stated in Ref. [16, 17].

Uncertainties: Diagnostic ultrasound, also called sonography, is used to determine the dimensions of the tumour in most cases. The height is often measured with the help of an axial scan and is limited by the resolution of the ultrasound, which is in the range of 0.1 to 0.2 mm [78]. In case of 3D sonography, a value of 0.15 mm is reported [30]. The sclera thickness between the tumour and the plaque should also be known for exact dosimetry. This results from the fact that the sclera varies in thickness depending on the location and between the eyes of different patients. Sclera thicknesses in the posterior half of the eye are reported to vary in the range of 0.05 to 1.52 mm [79]. The tumour base is determined by magnetic resonance image or ultrasound. The uncertainty resulting from the resolution of the 3D scan is 0.5 mm [30]. The intraobserver variability is stated to be in the range of 0.7 to 1.2 mm when a B-scan is used to measure the basal length of the tumour [80]. Regarding MRI, a dedicated three-element micro coil array can be used. It allows in vivo images with a resolution of 0.5 mm without visible motion effects [81].

[4] Eye Physics, LLC: Plaque Simulator, see Ref. [75, 76] for more information.

The accuracy of the applicator placement within the surgery varies due to several parameters, such as the location of the tumour in the eye and the surgeon's experience. For example, a tumour in the posterior half of the eye is harder to reach with an applicator [82]. No study, which has quantified the position uncertainty for ^{106}Ru applicators, has been found in published literature. Regarding COMS-plaques, an analysis has been performed with 29 patients undergoing an additional ultrasonic after placement to verify the position [83]. The results are fitted with a normal distribution and the standard deviation of 1.35 mm is assumed to quantify the position uncertainty [84]. Bleedings and other physical changes can result in a tilted applicator. This may result in insufficient treatment of the tumour [85].

Regarding the dosimetric values the manufacturer reports an uncertainty of 20 % for a confidence interval of 95 % in the certificates of the ^{106}Ru applicators [86]. The certificates of more recently produced ^{106}Ru applicators state the uncertainty to be 11 % [87].

Bi-nuclide plaques

At the UKE, highly prominent ophthalmic tumours were treated with so-called bi-nuclide applicators. They contain a ^{106}Ru applicator and ^{125}I seeds. Due to the combination, tumours exceeding the treatable size of ^{106}Ru applicators can be irradiated with a new apex height limit of 9 mm [2]. Compared to COMS plaques, which can be used to treat the same tumour sizes, the dose deposited in healthy tissue is significantly lower [2, 59]. Since 2021, the bi-nuclide applicators are no longer used because the corresponding medical device approval for the used ^{106}Ru applicator type has expired [88].

2.4 Treatment of highly prominent tumours

There is no consensus in science and clinical practice for highly prominent tumours on which modality is best suited for treatment.

As already described in section 2.3.4, all brachytherapy options have a limitation in tumour height due to the corresponding dose gradients. A recent project focussed on the utilisation of micro collimators for ^{125}I-seeds in applicators to overcome this problem [89–92]. Unfortunately, one of the results of this project was that around 30 to 80 % of the dose rate is absorbed. Thus, the method requires seeds with a higher activity than currently available [89–92]. The combination of transpupillary thermotherapy and brachytherapy for treating highly prominent tumours also showed no significant difference in tumour control rates and metastasis rates [46]. Due to reported complications and uncertainties of transpupillary thermotherapy, this modality is nowadays only used for flat marginal areas of tumour tissue at the UKE.

A systematic review of clinical studies shows potentially higher complication rates for patients with particle therapy treatments than brachytherapy [93]. Those complications include vision loss, enucleation, and neovascular glaucoma, and arise approximately 1.5

to 2.0 years after treatment. However, the review was limited due to various study designs, patient inclusion criteria, sample sizes, and follow-up times. Also, the stated complication rates might be biased due to the focus on specific tumour types, such as highly prominent tumours or those located near the optic nerve [93].

In addition, the side effect called Toxic Tumour Syndrome (TTS) is reported. TTS describes ischemic and exudative tumour tissue after treatments, which may spread and lead to severe complications such as macular oedema, retinal detachment, and neovascular glaucoma [45, 50]. Clinics combine surgical resection with radiation treatment modalities to overcome the problem of TTS and other complications due to radiation treatments of highly prominent tumours [33, 45]. However, the resection may be individually contraindicated due to the general risks of the surgery and the corresponding anaesthetics. In addition, endoresection bears the risk of metastatic spread, though advanced centres have low complication rates [44].

This means there is limited access to bulb-preserving modalities for patients with large tumours. Moreover, higher complication rates have to be expected after treatment [93].

All described points result in the motivation to find a modality that is easily accessible for most patients and which enables a homogeneous dose profile within the tumour, even if it is highly prominent. A high dose deposition in parts of the tumour, especially the tumour base, shall reduce the risk of TTS. The combined therapy concept, presented and analysed in this work, shall fill this gap and consists of both brachytherapy with ^{106}Ru and EBRT with X-rays.

2.5 X-ray therapy

Low Energy X-rays with an energy range of 10 to 300 kV is a widely spread modality. Approximately 50.000 patients with benign, non-malignant or functional disorders are treated with this modality yearly in Germany. Even though the concept of the so-called Orthovolt therapy is rather old, there is a positive trend in the number of patients treated and investments [94].

To produce a clinically usable photon spectrum, an X-ray therapy unit is required. The system consists of a vacuumed glass bulb containing the cathode and the anode, as shown in figure 2.5a. With a constant heating voltage, electrons are emitted by the cathode and then accelerated towards the anode with an electric field. The anode is usually made of a mix of tungsten and other materials to increase thermal conductivity and resistance to mechanical stress while a high yield of photons is achieved. Due to the interactions between the accelerated electrons and the anode, photons are produced resulting from two effects: bremsstrahlung and impact ionisation. These effects result in a photon energy spectrum, as shown in figure 2.5b. It consists of both a continuous and a material-specific line spectrum. This line spectrum is called characteristic X-rays [95].

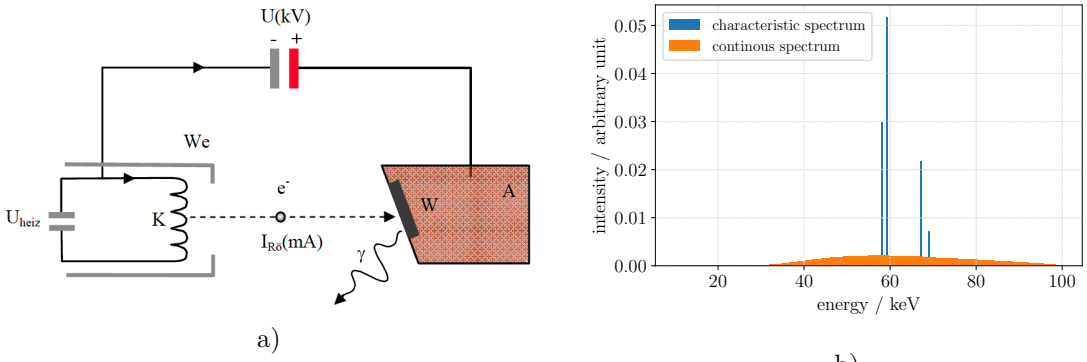

Figure 2.5: a) Schematic of an X-ray therapy unit. It comprises the cathode K and the anode A. Electrons produced by U_{heiz} are accelerated with the voltage U and add up to the current $I_{\text{Rö}}$. The illustration is obtained from Ref. [95]. b) Typical X-ray spectrum with an accelerating voltage of 100 kV. The filtering consists of 1 mm beryllium and 0.5 mm copper. The spectrum is calculated with the software SpekCalc, described in section 4.2. For visualisation reasons, the bars of the characteristic spectrum are displayed 4 times wider than their bin width.

Higher acceleration voltages are meant for deeper treatments. Therefore, the lower energetic part of the spectrum is counterproductive, as those photons deposit their dose in tissues near the surface. With additional filtering in the form of, for example, 1 to 2 mm aluminium or copper, the spectrum is hardened. This means the mean energy of the spectrum is shifted towards the maximum energy. Further information can be found in Ref. [95].

Successful treatments with low-energy X-rays and a small number of fractions are published in Ref. [96, 97]. Malignant skin tumours are treated with a minimum of 3 fractions [96]. In addition, small superficial skin carcinomas were irradiated with 18 Gy, 20 Gy and 22.5 Gy in a single fraction of either 45 keV or 100 keV X-rays [97]. More information on the treatment with low energy X-rays can be found in Ref. [98].

2.6 Interaction of particles with matter

As this thesis is focused on ^{106}Ru applicatorsand external X-ray therapy, only electron and photon interactions are presented. The information has been taken from Ref. [99, 100], if not explicitly stated otherwise.

2.6.1 Photon interactions

For monoenergetic photons, the exponential law describes the decrease of the intensity I after passing a distance d in matter:

$$I(d) = I_0 \cdot e^{-\mu d}, \tag{2.1}$$

where I_0 resembles the intensity at $d = 0$. The specific total attenuation coefficient μ depends on the photon energy E_γ and the material. It is defined as the sum of the coefficients for the most dominant interactions: the photoelectric effect τ, Compton scattering σ_C and pair production κ.

$$\mu = \tau + \sigma_C + \sigma_R + \kappa \tag{2.2}$$

Photoelectric effect: For energies up to $E_\gamma < 30\,\mathrm{keV}$, the photoelectric effect is dominant. The photon hits an electron, which absorbs the entire energy of the photon. The kinetic energy of the electron E_{e^-} after the impact is the difference between E_γ and the binding energy E_B. τ correlates with E_γ and the ordinal number Z by $\tau \sim {}^{Z^n}/_{E_\gamma^3}$ with $n = 4.0$ to 4.5 [100].

Compton scattering: The inelastic interaction of the photon with an outer, weakly bound electron while only transferring a fraction of its energy is called Compton scattering. The photon is deflected and the electron leaves the atomic shell. For $200\,\mathrm{keV} < E_\gamma < 10\,\mathrm{MeV}$ compton scattering is the dominant effect in most materials with $\sigma_C \sim Z \cdot E_\gamma^{-n}$ with $n = 0.5$ to 1.0 [100].

Pair production: If the energy of the photon is greater than the energy-mass equivalent for two electrons $E_\gamma > 2 \cdot 511\,\mathrm{keV}$, the photon can spontaneously transform into an electron-positron pair in the Coulomb field of an atomic nuclei. The exceeding energy is distributed as kinetic energy to the two particles. The pair production coefficient $\kappa \sim$ depends on the initial energy of the photon E_γ and the ordinal number Z [100]:

$$\kappa \sim Z \cdot \rho \cdot \log(E_\gamma). \tag{2.3}$$

2.6.2 Electron interactions

Due to their mass and charge, electrons have a much higher Linear Energy Transfer (LET) than photons. The LET is defined as the total energy loss of the particle over the distance covered $\mathrm{LET} = {}^{\mathrm{d}E}/_{\mathrm{d}x}$. Many interactions can occur, e.g., elastic scattering, inelastic scattering, hard collisions, and inelastic Coulomb scattering. The energy loss by those interactions is described as the total stopping power, which is the sum of the impact deceleration and the radiation deceleration

$$S = \frac{\mathrm{d}E}{\mathrm{d}x} = S_{\mathrm{col}} + S_{\mathrm{rad}}. \tag{2.4}$$

Radiation deceleration: The deflection of a charged particle produces radiation in the form of photons. Due to the German term 'bremsen' for decelerating, it is also called bremsstrahlung. Radiation deceleration occurs due to the interaction between an electron and the atomic nucleus of the material it travels through. The stopping power for bremsstrahlung for electrons with $E_{e^-} < 10\,\mathrm{MeV}$ is described in Ref. [100] with

$$S_{\mathrm{rad}} = \left(\frac{\mathrm{d}E}{\mathrm{d}x}\right)_{\mathrm{rad}} = 1.745 \cdot 10^{-3} \cdot \frac{\rho Z^2}{A} \cdot E_{e^-}. \tag{2.5}$$

In this formula, A resembles the mass number and E_{e^-} the total energy of the electron.

Impact deceleration: The so-called Bethe-Bloch formula describes the energy loss by collisions for heavy charged particles. For lighter particles, such as electrons, modifications resulting from the different calculations for hard binary collisions are necessary and lead to the Berger-Seltzer-formula. With all constants taken into account, the collision braking power is defined in Ref. [100] as

$$S_{\mathrm{col}} = \left(\frac{\mathrm{d}E}{\mathrm{d}x}\right)_{\mathrm{col}} = 0.15 \cdot \rho \cdot \frac{Z}{A} \cdot \frac{e^2}{\beta^2} \cdot R^*_{\mathrm{col}}(\beta), \tag{2.6}$$

where e is the electron charge and $\beta = {}^{v}/_{c}$ with the speed of the particle v and c the speed of light. $R^*_{\mathrm{col}}(\beta)$ is a residual function. Additional information can be found in Ref [100, 101].

2.7 Radiobiological effects

Radiation generally leads to deposited energy in tissue by interacting with atoms and results in changes in the molecular structures. According to Ref. [102, 103], several physical and biological effects have to be considered to determine the damage to both malignant and healthy tissue. The most common physical value to quantify the effects of radiation is dose. It is defined in Ref. [102] by the deposited energy $\mathrm{d}E$ per mass $\mathrm{d}m$ in a Volume $\mathrm{d}V$ with its density ρ:

$$D = \frac{\mathrm{d}E}{\mathrm{d}m} = \frac{\mathrm{d}E}{\rho \cdot \mathrm{d}V}. \tag{2.7}$$

The unit used for dose is $\mathrm{Gy} = {}^{\mathrm{J}}/_{\mathrm{kg}}$. The effect on cells with the same dose varies for different radiation qualities. Accordingly, the quality factor Q is introduced, which is correlated to the LET. The equivalent dose H is calculated as the product of D and Q [102]:

$$H = D \cdot Q(\mathrm{LET}), \quad \text{with} \tag{2.8}$$

$$Q(\mathrm{LET}) = \begin{cases} 1, & \mathrm{LET} \leq 10\,\mathrm{keV/\mu m} \\ 0.32 \cdot \mathrm{LET} - 2.2, & 10\,\mathrm{keV/\mu m} \leq \mathrm{LET} \leq 100\,\mathrm{keV/\mu m} \\ \frac{300}{\sqrt{\mathrm{LET}}}, & \mathrm{LET} \geq 100\,\mathrm{keV/\mu m}. \end{cases} \tag{2.9}$$

Of course, Q might change its value if radiation travels through matter due to the energy losses and the resulting change of the LET. Photons and electrons always have a $\mathrm{LET} < 10\,\mathrm{keV/\mu m}$ [102], while for protons the quality factor is often used as $Q = 1.1$ [55]. There are ongoing discussions on the change of the LET of protons on their path through tissue and a resulting varying Q value [104–108].

The physical processes of energy deposition lead to ionisations, chemical changes and the production of free radicals and happen on a timescale of 10^{-18} to $10^{-14}\,\mathrm{s}$. Afterwards, the chemical phase begins, in which the free radicals react within milliseconds, while other reactions occur after seconds or even minutes. The last phase is called the biological phase. Enzymatic and regulatory processes may lead to cell death, cell division and partial or complete repair. These processes may occur on very different time scales between seconds and years. Though damage to the cell affects all compartments, the deoxyribonucleic acid is particularly interesting, as it stores genetic information. Due to this reason, radiation damage to the deoxyribonucleic acid affects not only the living cell but also all daughter cells after cell division if the damages are not repaired in the meantime [103].

The effects following from radiation are categorised in the following two groups.

Deterministic effects: If the dose applied to a cell exceeds a certain threshold, the cell will be damaged irreparably in the short to medium term. This results in either apoptosis, a necrotic cell or non-viable daughter cells. If a larger group of cells is affected, this can lead to partial or complete failure of the organ [102, 103].

Stochastic effects: Even dose values much smaller than such thresholds can already impair the cells. These radiation effects lead to damages or mutations, which affect the cell in the long term. For example, healthy tissue might become malignant after being irradiated. The probability for such effects is correlated to the applied dose [102, 103]. Therapeutic modalities aim at dose values significantly higher than the threshold in the target volume to cause severe damage in tumour cells.

The clonogenic assay is used to quantify the effect of radiation on cells in experiments. The percentage of cells that can form colonies depends on the applied dose and can be described with the linear-quadratic model. Within this model, the survival fraction SF is given as

$$\mathrm{SF}(D) = \mathrm{e}^{-\alpha D - \beta D^2}. \tag{2.10}$$

The parameters α and β are calculated for different tissues from experimental data. This model is only valid for doses in the range of 1 to 6 Gy per fraction. The linear-quadratic

model predicts an ever-increasing slope for higher values, which can not be verified by the multi-target models and experimental data [103].

Conventional teletherapy often uses fractionated irradiation. This means the total target dose D_{tot} is not applied in one session but divided into several fractions over several days. This derives from the repair mechanisms of the cells. The difference of the survival fraction for fractionated irradiations correlates with both the dose per fraction D/fx and the ratio of α and β. The higher the ratio of α/β, the higher the effect of fractionation [103]. Because malignant cells mainly show lower α/β-ratios than healthy cells, fractionation is beneficial in teletherapy, resulting in fewer side effects. Typical numbers concerning conventional photon therapy are in the range of $D_{\text{tot}} = 40$ to $70\,\text{Gy}$ and 15 to 35 fractions [103].

The ratio of α and β gives an in-vitro approximation. In contrast, humans are affected by a significant number of free variables. Furthermore, the survival fraction can not be established in-vivo. Due to those reasons, dose-response relationships, also called dose-effect curves, are used as quantitative measures. These data are obtained for malign and healthy tissue using the fixed endpoint data of tumour control probability and normal tissue complication probability. Dose-effect curves have the form of a sigmoidal function. The space between the tumour control probability and the normal tissue complication probability curves is called the therapeutic window and gives the probability of maintaining tumour control without complications. Physical parameters are chosen to maximise the therapeutic window for a successful therapy [103].

2.8 Dose-volume histograms

The information regarding the irradiation of an organ is commonly visualised with the cumulative dose-volume frequency distribution, which is called Dose-Volume Histogram (DVH) for short. It visualises the dose distribution throughout the organs of interest, such as the primary target volume or any OAR [109].

As first described in Ref. [109], the volume percentage $V^{\text{O}}(D)$ is displayed as a function of the dose D for an organ O, as shown in figure 2.6. The volume percentage V^{O} is defined as the cumulative volume V_C^{O}, which received a dose equal to or greater than the dose D, over the total volume of the organ $V_{\text{tot}}^{\text{O}}$. For example, if for the given dose threshold $D_{\text{T}} = 1.76\,\text{Gy}$ a volume percentage of $60\,\%$ of the choroid is calculated, this is written as $V_{1.76\,\text{Gy}}^{\text{choroid}} = 60\,\%$ in the following.

Using the inverse definition, the dose D_V^{O} is computed as a function of the volume percentage V^{O}. The notation $D_{60\,\%}^{\text{choroid}} = 1.76\,\text{Gy}$ describes that $V = 60\,\%$ of the choroid received at least $1.76\,\text{Gy}$.

Though both definitions offer the same information, the notations are used with different meaningfulness depending on the given and computed value.

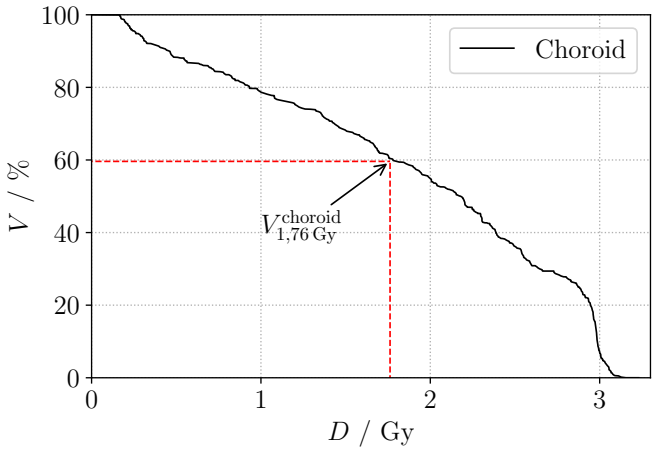

Figure 2.6: An exemplary dose-volume histogram. It displays the volume percentage V as a function of the dose D. The example of $V^{\text{choroid}}_{1.76\,\text{Gy}} = 60\,\%$ is displayed additionally.

Regarding tumour treatment, in an ideal treatment plan, the tumour is irradiated homogeneously with the prescribed dose D_P. This means the corresponding DVH is a rectangle and the area under the curve becomes exactly $1 \cdot D_\text{P}$. For the OARs, it would be best to apply no dose at all. Of course, due to their locations, this might not be possible. To reduce the risk of side effects the area under the curve or a critical value should be minimised.

3 Brachytherapy meets X-rays

In this chapter, a novel therapy concept to treat larger ophthalmic tumours is presented. It was developed in collaboration with Dirk Flühs[5] and Bernhard Spaan[6].

The combined therapy concept comprises brachytherapy and EBRT with soft X-rays. While the ^{106}Ru applicator is positioned on the eye and mainly irradiates the tumour base, simultaneously performed X-ray therapy applies a dose boost to the tumour apex via confocal irradiation, as visualised in figures 3.1a and 3.2. This results in a more homogeneous dose distribution in the target volume than with stand-alone brachytherapy. The entry points of the X-ray beams are positioned in the pars plana, which is a relatively insensitive area [110, 111]. The stereotactic radiotherapy device designed by Oraya[7] already used this approach to treat macular degeneration. The macula was irradiated to treat this disease with three X-ray beams entering the eye at the pars plana [111].

The novel combined therapy concept is expected to apply low dose values in OARs, such as the lens or the choroid. This shall reduce the risk of side effects and enhance the visual outcome. The X-ray beams are intended to hit the ^{106}Ru applicator after passing the tumour. As the plaque resembles a 1 mm thick silver target, it is expected that more than 90 % of the photons are absorbed. Accordingly, the plaque can also be referred to as a beam stop next to its actual purpose as a treatment modality. The presence of such an absorber significantly reduces the dose in healthy tissue behind it. Because the intention is that the X-ray beams hit the ^{106}Ru applicator, this concept best suits tumours located in the posterior part of the eye.

Therapy with X-rays alone could also be conceivable. However, the high dose applied by the ^{106}Ru applicator in healthy tissue near the base of the tumour is supposed to be advantageous. It provides basal vascular occlusion, possibly minimising the spread of ischemic tumour cells.

The X-ray therapy unit has to be flexible and precise in positioning to enable confocal irradiation with minimal uncertainties. An example of an established X-ray therapy

[5] Dr. rer. nat. Dirk Flühs, medical physics expert at the UKE, responsible for brachytherapy, including afterloading and treatment of ophthalmic tumours with COMS and ^{106}Ru applicators.

[6] Prof. Dr. rer. nat. Bernhard Spaan, physicist and professor at the Technical University Dortmund, research topics: high energy particle physics and medical physics, deceased December 2021.

[7] Formerly Oraya Therapeutics Newark, California, USA. Now Carl Zeiss Meditec AG, Jena, Germany.

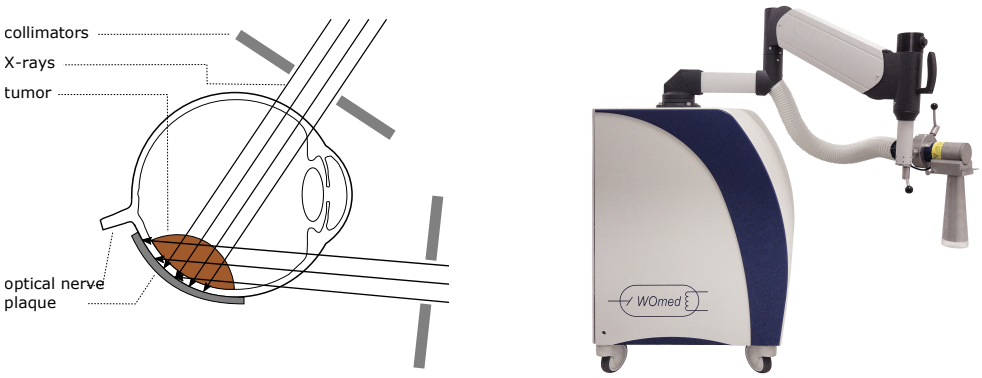

a) b)

Figure 3.1: a) The novel combined therapy concept. X-ray beams enter through the pars plana and irradiate the tumour in addition to the simultaneously performed brachytherapy. Most particles travelling through the target volume are absorbed in the ^{106}Ru applicator. For illustration reasons, only two X-ray beams are visualised. b) A T-105 X-ray therapy unit distributed by WOmed. The graphic is acquired from Ref. [112].

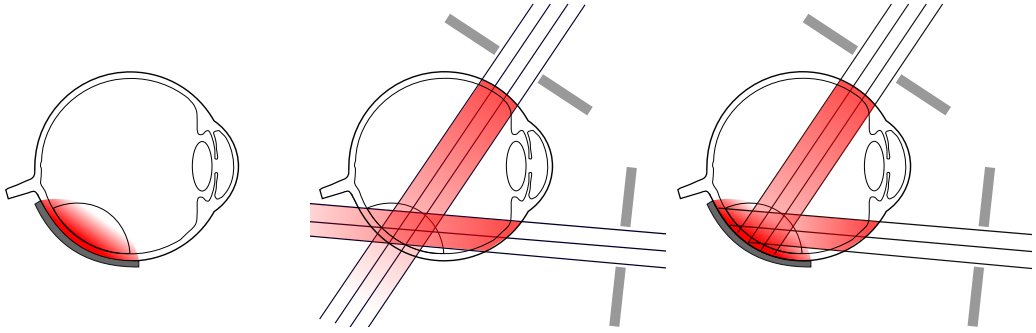

a) Brachytherapy b) X-ray therapy c) Combined concept

Figure 3.2: Illustration of the dose profiles of a) stand-alone brachytherapy with a ^{106}Ru applicator, b) stand-alone X-ray therapy and c) the combined therapy concept. For illustration reasons, only two X-ray beams are visualised. The dose is not to scale.

unit[8] is shown in figure 3.1b. As stated in section 2.5, such X-ray therapy units are already used for surficial treatments. The system is provided with a hydraulic spring arm. However, a more precise positioning system for the X-ray tube is indispensable. Therefore, it is intended to include a robotic device as a motorised positioning aid for the X-ray tube.

[8]Wolf Medizintechnik GmbH (WOmed), T-105

An additional position uncertainty derives from the patient's eye movement. The stereotactic radiotherapy device designed by Oraya to treat wet age-related macular degeneration already overcomes this problem with an eye fixation system, which is illustrated in figure 3.3. The system uses a sterile and disposable contact lens, placed centrally on the corner and sclera. The eye is kept in place by a light suction mechanism. Furthermore, the machine has an eye-tracking device integrated. This allows observing the eye position continuously and automatically shutting down the radiation treatment when excessive eye movement is detected [111]. This or a similar device is also intended to be used for the combined therapy concept as well. Due to the combination of the eye fixation system and the robotic guidance of the X-ray tube, small position uncertainties are expected.

a) b)

Figure 3.3: Illustration of the positioning system used for the stereotactic radiotherapy device designed by Oraya. a) 3D animation and b) photo of the system in use. The figures are obtained from Ref. [111].

Compared to current modalities, which are already able to treat tumours with apex heights of $> 6.5\,\mathrm{mm}$, the integrated concept has the advantage of confocal irradiation treatment planning. This results in a clinical advantage of the novel concept, as the user has control over the exposure of organs at risk with the help of the irradiation position, beam direction and dose rate of the X-ray therapy unit.In addition, the dose deposition of every X-ray beam and the ^{106}Ru applicator can be weighted individually to obtain an optimal dose profile. Thus, the collateral damage in OARs is significantly lowered. This might result in fewer side effects and greater visual outcomes. If a dose of 80 to 100 Gy can be delivered to the total tumour volume, a high tumour regression rate is foreseen. Moreover, fewer side effects may occur compared to established modalities to treat large intraocular tumours.

4 Basic Methods

To analyse the previously described therapy concept, several common methods are used and therefore introduced in the following.

4.1 3D modelling

In this work, the software Fusion360[9] and Inventor[10] are used for 3D modelling. Both are integrated commercial computer-aided design (CAD) software packages which offer many functionalities. The ability to set dependencies while creating sketches or volumes is particularly noteworthy. In this way, the programs offer the option of reducing the amount of work required in the event of possible changes to the model. Furthermore, Fusion360 provides an application programming interface, which allows automating the modelling with the help of scripts. These scripts can contain general Python or C++ code and commands provided by Fusion360 [113–116]. All scripts developed in this work are written in Python.

4.2 Computation of X-ray energy spectra

To obtain energy spectra of X-rays for certain parameters, the software SpekCalc[11] is utilised. It is based on a combination of theory, MC simulations and experimental data sets. The user can enter different parameters for the X-ray therapy unit, such as external filtering and acceleration voltage. SpekCalc then calculates the energy spectrum in a user-defined energy binning [117–119].

4.3 Monte Carlo simulation with Geant4

The calculation of dose profiles quickly becomes very complex for setups larger than a simple example. MC simulations are omnipresent to solve this problem. Developed to

[9] Autodesk® Fusion 360®. `www.autodesk.de/products/fusion-360`.
[10] Autodesk® Inventor®. `www.autodesk.de/products/inventor/`.
[11] SpekCalc, developed by Gavin Poludniowski and Phil Evans at The Institute of Cancer Research, London, UK. `http://spekcalc.weebly.com`

answer questions in high-energy physics, Geant4[12] is a framework written in C++ and published by the Geant4 Collaboration [120]. After several other brachytherapy sources, a simulation of a ^{106}Ru applicator using Geant4 was presented, including the source code of the simulation [63].

The dose distribution within a volume is determined for irradiating particles by the solution of the transport equation. Such a linear integral differential equation can be solved only under enormously simplified assumptions. Even the generation of secondary particles during the radiation effects, which is elementary for the dose contribution of the incident radiation, complicates this immensely. The MC method uses another approach to obtain the desired results. Though it is based on the fundamental laws of incident particles with matter, it does not solve the transport equations. Instead, in a MC simulation, many primary particles are generated and tracked through matter. All secondary particles, which are generated from randomised interactions, are also observed. The randomisation takes well-known data and cross-sections of effects into account. Therefore, simulations are close to measured results if physics parameters, geometries, material compositions and other variables are chosen accordingly [121]. As this method is based on randomised algorithms, many trajectories must be simulated to assess statistically accurate data. MC simulations are the gold standard for calculating dose distributions [120, 122].

Most important for low-energy applications is the choice of particle interaction algorithms. The used set[13] of interactions in all simulations presented in this thesis is based on the recommendations in Ref. [63]. The data are derived from the Livermore data libraries [123]. The configuration uses multiple scattering algorithms to determine the simulated path of a charged particle. The algorithms are based on the mathematical and physical theories published in Ref. [124–126]. The simulation includes a threshold called `cut-value` c that defines when a particle is not simulated any more. If a particle reaches an energy that results in a range smaller than c, it is deleted, and its energy is deposited at its current position. Accordingly, this threshold compromises resolution and computing time [121]. For all simulations in this thesis, c was set to 0.01 mm based on the information presented in Ref. [63]. By implementing the class `G4RadioactiveDecays`, a library with data on the entire decay chains of radioactive atoms is included. The data are derived from the Evaluated Nuclear Structure Data File (ENSDF), maintained by the National Nuclear Data Center of the Brookhaven National Laboratory [127].

All simulations presented in this thesis have been performed with Geant4 version 10.06. They are based on the simulation code published in Ref. [63] and the basic examples No. 2 and No. 3a of the official Geant4 examples.

[12] Geant4, free software published and maintained by the Geant4 Collaboration. `https://geant4.web.cern.ch`

[13] The configuration is included via the physics list `G4EmStandardPhysics_option4`.

STL implementation: Geant4 allows the definition of a particular set of basic geometries. Because the simulations presented in this thesis need more complex structures, the Geant4 library `CADmesh` is included [128]. This package allows the implementation of Standard Triangle Language or Standard Tessellation Language (STL) files which can be created with a 3D-modelling software, such as Fusion360 - see section 4.1. STL-files approximate the surface of a volume with many triangles. Thus, simulations with imported STL-files need more calculations to track the path of a particle and to determine in which volume the particle currently is. In Ref. [129], it was proven that the different qualities of exported STL-files have no impact on the results. Implementing this mechanism into the workflow was performed and documented in Ref. [129].

Data acquisition: The process of obtaining certain data or physical values within the MC simulation is called scoring. Two different techniques are used in this work to acquire such values. A Command Based Scorer (CBS) is implemented as a scoring mesh in a virtual parallel world into a simulation by simple command execution. For example, a simple volume like a cylinder or a cuboid can be used to measure dose. Due to its definition of being positioned in a parallel world, it does not interfere with the particles though it can still track them and score different physical parameters. To get a resolution within the volume, it can be binned. However, the amount of CBS is limited [121].

More complicated shapes can not be obtained with CBS. The definition of Sensitive Detectors (SDs) solves this problem. Every volume included in the simulation can be turned into a sensitive scorer. This results in the possibility of modelling a complex shape in 3D modelling software and defining it as a sensitive scorer after importing it with `CADmesh`.

Primary particle production: Geant4 simulations rely on generating primary particles, which the simulation tracks. In this work, two methods have been used to define those primary particles: `G4ParticleGun` and `GeneralParticleSource` (GPS). The latter allows implementing particles more easily via commands prompted to an already running Geant4 simulation or in a macro file. However, GPS is limited to a certain set of commands, but it is sufficient to include either radioactive atoms or X-rays in the simulation. Point-wise energy spectra for those X-rays can be derived from text files, which are lineary interpolated.

All simulations presented in this thesis are repeated with different seeding to obtain statistically independent results, which are averaged. Therefore, the uncertainty of simulated dose values is assumed by the standard error of the mean.

More information regarding Geant4 in general or the scoring processes can be found in the official documentation, see Ref. [121].

5 Measurements regarding the absorption of X-rays

To evaluate the feasibility of the ^{106}Ru applicator to serve as a beam stop for the combined therapy concept, measurements are performed with a novel phantom, which is constructed and built only for this purpose. Three different detector types are used to obtain the dose profiles.

Due to the complexity, the planning was performed in close cooperation with the construction office of the TU Dortmund University physics faculty. The construction and milling of the phantom were undertaken by the mechanical workshop of TU Dortmund University. The preparation laboratory of the TU Dortmund University physics faculty was involved in polishing and cutting scintillators and light guides. The measurements were performed at WOmed[14] in collaboration with Michelle Stroth. Basic dose profiles and a previous phantom version were simulated in Ref. [130, 131].

5.1 Selection of the material

The material for the new phantom should be as water equivalent as possible for both radiation qualities: γ with $E_\gamma \leq 100\,\mathrm{kV}$ and radiation emitted from a ^{106}Ru applicator, which means mainly e^- with $E_{e^-}^{\max} = 3.5\,\mathrm{MeV}$. To analyse different materials and their deviation from water, MC simulations are used. The materials analysed are:

- A150 Tissue equivalent plastic, no distributor found,
- PWLR Plastic Water® Low Range, distributed by Sun Nuclear GmbH, Norderstedt, Germany,
- PWO Plastic Water® Original, distributed by Sun Nuclear GmbH, Norderstedt, Germany,
- PMMA Polymethyl methacrylate, also known as acrylic,
- PS Polystyrene,
- RMI457 Certified Therapy Grade Solid Water® Gammex 457-CTG, distributed by Sun Nuclear GmbH, Norderstedt, Germany,

[14] Wolf Medizintechnik GmbH, St. Gangloff, Germany - a subsidiary of BEBIG Medical GmbH, Berlin, Germany.

- RW1 Water equivalent plastic, distributed by PTW Freiburg GmbH, Freiburg, Germany,
- RW3 Water equivalent plastic, distributed by PTW Freiburg GmbH, Freiburg, Germany, and
- VW Virtual Water™, no distributor found.

Though the materials A150 and VW are not distributed anymore, they were still simulated to be compared to newer materials. The composition data are listed in table 5.1 and the densities of all materials are displayed in table 5.2.

The density of RW3 was simulated as stated in table 5.2, which is derived from Ref. [132]. After the simulations had been performed, the manufacturer provided a more precise value of 1.045 g/cm^3 [133, 134]. The simulations were not repeated because the production of the phantom had already been completed by then. It is assumed that the decision would have been identical even if the more precise density had been included in simulations.

Table 5.1: Composition of the analysed materials in the form of mass fractions. Data taken from Ref. [132, 135–138][15]. PWO also has small inclusions of Br [132, 136].

Material	H	C	N	O	F	Ca	Mg	Cl	Ti
A150	10.13	77.55	3.51	5.23	1.74	1.84	—	—	—
PWLR	7.91	53.62	1.74	27.21	—	—	9.29	0.23	—
PWO	9.25	62.82	1.00	17.94	—	7.95	—	0.96	—
PMMA	8.05	59.98	—	31.96	—	—	—	—	—
PS	7.74	92.26	—	—	—	—	—	—	—
RMI457	8.09	67.22	2.40	19.84	—	2.32	—	0.13	—
RW1	13.19	79.41	—	3.81	—	2.58	0.91	—	—
RW3	7.59	90.41	—	0.80	—	—	—	—	1.20
VW	7.70	68.74	2.27	18.86	—	2.31	—	0.13	—

Table 5.2: Density of materials, which have been considered to be used for the phantom. Data taken from Ref. [132, 135–138][15].

Material	A150	PWLR	PWO	PMMA	PS	RMI457	RW1	RW3	VW
ρ / g/cm^3	1.127	1.029	1.013	1.19	1.06	1.03	0.97	1.05	1.03

[15]For PWLR and PWO, no data could be found in published literature and the manufacturer did not provide the information. Therefore, the data are taken from Ref. [135].

A sphere with a diameter of 24 mm made of the material to be analysed is the main part of the simulation geometry. It is embedded in water. A ^{106}Ru applicator of type CCB is implemented in the form of a calotte made of silver with $12\,\text{mm} < r < 13\,\text{mm}$ and $\theta < 50.98°$. ^{106}Ru-atoms are produced via the `GeneralParticleSource` on a sphere with a radius of 12.1 mm and confinement with the target volume of the applicator. The target volume is defined as another calotte with $12.05\,\text{mm} < r_\text{T} < 12.15\,\text{mm}$ and $\theta_\text{T} < 47.35°$. As rotation and translation have been set to 0 for those volumes, the middle point of the concave surface is positioned at $(0/0/12)^\text{T}$ [86].

To produce an X-ray beam, γ-particles are generated in a distance of 1 mm to the sphere surface via the `GeneralParticleSource`. The direction of flight is towards the centre of the sphere and the beam has a diameter of 2 mm. It is assumed to be perfectly collimated. The energy of each particle is randomised based on a 100 kV spectrum calculated with the software SpekCalc (see section 4.2). The filtering is considered to be 0.5 mm of aluminium, and the spectrum is binned with a bin width of 0.5 keV.

50 simulations are performed with 10^6 primary particles for each radiation quality and material. The dose is scored via a CBS. It is defined as a cylinder with a diameter of 1 mm and a length of 23.5 mm. The cylinder is binned at its height in 47 bins to ensure a depth dose profile. To not have contact between the first bin and the applicator, the cylinder is shifted by $(0, 0, -0.25\,\text{mm})^\text{T}$.

The depth dose curves for both radiation qualities are presented in figure 5.1.

A mean deviation for each radiation quality is computed to calculate which material is most similar to water concerning radiation absorption. Only the first 10 mm are considered for the ^{106}Ru applicator. Due to the steep dose gradient, farther distances are less important for brachytherapy. Meanwhile, the X-rays are meant to travel through the complete eye, which means the entire depth dose curve is considered. The average deviations are calculated using

$$\bar{s} = \sum_i^n \frac{D_i^m - D_i^W}{D_i^W}, \tag{5.1}$$

in which D_i describes the dose per primary particle in either water (W) or any of the other materials (m) for each bin i.

In figure 5.2, those deviations are presented in addition to the density of the materials. Even though PWO has the density closest to 1, it has the most significant deviation concerning radiation absorption of low-energy photons as it is designed explicitly for high-energy photons. With $\bar{s}_\gamma = (1.0 \pm 0.1)\,\%$ for X-rays and $\bar{s}_\text{Ru} = (3.0 \pm 0.3)\,\%$ for the ruthenium applicator PWLR has the minor deviations and is chosen for the phantom.

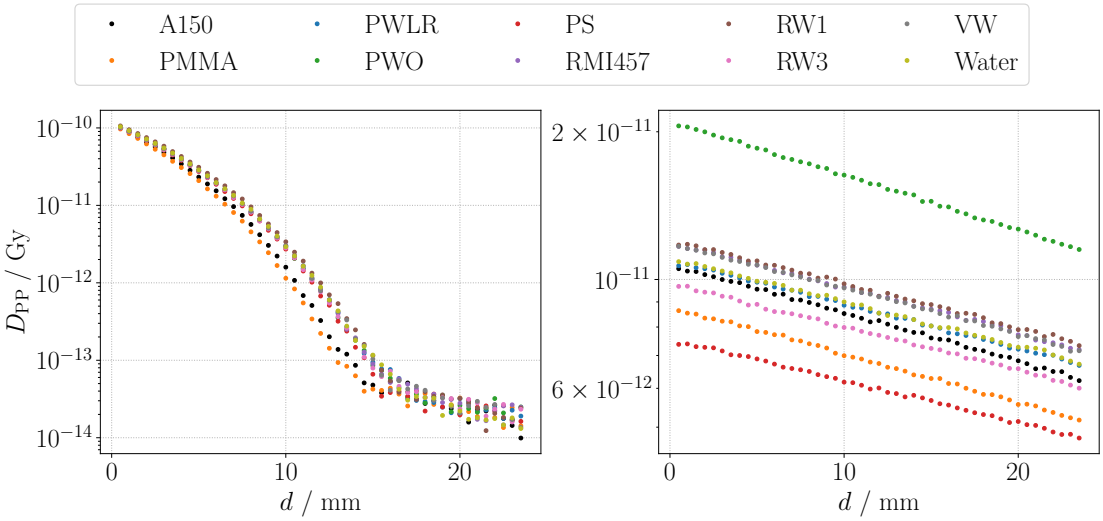

Figure 5.1: Depth dose curves in different materials for a ^{106}Ru applicator (left) and X-rays (right). D_{PP} is the deposited dose per primary particle.

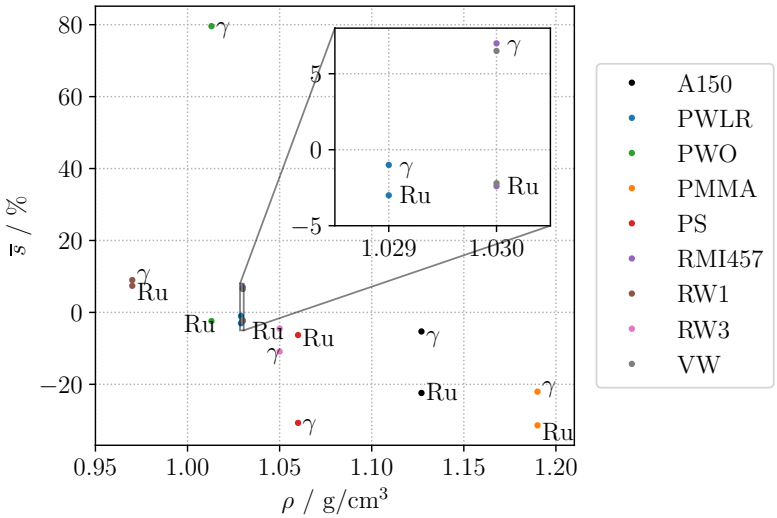

Figure 5.2: The average deviations $\overline{s}$ in depence on the density ρ for both X-rays and a ^{106}Ru applicator for all evaluated materials. The points annotated with Ru refer to the ^{106}Ru applicator, while those annotated with γ refer to the X-rays.

5.2 Utilised Detectors

The aim is to measure both depth dose curves and 2D dose profiles in the future. 2D dose profiles can be measured quickly and precisely with radiochromic films. These are mainly used to estimate beam quality, which is then measured perpendicular to the beam direction. The film can be positioned so one axis is parallel to the beam directio. However, as the film is made of several layers and not as water equivalent as other materials, scattering and absorption might be different compared to water or tissue dose profiles. Thus, a conventional soft X-ray chamber is utilised additionally to compare the results.

As the combined therapy concept also consists of a ^{106}Ru applicator, the sum of dose profiles of both X-rays and the applicator may be obtained in future experiments. Dose profiles of beta-emitting sources are usually measured with plastic scintillators [2, 139–145]. To assess the feasibility of self-made scintillation detectors based on PolyEthylene Naphthalate (PEN) to quantify dose rates applied by X-rays, scintillation detectors are also in this work.

5.2.1 Radiochromic film

2D dose profiles are obtained with radiochromic film[16]. For optimal results, the film shall be used for dose measurements in the range of 0.2 to 10.0 Gy. The film consists of two clear polyester bases of 125 µm as sheathing and an active layer with a thickness of 28 µm. Ionising radiation leads to colour changes in the active layer as a function of the deposited dose. With an RGB scanner and the software FilmQA Pro[17], it is possible to calculate the applied dose in each pixel from the RGB values of the scan. The manufacturer states, the uncertainty is $\sigma_{\mathrm{rf}} \leq 2\,\%$ if the corresponding guides are followed carefully [146, 147]. The film is near tissue equivalent with a high spatial resolution of 25 µm. The energy dependence shall not exceed 5 % in the range of 0.1 to 18.0 MeV [146]. The GAFChromic guide [147] is followed, and a test version of the commercial software FilmQA Pro is used to compute dose values from the RGB pixel values.

Cutting the film to the specific geometries needed for the phantom appeared difficult, as the polyester base layers shatter under pressure. Cutting with a scalpel, scissors or water jet is not practical. The best method encountered in this work is to dissect the film with a laser engraver[18]. The CO_2 laser is adjusted to 5.6 W at 35 % of its maximum speed. The cutting process is repeated two times to ensure high quality. A carpet pad is used to avoid imprints of the metal grid on the film. All films are cleaned thoroughly with isopropanol after the cutting and immediately before scanning. A detailed photo of one of the cuts is shown in figure 5.3a. Due to the thermal reaction on the film, the

[16] Ashland Inc., GAFchromic™ EBT3 radiochromic film, refer to [146, 147] for more information.
[17] Ashland Inc., FilmQA pro™ software v.7. `https://www.ashland.com/industries/medical/filmqa-pro-software`
[18] Gravotech GmbH, Laser engraver LS900, refer to [148] for more information.

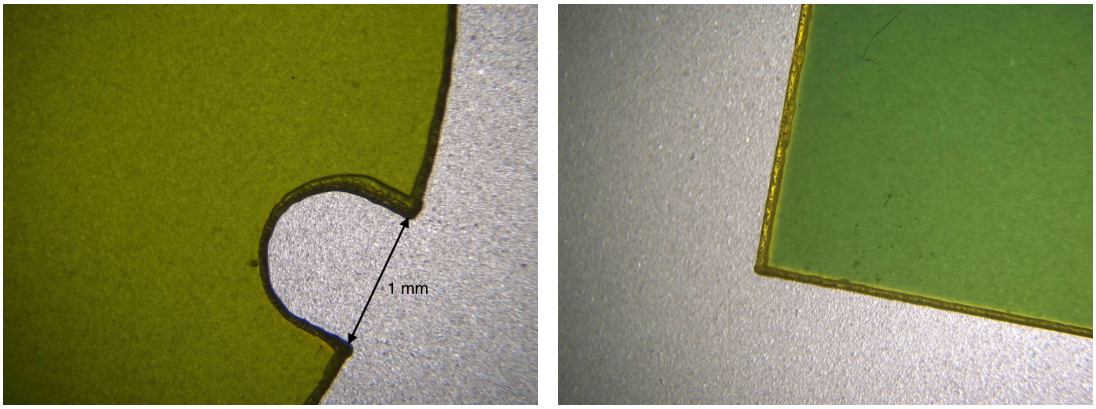

a) b)

Figure 5.3: Two photos of radiochromic film taken under a microscope. a) Round film to be placed in between the two hemispheres. The cutout is made for the pin, which connects the two hemispheres. b) Irradiated film with a focus on its edge, where the dose values fluctuate to the thermal damages caused by the laser engraver.

edges are slightly coloured and highly fluctuating measuring results are observed on the first few pixels, which is presented in figure 5.3b.

Two different forms of radiochromic films are cut with the laser engraver. The first form is a circle with a diameter of 24 mm fitting between the two hemispheres of the phantom. A little notch of 1 mm size, displayed in figure 5.3a, is made into the round films to achieve information regarding the angular position.

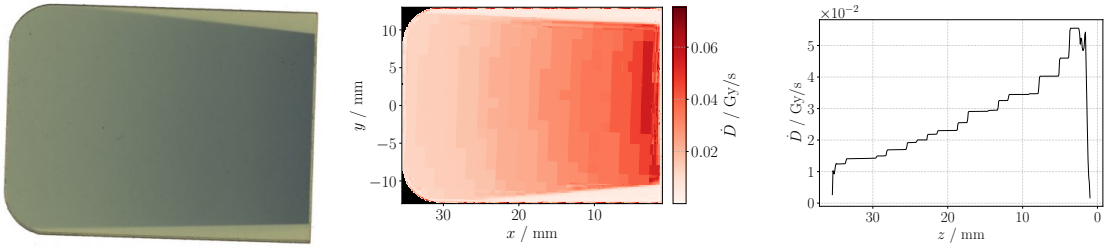

a) b) c)

Figure 5.4: Comparison of the original scan and the dose output of the FilmQA Pro test version. a) Original scan, b) dose rate profile calculated using FilmQA Pro and c) depth dose curve. The small difference in the rotation between the scan and the dose profile is due to imperfect positioning on the scanner, which is corrected within the Python script that reads and plots the dose values. The data set is not further modified.

All films with dose profiles are evaluated by the FilmQA Pro software. The results are processed with a Python script which starts by rotating the dose profiles to have the same orientation. The angle is calculated by either the `cv2.minAreaRect` function [149] for the larger films or by finding two circles with the `cv2.HoughCircles` function [150] for the round films positioned in the sphere. While the first circle describes the overall round form, the fit of the second circle finds the notch. Afterwards, the data sets are cut to the region of interest. Moreover, the data sets are rescaled to have the same dimensions of 280×280 pixels for the round films and 400×300 pixels for the rectangle films. As the laser destroys the edges, the first 20 pixels on each edge of each film measurement are ignored. The dose profiles of the same setup are averaged. In order to obtain a depth dose curve, the mean of the centre 20 rows of the dose profile is calculated.

At this point, it has to be pointed out that the direct output of the FilmQA Pro software shows unexpected results. In figure 5.4, a 2D dose profile and a DDC obtained with a single film are shown in comparison to the original scan. The PWLR duplicate was placed into the phantom. Thus, a steady exponential dose decrease over distance is expected and can be seen in the original RGB scan. The calculated dose output seems to be a rather stepwise function. No reason was found for this output. Measured fluctuations and deviations might result from this effect.

5.2.2 Soft X-ray chamber

A soft X-ray chamber is another conventional detector employed in clinical practice to perform quality assurance on low-energy X-ray therapies [151, 152]. As presented in figure 5.5, the soft X-ray chamber[19] is a thin window plane parallel chamber. It is designed for low-energy photons in the range of 15 to 70 keV but can also be calibrated for other radiation qualities such as 100 kV. The sensitive volume of only $0.006\,\mathrm{cm}^3$ is a cylinder with a radius of 1.45 mm and a height of 0.9 mm. The detector is vented and not waterproof accordingly. The entry window comprises a graphitised polyethylene foil with a total thickness of 0.06 mm. The reference point is centred on the inside of the entry window [152, 153].

The soft X-ray chamber is operated by an electrometer[20]. It provides the voltage for the detector while measuring the collected charge over time in the detector. With the calibration provided by the manufacturer, the values can be transferred directly to dose or dose rates. Dose rates $\dot{D}$ presented in this thesis are calculated by dividing dose by beam time. The general uncertainty of measured values is expressed to be $\sigma_{\mathrm{Romeo}} = 0.5$ % [153]. The calibration values are given with a relative uncertainty of $\sigma_{\mathrm{cal}} = 2\,\%$ [153–155].

[19] PTW Freiburg GbmH, Soft X-ray chamber type 34013, refer to Ref. [152, 153] for more information.
[20] PTW Freiburg GmbH, UNIDOS® Romeo in trigger mode, refer to Ref. [153–155] for more information.

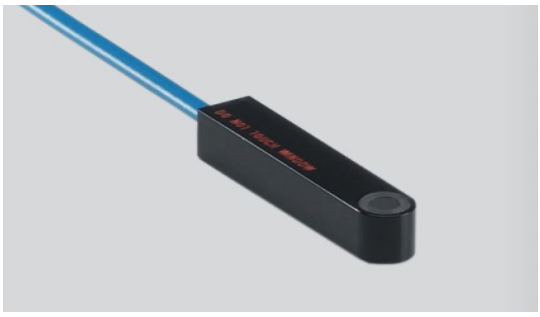

a)

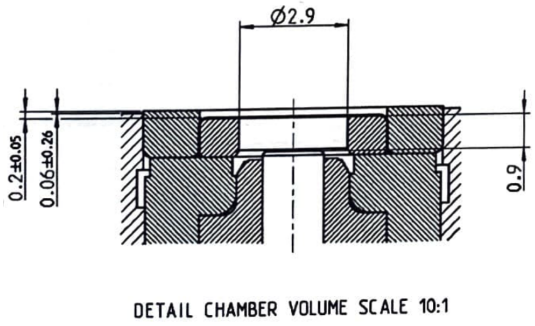

b)

Figure 5.5: a) Photo and b) dimension drawing of the soft X-ray chamber. Pictures acquired from Ref. [152, 153]

5.2.3 Scintillation detectors

The self-made scintillation detectors are similar to already published versions presented in Ref. [145]. The main differences between other versions of the scintillation detector in this and previous studies are that the scintillator BC-400 has been replaced by PEN and that no Čerenkov minimising approach is used since no Čerenkov light is expected in the setup with low-energy photons. All steps are described in the following, focusing on the new or changed processes to demonstrate the optimisation. A sketch of the final detector can be seen in figure 5.6. The detector is intended to be additionally used in test and measuring setups presented in Ref. [139–141]. The detector is based on the scintillator, which produces light in dependence on the deposited energy [142]. The light is transferred to a photomultiplier [21] via an optical fibre [22]. A sleeve made from PWLR encloses the detector. With a pico amperemeter [23] the signal of the photomultiplier is obtained and processed with the software first established in Ref. [139]. The software measures and averages the pico amperemeters data until the relative standard error is smaller than a defined threshold of 0.5 %. A minimum of 100 single values is always considered. After 30 s, the measurement is stopped nonetheless, whether the threshold is reached or not. More information regarding the basics of the scintillation detection system can be found in [59, 139, 145].

Production of the detectors

The manufacturing process is split into four steps.

1) Melting: The PEN granules are baked in a drying oven at approximately 80 °C overnight to dispose moisture. It is then melted in an oven in a mould lined with

[21] Hamamatsu Photonics K.K., H10721-210. see Ref. [156, 157] for more information.
[22] Cunz GmbH & CO.KG, CWKF-1001E22, see Ref. [158] for more information.
[23] Tektronix Inc., Keithley 6485, refer to Ref. [159] for more information.

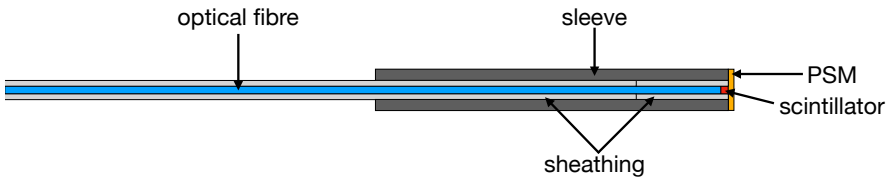

Figure 5.6: Sketch of the scintillation detector with the scintillator (red), the highly reflective foil (yellow), the optical fibre (blue), the light guides sheathing (light grey) and the sleeve (dark grey). The sketch is not to scale. Glue and paint are not illustrated.

aluminium foil at approximately 310 °C. After removing the mould and cooling, the block should be clear to bright yellowish with as few air bubbles as possible.

2) Milling: The PEN block is cut with the help of a milling machine moved precisely by an XYZ-apparatus. A double-edged cutter is used at a rotational speed of 6000 min^{-1} to mill out a cylinder with a diameter of 1 mm, as it is shown in figure 5.7a. To obtain good results, the miller has to be backed up after each millimetre progress in depth, so petroleum used as cooling fluid may reach the surfaces that have just been cut. The length of the final cylinders is in the range of 5 to 10 mm.

3) Cutting and polishing: Each cylinder is first inspected for air enclosures. If none are present, the PEN cylinders are glued on a saw holder with wax between two glass strips, which apply stabilisation and better orientation. After the resin is hardened, the saw holder is mounted to the head of a goniometer to obtain cuts orthogonal to the axis of the cylinder. With an internal diameter saw, 0.75 mm long cylinders are acquired. These short cylinders are then polished from both sides. The removal rate is monitored during polishing to achieve the desired length of slightly more than 0.5 mm. The polishing is performed on a polishing wheel with a silk cloth and polycrystalline diamonds with a grit of 1 µm. The final scintillators are cleaned thoroughly with isopropanol.

4) Assembling: The sheathing of the optical fibre is partly removed on both ends, and the surfaces are polished. On one of the sides, the scintillator is glued onto the light guide with an optical cement[24]. Pieces of sheathing are slipped over the exposed part of optical fibre and the scintillator as presented in figure 5.7b. Additionally, a sleeve protects the scintillator and light guide from external forces. It is made from PWLR to maintain as much water equivalence as possible. After this step, the detector is once more polished to remove sheathing remnants and to acquire the desired length of 0.5 mm for the scintillator. To enhance the light yield, a highly reflective polyester film[25] with a thickness of 10 µm is glued to the free side of the scintillator (see Ref. [161] for more

[24]Saint-Gobain Crystals, BC-600, refer to Ref. [160] for more information.
[25]Hahn Polyfilms GmbH, highly reflective polyester film called PSM with an optical density of 2.8.

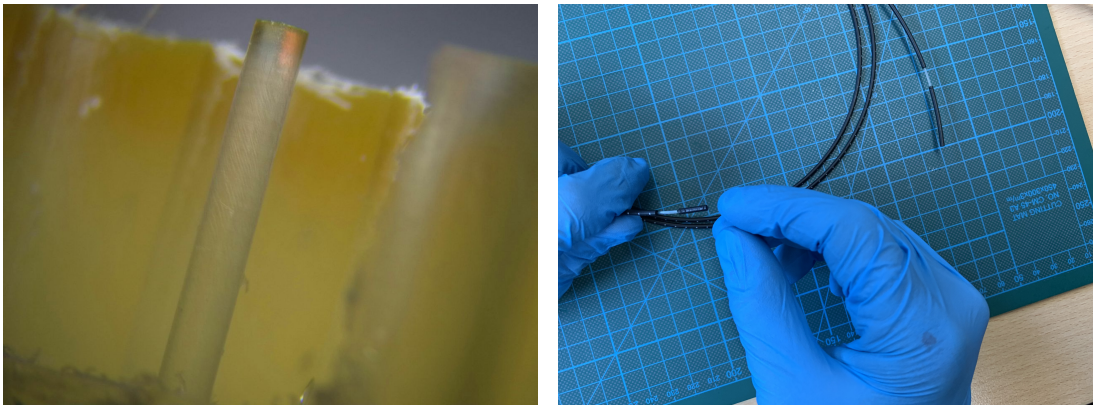

a) b)

Figure 5.7: a) Photo of a PEN probe. The cylinder in the middle of the picture was previously exposed with a milling machine but is still attached to the complete PEN block at the bottom. b) Assembling of the detector. In this step, an appropriate piece of sheathing is slid over the scintillator and the free light guide to protect it.

information). As the final step, the detector is painted black to protect it from incident light and to maximise the signal-to-noise ratio.

The described method of producing PEN scintillators in the desired cylindric shape is much quicker and more reliable than any other method previously employed by the working group.

Estimating the detectors output yield

To choose one of the 32 produced detectors, the complete documentation of the building process and various measurements are considered. The experimental setup to obtain the light yield of the detector, described in more detail in Ref. [145, 161], consists of a ^{90}Sr planar beta source[26] and the identical readout as described above. The current I_b is measured before the PWLR sleeve is assembled, which is shown in figure A.22. Only 17 of all 32 detectors are further processed, depending on I_b and observation of abnormalities, such as air enclosures or a tilted scintillator position. After completing the 17 processed detectors, the current I_a is measured. In addition, both dark current I_{dc} in the same setup and noise from incident room light I_a are quantified. The results are shown in figure 5.8.

[26]PTW Freiburg GmbH, T48010, refer to Ref. [162] for more information.

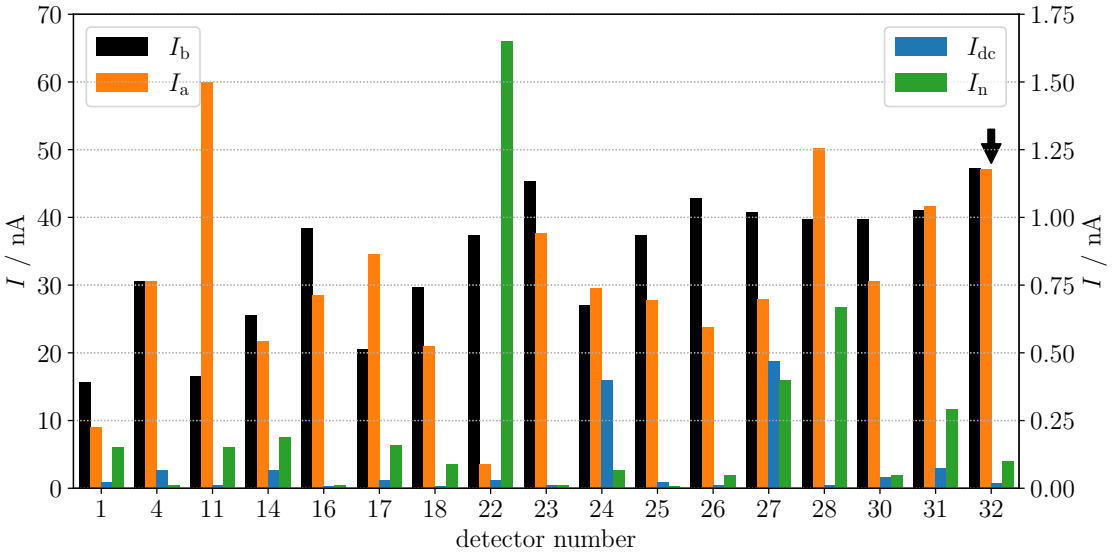

Figure 5.8: Signal and noise currents of the processed scintillation detectors. The current I_b before and I_a after assembling, dark current in the measurement setup I_{dc}, and current from incident room light I_n. I_b and I_a are associated with the left y-axis, I_{dc} and I_n are associated with the right y-axis. The arrow points at the detector, which is chosen for further measurements.

A detailed evaluation is performed to discern the most suitable option from among the three detectors which demonstrate the highest levels of signal intensity. Detector number 28 is relatively susceptible to room light and therefore excluded. Meanwhile, detector number 11 shows a signal increase of approximately 3.5 from I_b to I_n. Even with a signal enhancement due to the high reflective foil at the tip of the detector, this signal increase is unaccountable. Due to this inconsistency, the detector is rejected. Detector number 32 has a signal-to-noise ratio of approximately 2500 with I_a being the third highest measured. In the production process, no inconsistencies or abnormalities were observed. It fits perfectly into the holes drilled in the brackets and is consequently selected for the subsequent measurements.

For the scintillation detector, a general systematic uncertainty of $\sigma_{SD} = 1\,\%$ is assumed due to the information given in Ref. [140, 163].

5.3 General setup

The final phantom consists of several parts which are combined depending on the detector used. As an example, the setup for the scintillation detector is presented in figure 5.9. All parts except the detectors are entirely made from PWLR.

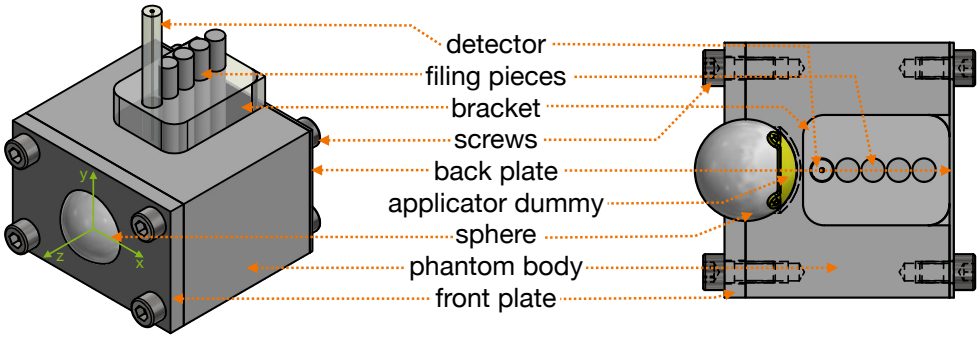

Figure 5.9: The phantoms setup for a scintillation measurement as a representation of the general idea of the phantom. The complete phantom is shown on the left, while a cut through the phantom in the origin level is presented on the right. The screws are still made visible for orientation reasons. The used coordinates system is drawn in the left visualisations. Its origin is located in the centre of the sphere.

The main body of the phantom has several recesses, which are meant for an ^{106}Ru applicator of type CCB, a sphere and a detector bracket. Only the dose profiles of the X-ray beams are to be measured in this work. To quantify the dose values without the background of an active ^{106}Ru applicator, a ^{106}Ru dummy of type CCB is used instead. It is manufactured identically to standard applicators, just without radioactive material. The sphere represents the eye and has a diameter of 24 mm. Instead of the ^{106}Ru dummy, a PWLR dummy can be positioned behind the sphere to measure dose profiles of X-rays without the influence of the absorber. The detector bracket is placed behind the applicator with only 0.25 mm material in between. The sphere and the bracket are held in position by the front and back plates of different thicknesses. The phantom is intended to be irradiated from the front and the back. While the front plate is not in the path of the X-rays and can be thicker, the back plate should be of minimal thickness to minimise the distance of the particles in the phantom before reaching the detectors. As a compromise between stabilisation and minimal distance, a thickness of 1 mm is chosen. Each plate is secured with four screws made.

The coordinate system is defined as displayed in figure 5.9. The origin is located in the centre of the sphere, and the z-axis is parallel to the direction of the X-ray beams.

Different brackets, which can be positioned in the biggest recess of the phantom body, are constructed for the three detector types. The resulting setups are visualised in figure 5.10. The radiochromic film enables 2D measurements. Its bracket consists of two parts positioned below and above the film. Due to the dimensions, the middle of the sensitive layer is lifted to the z-axis. In addition, the radiochromic film is the only detector type to be placed in front of the applicator. This is enabled by having not only an entire sphere but also two hemispheres with a gap in between, in which the

film can be placed. The two hemispheres are precisely oriented through a small pin and corresponding notch. A visual check of the pin and the position of the film allows a reproducible location of the film and the hemispheres in the phantom. The sensitive area of the radiochromic film in the phantom can be obtained from figure 5.10a.

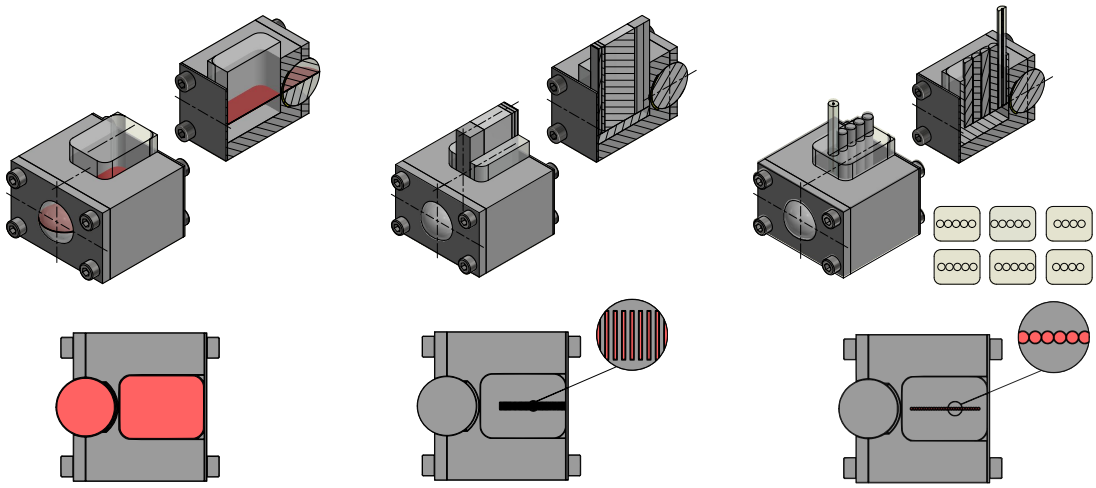

a) b) c)

Figure 5.10: The three different detector setups: a) radiochromic film, b) soft X-ray chamber and c) scintillation detector. The red volumes represent the sensitive volumes, of which the ones in the chamber do not scale due to visualisation reasons. The soft X-ray chamber is rotated to measure irradiation from the back of the phantom. It is turned around for front irradiation, so the sensitive volumes are close to the applicator. Half of the scintillation detector's measuring points are depicted in the sketch to prevent overlap.

Due to the geometry of the soft X-ray chamber, a holder with a matching recess along the entire z-axis was designed. The chamber is intended to be placed into this bracket with the entrance window rotated toward the incident particles. The recess is filled with PWLR pieces of different dimensions. The thinnest piece with 0.5 mm defines the minimal possible step width. This results in 54 possible measuring points. The recess is made so that the centre of the entry window of the soft X-ray chamber is positioned on the z-axis. A visualisation of the measuring points of the soft X-ray chamber is provided in figure 5.10b.

As the scintillation detector is a cylinder with a diameter of approximately 5 to 5.5 mm, the mount was constructed to have holes in which the detector can be placed. They are positioned so that the centre of the scintillator is located on the z-axis at different distances from the origin. To enable a depth dose curve in higher resolution, a total of 6 brackets with varying hole positions for the scintillation detector are built. The amount of measuring points with different distances can be doubled by rotating the bracket. This

leads to a total of 56 measuring points with a distance of 0.5 mm to each other. The distances between the centre of the scintillator and the lateral surface of the bracket are within 3.5 to 31 mm, and the measuring points are visualised in figure 5.10c. Because these brackets are supposed to be rotatable, they are constructed with four rounded edges. Two thin filling pieces are manufactured to fill the gap between the bracket and the back plate (see figure 5.9).

Photos of the final phantom are provided in figure 5.11, and all construction drawings are attached in appendix A.1.

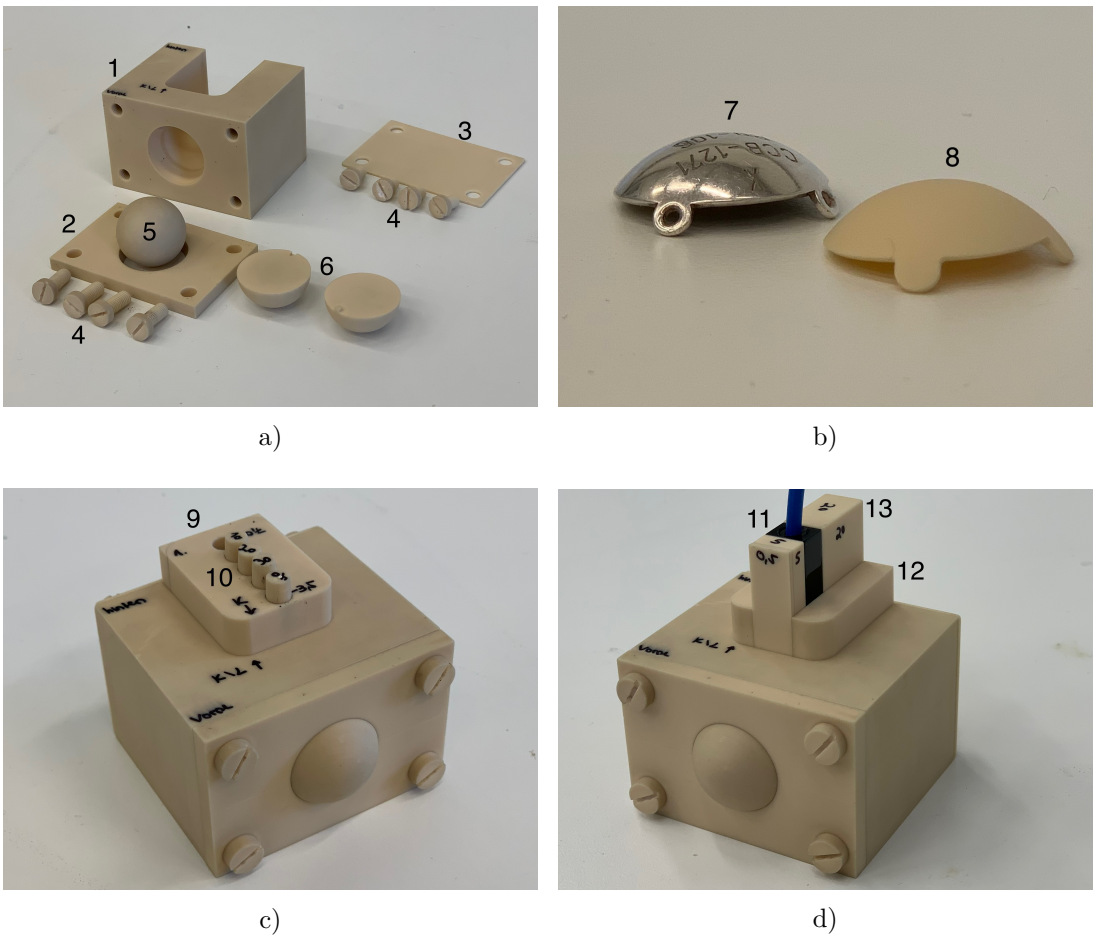

a) b)

c) d)

Figure 5.11: Photos of the novel PWLR phantom. a) Main components: phantom body (1), front (2) and back plate (3), corresponding screws (4), sphere (5) and two hemispheres (6). b) ^{106}Ru dummy (7) and PWLR plaque (8). c) Assembled phantom, including one of the brackets for the scintillation detector (9) and the corresponding filling pieces (10). d) Setup for the soft X-ray chamber (11), including its bracket (12) and corresponding filling pieces (13).

5.4 The T-105 X-ray therapy unit

Measurements were performed with a T-105 X-ray therapy unit manufactured by WOmed at the place of production. The therapy unit is mainly designed for superficial therapies in the range of 10 to 100 kV. The X-ray therapy unit, which mobile trolley is presented in figure 3.1b, is connected to a control station to be placed in a shielded area for the users. The X-ray tube is attached to a spring arm, which allows precise movement by the user and stable positioning during therapy. The unit has an in-built filter wheel to choose from a maximum of four filters to choose the radiation quality. The therapy unit is programmed to select a predefined radiation quality profile by turning the wheel to another filter. All parameters could be changed to our preferences for the measurements in collaboration with the manufacturer [164].

The X-ray therapy unit is water-cooled to overcome the problem of overheating. The maximum consumption of the X-ray therapy unit is 1200 W, and the maximum current is 12 mA [164, 165].

Two standard therapy spectra are chosen for the measurements. The first consists of an acceleration voltage of $U_1 = 100\,\mathrm{kV}$ with a current of $I_1 = 12\,\mathrm{mA}$. As external filtering, 0.5 mm copper is used in addition to the inherent filtering of 1 mm beryllium. For the second spectrum, both the voltage and the current are lowered to $U_2 = 70\,\mathrm{V}$ and $I_2 = 10\,\mathrm{mA}$. The photons are filtered by 1 mm aluminium. To minimise the risk of overloading the photomultiplier, which is part of the scintillation detection system described in section 5.2.3, the current is reduced to $I_2^* = 3\,\mathrm{mA}$ for measurements containing the scintillation detectors.

The phantom is placed close to the opening of the X-ray tube. To minimise the uncertainty due to repositioning the PWLR phantom, the phantom is placed on a fixed plate with a right-angle recess. This allowed to find the identical position relatively precisely after switching detector positions or the used detector itself. The X-ray therapy unit was not moved between measurements, if possible. The sphere is positioned close to the X-ray tube to irradiate from the front. For back irradiation, the phantom is turned. All cables and light guides were kept out of the beam as well as possible. The photomultiplier, the amperemeter, the UNIDOS and other radiation-sensitive parts were positioned behind lead shieldings, as shown in figure 5.12.

5.5 Corresponding Monte Carlo simulations

To validate measured data, MC simulations are performed in Geant4, which basics are described in section 4.3. For the most realistic results, the 3D models of the phantom are imported using the STL-files. The surrounding of the phantom is defined as air. PWLR is implemented as defined in table 5.1. The energy spectrum of the photons is calculated using SpekCalc (see section 4.2) with the parameters of the X-ray therapy unit used for the measurements (see section 5.4).

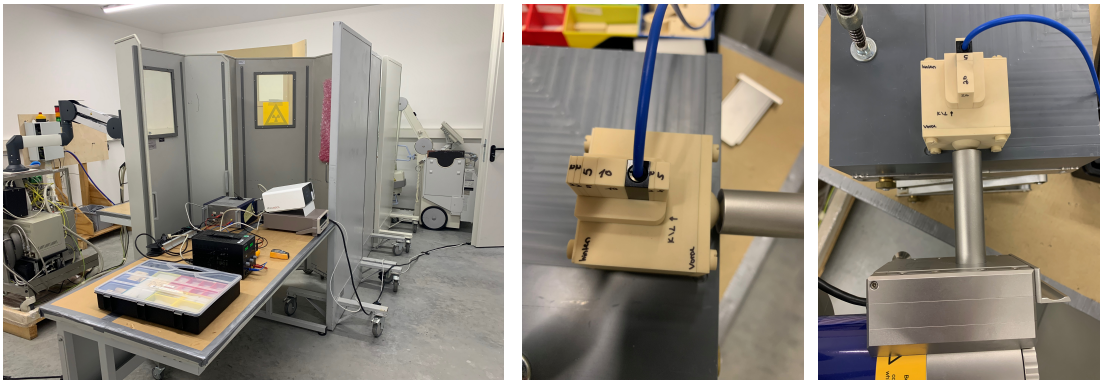

a) b) c)

Figure 5.12: General setup for the measurements. a) The X-ray therapy unit without its chassis can be seen on the left. The readout hardware for the soft X-ray chamber and the scintillation detector are shown in the middle of the photo. Lead shielding is placed between the X-ray therapy unit and the readout hardware. b) and c) The phantom with the soft X-ray chamber is positioned in front of the X-ray tube.

The detector components are not included in the simulation to balance simulation efficiency and a realistic setup. Instead, only sensitive detector volumes are created with the exact dimensions as the active measuring volume of the soft X-ray chamber or the scintillation detector. The material is chosen to be PWLR.

Regarding the soft X-ray chamber, the positions of the SDs are slightly changed to achieve the same effective measuring point. It is assumed that the effective point of the simulated SD is in the centre of the volume. However, the actual effective measuring point of the soft X-ray chamber is located on the inside centre of the entry window. Accordingly, all cylinders are shifted towards the radiation source. This shift is done for both front irradiation and back irradiation separately.

The effective measuring point of the scintillator is assumed to be in its centre [140]. Thus, the SD volumes with the exact dimensions and position are used in the MC simulation. The scintillator is simulated as a PWLR volume without a light guide, glue, paint or high reflective foil.

To enhance the efficiency of the simulations, as many SD volumes as possible are placed into one simulation without having overlaps. This means several simulation setups are built for each plaque material - silver and PWLR.

To obtain simulation results in 2D as the radiochromic film does, two CBS are added to every macro file. Both scorers are located in the $x-z-$ plane and score the deposited dose with a resolution of 0.5 mm.

A cylindrical CBS is introduced in the sphere perpendicular to the centre of the plaque to allow easy access to depth dose curve information. It has a length of 23 mm and a diameter of 1 mm. By binning the scorer along the z axis, a 0.5 mm resolution is enabled.

5.6 Results

In the following, the results of the measurements are presented. At first, the estimated uncertainties of the setup are displayed, followed by the calibration of the radiochromic films. In section 5.6.3 the investigation of the suitability of the brachytherapy plaque as a beam stop is presented.

5.6.1 Uncertainties

The new setup and phantom are analyzed concerning its uncertainties. The uncertainties are measured using one of the two spectra for time reasons. Only the uncertainty from switching the X-ray tube inside the therapy unit has been measured for both spectra. The uncertainties are assumed to be very similar for the other spectrum.

The repositioning of the phantom in between measurements and repositioning of the X-ray therapy unit, which could not always be avoided, can lead to signal fluctuation. Therefore, the soft X-ray chamber is used at a depth of 21 mm to quantify this uncertainty. The phantom is irradiated from the back with the 100 kV spectrum. The dose rate $\dot{D}$ is measured five times. The phantom and X-ray therapy unit are randomly moved and repositioned between measurements. The relative uncertainty is considered as

$$\sigma_\mathrm{p} = {}^{\sigma_{\dot{D}}}\!/_{\mu_{\dot{D}}} = \begin{cases} 0.34\,\% & \text{for the Slab phantom and} \\ 0.48\,\% & \text{for the PWLR phantom.} \end{cases} \tag{5.2}$$

First cross-checks with the scintillation detector showed a higher light yield output for the X-rays than expected. Accordingly, the current is changed for the 70 kV spectrum when the scintillation detector is used to avoid damage to the photomultiplier. The corresponding signals are scaled up to be comparable to the soft X-ray chamber and the radiochromic films. A depth dose curve with four points is measured in a conventional slab phantom to calculate the uncertainty of the dose rate output of the X-ray therapy unit and the proceeding upscaling of results. The depth varies between 0 to 30 mm in 10 mm steps. Each measuring point is quantified three times, and the average data $\dot{D}_{i,2}$ and $\dot{D}_{i,2*}$ for $I_2 = 10\,\mathrm{mA}$ and $I_{2*} = 3\,\mathrm{mA}$ are processed to calculate the uncertainty σ_c:

$$\sigma_\mathrm{c} = \frac{\sum_i^n \frac{\dot{D}_2^i - \dot{D}_{2*}^i \cdot \frac{I_2}{I_{2*}}}{\dot{D}_2^i}}{n} = 0.50\,\%. \tag{5.3}$$

The filling pieces for the holes in the bracket for the scintillation detector showed small discrepancies concerning their form because they were made by hand. This results in small air enclosures of different sizes, leading to dose rate fluctuations if the detector is placed behind the filling piece, e.g., in the second hole of a bracket. To quantify this uncertainty, the phantom is irradiated from the back with the 70 kV spectrum while a bracket with five holes is inserted. The detector was placed in the second hole. The current is recorded for every filling piece in front of the detector in both orientations. The uncertainty is considered as

$$\sigma_{\mathrm{fs}} = \frac{\sigma_I}{\mu_I} = 0.31\,\%. \tag{5.4}$$

The amount of filling pieces due to the combination chosen for the setup in front of the soft X-ray chamber may also lead to fluctuations, especially if many pieces are introduced into the path of the particles. This is analyzed with a total of 21 mm of PWLR between the soft X-ray chamber and the entry surface of the photons with 100 kV irradiation from the back. Eight different combinations with a varying number of 1 to 12 pieces are used. For each combination, the dose rate is measured three times. The relative uncertainty is considered as

$$\sigma_{\mathrm{fc}} = \frac{\sigma_{\dot{D}}}{\mu_{\dot{D}}} = 0.15\,\%. \tag{5.5}$$

Unfortunately, the X-ray tube had to be replaced during the period the measurements were taken. Due to this fact, the results of the measurements taken with different X-ray tubes must be corrected. X-ray tubes of the same type may deviate concerning dose rate output for the same settings. Before replacement, depth dose curves in a conventional slab phantom were taken with both X-ray spectra in addition to other measurements. These depth dose curves are repeated after replacement to calculate a correction factor r. The depth of the measuring points is varied in the interval of $[0\,\mathrm{mm}, 30\,\mathrm{mm}]$ with a stepsize of 10 mm. r is calculated for both spectra and describes the average ratio of dose rates:

$$r^U = \frac{\sum_i^n \frac{\dot{D}_{i,1}}{\dot{D}_{i,2}}}{n} = \begin{cases} 0.983 \pm 0.003 & \text{for } 70\,\mathrm{kV} \text{ and} \\ 0.989 \pm 0.003 & \text{for } 100\,\mathrm{kV}. \end{cases} \tag{5.6}$$

All data taken with the second X-ray tube inserted into the therapy unit is multiplied with the factor $r^{70\,\mathrm{kV}}$ or $r^{100\,\mathrm{kV}}$ depending on the used energy spectrum.

In table 5.3, all calculated uncertainties are listed together with the general uncertainties of the detectors.

All calculated uncertainties of the novel phantom and the general measurement setup are less dominant than the uncertainties of the detectors given by the manufacturer. The uncertainties or correction factors are propagated in all subsequent measurements if the corresponding cause of uncertainty is present in the setup.

Table 5.3: Uncertainties regarding the measurements and the factors $r^{70\,\mathrm{kV}}$ and $r^{100\,\mathrm{kV}}$.

Uncertainty	Value
σ_{rf} [147]	2.00 %
σ_{Romeo} [153]	0.50 %
σ_{cal} [154]	2.00 %
σ_{SD} [140, 163]	1.00 %
σ_p^{Slab}	0.34 %
σ_p^{PWLR}	0.48 %
σ_c	0.50 %
σ_{fs}	0.31 %
σ_{fc}	0.15 %
$r^{70\,\mathrm{kV}}$	0.983 ± 0.003
$r^{100\,\mathrm{kV}}$	0.989 ± 0.003

5.6.2 Radiochromic film calibration

For each spectrum, eight pieces of film are irradiated with the doses stated in table 5.4. Unfortunately, film #2 irradiated with 100 kV broke and could not be used for the calibration with FilmQA Pro. A reciprocal linear function is used to describe the colour values f in dependence on the dose D for each of the three colour channels individually:

$$f(D) = A + \frac{B}{D - C} \tag{5.7}$$

The colour values and fit curves are visualised in figure 5.13, and the fitted values of A, B and C are listed in table A.1.

Table 5.4: Dose applied to the radiochromic films for calibration.

#	$D_{70\,\mathrm{kV}}$ / mGy	$D_{100\,\mathrm{kV}}$ / mGy
1	0.0	0.0
2	797.5	-
3	1196.3	1286.7
4	1834.3	1930.0
5	2711.5	2895.0
6	4067.3	4353.2
7	6061.0	6519.1
8	9091.5	9778.7

These calibration curves calculate the dose rate profiles from radiochromic films irradiated during the measurements. The deposited dose is calculated for each pixel from the

scaled colour values. Then, the dose rate $\dot{D}$ is computed by dividing the dose D by the beam time.

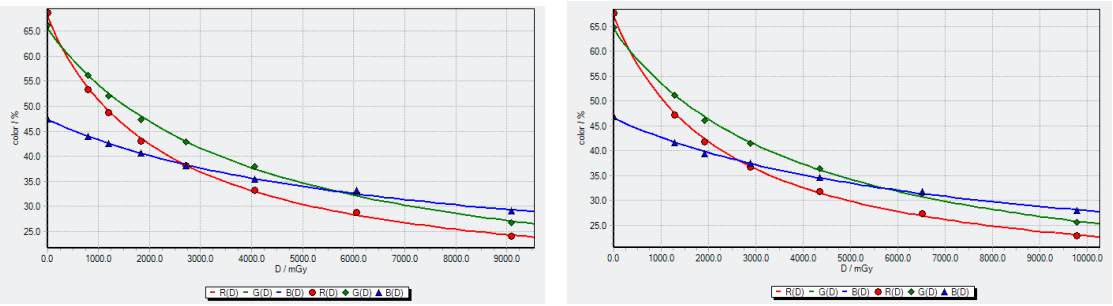

a) b)

Figure 5.13: Screenshots of the film calibration fit functions for the a) 70 kV and b) 100 kV spectrum performed in FilmQA Pro

5.6.3 Change of the dose profile due to the ^{106}Ru applicator

The measurements aim to evaluate the suitability of the ^{106}Ru applicator as a beam stop. Thus, the dose profiles obtained with either the PWLR or the ^{106}Ru dummy positioned are acquired. To compare both parts of the depth dose curve with all three detector types, measurements are performed with irradiation from the front and once from the back. The measurements are entirely performed with two different X-ray energy spectra: 70 kV and 100 kV.

2D film measurements

The results acquired with radiochromic film are presented in figure 5.14. The expected exponential decrease of the dose rate over distance can be seen when the PWLR plaque is inserted. In addition, if the ^{106}Ru dummy is positioned in the phantom, the dose rate is significantly lower behind the plaque compared to the measurement with the PWLR plaque. This can be seen for both front and back irradiation, though it is more evident for front irradiation due to the overall higher dose rate values close to the plaque.

In addition, the divergence of the beam can be observed, especially in the plots showing the dose profiles for back irradiation. However, the divergence is not further investigated because the collimators utilised for the combined therapy concept are unknown.

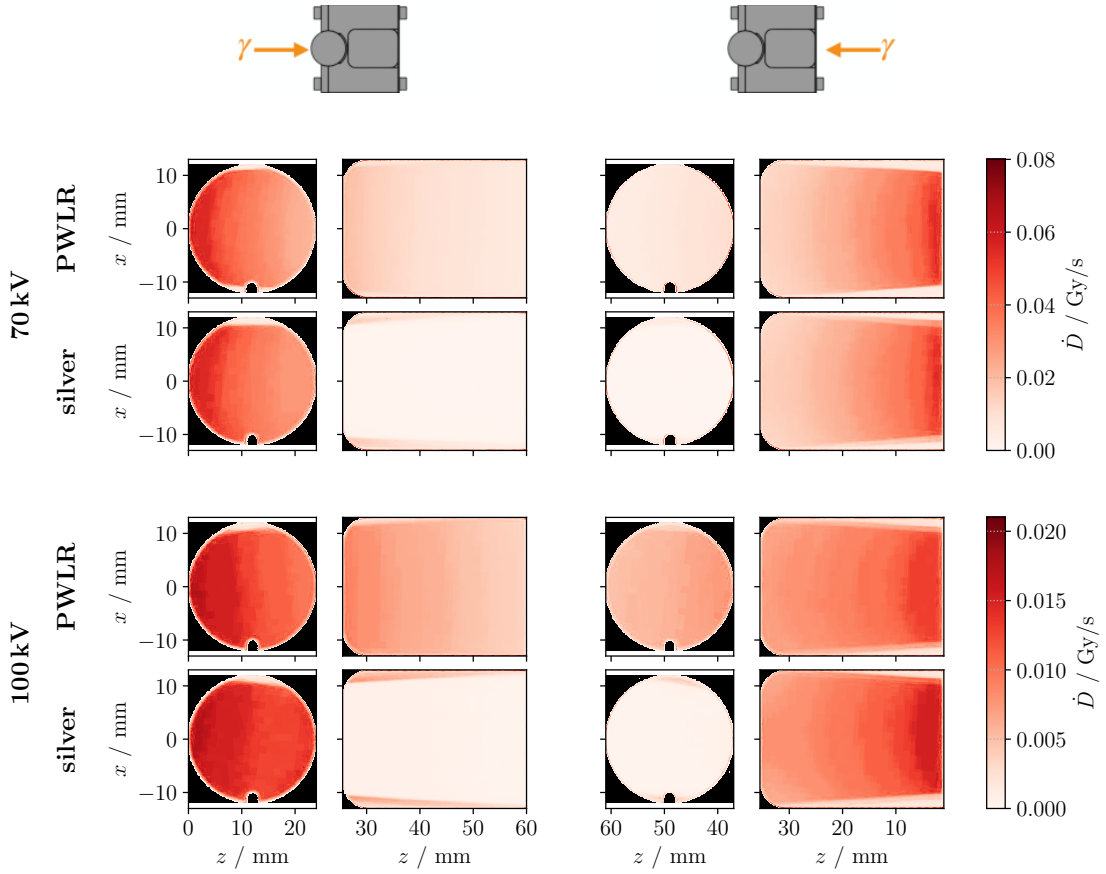

Figure 5.14: Two-dimensional dose profiles obtained with radiochromic film. Each plot shows the average of the five measurements for the same setup. All plots in the left column are created with front irradiation, while all plots in the right column present back irradiation data sets. The upper two rows represent the data sets obtained with 70 kV, while the lower two rows show the dose profiles for the 100 kV spectrum. For each spectrum, the corresponding colour bar is shown on the right. The first and third rows are data sets measured with a PWLR applicator, while the second and fourth rows are data sets obtained with a silver applicator in the simulations.

Depth dose curves of all detector types

To examine the dose profiles more closely, the depth dose curves obtained with all detectors are visualised in figure 5.15 and figure 5.16. As explained in section 5.2.3, the scintillation detector is not calibrated. Accordingly, it can only be compared relatively with the other two detector types.

The depth dose curves of all detector types show the same result concerning the overall shape. Regarding the agreement of the detector types, the dose rate profiles measured with the radiochromic films fluctuate and demonstrate deviations from the soft X-ray chamber. For the 70 kV spectrum, those deviations are highest in the first millimetres for back irradiation. In farther depths, the curves overlap. Meanwhile, measurements with the 100 kV spectrum tend to have higher deviations between the results from the soft X-ray chamber and the radiochromic films. In three of the four setups, the dose rates measured with the soft X-ray chamber are approximate 10 to 30 % higher than those computed from film scans. As explained before, the fluctuations and deviations in dose rates obtained with radiochromic film may derive from the stepwise output of the corresponding software (compare with section 5.2.1).

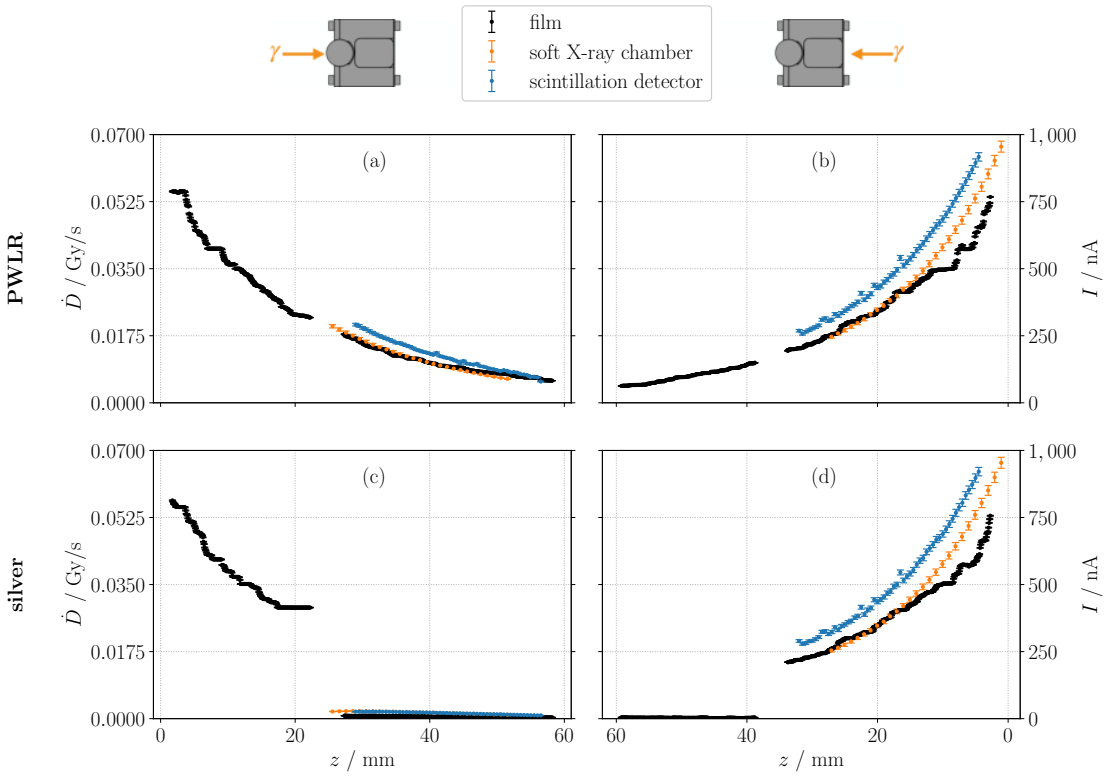

Figure 5.15: Depth dose curves for the 70 kV spectrum obtained with three different detector types. Values of the soft X-ray chamber and the films are associated with the left y-axes. Values of the scintillation detector are associated with the right y-axes. a) and c) show the results for front irradiation, b) and d) for back irradiation. In a) and b), the PWLR plaque is used, while c) and d) are obtained with the ^{106}Ru-dummy inserted.

All dose profiles measured with the PWLR dummy in place have the shape of an exponential function, as expected. But, of course, due to the higher energies, the depth dose

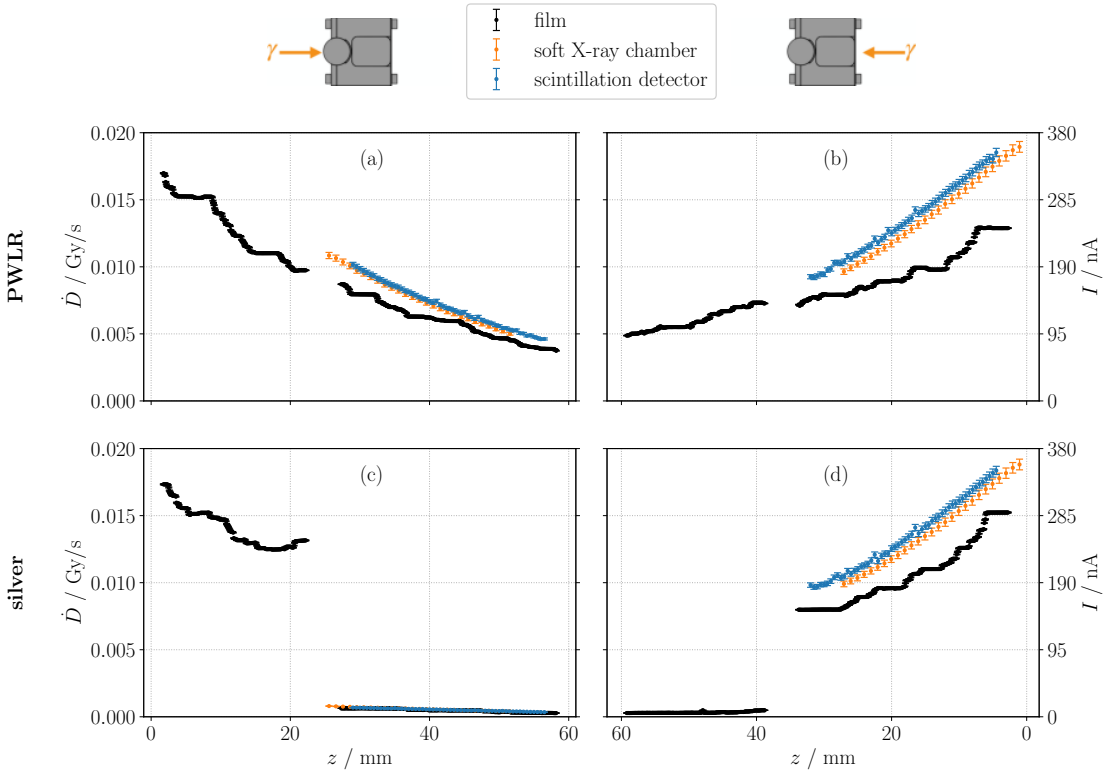

Figure 5.16: Depth dose curves for the 100 kV spectrum obtained with three different detector types. Values of the soft X-ray chamber and the films are associated with the left y-axes, while values of the scintillation detector are associated with the right y-axes. a) and c) show the results for front irradiation, b) and d) for back irradiation. In a) and b), the PWLR plaque is used, while c) and d) were performed with the ^{106}Ru-dummy inserted.

curve of the 100 kV spectrum is less steep than the one of the 70 kV. Small plateaus are observed in the curves obtained with radiochromic film, deriving from the output of the corresponding software, which is explained in section 5.2.1.

Regarding the suitability of the ^{106}Ru applicator, the plots show a significant dose rate drop behind the ^{106}Ru dummy for both spectra with all three detector types for front irradiation. Due to the construction of the phantom for back irradiation, the decrease in dose rate due to the ^{106}Ru dummy can only be seen within the results of the film measurements. For front irradiation with the 70 kV spectrum, the absolute dose rate in front of the plaque of $(2.898 \pm 0.006) \cdot 10^{-2}$ Gy/s sinks to $(7.656 \pm 0.016) \cdot 10^{-4}$ Gy/s behind the plaque. This means, the dose rate is reduced by (97.358 ± 0.008) % over approximately 5 mm including the 1 mm thick silver plaque. Similar results can be established from the 100 kV data set, in which the dose rate sinks from $(1.3152 \pm 0.0027) \cdot 10^{-2}$ Gy/s to $(6.292 \pm 0.013) \cdot 10^{-4}$ Gy/s, which equals a decrease of (95.216 ± 0.014) %. With the

PWLR-dummy inserted, the reduction amounts to $(19.34 \pm 0.23)\,\%$ and $(10.67 \pm 0.26)\,\%$ due to the exponential decrease over distance.

In addition, the film results show a dose rate increase in front of the inserted CCB dummy, especially for front irradiation. With a 70 kV spectrum being used, the dose profile shows a constant value for approximately 5 mm close to the silver plaque instead of the steady decrease over distance (compare figure 5.15). For the 100 kV spectrum, the dose profiles show even an absolute increase over distance in front of the ^{106}Ru dummy (see figure 5.16). In addition to backscattering, the excitation of silver atoms is an explanation. The excitation of the atoms leads to isotropic emission of photons with an energy of up to 25.5 keV [166]. Due to the energy spectrum, these secondary particles deposit dose close to the silver plaque.

The results from back irradiation measurements have the advantage that the radiochromic film between the two hemispheres is positioned in direct contact with the ^{106}Ru dummy. Dose rate decreases of $(93.927 \pm 0.018)\,\%$ and $(97.953 \pm 0.006)\,\%$ are observed for the two spectra due to the absorption in the ^{106}Ru dummy. Closely behind the silver plaque, no significant dose values are observed in the data. Thus, it can be concluded that the photons interact at a short distance to the entry surface in the ^{106}Ru applicator because of the high cross-section. The excitation of silver atoms results in isotropic radiation of low-energy photons with an energy of ≤ 25.5 keV. Suppose these photons are produced with momentum in the direction of the entry surface. In that case, they have a short distance to travel in silver. Accordingly, they also have a higher probability of being able to deposit the dose in front of the plaque. If their direction is the other way, the distance to travel in silver is longer, and the probability of leaving the ^{106}Ru applicator is more negligible. Thus, their impact on the dose profile is higher on the side the X-ray beam hits the ^{106}Ru applicator.

For better comparison, figure 5.17 displays the dose rate ratios $r = \dot{D}_{\mathrm{silver}}/\dot{D}_{\mathrm{PWLR}}$ for both spectra and both irradiation directions. Regarding the data acquired with the scintillation detector, the ratio $r = I_{\mathrm{silver}}/I_{\mathrm{PWLR}}$ is calculated and presented. A ratio > 1 means an increase of dose rate respectively current, while a value < 1 expresses a decrease due to the ^{106}Ru dummy.

For both front and back irradiation, the plot demonstrates the suitability of the silver plaque to be used as a beam stop. Front irradiation with the 100 kV spectrum shows ratios in the range of $(6.76 \pm 0.25) \cdot 10^{-2}$ to $(9.240 \pm 0.027) \cdot 10^{-2}$ for all detector types behind the plaque. The results for the 70 kV spectrum diverge between the different detectors. While the radiochromic film has values in the range of $(3.658 \pm 0.011) \cdot 10^{-2}$ to $(6.636 \pm 0.020) \cdot 10^{-2}$, the soft X-ray chamber and the scintillation detector show ratios in the range of $(9.0 \pm 0.4) \cdot 10^{-2}$ to $(1.65 \pm 0.05) \cdot 10^{-1}$. With back irradiation, the ratio behind the plaque is only accessible for the film data. The ratios are in the range of $(1.206 \pm 0.005) \cdot 10^{-2}$ to $(7.607 \pm 0.024) \cdot 10^{-2}$ for the 70 kV and in the range of $(4.646 \pm 0.015) \cdot 10^{-2}$ to $(8.34 \pm 0.05) \cdot 10^{-2}$ for the 100 kV spectrum. The ratios

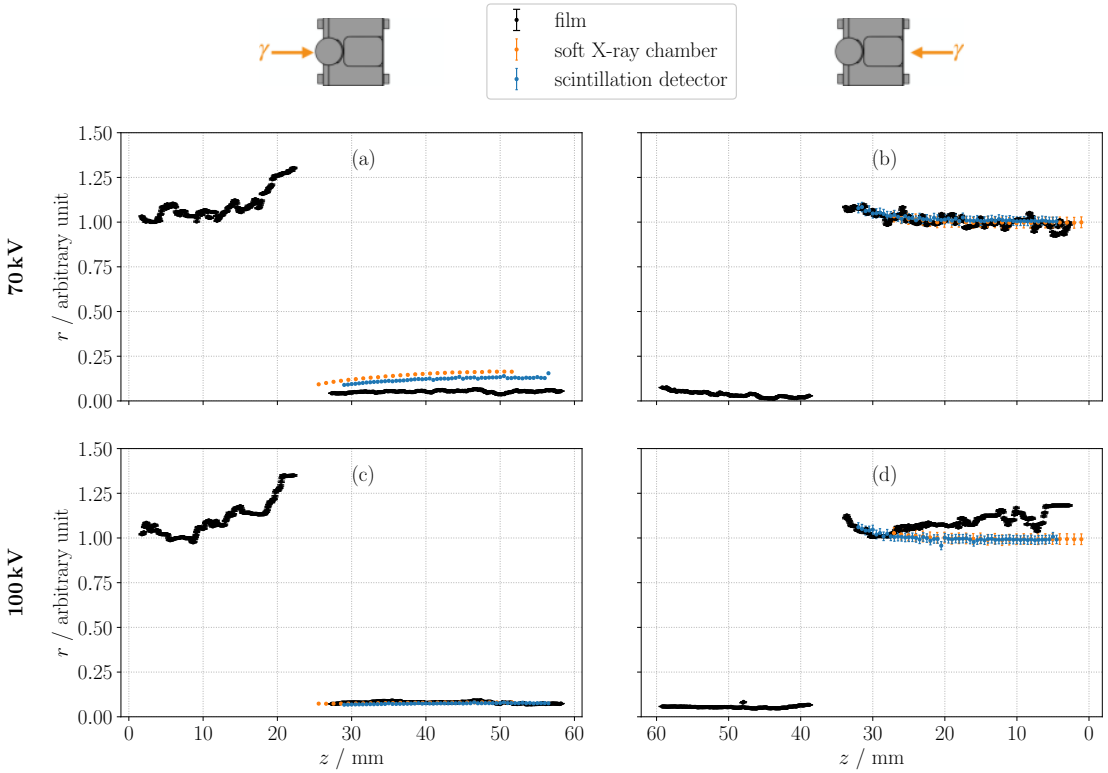

Figure 5.17: Ratios of the dose rates $r = \dot{D}_{\text{silver}}/\dot{D}_{\text{PWLR}}$ or currents $r = I_{\text{silver}}/I_{\text{PWLR}}$ respectively. The results from measurements with the 70 kV spectrum are displayed in a) and b), and for the 100 kV spectrum in c) and d). In a) and c), the results with front irradiation are shown, while in b) and d), results with back irradiation are presented.

indicate that most photons are absorbed in the plaque and deposit no dose in materials, respectively, healthy tissue behind the plaque.

The ratios also underline the relative dose increase in front of the plaque. Maximum ratios of 1.303 ± 0.004 and 1.350 ± 0.004 are calculated for the film data sets acquired with 70 kV and 100 kV accelerating voltage and front irradiation. As previously explained, this increase results from backscattering and excited silver atoms.

The ratios obtained with the three different detector types show deviations from each other for front irradiation with 70 kV behind the ^{106}Ru dummy (see figure 5.17). Compared to the results acquired with 100 kV, the 70 kV ratios are lower for the data of the films and higher for the other two detector types. As described in section 2.6, the cross-section of the photoelectric effect is proportional to E_γ^{-3}. Therefore, a larger fraction of the 70 kV photons are absorbed in the ^{106}Ru applicator compared to 100 kV. It

is expected to measure higher relative values for the 100 kV spectrum behind such an absorber, even though the general dose rate is lower for higher energies.

5.6.4 Corresponding simulation results

In the following, the data sets are referred to by the detector name the scorers represent. For example, the film simulation results represent the scored dose profiles obtained with the scorer that is dimensioned and positioned like the film in the measurements.

The 2D colour plots of the film scorer of the MC simulations are shown in figure 5.18. The dose profiles show similar results to figure 5.14, though the beam profile of the simulations has no divergence implemented. All dose profiles with a ^{106}Ru dummy included show significantly lower dose values behind plaque than those obtained with the PWLR plaque. A more detailed evaluation is carried out by analysing the DDCs.

Figure 5.19 presents the corresponding depth dose curves for both spectra and applicator materials in direct comparison. The simulated depth dose curves confirm the measurement results. The inserted ^{106}Ru dummy results in a drastic dose decrease behind the applicator. For front irradiation, the dose rate sinks to $(0.090 \pm 0.018)\,\%$ for the 70 kV spectrum and $(2.23 \pm 0.11)\,\%$ for the 100 kV spectrum compared to the dose rate in front of the ^{106}Ru dummy.

As seen in section 5.6.3, the ^{106}Ru applicator also leads to a dose increase in front of the plaque. Due to the steeper depth dose curve of the 70 kV spectrum, it seems like the effect is less relevant than for 100 kV. However, in figure 5.20 the ratio of the simulated dose values $r_\mathrm{S} = {}^{D_\mathrm{silver}}/_{D_\mathrm{PWLR}}$ are shown. The ratios for both spectra agree with each other in front of the plaque. Close to the plaque, the ratio reaches a value of approximately $r_\mathrm{S} = 1.5$, which is higher than the measured ratio of approximately $r = 1.3$. r_S of the 100 kV spectrum is in average 22 ± 5 times higher than the one of the 70 kV spectrum for front irradition. The average ratios behind the plaque are $r_\mathrm{S}^{70\,\mathrm{kV}} = (0.15 \pm 0.30)\,\%$ and $r_\mathrm{S}^{100\,\mathrm{kV}} = (3.52 \pm 0.18)\,\%$ for front irradiation.

The data sets need to be normalised to allow the comparison between simulations and measurements. The dose per primary particle of the measured X-ray beam can not be computed from the measurement results because the number of the primary particles that left the X-ray tube can not be established. Also, no beam time can be established from the simulation to transfer dose to dose rate. All dose $D(z)$, dose rate $\dot{D}(z)$, or current profiles $I(z)$ are normalised to 1 on a position z^* in the depth dose profile using

$$Y^*(z) = \frac{Y(z)}{Y(z^*)}, \qquad Y \in \{D, \dot{D}, I\} \tag{5.8}$$

This means, that $Y^*(z^*)$ equals 1 for all data sets. To compare all detector types within the same plot, the normalisation distance z^* is chosen to be 10 mm behind the entry surface of the brackets. This means, for front irradiation, the normalisation point is at $z_\mathrm{f}^* = 35.5\,\mathrm{mm}$ and at $z_\mathrm{b}^* = 11\,\mathrm{mm}$. The value of $Y(z^*)$ is calculated using a spline

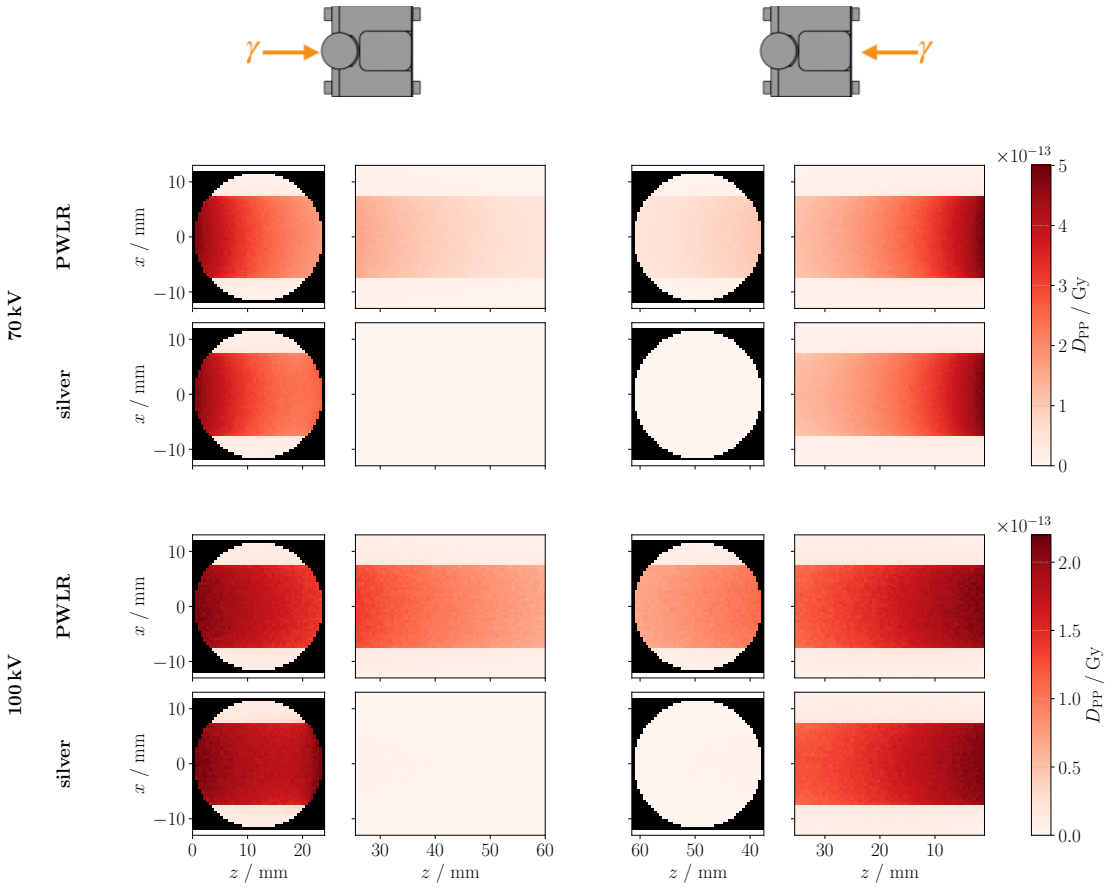

Figure 5.18: Two-dimensional dose profiles obtained from MC simulations. The dose is scaled to a single primary particle. All plots in the left column are created with front irradiation, while all plots in the right column present back irradiation data sets. The upper two rows represent the data sets obtained with 70 kV, while the lower two rows show the dose profiles for the 100 kV spectrum. For each spectrum, the corresponding colour bar is shown on the right. The first and third rows are data sets simulated with a PWLR applicator, while the second and fourth rows are data sets obtained with a silver applicator in the simulations.

function S through the corresponding measurement data. The function S is a polynomial of third degree. A standard spline takes every data point as a knot for the function. With the smoothing factor s provided by the function, the number of knots is calculated by increasing the number starting from 1 until the condition.

$$\left| \sum_i \{w_i \cdot [y_i - S(x_i)]\}^2 \right| - s < 0.001 \cdot s \tag{5.9}$$

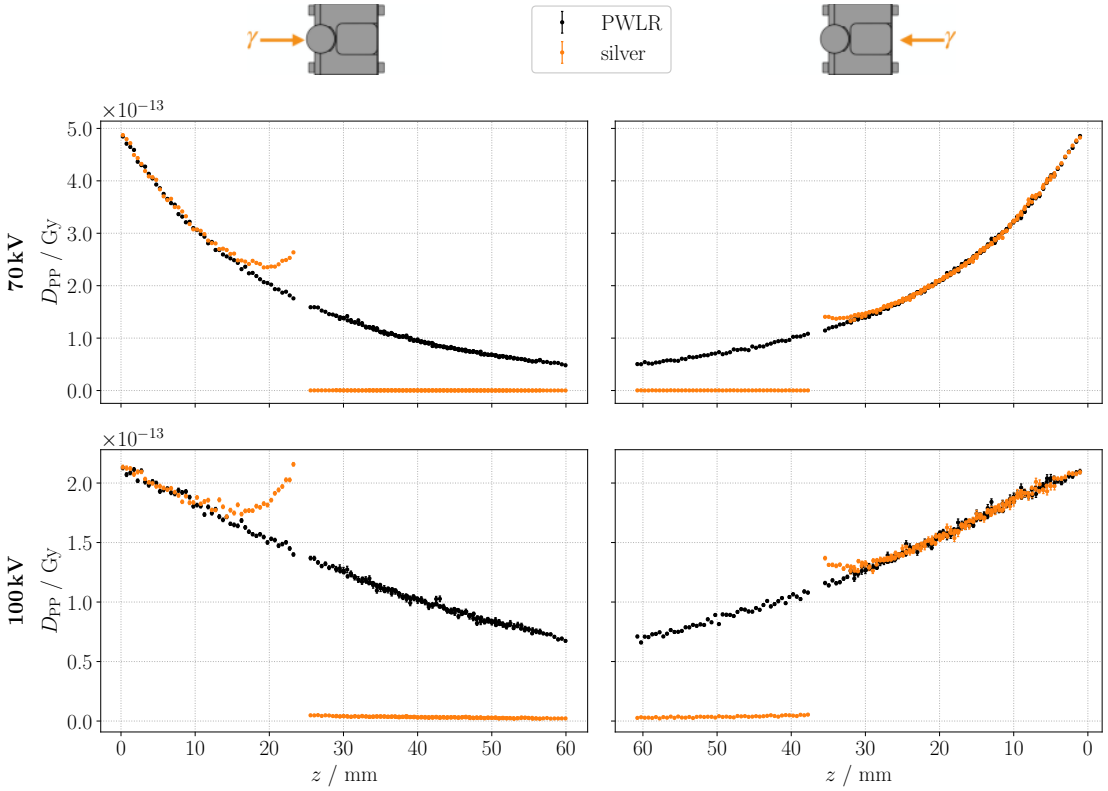

Figure 5.19: Depth dose curves obtained from MC simulations. The upper plots show results for the 70 kV spectrum, while the lower plots present data sets with 100 kV. Within the depth dose profile, the plaque is positioned in between 24 to 25 mm for front and 35.5 to 36.5 mm for back irradiation.

is fulfilled. In this equation, w_i is the weight for the data point (x_i, y_i). The weights are calculated as the inverse of the uncertainty $w_i = {}^1/_{\sigma_{y_i}}$. The smoothing factor is set to $s = \#(x, y) \cdot 5$ for the data obtained with the scintillation detector, the soft X-ray chamber, and the simulated data. Because of the higher fluctuations, a value of $s = \#(x, y) \cdot 150$ is set for the data obtained with the radiochromic films.

The normalised data are shown in direct comparison to each other in figure 5.21 for 70 kV and figure 5.22 for 100 kV. All normalised data agree with each other for front irradiation with 70 kV and an inserted PWLR dummy. The only difference between simulated and measured data can be seen in distances far away from z^*, where the simulated normalised values are higher than measured ones. This can be explained by the beam divergence that is not implemented in the simulation. In addition, there is a factor of approximately 10 between simulated and measured data in the sphere for the data with a ^{106}Ru applicator included in the setup, both for front and back irradiation. One explanation could be that there is background in the data set of the radiochromic

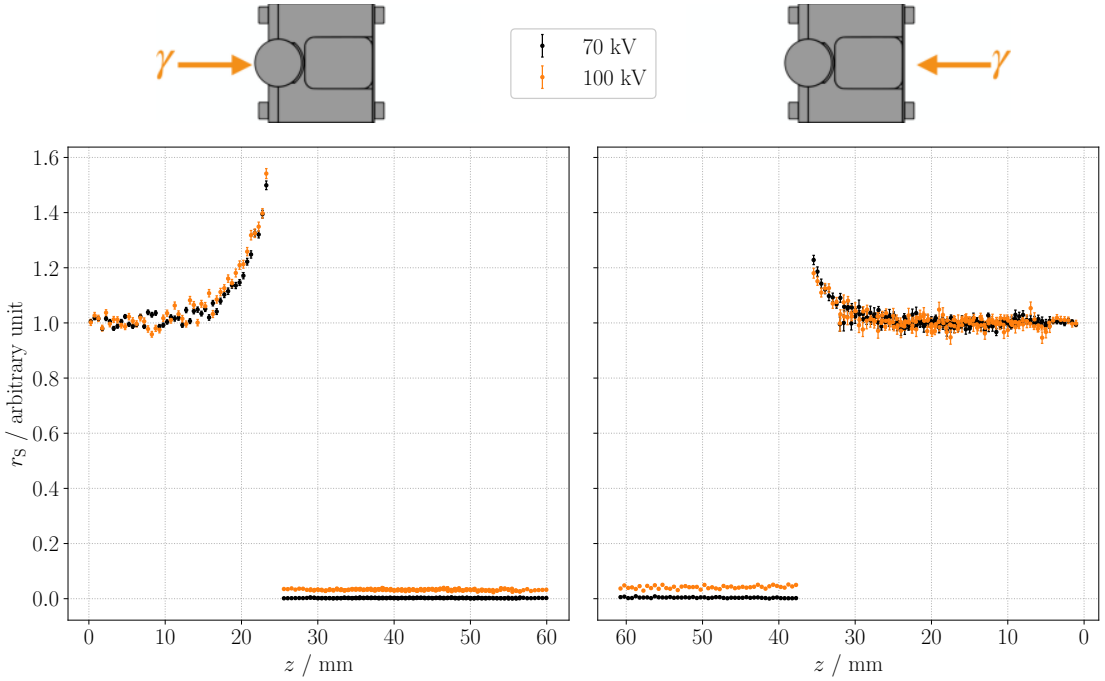

Figure 5.20: Ratios of the simulated dose profiles $\dot{D}_{\mathrm{silver}}/\dot{D}_{\mathrm{PWLR}}$ for a) front irradiation and b) back irradiation.

films, though two methods to correct the measured data for underground are included in the procedure. First, the calibration curve consists of a point for $D = 0\,\mathrm{Gy}$. Second, every scan consisted of the irradiated film and a not irradiated film. The software FilmQA Pro corrects the RGB values of the irradiated film with the ones of the not irradiated film. For low dose rate values, this background is more significant than for high dose rate values. Another explanation could be a substantial change in the energy spectrum of the photons behind the silver ^{106}Ru applicator. The energy dependence of the film is not included in the analysis due to missing information. Both reasons lead to higher dose rate values behind the silver plaque than simulated dose values. Due to the localisation of the normalisation point, this results in higher normalised film values behind the ^{106}Ru applicator for back irradiation and higher normalised simulated values in front of the ^{106}Ru applicator for front irradiation.

The normalised data for 100 kV presented in figure 5.22 show fewer deviations between the simulated and the measured data. With the ^{106}Ru applicator included in the setups, the factor between the data sets in the sphere is approximately 1.25. Due to the higher energies within the X-ray spectrum, the dose rate values are higher behind a silver target for 100 kV than for 70 kV irradiation. Thus, the background in the data sets obtained with the film has less influence.

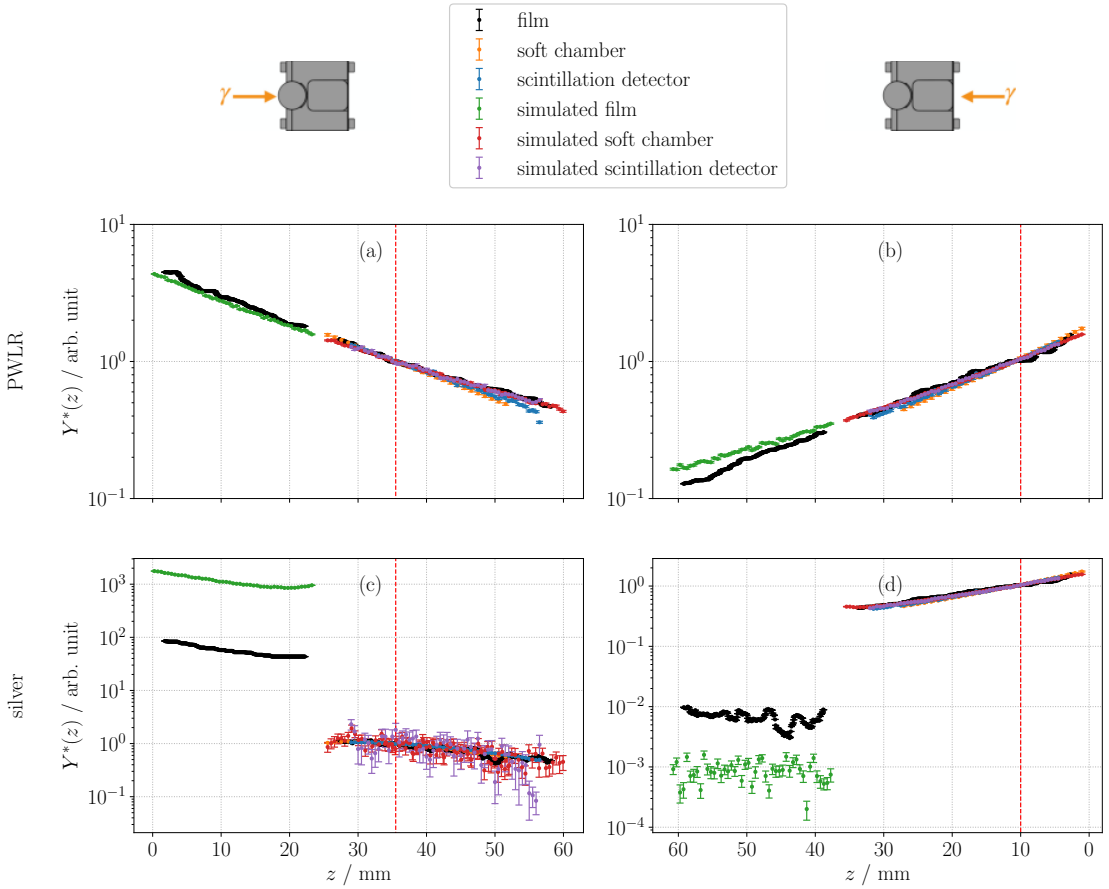

Figure 5.21: Normalised dose profiles $Y^*(z)$ of all simulated and measured types for the 70 kV spectrum. The red line shows the position of the normalisation value.

The normalised data show the impact of a ^{106}Ru applicator as an absorber on the dose profile of X-rays once more. For example, in figure 5.21, the factor between values before and behind the silver target for front irradiation with 70 kV is approximately 10^2 for measured data. The normalised values of the simulation even show a factor of 10^3. This underlines that many photons or large fractions of their energy are absorbed in the silver absorber the ^{106}Ru applicator resembles. With 100 kV X-rays this factor equals approximately 11 to 12 for the measured and 15 for simulated data.

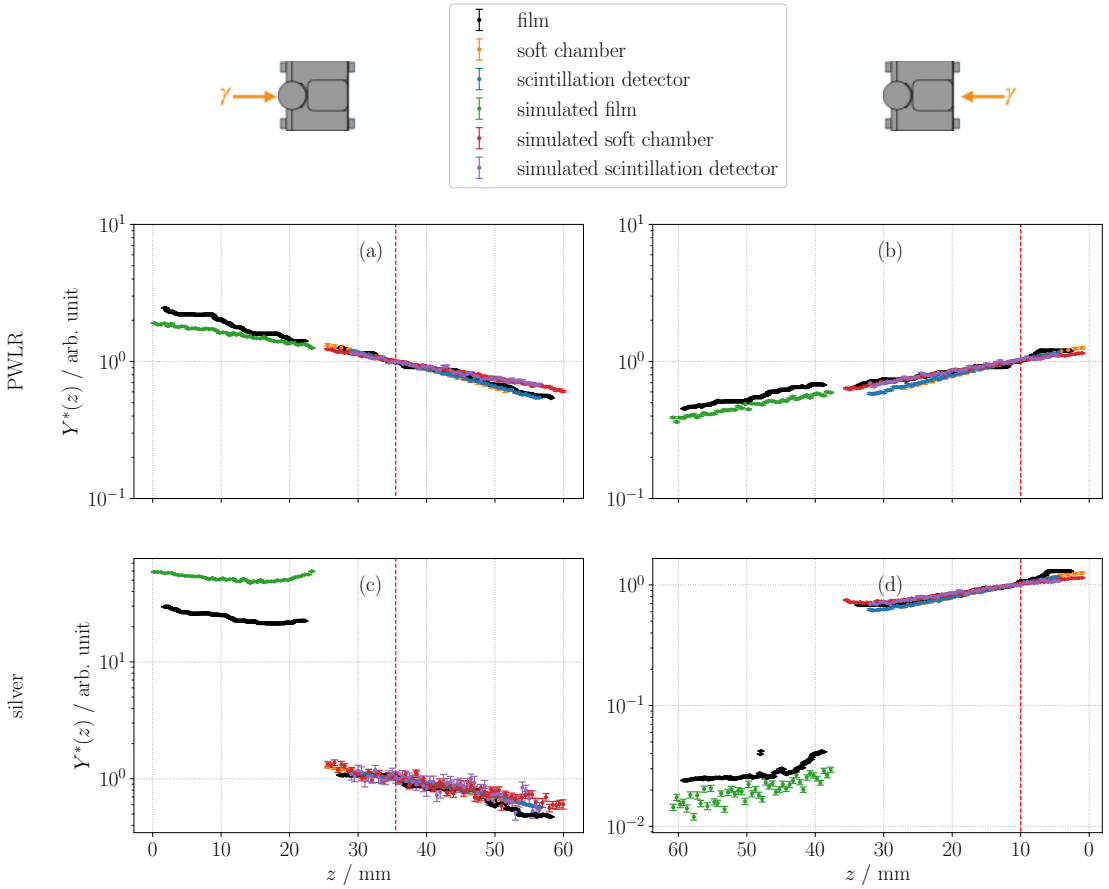

Figure 5.22: Normalised dose profiles $Y^*(z)$ of all simulated and measured types for the 100 kV spectrum. The red line shows the position of the normalisation value.

5.7 Summary and discussion

In this chapter, measurements regarding the combined therapy concept were presented. These measurements focussed on the interaction of X-rays with an ^{106}Ru applicator. For these measurements, a phantom was constructed. The material PWLR is chosen due to the simulation results regarding the water equivalence for both X-rays and irradiation with a ^{106}Ru applicator. In this phantom, three detector types can be used to obtain dose profiles: a self-build scintillation detector, a soft X-ray chamber and radiochromic film. The phantom consists of several parts, of which one sphere resembles the eye. A recess for a ^{106}Ru applicator of type CCB is positioned behind this sphere, followed by a cutout for various detector brackets. The soft X-ray chamber and the scintillation detector can be placed in corresponding brackets to obtain a depth dose curve. In addition, the

radiochromic film may be placed in the bracket or between two hemispheres. Therefore, with the film, it is also possible to obtain dose profiles in front of the ^{106}Ru applicator.

A novel approach to obtain transparent scintillators from PEN was introduced in the context of the scintillation detector construction. The PEN granulate is melted to form a block larger than the intended dimensions and subsequently processed with a milling machine, which an XYZ-apparatus precisely moves. This process offers a more efficient and convenient alternative to previous methods utilised in the working group. The selected scintillation detector exhibited a signal-to-noise ratio of approximately 2500, and no abnormalities were observed in the production process.

The measurements were performed with an X-ray therapy unit of type T-105 provided by the manufacturer WOmed. To be able to evaluate the measurements, the uncertainties resulting from the phantom and the setup were calculated first. These uncertainties included the influence of repositioning the phantom relative to the X-ray tube, the current up and downscaling, the filling pieces with minor deviations from each other, and the X-ray tube replacement within the period of data taking. All measured uncertainties were in the range of 0.15 to 0.50 %. Accordingly, the systematic uncertainties of the detectors outweigh the uncertainties calculated for the novel phantom.

Dose profiles were obtained for front and back irradiation, with either the ^{106}Ru dummy or a PWLR dummy inserted. Two energy spectra were used for the measurements: 70 kV and 100 kV. The overall shape of the dose rate or current profiles obtained with the detector types were similar. However, the radiochromic film data had higher fluctuations and deviations of up to 30 % to the soft X-ray chamber. This may result from various reasons. Even with all the efforts, ensuring that all films were always positioned in the same direction while scanning was not possible. Furthermore, the films were placed parallel to the direction of the beams, which is not the intended use case.

The measurement results show a strong dose rate drop behind the ^{106}Ru dummy to approximately 2 to 5 %. This means a ^{106}Ru applicator can be used as a beam stop for low energy X-rays with energies up to 100 kV. The interaction of the photons with the silver atoms also leads to a dose rate increase in the DDC beginning approximately 10 mm in front of the applicator. Most likely, this results from the excitation of silver atoms, which emit photons isotropically. As these photons are produced near the entry surface of the X-rays into the ^{106}Ru applicator, these photons had no impact on the measured data on the other side of the applicator.

Corresponding MC simulations were performed with Geant4. The sensitive volumes of all detector types were included in the simulation and defined as PWLR to reduce the influence of those volumes on each other results. The ^{106}Ru applicator was important as a silver absorber without irradiation from ^{106}Ru-decays. The simulations confirmed the general results from the measurements. The DDCs consist of a substantial dose drop behind the ^{106}Ru applicator and an increase in front of the applicator. The simulations show a higher dose growth for 100 kV in front of the applicator than the measurements. Furthermore, the simulation data exhibit that for 100 kV, a higher fraction of dose

persists behind the applicator than for 70 kV, which was expected due to the known cross-sections. Meanwhile, in the measurement data, the opposite was observed. An explanation can be found in the overall very small values observed behind ^{106}Ru applicator. The smaller the dose rate, the higher the influence of underground and noise on this value. Regarding the soft X-ray chamber and the radiochromic films, the measured values are smaller than the lower limits of the corresponding measuring range [146, 153].

The choice of the X-ray energy spectrum for the combined therapy concept is ultimately based on a trade-off between two parameters. The less steep dose gradient of the 100 kV spectrum results in lower dose values in the anterior parts of the eye when the same dose is deposited in the tumour. However, the higher energies also result in a lower absorption rate and, therefore, in higher dose values behind the ^{106}Ru applicator. Because the absolute dose values in front of the ^{106}Ru applicator are overall higher than behind it, the positive effect of higher energies to reduce dose in the anterior parts of the eye is evaluated more positively. This results in the recommendation to use relatively high energy spectra like 100 kV for the combined therapy concept. The evaluation and decision should be made again when more information is available. It is unknown what dose has to be applied by a single field and what effects on the DVH are observed for different energy spectra. More energy spectra in the range of $50\,\mathrm{kV} < U < 300\,\mathrm{kV}$ should be considered, measured and evaluated to find the best possible setup for the combined therapy concept.

The results of the measurements confirm the idea of using a ^{106}Ru applicator as a beam stop within the combined therapy concept. The dose increase in front of the ^{106}Ru applicator due to the interactions of the X-rays with the silver atoms is a slight disadvantage, as the X-rays are intended to provide a dose boost to the tumour apex and not to the tumour base. However, the gradient of the increase is less steep than the gradient of the dose profile of an active ^{106}Ru applicator. The dose increase in front of the ^{106}Ru applicator might result in an additional decrease in the application time for the brachytherapy source, which restricts the time window for the X-ray therapy.

The data obtained with the radiochromic film showed high deviations and fluctuations. To avoid this, several approaches can be used in the future. With a second cutout on the round films and a single cutout on the rectangle films, which are positioned away from axes of symmetry, the scanning direction of the film can consistently be reproduced. However, the software used to compute dose profiles from the RGB values of the scan - FilmQA Pro - leads to unexpected dose profiles, as no steady but a stepwise curve was observed. A study on the parameters during calibration and dose calculation should be performed to gain more information and control. Furthermore, the energy dependence of the films was not considered in this analysis. With additional information, the energy dependence can be evaluated, which leads to the possibility to convolute the spectrum with the corresponding efficiency of the film to obtain more precise dose profiles. The bracket for the films should be modified to minimise the effect of the film on the obtained DDC itself. An angle between the plane of the film and the direction of the X-ray beam decreases the influence [167–171]. With an increase of the beam time, the acquired doses

behind the ^{106}Ru applicator can be increased to values in the optimal measurement range stated by the manufacturers to minimise the signal-to-noise ratio. When all approaches have been implemented, the measurements should be repeated with higher precision.

A few modifications of the phantom can improve its suitability for measurements regarding the combined therapy concept. The position uncertainty of the two hemispheres and the radiochromic film in front of the ^{106}Ru applicator can be minimised by having an elevation at one point of the hemispheres that fits into a corresponding recess in the front plate of the phantom. The sphere with the detector inside can not freely rotate in its cavity.

The next step to the combined therapy concept is obtaining confocal irradiation dose profiles. The X-ray tube should be mounted to a robotic device to provide a low position uncertainty of the incident X-ray beams.

6 Clinical software for retrospective dose evaluation

As described in section 2.3, most retrospective studies on dose-effect ratios regarding ^{106}Ru brachytherapy rely on values obtained from treatment planning. Due to the position uncertainty and the steep dose gradient, particularly present near the rim of the applicator, the dose values underly considerable systematic uncertainties. So far, no software is allowing the computation of retrospective dose values in OARs or the tumour while considering the exact position of the ^{106}Ru applicator. This chapter presents such software. It enables the user to calculate critical dose values and dose area histograms for various organs of interest depending on the previous placement of the ^{106}Ru applicator during therapy.

The chapter begins with an introduction to fundus photos, followed by the basics of the software in section 6.2. Next, an explanation of transferring 2D pixel coordinates into spherical coordinates in the system of the eye is presented. The software relies on information regarding the position of the ^{106}Ru applicator during the treatment, which is solved in section 6.4. The MC simulations to generate the corresponding dose information are explained in section 6.5. Finally, a summary is provided at the end of the chapter. In addition, in this section, the results are discussed in the context of the current scientific status, and an outlook on future possibilities is given.

The software presented in this chapter and the underlying considerations and assumptions were developed in collaboration with Dirk Flühs[27].

6.1 Fundus photos

After the diagnosis of an intraocular tumour, the fundus photo is taken with a special camera to document the tumour. An example is displayed in figure 6.1.

The fundus photo is repeated at each follow-up appointment of the patient to record the changes. Essential structures such as the papilla, the macula, blood vessels and the retina can be seen. In the case of an intraocular tumour, the malignant tissue appears

[27] Dr. rer. nat. Dirk Flühs, medical physics expert at the University Hospital Essen, Essen, Germany.. Responsible for brachytherapy, including afterloading and treatment of ophthalmic tumours with COMS- and ^{106}Ru applicators.

as a dark area in the photo. In addition, approximately 1 to 2 y after brachytherapy, a radiation scar gets visible as shown in figure 6.1.

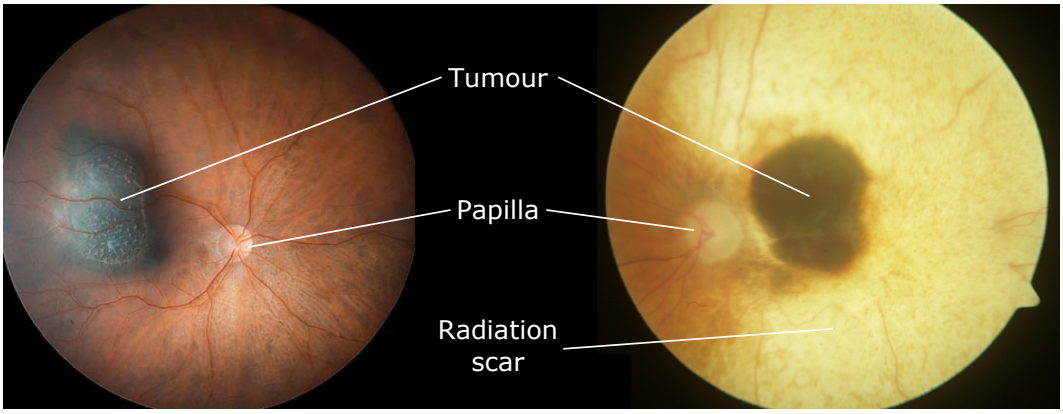

Figure 6.1: Two examples of fundus photos. In the right photo, a radiation scar from a ^{106}Ru applicator of type COB can be seen. The left picture is obtained from Ref. [26].

The conventional fundus photography images about 20° of the eye. The image is taken with a camera through the pupil. These photos can be combined to obtain a complete image called a fundus puzzle. In some cases, the distortion of the individual photos makes it difficult to create a fundus puzzle. However, modern wide-angle fundus photography allows the fundus of the eye to be imaged with an aperture angle of 120°. This is enabled by placing an imaging head directly on the cornea. Nevertheless, the image is distorted since the spherical structures are projected on a plane. Distortions are also well-known in cartography. At least for wide-angle fundus photography, the distance between a point and the centre of the image is proportional to the arc length on the surface of the retina. It is also assumed to be the correct projection for the conventional method [172, 173].

For the following analysis, it is assumed that the photo is taken on a sphere with a radius of curvature of 11 mm. This value is chosen due to the approximate eye diameter of 24 mm and the sclera thickness, which is assumed with 1 mm in the treatment planning at the UKE.

The fundus photo is a 2D image in which pixels or contours are transferred to the surface of this sphere. However, it does not provide any information regarding the height of structures. In addition, the software MS Excel[28] and VBA[29] are not intended for 3D modelling. Because of this, the software further described only aims at analysing dose profiles of points on the surface. Thus, instead of DVHs, which are very common in medical physics, dose-area histograms are calculated.

[28] Microsoft® Excel®.
[29] Microsoft® Visual Basic® for Applications.

6.2 Basics of the software

The software is written in MS Excel and VBA. This choice is based on two reasons. First, the software regulations in hospitals are sometimes rather strict, and many software tools are not allowed to be installed due to data protection guidelines. Second, the existing treatment planning software at the UKE is also based on MS Excel and VBA. The different subprocesses of the software are available by the graphical user interface, which is displayed in figure 6.2. In addition, if the software needs information from the user or detects false or missing data, so-called user forms are implemented to communicate.

After loading a fundus photo into the spreadsheet, the contours of several structures can be drawn. The tumour, papilla and fovea are obligatory to continue with the dose calculation. Depending on the expected shape of a structure, the user either contours freehand or positions an ellipsis on the fundus photo. The VBA code that runs in the background continuously secures the spreadsheet to avoid the accidental deletion or modification of any contour or the fundus photo. However, the user is enabled to save, redraw or delete already drawn contours.

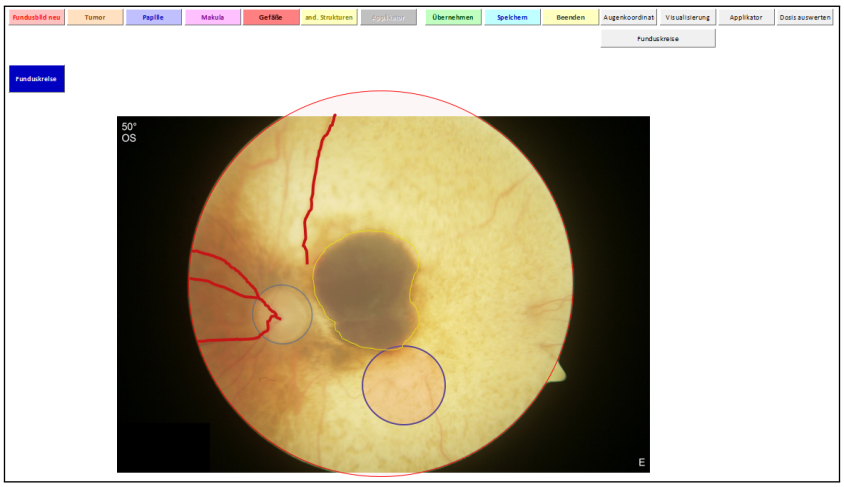

Figure 6.2: Screenshot of the software realised in MS Excel and VBA. In the middle, a fundus photo is implemented. The contours are outlined to provide examples and were not used for dose analysis, as they were included by a non-professional. The following structures can be seen: tumour (yellow), papilla (bright blue), macula (dark blue), blood vessels (red), and fundus circle (red circle).

The implemented photo often shows the fundus as a circular photo on a black rectangular background. However, the centre of the circle containing the information is not always positioned in the centre of the rectangle. Thus, the user is asked to include a fundus circle, which can be shifted and varied in scale to overlay the circular fundus photo. Regarding a fundus puzzle, the image containing the most information has to be selected.

All computed pixel coordinates (x, y) are the relative coordinates between the centre of this fundus circle and the analysed point.

6.3 Calculation of 3D-coordinates from fundus photos

The distortion must be considered to calculate distances within the fundus photo precisely. The projection that describes this distortion best is the Azimuthal Equidistant Projection (AEP) [172, 174].

6.3.1 Azimuthal equidistant projection

This type of projection has the characteristic that all directions between any point of the image and the chosen centre are preserved. In addition, it is equipped with the feature that distances between the centre and any point are only linearly scaled. As with any other azimuthal projection, the distortion is minimal at the centre and increases with the distance to the centre [175].

The following mathematics, which builds the fundament of the AEP, is derived from the comprehensive description in Ref. [175]. In cartography, the projection is calculated with the function $f_{\mathrm{AEP}} : P \to P'$. The domain of this function comprises all points $P(r, \theta, \phi)$ on the surface of the sphere with the radius r, the inclination θ and the azimuth ϕ. They are transferred to the points $P'(x, y)$ in the cartesian system of the 2D plane they are projected on. The point $P_0(r, \theta_0, \phi_0)$ is defined as one pole of the globe and is transferred to the centre of the 2D image. This means the distortions are smallest around P_0. The following equations compute x and y from the spherical coordinates of P:

$$f_{\mathrm{AEP}} : P(r, \theta, \phi) \longrightarrow P'(x, y)$$

$$x = r \cdot k \cdot \cos(\theta) \cdot \sin(\phi - \phi_0), \tag{6.1}$$

$$y = r \cdot k \cdot [\cos(\theta_0)\sin(\theta) - \sin(\theta_0)\cos(\theta)\cos(\phi - \phi_0)], \tag{6.2}$$

$$\text{with} \quad k = \frac{c}{\sin(c)} \tag{6.3}$$

$$\text{and} \quad c = \arccos[\sin(\theta_0)\sin(\theta) + \cos(\theta_0)\cos(\theta)\cos(\phi - \phi_0)] .. \tag{6.4}$$

If $\cos(c) = 1$, the point P resembles the centre of the image P_0. Meanwhile, $\cos(c) = -1$ means the opposite pole is transferred and illustrated as a circle in the picture.

The inverse function calculates 3D coordinates on the surface of the sphere from the 2D image coordinates:

$$f_{\mathrm{AEP}}^{-1} : P'(x,y) \longrightarrow P(r,\theta,\phi)$$

$$\theta = \arcsin\left[\cos(d)\sin(\phi_0) + \frac{y\sin(d)\cos(\theta_0)}{\rho}\right], \tag{6.5}$$

$$\phi = \phi_0 + \arctan\left[\frac{x\sin(d)}{\rho\cos(\theta_0)\cos(d) - y\sin(\theta_0)\sin(d)}\right], \tag{6.6}$$

$$\text{with} \quad d = \frac{\rho}{r} = \frac{\sqrt{x^2+y^2}}{r}. \tag{6.7}$$

6.3.2 Scaling and computing

To compute the absolute coordinates, the following assumptions and definitions are made. The rear eye pole is defined to be on the z-axis at $r = 12\,\mathrm{mm}$. To scale the distances in the picture, the distance of $(4.76 \pm 0.34)\,\mathrm{mm}$ [176] between the centre of the fovea and the centre of the papilla is used. The distance is not corrected with the distortion because one absolute distance has to be known to apply a distortion correction. The papilla and macula are close to the rear pole and, therefore, to the centre of the picture, where the distortion is smallest, as explained in section 6.1. The triangular information of the rear pole, papilla and fovea, illustrated in figure 6.3a, is used to obtain the position of the rear pole. The angle between a horizontal axis and the connection line between the papilla and the fovea is stated to be $\alpha_{\mathrm{pf}} = (6.08 \pm 3.48)^\circ$ [177]. This angle is also derived from the pixel coordinates of the contours. Together with the information that the foveal shift to the rear pole is $(\Delta x_{\mathrm{M}}, \Delta y_{\mathrm{M}}) = (1.25\,\mathrm{mm}, 0.5\,\mathrm{mm})$ [178], the position of the rear pole is calculated. Its angles θ_{RP} and ϕ_{RP} are further used in addition to θ_0 and ϕ_0 in the calculation of the AEP.

In the next step, all contours are transferred to the 3D coordinate system and saved on another spreadsheet. The user may check the computation with an implemented feature that displays the contours on the surface of a sphere in a 3D plot. The user may change the point of view by entering three angles α, β, γ. The corresponding rotation matrix is computed using the roll-pitch-yaw definition presented in Ref. [179].

6.4 Implementation of the ^{106}Ru applicator

After the contouring is finished and checked with the inbuilt visualisation, the ^{106}Ru applicator can be implemented. After choosing the model, the software draws two contour lines on the spreadsheet with the fundus photo, representing the outlines of the corresponding model and its target. Their shape is projected from the form of the 3D model, which is first assumed to have its centre in the centre of the photo. All points of the contour are transferred into the 2D coordinate system using the function of the

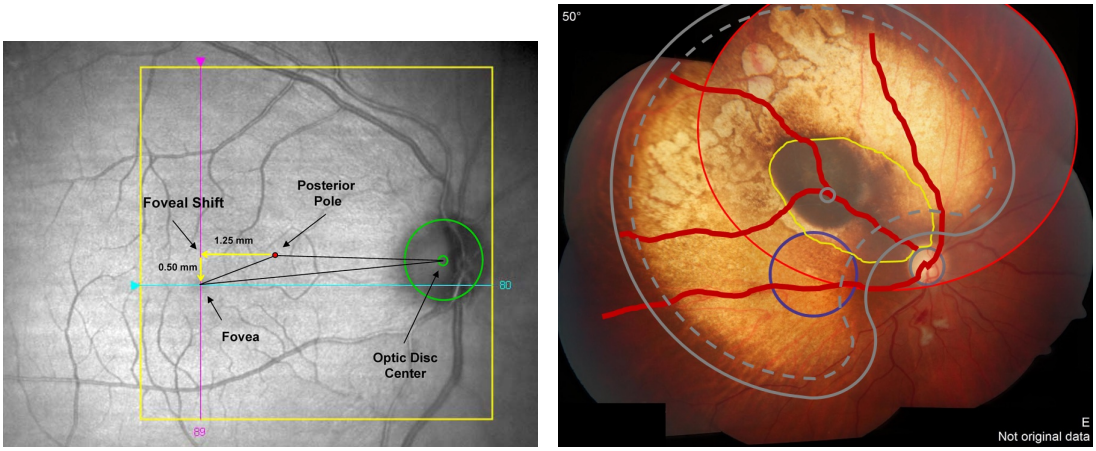

a) b)

Figure 6.3: a) Image of the retinal geography including highlighting the optic disc, fovea, geometric axis and the foveal shift. The picutre is obtained from Ref. [178]. b) Screenshot of a fundus photo with a projected COB and various contours: tumour (yellow), papilla (bright blue), macula (dark blue), blood vessels (red), and fundus circle (red circle). The outline of the COB is displayed as a solid grey line, while the outline of the target is displayed as a dashed grey line.

AEP, which is written in equations (6.1) to (6.4). By alternately shifting the contour of the ^{106}Ru applicator to a new position and reprojecting the contours considering the distortion, the user finds the best overlay between the contour of the ^{106}Ru applicator and the radiation scar, as displayed in figure 6.3b. In the background, not only the contour but also the centre of the concave surface of the applicator is transferred.

6.5 Monte-Carlo simulations of dose profiles

The software aims to provide retrospective dose calculations. To achieve this, the dose profiles of the ^{106}Ru applicators are obtained from MC simulations (see section 4.3 for basic information).

To compute a dose value for a point $P(r, \theta, \phi)$, it is derived from the corresponding dose profile of the ^{106}Ru applicatoremployed during the treatment. All rotationally symmetrical ^{106}Ru applicators the manufacturer offers are simulated (compare with Ref. [180]). Each applicator is described using its opening angle θ and inner radius of curvature r_i. The outer radius of curvature is defined as $r_\mathrm{O} = r + 1\,\mathrm{mm}$. Their geometric data are listed in table A.2. In addition, data for the applicator of type COB is computed. Its simulation is derived from Ref. [84], and its geometric data are presented in table A.3

and figure A.23. The eyelets of the ^{106}Ru applicator and the inner golden layer of the target are neglected in all simulations, as suggested in Ref. [63].

Each ^{106}Ru applicator model is simulated independently within a water surrounding. ^{106}Ru-atoms are positioned homogeneously on the spheric surface with $r_\mathrm{T} = r_\mathrm{i} + 0.1\,\mathrm{mm}$. The target is defined as a spheric volume with a radius of $r_\mathrm{i} + 0.05\,\mathrm{mm} < r_\mathrm{T} < r_\mathrm{i} + 0.15\,\mathrm{mm}$ and its opening angle $\theta_\mathrm{T} < \theta$. The ^{106}Ru-atoms are placed correctly by confining the particle generator sphere with the target volume.

For this software, two different dose profiles are of interest. On the one hand, the dose profile in a 1 mm distance to the concave surface of the applicator is obtained to compute dose values for the structures. On the other hand, the DDC is acquired because the simulated dose profile needs to be normalised to the actual therapy. In clinical practice, the treatment planning is performed with the DDC. Therefore, the dose applied to the tumour apex, which is assumed to be on the axis of the DDC, is well known and can be used for further calculations.

The dose profile of a rotationally symmetrical applicator only depends on the distance d and the angle between the axis of symmetry and the scorer $\Delta\theta$. Therefore, the dose profile is scored with 45 cylinders implemented as CBS. The placement varies depending on $\Delta\theta$, which is altered in the interval of $[0°, 90°]$ in steps of 2°. The cylinders each have a diameter of 1 mm and a height of 0.5 mm. They are rotated so their ground surfaces are parallel to the concave surface of the ^{106}Ru applicator. The distance Δd between the concave surface of the applicator and the centre of the cylinder equals $\Delta d = 1\,\mathrm{mm}$. In addition, a full DDC is scored on the axis of symmetry of the ^{106}Ru applicator with a 24 mm long and 1 mm thick cylinder. The DDC is obtained with a resolution of 0.5 mm.

Due to the notch in the ^{106}Ru applicator of type COB, its dose profile also depends on the angle $\Delta\phi$, which is the angular position. It is defined as the angular difference between the scorer and the middle line of the notch. 200 SD are implemented to calculate the dose profile. They cover one half of the ^{106}Ru applicator with $0° < \Delta\phi < 180°$ as illustrated in figure 6.5a. The dose profile of the other half is obtained by mirroring the scored values. These sensitive scorers have the same dimensions and placement settings as the CBS for the rotationally symmetrical ^{106}Ru applicator types but follow a new pattern regarding $\Delta\phi$ and $\Delta\theta$. While $\Delta\theta$ is varied in the interval of $[0°, 71.5°]$ in 5.5° steps, the number of scorers per row with the same $\Delta\theta$ differs from 1 to 20. For $\Delta\theta_\mathrm{max} = 71.5°$ the angle $\Delta\phi$ is altered in the interval of $[0°, 180°]$ with a stepsize of 9°.

The scored dose profiles of the MC simulations shall be implemented in VBA as a continuous function of the corresponding parameters. This means each dose profile is interpolated using different techniques. Regarding the DDC, the dose d is fitted with the function

$$D(d) = \exp\left(a \cdot d^2 + b \cdot d + c\right), \tag{6.8}$$

where d is the distance to the ^{106}Ru applicator.

The dose profiles depending on $\Delta\theta$ for the rotationally symmetrical ^{106}Ru applicators are interpolated with a cubic spline function of the third degree. Because the dose profile of the model COB depends on $\Delta\theta$ and $\Delta\phi$, it is interpolated using a bi-cubic spline of the third degree. The splines are implemented in VBA using Ref. [181, 182].

The scored dose profiles are displayed in figure 6.4a and figure 6.4b. The dose is divided by the number of generated ^{106}Ru-atoms $D_{\mathrm{PP}} = {}^{D}/_{\#\mathrm{PP}}$.

As expected, the DDCs show an exponential decrease with the distance d. The DDCs are generally lower for bigger applicator dimensions. Due to the wider target area on which the radioactive atoms are placed, fewer particles reach the central axis where the DDC is scored.

A plateau of varying size is observed regarding the dose profiles as a function of $\Delta\theta$. The plateau size is correlated to the geometric dimensions of the target in the ^{106}Ru applicator model. Behind the plateau, the decrease is similar to a logistic function. Due to the notch of the COB, the dose profile is more complex and a gap in the high dose profile is observed at $\Delta\phi = 0°$. The complete profile is displayed in figure 6.5b.

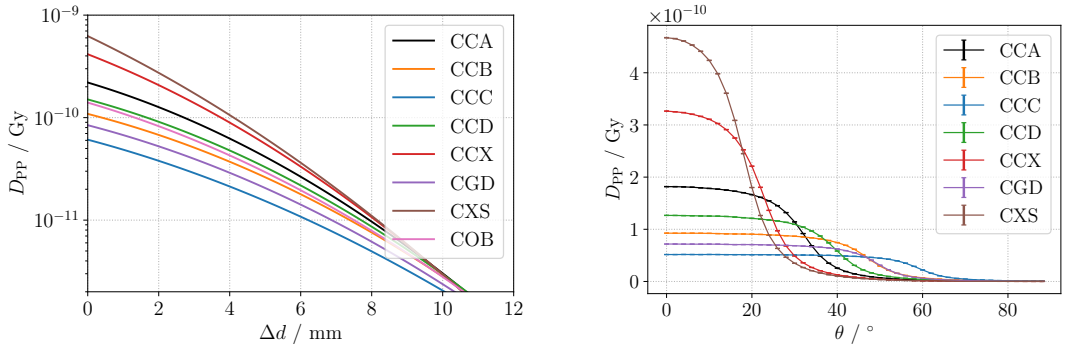

a) b)

Figure 6.4: a) DDCs of all simulated ^{106}Ru applicators. b) Dose profiles as a function of $\Delta\theta$ for all rotationally symmetrical ^{106}Ru applicators. In both plots, the dose is normalised to a single ^{106}Ru-decay.

6.6 Dose profiles for organs of interest

The calculation of the dose profiles for all structures of interest is performed using a homogeneous point cloud, as displayed in figure 6.6. In the enclosed area of the structure, a set of points is defined $S = \{\vec{s}, \vec{s} \in \vec{P}(x, y)\}$. Each point P_i is transferred to the 3D coordinate system using the AEP with equations (6.5) to (6.7):

$$P_i(x, y) \xrightarrow{\mathrm{AEP}} P_i'(r, \theta, \phi). \tag{6.9}$$

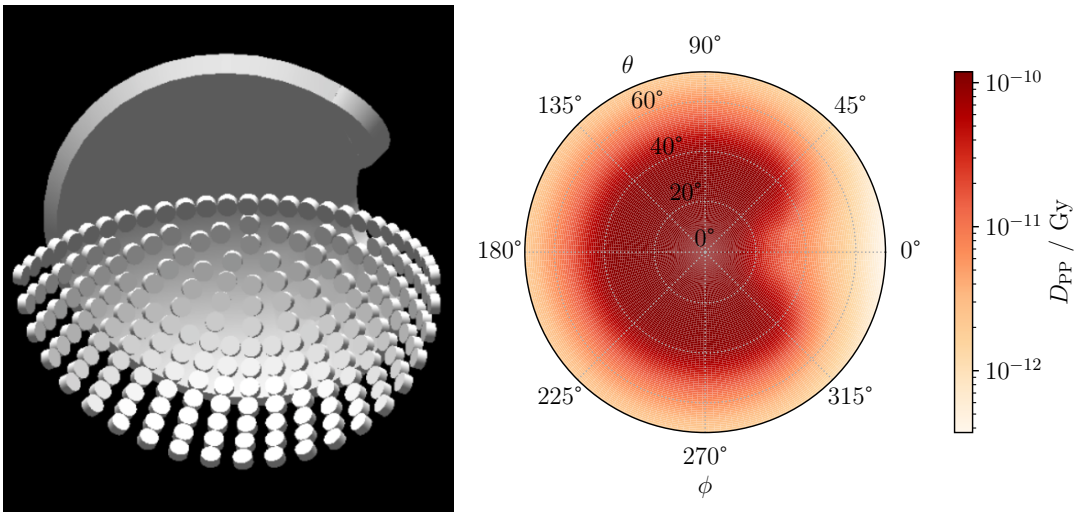

a) b)

Figure 6.5: a) Scoring mesh, which comprises 200 SD, to quantify the dose profile of the COB. The picture is acquired from Ref. [84]. b) Dose profile as a function of $\Delta\theta$ and $\Delta\phi$ of the COB. The profile is obtained at a distance of 1 mm to the concave surface of the ^{106}Ru applicator and normalised to a single ^{106}Ru-decay.

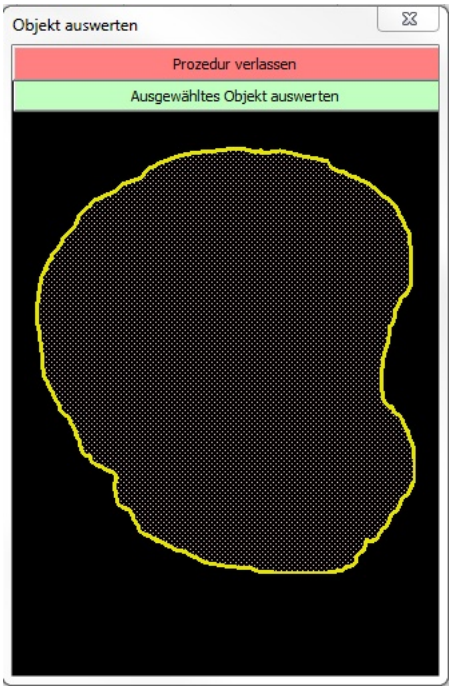

Figure 6.6: Isolated tumour contour with a homogeneous array of points in its area to analyse the dose profile of the structure.

Furthermore, the centre of the ^{106}Ru applicator P'_{Ru} is known due to the previously described implementation of the ^{106}Ru applicator. By comparing the calculated point P'_i to P'_{Ru}, the angular distance $\Delta\theta_i$ and for the COB also $\Delta\phi_i$ between these two points is obtained.

The user is asked to enter the applied dose at the tumour apex D_{TA} and the tumour height h_{T}, including the sclera thickness. The sclera thickness is assumed to be 1 mm during treatment planning at the UKE. With these two pieces of information and the DDC fit described in section 6.5, the factor f is calculated. It is defined by the ratio of D_{TA} and the value $D(h_{\mathrm{T}})$ of the DDC obtained from the simulations. This factor is used to normalise all upcoming calculated dose values, which means that after the normalisation, the dose value corresponds to the total dose applied by the treatment. Next to its normalisation purpose, the factor can be interpreted as the approximate number of ^{106}Ru-decays during the treatment period.

$$f = \frac{D_{\mathrm{TA}}}{D(h_{\mathrm{T}})} \tag{6.10}$$

With the interpolated profiles, the dose value for each point D_i is calculated from the interpolated dose profile, the factor f and the angles $\Delta\theta_i$ and $\Delta\phi_i$.

$$D_i(\Delta\theta_i) = D_{PP,i}(\Delta\theta_i) \cdot f, \qquad ^{106}\text{Ru applicator} \neq \text{COB} \tag{6.11}$$

$$D_i(\Delta\theta_i, \Delta\phi_i) = D_{PP,i}(\Delta\theta_i, \Delta\phi_i) \cdot f, \qquad ^{106}\text{Ru applicator} = \text{COB} \tag{6.12}$$

With this set of dose values D for each point of the set S, the dose profile of the structure can be statistically evaluated. The mean, the median and different quantiles are computed and saved in a spreadsheet. In addition, a numerical algorithm analyses the set D to obtain a dose area histogram. The algorithm calculates the fraction F of dose values in D, which are smaller than a threshold value. Due to the homogeneous spread of the points in the structure, F is interpreted as the fraction of the area of the structure, which was irradiated with a dose smaller than the threshold. The data set for the dose-area histogram is obtained by repeating this analysis for thresholds in the range of the dose values of the corresponding structure.

6.7 Summary and Discussion

In this chapter, a novel software is presented. It allows the user to contour various structures in a fundus photo, implement a distorted ^{106}Ru applicator, transfer those contours into the 3D coordinate system of an eye model and calculate different dose values and histograms to evaluate the therapy retrospectively.

After loading a retrospective fundus photo, the user may contour structures such as the papilla, the macula and the tumour. The fundus photo is distorted because it is a projection of a sphere on a plane. The Azimuthal Equidistant Projection, well known from cartography, allows the computation of the 3D coordinates of structures from the photo and vice versa. The scaling is computed employing the distance between the macula and papilla. The distorted projection of a ^{106}Ru applicator is visualised in the photo by two contours, one resembling the outline of the plaque and one for the target. By shifting these contours to the radiation scar, the position of the ^{106}Ru applicator during the treatment is found. The ^{106}Ru applicator contours are recalculated after each shift considering the AEP.

MC simulations of eight different ^{106}Ru applicators provide results concerning their DDC and their dose profile on a surface parallel to the concave surface of the plaque in 1 mm distance. With the information on the relative position of the organs of risk to the applicator, the dose profile of the structure is calculated. Therefore, the user may evaluate the therapy retrospectively.

The software presented in this thesis is based on the AEP. It may be used for conventional fundus photos, but especially for large fundus puzzles, the projection algorithm can not cover the distortion in the picture or only with considerable uncertainties. Modern widefield devices often come with a large field of view, resulting in fundus puzzles no longer needed. Thus, this software is best used with images obtained with such modern systems. Furthermore, juxta papillar tumours are best suited to be analysed with this software due to low distortions near the rear pole of the eye.

The scaling and rotation of the picture are based on values from cohort studies because those values are not available in the data sets of the UKE. However, some of these values are associated with significant uncertainties. For example, the relative standard deviation of the angle α_{pf} used to calculate the position of the pole equals 57 % [177]. The resulting uncertainty of the calculated coordinates is expected to be smaller for structures near the rear pole and the papilla and more significant for structures near the equator of the eye. In addition, the intra-observer variability has to be taken into account. This means that different users may contour the structures differently. However, there is no study quantifying the intra-observer variability yet.

Assuming a standard sclera thickness of 1 mm introduces additional systematic uncertainties. If the sclera in the patient's eye differs from 1 mm, the analysed structures are closer or farther to the ^{106}Ru applicator, which correlates with smaller or larger dose values during the treatment.

All uncertainties should be studied and have to be propagated to the calculation of dose values. Due to the extensive range of the dose gradient of a ^{106}Ru applicator, it is not possible to give an overall uncertainty. For example, the dose gradient is relatively small if a structure lies within the radiation scar. Meanwhile, structures close to the edge of that scar were positioned in the area of the dose profile, in which the dose gradient is

approximately 10 % per 0.1 mm. Caution is necessary when evaluating dose profiles of structures located close to the edge of the ^{106}Ru applicator accordingly.

The simulated DDCs and angular dose profiles consider a radioactive model of the ^{106}Ru applicator with a homogeneous density of ^{106}Ru-atoms. However, the ^{106}Ru applicators have so-called hot- and cold spots, which lead to an inhomogeneous dose profile [143]. In addition, the dose profile was scored in water surrounding. Therefore, the tissue compositions of the various structures in the eye are not considered. This leads to deviations in scored dose values as shown in Ref. [183–185].

It is suggested to measure the distance on fundus photos as in Ref. [186], so the picture could be scaled with the specific data of the patient's eye. The software can be changed to compute the scaling based on this input. Additional measurements of distances, such as the diameter of the papilla, should be included to minimise uncertainties further.

The software was already used on an extensive retrospective data set in a slightly different version [18, 19]. Dirk Flühs implemented an additional scaling with the area of the papilla and a variable weight factor whose value can be freely selected by the user. This feature allows the user to adjust the scaling to fit the patient's eye best. This can be seen with the projected ^{106}Ru applicator and the radiation scar. Especially for those cases, which have been performed with a COB, the scaling factor showed great potential. The retrospective data analyses presented in Ref. [18] was the first evaluation of brachytherapy of intraocular tumours and the corresponding dose-response relationship that considered the actual plaque position during treatment and not only the treatment plan.

Furthermore, the software is used further to evaluate the combined therapy concept in this thesis to provide 3D eye tumour models, which are presented in the next chapter.

7 Evaluation of the clinical benefit

This chapter aims to analyse the potential clinical benefit of the combined therapy concept with the calculation and evaluation of DVHs. Due to the novelty of this concept, no established software exists that allows these computations.

To overcome this lack of information, a new software workflow is developed. It allows the MC simulation of real or fictional cases. The workflow, which is also visualised in figure 7.1, consists of a generic eye model constructed using Fusion360 with authentic case data derived from the software presented in chapter 6. With the implementation of the patient's information into the generic eye model, a specific 3D model of each case is created. The patient's eye model and the corresponding ^{106}Ru applicator position are implemented into MC simulations. The brachytherapy and each incident X-ray beam of the confocal irradiation represent a separate simulation and, therefore, have their own dose profile. The combination of brachytherapy and the EBRT is calculated using weights for each modality to obtain the best outcome.

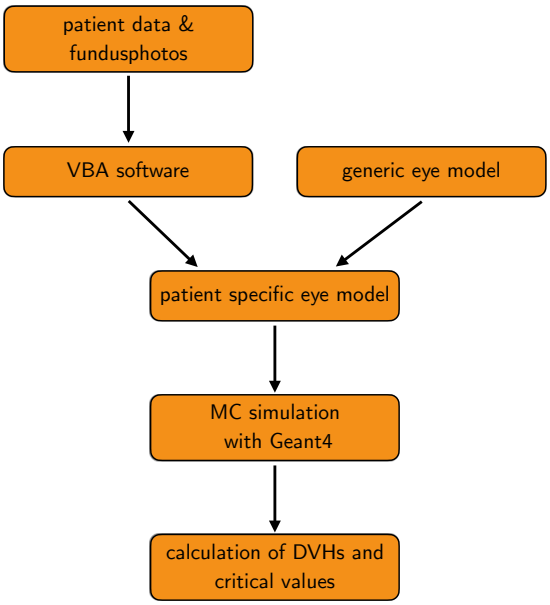

Figure 7.1: Simplified workflow flowchart to obtain simulated data of the combined therapy concept.

This generic eye model and first analyses regarding the tissue equivalence of water have been performed in Ref. [183]. In Ref. [129], Fusion360 scripts have been developed, allowing tumour contours and plaque positions to be implemented into the generic eye model. Moreover, the software workflow has been expanded regarding the retrospective calculation of DVHs of brachytherapy cases with Geant4. The implementation of an X-ray spectrum has been accomplished in Ref. [41, 130].

7.1 Patient specific eye model

To obtain the most realistic dose values for individual organs and the tumour, a 3D model of the human eye is constructed. Many important eye structures are implemented using data from the literature regarding their mean size and composition. Mean values are used because, at this point, the workflow is intended to be used with retrospective patient cases in which no data on the specific eye dimensions are given. The ciliary body is not comprised since no information about its exact dimensions has been found. The generic eye model is visualised in figure 7.2.

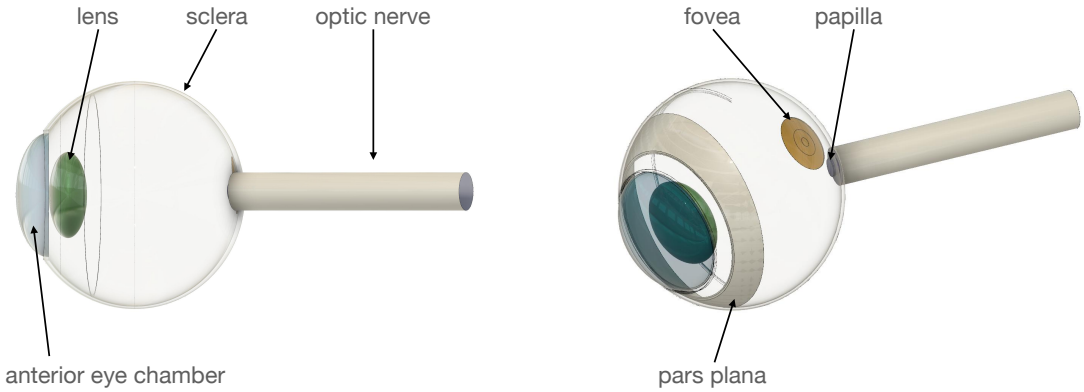

Figure 7.2: Visualisation of the generic eye model with annotation of the most important structures.

A list of all structures and their most important values, composition and densities can be found in tables A.4 to A.9.

As no information was found in the literature regarding the composition of the retina and choroid, these data have been replaced with information on the glass bulb and the sclera. Moreover, the macula lutea is assumed to be part of the sclera. The composition of the papilla is set to the tissue, which overlaps the corresponding partial volume. The density of the tumour could not be established from publications and was replaced by the density of the sclera [187].

For constructing the eye model with Fusion360, the sizes listed in table A.4 are used. Each organ or structure is created as a single object to allow for dose calculation in that particular structure. At first, the bulbus oculi is constructed, and the three layers sclera, choroid, and retina are created and subtracted from it. The retina borders the vitreous body in the model. In the next step, the anterior chamber of the eye, the aqueous humor, the cornea and the lens are created. The following angles and distances are employed to position the macula lutea. The horizontal angle between the optic and visual axis is set to 5.2° [188], while the vertical angle between those axes is defined as 1.4° [188].

For the distance between the centres of the papilla and the macula lutea, a value of 4.74 mm [176] is used. The angle between papilla and fovea is fixed to 7.76° [189]. The result is shown in figures 7.2 and 7.3.

The macula lutea is subtracted from the retina to ensure no structures overlap. Next, the optic disc is divided into three parts regarding the three skin layers, and each is cut out from the layer to which it belongs so that the optical disc comprises three volumes. The optic nerve is added to the model perpendicular to the optic disc.

A simple cuboid is added around the generic eye model to resemble the surrounding tissue (see figure 7.3). Its material is defined as water.

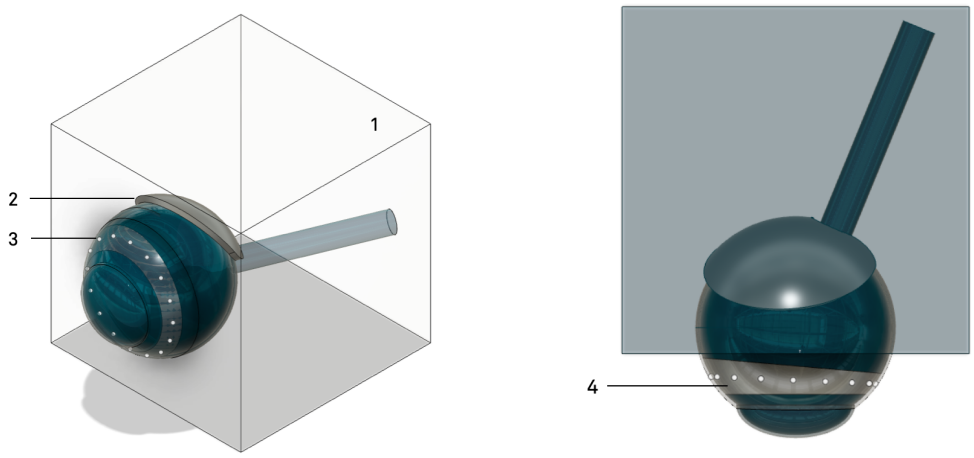

a) b)

Figure 7.3: The generic eye model from two different point of views. a) Additional structures: Tissue cuboid (1), ^{106}Ru applicator (2), and the construction points for the X-ray beams (3). b) Pars plana (4). The figures are acquired from Ref. [41].

7.1.1 Implementation of patient data

The software described in chapter 6 is employed to include the data of a retrospective case. The output of this software consists of the tumour contour T, the position of the macula and the papilla, and the coordinates of the centre of the convex surface of the ^{106}Ru applicator $\vec{A}$, which are implemented into the generic eye model after postprocessing of the coordinates.

Smoothing

Because the tumour contour is drawn by hand into the fundus photo, it may contain small loops and an inhomogeneous density of points as presented in figure 7.4a. Thus, the following two functions are used to smooth the contour.

1) Travelling Salesman algorithm: The minimising problem, in which a set of points $M = \{\vec{x}, \vec{x} \in \mathbb{R}^3\}$ has to be connected with the shortest path p, is called the travelling salesman problem. It starts and ends at one point $\vec{x}_0$ [190]. The implementation of the algorithm to solve the travelling salesman problem into the workflow is adapted from Ref. [191]. The route given by the order of points in the set M is the initial distance p_0. In each iteration, the order is changed, and the route's total distance is compared to the yet best route with its distance p_{best}. The improvement factor I is defined as $I = 1 - p_{\text{best}}/p_0$ and is computed within each iteration. If I reaches a threshold of 0.001, r_{best} is accepted as the final result of the algorithm and further iterations are skipped. The result of a subset of a tumour contour is presented in figure 7.4b.

2) Ramer-Douglas-Peucker algorithm: The number of coordinates in T may lead to problems with Fusion360 due to the computational power needed to visualise the contour and the corresponding tumour volume. Accordingly, the amount of points is reduced with the Ramer-Douglas-Peucker algorithm, which finds a similar polyline with fewer points as presented in figure 7.4c. The starting curve consists of an ordered set of coordinates. The first point P_0 is marked to be kept within the set. The algorithm finds the point P_i farthest away from P_0 and creates a line between those points. It then locates the point P_j located farthest from that line and compares its distance to the line segment d_i to a user-specified threshold ϵ. If $d_i > \epsilon$, the point is marked to be kept within the set. If $d_i < \epsilon$, all points not yet marked to be kept are discarded. The algorithm now recursively defines the new lines from P_i to P_j and from P_j to P_n and searches for the new points that are furthest away to compare their distance with the threshold ϵ [192, 193].

The deviations between the original and the modified contour are assumed to be negligible to the area of the tumour base and the systematic uncertainties in contouring the tumour in the fundus photo. This is visualised in figure 7.4d, where one of the tumour contours can be seen before and after smoothing.

Adjustements to the generic eye model

The primary form of the generic eye model is an ellipsoid, while the algorithm presented in chapter 6 assumes the eye to be a sphere. Furthermore, the variability of the dimensions of a patient's eye leads to deviations between the contour and the generic eye model. Thus, all contours and positions implemented from the patient's case are modified. First, all points are rotated around the origin so that the connecting line between the macula and papilla of the implemented data is parallel to the same line of the generic eye model. A second rotation places the two papillae centres onto each other.

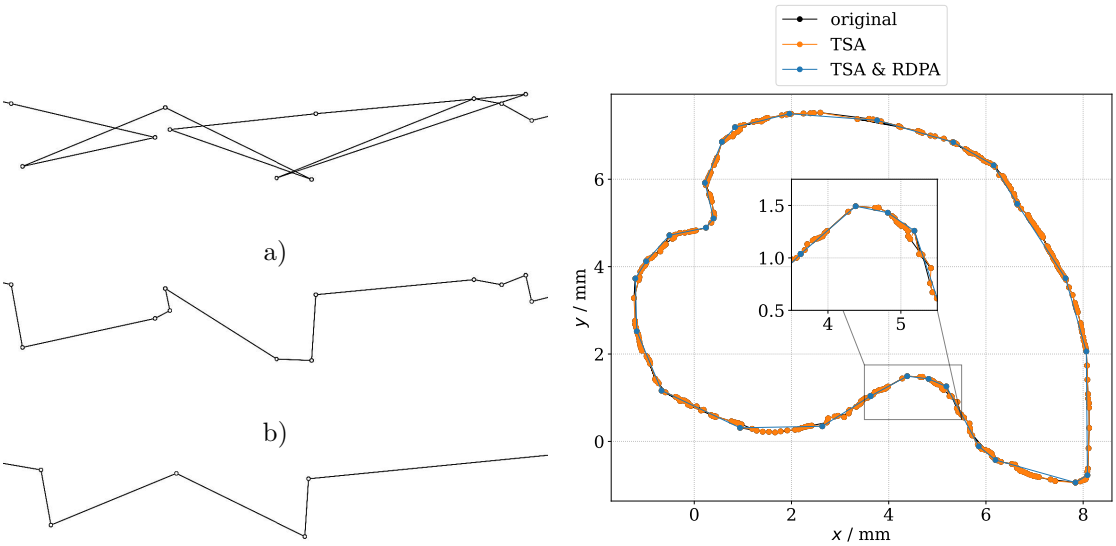

Figure 7.4: Visualisation of the smoothing of the tumour contour. a) Subset of an original tumour contour. b) The same subset after finding the shortest route with the travelling salesman algorithm (TSA). c) Reduced set of points after utilisation of the Ramer-Douglas-Peucker algorithm (RDPA). d) Tumour contour in its original form, after modification with the travelling salesman algorithm and additional utilisation of the Ramer-Douglas-Peucker algorithm with $\epsilon = 0.15\,\mathrm{mm}$ in direct comparison. The figures figures 7.4a to 7.4c are obtained from Ref. [129].

7.1.2 Construction of the tumour body

The information regarding the three-dimensional tumour shape can not be obtained from the data given by the UKE, as a magnetic resonance image is only performed for special indications. Therefore, the present information is the contour T from the fundus photo and the tumour height h. To create a volume, the apex is created in the first step. The centre of the tumour $\vec{T}_\mathrm{c}$ is found by calculating the mean of the contour. It is assumed the tumour grows in the direction of the origin of the generic eye model, which is the centre of the eye. An axis in the same direction as $\vec{T}_\mathrm{c}$ can be interpreted as the central tumour axis t accordingly. The tumour apex $\vec{T}_\mathrm{a}$ is created on the axis t with a distance of h between the center and the apex $\mid \vec{T}_\mathrm{c}\vec{T}_\mathrm{a} \mid = h$. An inbuilt function of Fusion360 creates a mantle from a given contour and one point where the mantle closes flat. In addition, a second contour is projected to the parallel plane at a distance of $\overrightarrow{T_\mathrm{c}T_\mathrm{a}}/2$ with a scaling factor of 0.75 and used as an intermediate step for the mantle computation. The result can be seen in figure 7.5.

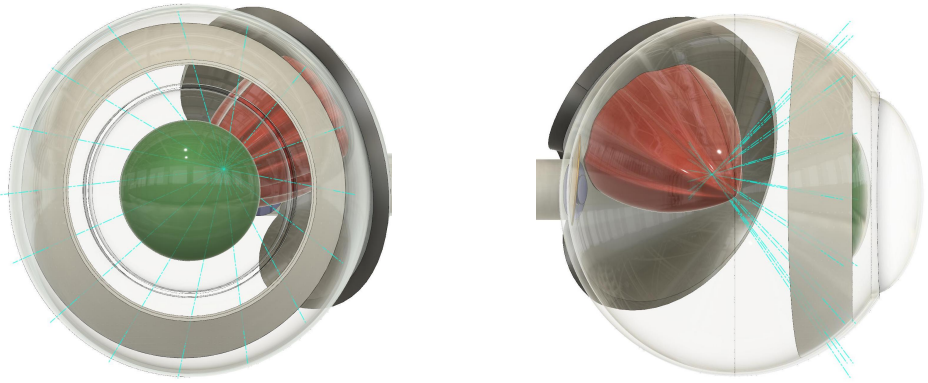

a) b)

Figure 7.5: Visualisation of the generic eye model and the construction axes for the X-ray beams from different points of view. The central axis of each X-ray beam is presented in teal, the tumour in red, the lens in green, the ^{106}Ru applicator in dark grey and the pars plana in light grey.

7.1.3 Implementation of the ^{106}Ru applicator

The script automatically implements and positions the ^{106}Ru applicator, which model type is derived from the case name. The applicator and its target volume are defined with the information regarding the rotationally symmetrical models from Ref. [86] and the COB presented in Ref. [84]. The centre of the convex side of the applicator is rotated towards the calculated and post-processed point $\vec{A}$. Due to the irregular shape of the generic eye model, the applicator sometimes overlaps with structures of the eye, such as the sclera. To prevent any overlap, the applicator is first translated into the eye and afterwards shifted to the outside in 0.01 mm steps until no overlap is detected by Fusion360.

The COB is the only non-rotationally symmetrical model implemented. It has a notch to be placed at the optic nerve. Therefore, the applicator is rotated by hand in Fusion360 so the notch is symmetrical around the optic nerve. Deviations in the rotation lead to negligible changes in the dose-volume histogram, as shown in Ref. [194].

7.2 Monte Carlo simulation

The MC simulation is based on a published simulation of a ^{106}Ru applicator presented in Ref. [63] and the basic examples No. 2 and No. 3a provided by Geant4. The generic eye model is exported as STL-file and included in Geant4. The following sections describe the scoring and the primary particle generation. More information regarding the simulations can be found in Ref. [41, 129].

7.2.1 Primary Particle Generation

The GPS generates the primary particles of either the ^{106}Ru applicator or the X-ray beams. For each radiation source, 1000 simulations with $3 \cdot 10^5$ particles were simulated to obtain a statistical uncertainty of less than 1 % on the complete DDC of the X-ray beams and the first 10 mm of the DDC of the ^{106}Ru applicator.

^{106}Ru-atoms are created on the surface of a sphere with a radius of $r = 12.1$ mm. The centre of this sphere is calculated to be at the focal point of the plaque. The generated particles are only considered if they are computed to be in the confinement of the sphere and the target foil of the ^{106}Ru applicator.

The combined therapy concept is based on confocal irradiation with soft X-rays. In this approach, 16 different X-ray beams are simulated for each case. On the pars plana, 16 construction points are regularly spread in the interval of $[0°, 337.5°]$. Another construction point, the so-called target point, is created on the central axis of the tumour, with a distance of 3 mm to the tumour apex. The axis between each construction point and the target point is defined as the direction of the X-ray beam, which is visualised in figure 7.5. A circle with a diameter of 5 mm is placed orthogonal to each axis with a 10 cm distance to the generic eye model. It resembles the beam's cross-section in which the particles are generated homogeneously. The positions of the primary particles of the X-ray beams are calculated in Fusion360 and exported to Geant4.

At this point, it has to be said that the diameter of the X-ray beams of 5 mm is greater than the width of the pars plana. Previous analyses have used the width of the pars planas at each construction point as the diameter of the corresponding beam cross-section. The diameter of the X-ray beams varied between 2.40 mm and 4.14 mm. Moreover, the target point was defined to be at the tumour apex. Unfortunately, large parts of the tumour were not directly targeted by any beam, which resulted in under dosages in those parts [41]. With the treatment plan used in this analysis, the coverage of the X-ray beams was improved.

The energy of the X-rays is derived from the 100 kV spectrum described in section 5.4. The spectrum is calculated with the help of SpekCalc - see section 4.2 for more information. It is implemented via the GPS as an arbitrary point-wise spectrum from a file with linear interpolation. The SpekCalc output is reformatted to be readable for Geant4.

7.2.2 Scoring

The simulation automatically imports all STL-files found in a specified directory. In addition, they are either included as a SD or not, depending on whether a dose value is of any interest for this particular volume. In this work, the applicator, its target foil, the vitreous body, and the surrounding water box are defined as non-scoring structures.

To enable binned scoring of dose profiles within the volumes, each structure is cut in pieces with a maximum size of 1 mm × 1 mm × 1 mm as illustrated in figure 7.6. This is

achieved via the confinement of the complex structure and a binned cuboid. This means that the outer surface of the structure and total volume remains. Exporting, importing and adding this volume as SD is automatically done for each partial volume. In addition, the software saves the dimensions and locations of the partial volumes.

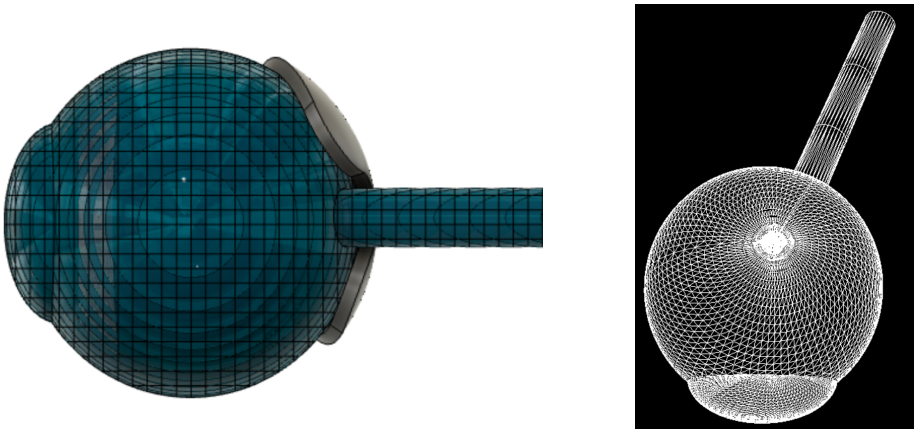

a) b)

Figure 7.6: a) The generic eye model after the cut process visualised in Fusion360. b) The uncut generic eye model in Geant4. The pictures are taken from Ref. [41].

In addition, CBS are used to score DDCs. A cylinder with a diameter of 1 mm and 0.5 mm bins on the construction axes of the corresponding X-ray beam. The centre of the nearest bin is defined as the construction point on the pars plana. For the depth dose curve of the ^{106}Ru applicator, the scorer is placed perpendicularly at the centre of the concave surface of the plaque. The DDC is fitted with the function $D(x)$ to obtain dose values for any distance x. This is later used to normalise the whole dose profile obtained for this radiation source.

$$D(x) = \exp\left(a \cdot x^2 + b \cdot x + c\right) \tag{7.1}$$

7.3 Cases and treatment plans

The UKE has approximately one hundred retrospective cases in which ^{106}Ru applicators were used and which have sufficient documentation of data and photos. These cases were all part of the study in Ref. [18]. Three cases are chosen from this set to be analysed in this work. All tumours are located near the optic nerve. Tumour heights are 6.3, 7.0 and 7.2 mm. The model COB is used in all cases due to the location of the tumour. To expand the data set with tumours significantly higher than the maximum treatable tumour height, the cases are duplicated and modified to a tumour height of $h = 10$ mm. With the help of the software presented in chapter 6, all six cases are

implemented into the generic model, as shown from two perspectives each in figure 7.7. More views of each case can be found in appendix A.6.

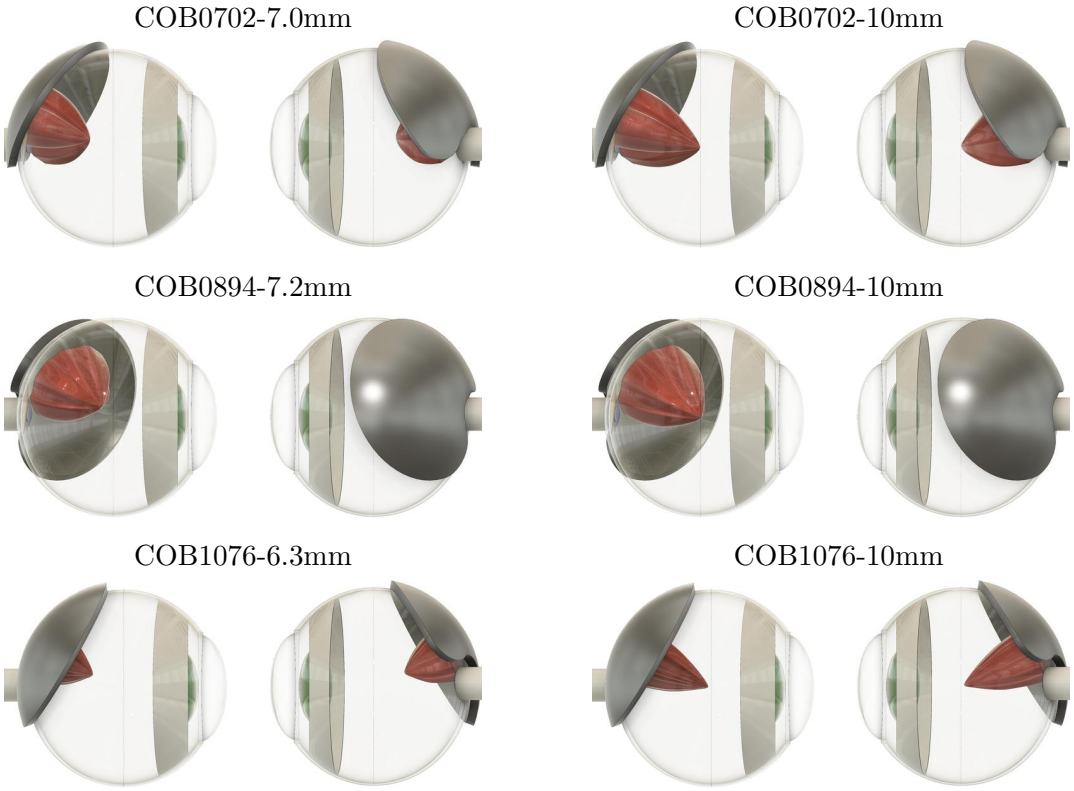

Figure 7.7: Tumour shapes within the generic eye model for all cases. For each case, a view from the left and right is presented, in which, among other structures, the tumour (red), the ^{106}Ru applicator (dark grey), the pars plana (light grey) and the lens (green) are visualised. More views of each case can be found in appendix A.6.

The anonymised names COB0702, COB0894 and COB1076 are derived from the serial number of the ^{106}Ru applicator used for therapy. To distinguish between the original and the modified cases, each name is expanded by the height of the tumour.

The intersection of the X-ray beam and the ^{106}Ru applicator is defined as the absorption A. In Fusion360, a projection of the ^{106}Ru applicator is drawn onto the cross-section plane described in section 7.2. This is visualised in figure 7.8a. If the X-ray beam partially hits the ^{106}Ru applicator, its cross-section is divided into two areas, measured within the inbuilt methods of Fusion360.

The absorption A is defined as $A = {}^{A_\mathrm{P}}/_{A_\mathrm{CS}}$, where A_CS is total area of the cross-section plane and A_p the partial area which confines the ^{106}Ru applicator. If all X-ray beams are considered for the treatment plan, the set is denoted as the full set S_F. However,

it is later intended that the therapy concept only uses a partial set S_P comprising the X-ray beams X_i with $A_i = 1$.

For the original tumours, the partial sets consist of 7 to 9 X-ray beams. Only one beam misses the ^{106}Ru applicator completely. Due to the definition of the direction of the X-ray beams associated with the tumour height, the beams miss the ^{106}Ru applicator more often for the modified cases, and only 6 to 7 beams have a value of $A = 1$. All partial sets can be obtained from figure 7.8b.

To quantify the tumour volume V_NI, which the X-ray beams do not directly cover, the tumour parts that do not intersect with at least one of the X-ray beams are calculated in Fusion360. As these parts of the tumour are not directly irradiated by any X-ray beam, the ^{106}Ru applicator is required to irradiate these remnants. This analysis is performed for the full and partial set of beams. The coverage $C = 1 - {}^{V_\mathrm{NI}}/_{V}$ is defined as the proportion of the volume directly irradiated by the X-ray beams in the total volume. These values are presented in figure 7.9 for each case.

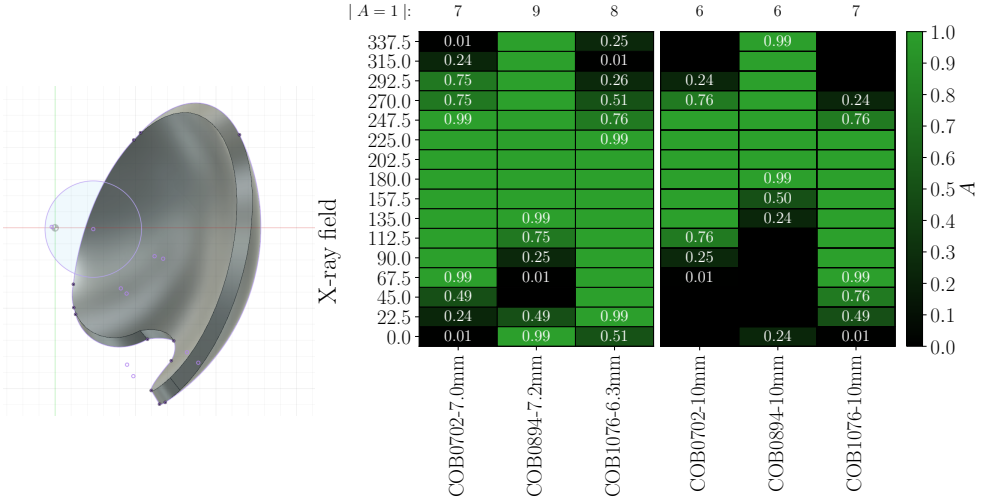

a) b)

Figure 7.8: a) Visualisiation of the method to quantify the absorption A for each X-ray beam. The ^{106}Ru applicator (dark grey) is projected onto the cross-section of an X-ray beam (purple circle). b) Absorption A of the X-ray beams in the ^{106}Ru applicator for each case. Values in the range $0 < A < 1$ are printed. The partial set of each case comprises all corresponding beams with $A = 1$. The number of beams with full absorption ($A = 1$) is stated at the top.

The X-ray beams directly irradiate large amounts of tumour volume in all cases. For the full sets S_F, the coverage is in the range of $88.5\,\% < C_\mathrm{F} < 99.4\,\%$, while for the partial sets, it is in the range of $64.0\,\% < C_\mathrm{P} < 85.0\,\%$. The remaining tumour volumes V_NI^F and V_NI^P are visualised in appendix A.6. Most of the remaining volumes are lateral parts of the tumour tissue close to the ^{106}Ru applicator. The height of the remaining

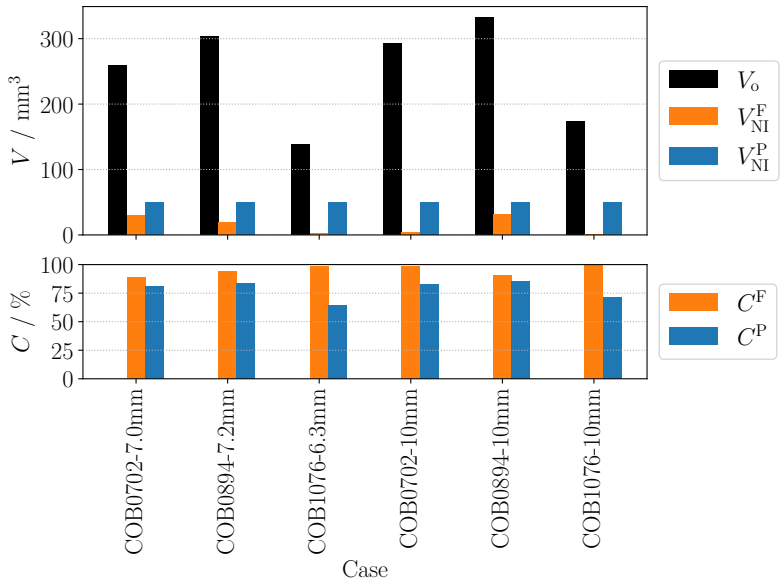

Figure 7.9: Visualisation of the tumour volumes V_o, and the tumour volumes V_{NI}^F and V_{NI}^P that do not intersect with any beam of the full set S_F or the partial set S_P. In addition, the corresponding coverage C is presented in the lower plot.

volume is smaller than the original tumour in all cases. This means that tumour parts not directly irradiated by the X-ray beams are most likely sufficiently irradiated by the ^{106}Ru applicator, which leads to a high probability of tumour control. However, a precise evaluation is only possible by assessing DVHs.

7.4 Tuning of the treatment plan with weights

Each individual tumour requires a different dose boost from X-ray therapy. This is evaluated by tuning the weights for each radiation source X_i comprising 16 X-ray beams and one ^{106}Ru applicator, resulting in a total amount of $n = 17$. All dose profiles are normalised to 100 Gy at the tumour apex by using the fit of the DDC of the corresponding dataset, which is derived from the dose concept of brachytherapy (see section 2.3.4). Each radiation source X_i is weighted afterwards by multiplication with a specific factor w_i. This means the weight w_i can be transferred to the dose at the tumour apex applied by the corresponding radiation source X_i. The weighted sum of dose D_{tot}^{SD} of all weighted dose values D_i^{SD} belonging to one sensitive detector SD can be written as

$$D_{tot}^{SD} = \sum_{i}^{n} w_i \cdot D_i^{SD}. \tag{7.2}$$

To compute the DVH, an algorithm sorts the dose values of the SDs belonging to the same structure and calculates the corresponding cumulative volume percentages V^O.

The weights w_i are defined by the following rules. The ^{106}Ru applicator shall deliver 100 Gy to the tumour apex, which is defined by $w_{\mathrm{Ru}} = 1$. If this is not feasible due to the limitation of 1500 Gy at the sclera (compare to section 2.3.4), the weight is lowered to the maximum possible value which fulfils this requirement.

Given the normalised dose profile of 100 Gy at the apex location on the DDC, it may be assumed that the entire tumour receives a minimum radiation dose of 100 Gy. But the DDC of the ^{106}Ru applicator is scored on the centre of the plaque, as it is also performed in clinical practice. Due to the relative position of the ^{106}Ru applicator to the tumour and the dose profile of the applicator, the tumour coverage may not be sufficient. This is especially relevant if the ^{106}Ru applicator is not placed centrally over the tumour due to the steep dose gradient near the rim of the plaque.

The weights of the X-ray beams $w_{\text{X-ray}}$ are analysed in the range of 0 to 15 % with a stepsize of 0.1 %. This means a dose of 0 to 15 Gy is delivered by every single beam to the tumour apex region. This interval is chosen due to a first conducted analysis, which shows that the maximum required weight is 11.6 % (see table 7.5), except for one case which needs an X-ray weight in another order of magnitude. This results from a disadvantage in the treatment plan discussed in the following analysis. However, an X-ray weight this high is not clinically feasible.

The X-ray weights irradiating one case are changed in parallel and thus always have the same value. For every value of the weights, the combined DVH is calculated, and critical dose values are derived (see section 7.5 for more information). The analysis is performed for stand-alone brachytherapy, the full set S_{F} and the partial set S_{P} of X-ray beams for each case.

As explained in chapter 3, a secondary goal of the combined therapy concept is to optimise the dose profile in the OARs. With the combined therapy concept, it might be possible to reduce the treatment time of brachytherapy and to balance this out with soft X-rays. The X-ray beams are, unlike the radiation emitted by the ^{106}Ru applicator, collimated beams. Therefore, this shift of weights might reduce exposure in OARs while maintaining tumour control. However, due to the finite nature of this work, the shift of weights is not further analysed and discussed in detail here.

7.5 Critical dose values

The following five important variables are used to evaluate the DVHs of stand-alone brachytherapy and the combined therapy concept. The tumour control as the primary goal of the treatment is determined by the relative tumour volume $V^{\mathrm{tumour}}_{100\,\mathrm{Gy}}$, which receives at least 100 Gy and additionally by the dose $D^{\mathrm{tumour}}_{99\,\%}$ which is applied to 99 % of the tumour volume. In this work, a coverage of $V^{\mathrm{tumour}}_{100\,\mathrm{Gy}} \geq 99\,\%$ and a minimum dose of $D^{\mathrm{tumour}}_{99\,\%} \geq 100\,\mathrm{Gy}$ are defined as sufficient tumour irradiation. Tumour tissue is often destroyed for lower doses which can be derived from the dose concepts of conventional

radiotherapy. However, the dose prescription used in this thesis shall already include general therapy uncertainties, such as the positioning of the X-ray beams and the ^{106}Ru applicator.

Moreover, the risks of side effects explained in section 2.3 are evaluated, and derived critical dose values are analysed. The mean dose of the leans $\overline{D}^{\text{lens}}$ shall not exceed 5 Gy to avoid the risk of opacification. Radiation-induced optic neuropathy correlates with the maximum dose in the optic nerve, and the risk equals 3 to 7 % if the maximum dose is above 55 to 60 Gy. To avoid statistical outliers in the DVH, the dose $D^{\text{ON}}_{1\,\%}$ applied to 1 % of the volume of the optic nerve is considered. Because of the nature of the dose-effect curve, the dose exposure should be as low as possible. In this work, 55 Gy is defined as the boundary. Additionally, the relative volume $V^{\text{retina}}_{50\,\text{Gy}}$ of the retina receiving at least 50 Gy is obtained for each case as a function of the X-ray weights. This value estimates the risk of retinopathy and partial vision loss in the eye.

For overview purposes, these critical variables, their definition and their target values are listed in table 7.1.

The precise values are calculated from the corresponding DVH employing linear interpolation.

Table 7.1: List of critical dose values and their target value used in the further evaluation of intraocular tumour treatment modalities.

Variable	Definition	Target value and reason
$V^{\text{tumour}}_{100\,\text{Gy}}$	Relative volume of the tumour which is irradiated with at least 100 Gy	$V^{\text{tumour}}_{100\,\text{Gy}} \geq 99\,\%$ to sufficiently destroy tumour tissue, including systematic treatment uncertainties.
$D^{\text{tumour}}_{99\,\%}$	Minimal dose in the most irradiated 99 % of the tumour	$D^{\text{tumour}}_{99\,\%} \geq 100\,\text{Gy}$ to sufficiently destroy tumour tissue, including systematic treatment uncertainties.
$D^{\text{ON}}_{1\,\%}$	Minimal dose in the most irradiated 1 % of the optic nerve	As small as possible $D^{\text{ON}}_{1\,\%} \leq 55\,\text{Gy}$, to minimise the risk of radiation-induced optic neuropathy to 3 to 7 %.
$V^{\text{retina}}_{50\,\text{Gy}}$	Relative volume of the retina which is irradiated with at least 50 Gy	As small as possible to minimise vision loss.
$\overline{D}^{\text{lens}}$	Mean dose in the lens	As small as possible $\overline{D}^{\text{lens}} \leq 5\,\text{Gy}$, to minimise the risk of opacification.

7.6 Analysis of dose profiles

To start with the analysis, first, an evaluation of stand-alone brachytherapy for those cases is presented in section 7.6.1, followed by an assessment of the combined therapy concept based on the full and partial sets of beams in section 7.6.2.

7.6.1 Stand-alone brachytherapy

The calculated weights for brachytherapy w_{Ru} are presented in table 7.2.

Table 7.2: Weights w_{Ru} for the brachytherapy treatment. $w_{\mathrm{Ru}} = 1$ means the brachytherapy is sufficient to irradiate the tumour apex with 100 Gy without exceeding the limitation of the sclera contact dose.

Case	w_{Ru}	Case	w_{Ru}
COB0702-7.0mm	1	COB0702-10mm	0.199
COB0894-7.2mm	0.921	COB0894-10mm	0.195
COB1076-6.3mm	1	COB1076-10mm	0.203

The weights w_{Ru} indicate that two original cases can be sufficiently treated with brachytherapy. For the third, which is COB0894-7.2mm, the weight is lowered not to exceed the sclera dose limitation. The modified cases with tumour heights of 10 mm have weights of approximately 20 % due to the same limitation.

The DVH of every case treated with stand-alone brachytherapy is presented in figure 7.10. In addition, the calculated five critical values regarding tumour control and side effects derived from the DVHs are listed in table 7.3.

Table 7.3: Critical dose values applied by stand-alone brachytherapy for every case. For the definition and the target values of these values, refer to table 7.1.

Case	$V_{100\,\mathrm{Gy}}^{\mathrm{tumour}}$ / %	$D_{99\,\%}^{\mathrm{tumour}}$ / Gy	$V_{50\,\mathrm{Gy}}^{\mathrm{retina}}$ / %	$D_{1\,\%}^{\mathrm{ON}}$ / Gy	$\overline{D}^{\mathrm{lens}}$ / Gy
COB0702-7.0mm	96.00 ± 0.29	77.00±0.50	31.81 ± 0.02	81.00±0.40	0.4477 ± 0.0015
COB0894-7.2mm	98.12 ± 0.01	83.90±0.40	34.31 ± 0.01	73.42±0.29	0.9245 ± 0.0024
COB1076-6.3mm	96.73 ± 0.01	87.90±0.40	29.13 ± 0.08	37.21±0.20	0.2704 ± 0.0010
COB0702-10mm	83.40 ± 0.40	20.59±0.18	31.86 ± 0.03	83.60±0.40	0.4604 ± 0.0016
COB0894-10mm	86.31 ± 0.08	22.41±0.22	34.40 ± 0.21	73.24±0.31	0.9223 ± 0.0023
COB1076-10mm	87.05 ± 0.02	26.20±0.50	32.83 ± 0.19	53.70±0.50	0.3927 ± 0.0014

For stand-alone brachytherapy the value of $V_{100\,\mathrm{Gy}}^{\mathrm{tumour}}$ is in the range of 96.00 ± 0.29 to $(98.12 \pm 0.01)\,\%$ for the authentic cases. Meanwhile, the cases with a modified tumour height of 10 mm have significantly lower tumour control values in the range of (83.40 ± 0.40) to $(87.05 \pm 0.02)\,\%$. The minimum dose deposited in 99 % of the tumour is $\geq (77.0 \pm 0.5)$ Gy for the authentic cases. However, due to their dimensions, the modified

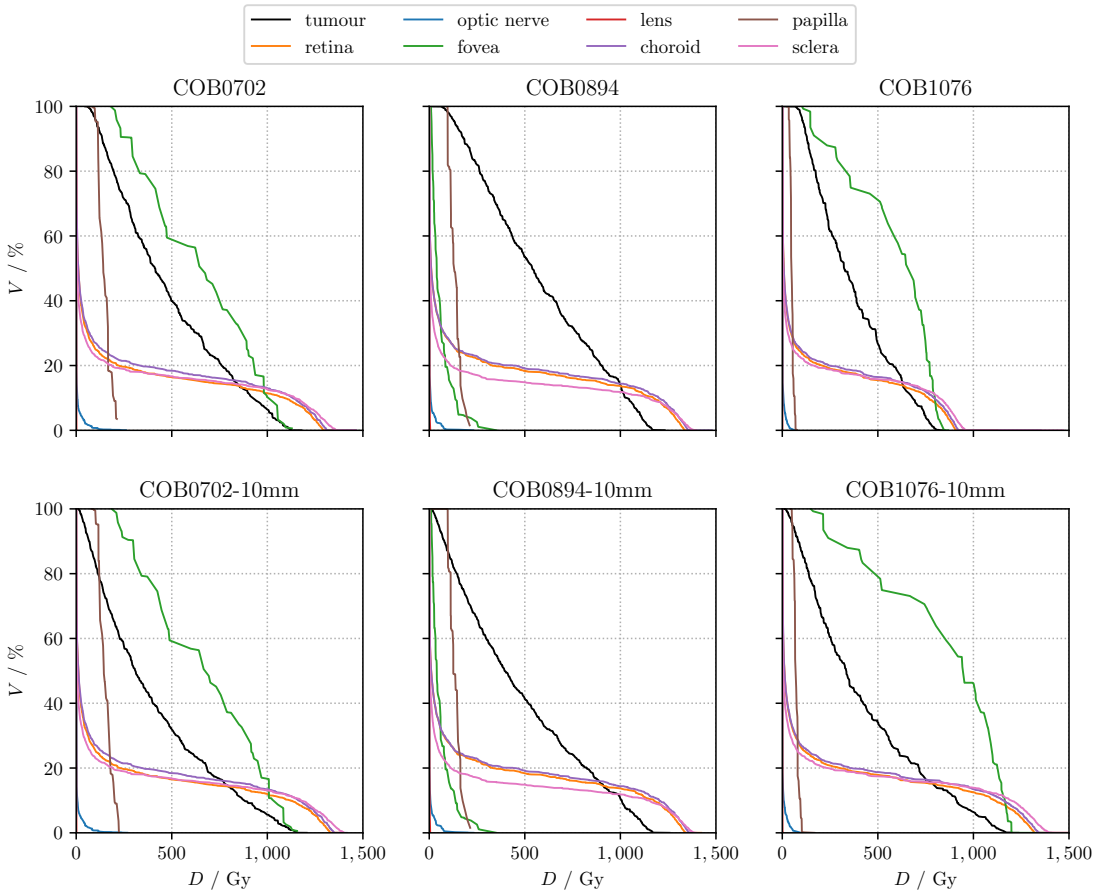

Figure 7.10: DVH of stand-alone brachytherapy for every case.

cases show values in the range of $(20.59 \pm 0.18)\,\mathrm{Gy} \leq D_{99\,\%}^{\mathrm{tumour}} \leq (26.20 \pm 0.50)\,\mathrm{Gy}$. This means large parts of the modified and small parts of the original tumours are not irradiated sufficiently, and the normalisation of the dose profiles with the depth dose curve, which is unprecise for brachytherapy if the ^{106}Ru applicator is not placed centrally over the tumour (see section 7.4). Especially for the modified tumours, the underdosing might result in further tumour growth and metastasis.

Regarding the side effects, the risk of lens opacification is low for all cases with stand-alone brachytherapy because the mean dose in the lens amounts to $\overline{D}^{\mathrm{lens}} < (0.9245 \pm 0.0024)\,\mathrm{Gy}$, which is only approximately $1/5$ of the critical value of 5 Gy. This results from the distance between the lens and the position of the ^{106}Ru applicator close to the optic nerve and the steep dose gradient of the ^{106}Ru applicator. Meanwhile, partial vision loss can be expected for all cases, as the relative volume of the retina, which is irradiated with at least 50 Gy is in the range of (29.13 ± 0.08) to $(34.40 \pm 0.21)\,\%$. Regarding optic neuropathy, the cases show very different results due to the individual

distance of the ^{106}Ru applicator to the optic nerve. For COB0702-7.0mm, COB0894-7.2mm and their modified 10 mm versions the maximum dose in the optic nerve is in the range of $(73.24 \pm 0.31)\,\mathrm{Gy} \leq D_{1\,\%}^{\mathrm{ON}} \leq (83.60 \pm 0.40)\,\mathrm{Gy}$. Therefore, these four cases have a risk of at least 3 to 7 % for radiation-induced optic neuropathy, even if only stand-alone brachytherapy is performed. Meanwhile, the case COB1076-6.3mm and its modified version have values of $D_{1\,\%}^{\mathrm{ON}} = (37.21 \pm 0.20)\,\mathrm{Gy}$ and $(53.70 \pm 0.50)\,\mathrm{Gy}$, which leads to a risk of less than 3 to 7 % for optic neuropathy.

The DVH presented in figure 7.10 provides additional information on the dose profile of all structures. Most important is the high dose in the fovea observed for the cases COB0702-7.0mm, COB1076-6.3mm and their modified versions. Within these data sets, the tumour is close to the fovea and even partly overlaps it. This leads to an unavoidable high dose when irradiating the target volume. As the fovea is responsible for the sharp central vision, partial vision loss in this area considerably impacts the patient's quality of life. Vision loss may occur because of the tumour itself and its irradiation.

However, the main point is the insufficient irradiation of the tumour volumes. The primary goal of radiotherapy is to control the tumour and avoid further growth.

7.6.2 Combined therapy concept

To overcome the insufficient tumour irradiation, the X-ray weights $w_{\text{X-ray}}$ are now increased in the range of 0 to 15 % with a stepsize of 0.1 %. This means, by every step, the dose applied to the tumour apex by each X-ray beam grows by 0.1 Gy with a maximum of 15 Gy per beam. All analysed critical values are expected to increase due to the additional dose. The brachytherapy weights w_{Ru} are not changed.

Full set of X-ray beams

Due to the additional dose boost by the X-ray therapy, all dose values increase as a function of the X-ray weights $w_{\text{X-ray}}$. Therefore, the critical values for tumour control and the risk of side effects increase as shown in figure 7.11.

$V_{100\,\mathrm{Gy}}^{\mathrm{tumour}}$ builds up lineary for the cases COB0894-7.2mm, COB1076-6.3mm and their modified versions. Meanwhile, COB0702-7.0mm and COB0702-10mm show a corollary as an exponential saturation curve. Most likely, this results from parts of the tumour volume which are neither sufficiently irradiated from the ^{106}Ru applicator nor directly from the X-ray beams. Therefore, the irradiation of these parts is based on scattered radiation, and higher X-ray weights are necessary to achieve sufficient irradiation. Due to the bigger tumour volumes of the modified cases, less dose is applied in the apex region by the ^{106}Ru applicator. This results in smaller percentages of the tumour volume irradiated with 100 Gy for the same X-ray weights. Therefore, higher weights to reach sufficient irradiation are required. With all sixteen X-ray beams irradiating the tumour,

the desired tumour control value of $V_{100\,\mathrm{Gy}}^{\mathrm{tumour}} \geq 99\,\%$ is reached for the case-specific weight $w_{\mathrm{X\text{-}ray}}^{\mathrm{TC}}$ as listed in table 7.4.

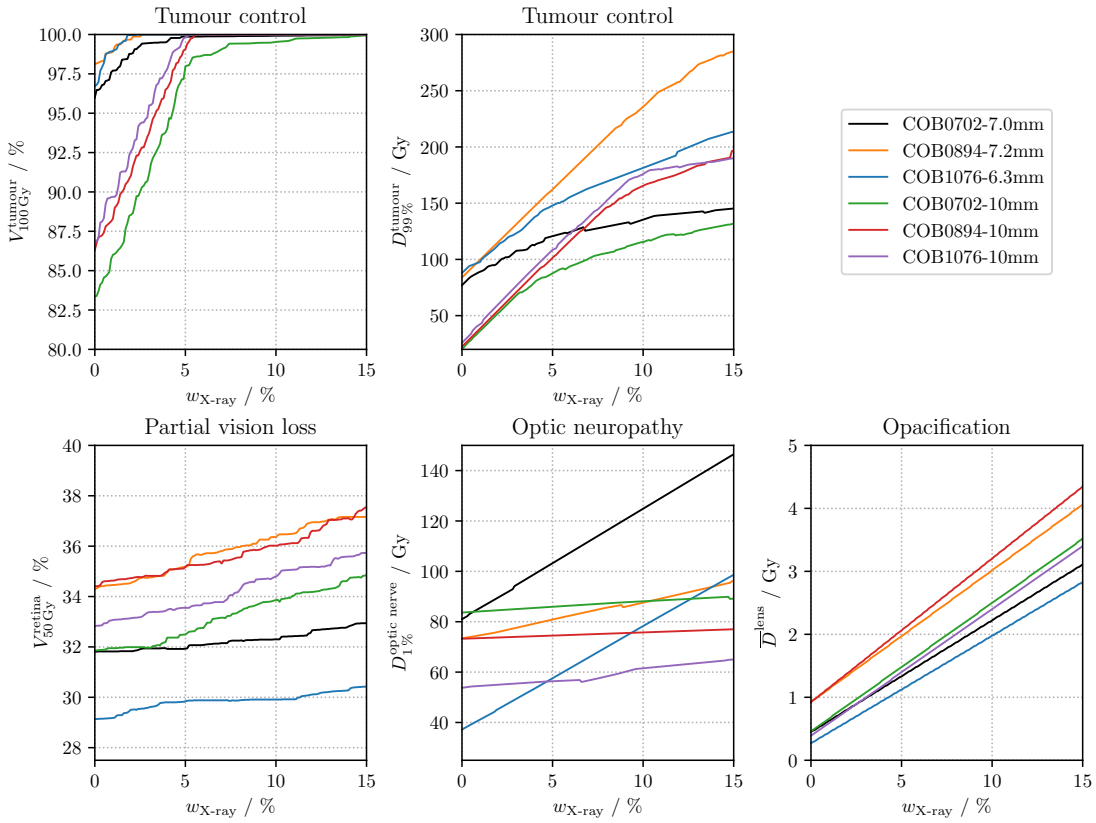

Figure 7.11: Presentation of the five critical dose values as a function of the X-ray weights $w_{\mathrm{X\text{-}ray}}$ for all cases treated with the combined therapy concept using the full sets of X-ray beams S_{F}.

The dose applied to 99 % of the tumour volume $D_{99\,\%}^{\mathrm{tumour}}$ increases as a linear function of the X-ray weights $w_{\mathrm{X\text{-}ray}}$ until it transforms into a second linear function with a smaller slope. Certain parts of the tumour can explain this. As the apex is the part of the tumour with the lowest dose applied by the ^{106}Ru applicator and also directly irradiated by the X-ray beams, the dose in this region significantly increases as a function of the X-ray weights. Other parts of the tumour, not directly irradiated by the X-ray beams but with a higher dose value for $w_{\mathrm{X\text{-}ray}} = 0$ due to the irradiation by the ^{106}Ru applicator, have a smaller slope. Therefore, they define the minimum dose in the tumour for higher X-ray weights $w_{\mathrm{X\text{-}ray}}$. $D_{99\,\%}^{\mathrm{tumour}}$ starts in the range of (20.59 ± 0.18) to (87.90 ± 0.40) Gy for $w_{\mathrm{X\text{-}ray}} = 0\,\%$ and ends in the range of (131.9 ± 1.2) to (285.1 ± 0.8) Gy for $w_{\mathrm{X\text{-}ray}} = 15\,\%$. This underlines that with appropriate X-ray weights, all tumours can be sufficiently irradiated with the full set of beams S_{F}.

Due to the required irradiation of the tumour, healthy tissue is also impaired. The relative volume of the retina $V_{50\,\mathrm{Gy}}^{\mathrm{retina}}$, which is irradiated with at least 50 Gy, increases approximately linearly as a function of the X-ray weights $w_{\text{X-ray}}$. For each case, the volume of the retina that is severely damaged by the applied dose of at least 50 Gy grows by (3.55 ± 0.17) to $(9.35 \pm 0.19)\,\%$ for $w_{\text{X-ray}} = 15\,\%$ relatively to its value for $w_{\text{X-ray}} = 0\,\%$. This results from using all X-ray beams, even if they miss the ^{106}Ru applicator. By doing so, they irradiate parts of the retina that were not or only slightly impaired by the ^{106}Ru applicator.

A 3 to 7 % risk of optic neuropathy persists if the maximum dose in the optic nerve is at least 55 Gy. That said, four cases already exceed this threshold for stand-alone brachytherapy. However, in case of COB1076-6.3mm $D_{1\,\%}^{\mathrm{ON}}$ reaches 55 Gy for $w_{\text{X-ray}} \geq 4.4\,\%$ and in case of COB1076-10mm for $w_{\text{X-ray}} \geq 2.0\,\%$. The overall increase of $D_{1\,\%}^{\mathrm{ON}}$ varies for the different cases depending on the target point of the X-rays. The cases COB0702-7.0mm and COB1076-6.3mm increase to 1.809 ± 0.010 and 2.651 ± 0.016 times the initial value for stand-alone brachytherapy. This results from some beams directly irradiating the papilla and the optic nerve due to their incident point on the pars plana and the target point close to the tumour apex. For the other four cases $D_{1\,\%}^{\mathrm{ON}}$ increases by a factor in the range of 1.051 ± 0.006 to 1.310 ± 0.007.

The risk of lens opacification is very low for stand-alone brachytherapy due to the low mean dose in the lens of $\overline{D}^{\mathrm{lens}} < 1\,\mathrm{Gy}$. The dose steadily increases with the X-ray weights $w_{\text{X-ray}}$ in the form of a linear function. However, for $w_{\text{X-ray}} = 15\,\%$, $\overline{D}^{\mathrm{lens}}$ reaches a maximum of (4.343 ± 0.004) Gy which is still below the critical value of 5 Gy.

If each case is irradiated with the full set of X-ray beams S_{F} with a minimum X-ray weight $w_{\text{X-ray}}^{\mathrm{TC}}$ to reach sufficient irradiation, the critical dose values listed in table 7.4 are deposited. Based on $V_{50\,\mathrm{Gy}}^{\mathrm{retina}} \approx 1/3$, all patients most likely have partial vision loss after the treatment. However, the $V_{50\,\mathrm{Gy}}^{\mathrm{retina}}$ and the correlated risk only increased by (0.12 ± 0.17) to $(4.0 \pm 0.7)\,\%$ compared to stand-alone brachytherapy. The maximum dose in the optic nerve $D_{1\,\%}^{\mathrm{ON}}$ is raised by (1.7 ± 0.6) to $(11.7 \pm 1.1)\,\%$. Due to the X-ray beam's entry point in the pars plana, secondary particles reach the lens leading to a higher dose deposition. Compared to stand-alone brachytherapy, the mean dose of the lens $\overline{D}^{\mathrm{lens}}$ is increased by up to $(309.6 \pm 1.5)\,\%$. However, the absolute maximum value observed is (2.0626 ± 0.0025) Gy, which is only 40 % of the derived limitation.

Table 7.4: Calculated weights $w^{\mathrm{TC}}_{\mathrm{X\text{-}ray}}$ for each case to reach the desired value of $V^{\mathrm{tumour}}_{100\,\mathrm{Gy}} \geq 99\,\%$ for the full set S_{F} and the corresponding calculated critical dose values.

Case	$w^{\mathrm{TC}}_{\mathrm{X\text{-}ray}}$ / %	$D^{\mathrm{tumour}}_{99\,\%}$ / Gy	$V^{\mathrm{retina}}_{50\,\mathrm{Gy}}$ / %	$D^{\mathrm{ON}}_{1\,\%}$ / Gy	$\overline{D}^{\mathrm{lens}}$ / Gy
COB0702-7.0mm	2.2	100.5 ± 0.5	31.85 ± 0.05	90.40±0.40	0.8378 ± 0.0016
COB0894-7.2mm	1.1	101.3 ± 0.4	34.46 ± 0.09	74.74±0.29	1.1544 ± 0.0024
COB1076-6.3mm	1.1	100.4 ± 0.5	29.20 ± 0.80	41.55±0.33	0.4580 ± 0.0010
COB0702-10mm	7.0	100.8 ± 0.3	33.15 ± 0.21	86.80±0.50	1.8857 ± 0.0020
COB0894-10mm	5.0	101.4 ± 0.3	35.20 ± 0.40	74.49±0.31	2.0626 ± 0.0025
COB1076-10mm	4.5	100.7 ± 1.1	33.51 ± 0.29	56.20±0.50	1.2945 ± 0.0017

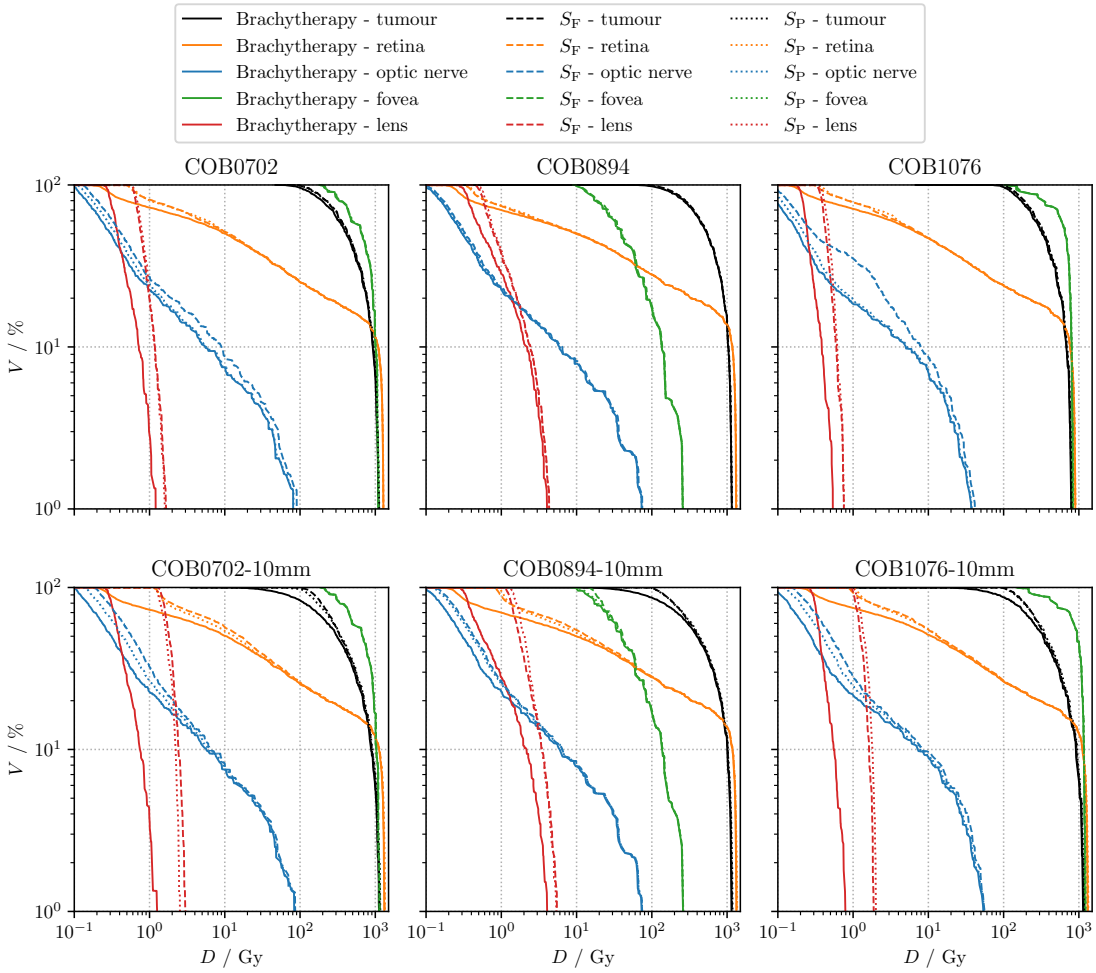

Figure 7.12: DVHs of the most important structures for the combined therapy concept in comparison to stand-alone brachytherapy. The visualisation includes the results for the full sets S_{F} and partial sets S_{P} of X-rays. For each case, the modalities are weighted with the corresponding weights listed in tables 7.2, 7.4 and 7.5. Both axes are logarithmically scaled, refer to figure A.42 for linearly scaled axes.

Figure A.42 presents the corresponding DVHs for the most critical structures compared to the stand-alone brachytherapy. To provide more detailed versions, the DVHs with a zoom on the dose range of 0 to 150 Gy can be found in figure A.43, while in figure 7.12 the DVHs are shown with a logarithmic scale on both axes.

The DVHs presented in figures 7.12, A.42 and A.43 show the impact of the X-ray beams on the tumours dose profile, especially in the dose range of 0 to 150 Gy. Due to the dose boost in the apex region, the minimal dose applied to the target volume increases, and the DVH is more homogeneous. Figure 7.12 underlines the impact of the X-ray therapy on the dose profiles of the lens and the optic nerve as they are shifted towards higher dose values. A higher percentage of the retina is irradiated with doses $D < 10\,\mathrm{Gy}$. However, the risk of partial vision loss in the affected areas remains low. The additional X-ray treatment does not significantly impair the dose profile of the fovea, most likely resulting in the same visual outcome in the patient's central vision compared to stand-alone brachytherapy with ^{106}Ru.

Partial set of X-ray beams

To further spare OARs from irradiation, especially the retina and the optic nerve, only the partial set S_P of X-ray beams is used. As stated in section 7.3, only those X-ray beams that entirely hit the ^{106}Ru applicator are used for the combined therapy concept. This decreases the number of beams to 6 to 9 per case (see figure 7.8b). As previously, the X-ray weights $w_\text{X-ray}$ for each beam in S_P are simulatenously increased from 0 % to 15 % in steps of 0.1 %. This results in a lower applied dose for the partial set S_P than for the full set S_F because fewer beams are used.

Figure 7.13 presents the critical dose values for tumour control and the three evaluated side effects as a function of $w_\text{X-ray}$. As expected, a smaller slope of $V^\text{tumour}_{100\,\mathrm{Gy}}$ and $D^\text{tumour}_{99\,\%}$ is observed. Therefore, higher X-ray weights $w^\text{TC}_\text{X-ray}$ are required to reach sufficient irradiation in the target volume, as listed in table 7.5. However, COB0702-10mm is an exception within this analysis. Even for the maximum value of $x_\text{X-ray} = 15\,\%$, the tumour control does not reach the desired values. $V^\text{tumour}_{100\,\mathrm{Gy}}$ and $D^\text{tumour}_{99\,\%}$ equal $(97.68 \pm 0.01)\,\%$ and $(76.19 \pm 0.29)\,\mathrm{Gy}$, which means that already large parts of the tumour will be destroyed to the high dose. The remaining 2.3 % of the tumour tissue have doses $D > 75\,\mathrm{Gy}$. Throughout medical physics, this is also considered sufficient but was defined otherwise in this work due to the uncertainties of the therapy, which have yet to be studied and included. A short analysis showed that for this case, sufficient irradiation is not even reached for $x_\text{X-ray} = \mathcal{O}100$

Due to the reduced number of beams, the weights $w^\text{TC}_\text{X-ray}$ are higher than for the full set of beams. The authentic cases require weights in the range of 1.8 to 4.9 %. This means that the original cases require a dose boost of 16.2 to 34.3 Gy at the tumour apex by the partial set of X-ray beams. At the same time, higher tumours also need a higher applied dose by the X-ray therapy to irradiate the target volume sufficiently. Derived from the

X-ray weights for the modified cases, which equal 15.0 %, 11.6 % and 10.6 %, the total dose delivered to the tumour apex by the X-ray therapy is 90 Gy, 69.6 Gy and 74.2 Gy. The increase of the weights compared to the full set of X-ray beams is in the range of 63.6 to 135.6 %.

The use of the partial instead of the full set of X-ray beams leads to a significantly different form of $V_{50\,\mathrm{Gy}}^{\mathrm{retina}}$ as a function of $w_{\text{X-ray}}$ (see figure 7.13). For all cases, over the full spectrum of $w_{\text{X-ray}}$, an absolute increase in the range of (0.068±0.032) to (0.6±1.3) % is observed. In addition to the less deposited dose, this results from using the partial set S_{P}. As all included X-ray beams hit the ^{106}Ru applicator, only those parts of the retina in front of the ^{106}Ru applicator are directly irradiated by the beams. But the ^{106}Ru applicator already applies high dose values to this region. Therefore, $V_{50\,\mathrm{Gy}}^{\mathrm{retina}}$ is raised only due other parts of the retina irradiated by scattered radiation from the X-ray beams. Compared to the full set of X-ray beams, the calculated volume of the retina with more than 50 Gy is reduced by up to 1.22 ± 0.30 percentage points.

A similar trend is observed for $D_{1\,\%}^{\mathrm{ON}}$, which is associated with optic neuropathy. Compared to stand-alone brachytherapy, the critical dose value is increased by 2.5 ± 0.8 to (9.1 ± 0.8) % for a maximum X-ray weight of $w_{\text{X-ray}} = 15\,\%$. The slope of $D_{1\,\%}^{\mathrm{ON}}$ as a function of $w_{\text{X-ray}}$ is less steep compared to the use of the full set S_{F}, which is most obvious for the cases COB0702-7.0mm and COB1076-6.3mm. Again, the absorption of the X-rays in the ^{106}Ru applicator is the main reason for this effect. This results in a (1.8 ± 1.2) to (9.2 ± 0.6) % decrease of $D_{1\,\%}^{\mathrm{ON}}$ for the partial set compared to the full set for all cases except for COB0894-10mm, which has an increase of (0.3 ± 0.6) %. Due to the dose boost, $D_{1\,\%}^{\mathrm{ON}}$ exceeds the critical value of 55 Gy for case COB1076-10mm with the partial set of X-ray beams.

Table 7.5: Calculated weights $w_{\text{X-ray}}^{\mathrm{TC}}$ for each case to reach the desired value of $V_{100\,\mathrm{Gy}}^{\mathrm{tumour}} \geq 99\,\%$ for the partial set S_{P} and the corresponding calculated critical dose values. For COB0702-10mm, the desired threshold $V_{100\,\mathrm{Gy}}^{\mathrm{tumour}} \geq 99\,\%$ was not reached, and the corresponding weight has therefore been set to 15 %.

Case	$w_{\text{X-ray}}^{\mathrm{TC}}$ / %	$D_{99\,\%}^{\mathrm{tumour}}$ / Gy	$V_{50\,\mathrm{Gy}}^{\mathrm{retina}}$ / %	$D_{1\,\%}^{\mathrm{ON}}$ / Gy	$\overline{D}^{\mathrm{lens}}$ / Gy
COB0702-7.0mm	4.9	100.1 ± 0.5	31.83 ± 0.03	82.10±0.40	0.8592±0.0016
COB0894-7.2mm	1.8	100.2 ± 0.4	34.42 ± 0.08	73.73±0.29	1.1804±0.0024
COB1076-6.3mm	2.4	100.1 ± 0.5	29.18 ± 0.20	37.75±0.20	0.4902±0.0010
COB0702-10mm	15.0	76.2 ± 0.3	31.93 ± 0.21	85.70±0.50	1.7282±0.0024
COB0894-10mm	11.6	100.5 ± 0.4	34.70 ± 0.05	74.68±0.31	2.2558±0.0028
COB1076-10mm	10.6	100.6 ± 0.4	33.10 ± 0.40	55.20±0.50	1.4276±0.0020

Lens opacification, which is associated with $\overline{D}^{\mathrm{lens}}$, shows a very similar slope as with the utilisation of the full set of X-ray beams in section 7.6.2. With correction of $\overline{D}^{\mathrm{lens}}$ with

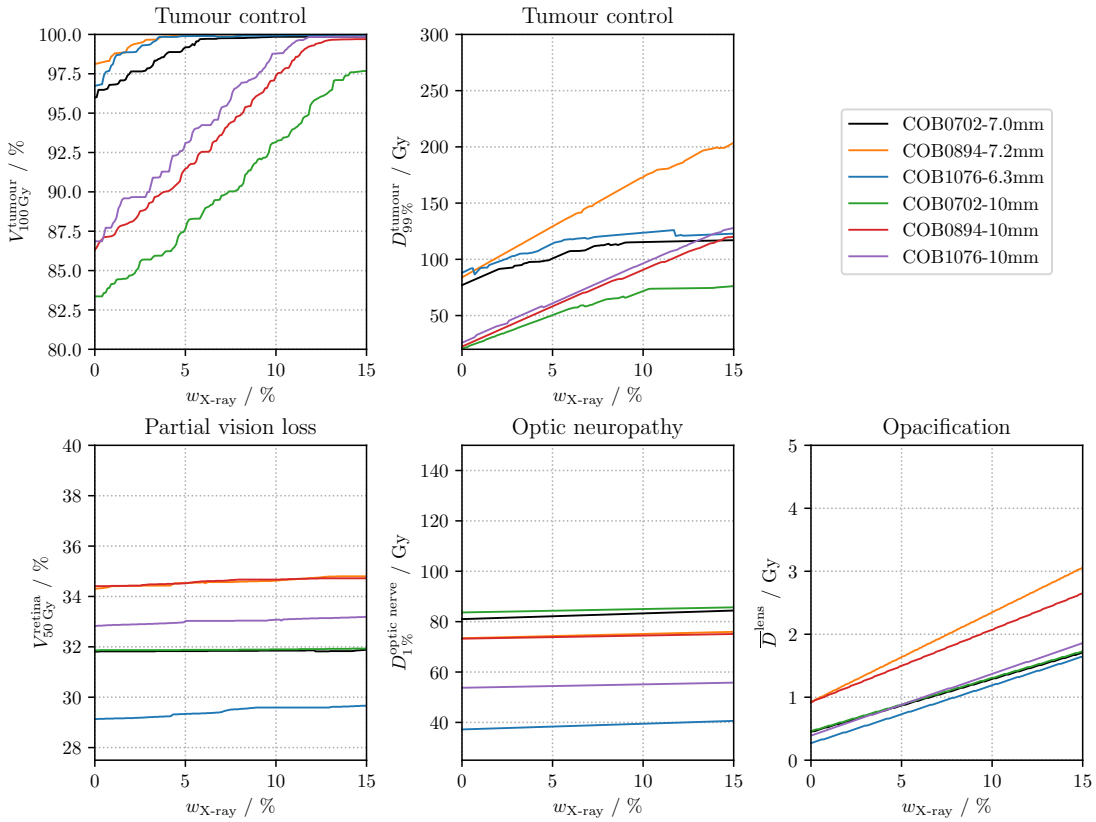

Figure 7.13: Presentation of the five critical dose values associated with the tumour control and three side effects as a function of the X-ray weights for several cases treated with the combined therapy concept using the partial sets of X-ray beams S_{P}. For better comparison, y-limits of the plots are adopted from figure 7.11. For the definition and the target values of these values, refer to table 7.1.

its value for stand-alone brachytherapy, the ratio

$$\frac{\overline{D}^{\text{lens}}_{S_{\text{F}}} - \overline{D}^{\text{lens}}_{\text{Ru}}}{\overline{D}^{\text{lens}}_{S_{\text{P}}} - \overline{D}^{\text{lens}}_{\text{Ru}}} \tag{7.3}$$

is in the range of 0.9165 ± 0.0016 to 1.1028 ± 0.0021. Since higher X-ray weights are required to sufficiently irradiate the tumour with the partial set of X-ray beams, the number of beams in the set and the higher corresponding weights roughly balance each other out. Therefore, the calculated critical values of $\overline{D}^{\text{lens}}$ with the minimum weight to achieve sufficient irradiation are of the same order of magnitude for S_{P} as for S_{F}. The highest value of (2.2558 ± 0.0028) Gy is observed for case COB0894-10mm.

Figures 7.12, A.42 and A.43 show the DVHs for the combined therapy concept with the partial sets S_{P} compared to stand-alone brachytherapy and the combined therapy concept with the utilisation of the full set S_{F}. It underlines that using the partial sets with the corresponding weights $w^{\mathrm{TC}}_{\text{X-ray}}$ leads to a similar dose profile in the target volume and the lens compared to the irradiation with the full set of beams. Meanwhile, the dose profile of the optic nerve is shifted towards smaller dose values, even though it remains higher than for stand-alone brachytherapy due to the additional irradiation. The volume percentage of the retina, which is irradiated with low doses $D < 10\,\mathrm{Gy}$, is significantly higher. However, following the information presented in section 2.3, the risk of partial vision loss in these areas remains small. As for the full set of beams, the dose profile of the fovea is not significantly impaired by the X-ray treatment with the partial set. Therefore, the visual outcome in the patient's central vision can be expected to be the same as if stand-alone brachytherapy is performed as treatment.

7.7 Summary and discussion

In this chapter, a novel simulation workflow and the results regarding the clinical benefit obtained with this workflow are presented. The workflow allows the user to calculate DVHs for the tumour and the OARs for stand-alone brachytherapy and the combined therapy concept.

The workflow is based on a generic 3D eye model designed in the computer-aided design software Fusion360. The model consists of many essential eye structures, such as the optic nerve, the fovea and the lens. The generic eye model can be individualised with patient data obtained from the software presented in chapter 6. This results in a 3D model including the patient-specific tumour and, in case the patient data are evaluated retrospectively, the position of the ^{106}Ru applicator. The tumour derived from the VBA software is post-processed with the Ramer-Douglas-Peucker and the travelling salesman algorithms.

Within Fusion360, the X-ray beam entry points and directions for the EBRT are constructed. A simple geometrical analysis enables the treatment plan evaluation concerning the tumour volume coverage and the absorption of the X-ray beams in the ^{106}Ru applicator. In this work, 16 X-ray beams are used to irradiate the tumour while entering the eye through the pars plana, an insensitive part of the eye. The 3D eye model and the treatment plan are exported to be simulated with the MC software framework Geant4. By dissecting the structures of interest and automatic implementation of each partial volume as a sensitive scorer, the dose profile of those structures can be calculated for each modality separately. This means that a single dose data set is available for each X-ray beam and the ^{106}Ru applicator, which can be combined as desired by the weighted summation to achieve the best possible irradiation for each case.

In this work, a total of six cases are analysed. Three are unmodified retrospective data of patients treated at the UKE. The other three are modified to a tumour height of

10 mm to evaluate the combined therapy concept for tumours of such size. All cases were assessed concerning stand-alone brachytherapy and the combined therapy concept with X-ray beams. The partial set of beams comprises only those that completely hit the ^{106}Ru applicator, leading to 6 to 9 beams per case. The evaluation is conducted due to the critical dose values for tumour control and four side effects: lens opacification, optic neuropathy, partial vision loss and retinopathy. Manual analysis is performed based on the maximum possible irradiation with a ^{106}Ru applicator and varying X-ray weights in the range of 0 to 15 %, which can be transferred to 0 to 15 Gy to the tumour apex by each beam. The additional dose boost to the tumour apex region from the EBRT generally increases tumour control to the desired values without significantly enhancing the risk of side effects compared to stand-alone brachytherapy.

The analysis of all cases showed that depending on the case and the set of X-ray beams used, an additional dose of 18 to 112 Gy applied by the X-ray therapy is necessary to achieve the aim of $V_{100\,\mathrm{Gy}}^{\mathrm{tumour}} \geq 99\,\%$ defined in this work. Due to the steep dose gradient of the ^{106}Ru applicator, the necessary dose boost is correlated to the individual height of the tumour. It further relies on the relative position between the tumour and ^{106}Ru applicator, which can only be planned with limited precision. Treatment with all 16 beams leads to the desired dose in the target volume for all cases. Because of the treatment plan in this thesis, some of the X-ray beams miss the ^{106}Ru applicator and this results in a maximum dose in the optic nerve of (41.55 ± 0.33) to (90.40 ± 0.40) Gy, which is (1.8 ± 0.6) to $(11.7 \pm 1.1)\,\%$ higher than for stand-alone brachytherapy of those cases. In addition, the volume of the retina irradiated with at least 50 Gy is increased by (0.12 ± 0.17) to $(4.0 \pm 0.7)\,\%$, which might lead to an increased loss of vision. ^{106}Ru applicators cause almost no dose in the lens in most cases, while the X-ray therapy impairs it due to secondary or scattered particles. However, the critical value of 5 Gy is not reached for any case in this work.

By using the partial set of beams and reweighting the dose profiles, the critical dose values associated with side effects are lowered and shifted towards values for stand-alone brachytherapy. However, for one case with a height of 10 mm treated with the partial set and maximum weights, the tumour volume irradiated with 100 Gy only reached $V_{50\,\mathrm{Gy}}^{\mathrm{tumour}} = (97.68 \pm 0.01)\,\%$ with a minimum dose of (76.19 ± 0.29) Gy in the target volume. This is associated with a high probability of tumour control but was defined as insufficient in this thesis. With $(29.18 \pm 0.20)\,\% < V_{50\,\mathrm{Gy}}^{\mathrm{retina}} < (34.70 \pm 0.05)\,\%$ the area with risk of partial vision loss is increased by up to $(0.9 \pm 0.6)\,\%$ compared to stand-alone brachytherapy. The maximum dose in the optic nerve is lowered in five of six cases compared to the full set of X-ray beams, especially for COB0702-7.0mm and COB1076-6.3mm. In those cases, at least one X-ray beam does not only miss the ^{106}Ru applicator but also irradiates the optic nerve directly. Therefore, by sorting out the beams that miss the ^{106}Ru applicator, the maximum dose in the optic nerve is decreased by approximately 9 %, even though 89 % of the dose is not caused by X-rays but by the ^{106}Ru applicator. This analysis enhances the importance of individually planning the

X-ray treatment of the combined therapy concept to minimise the risk of side effects. It confirms that the ^{106}Ru applicator serves this additional purpose as a beam stop.

Therefore, it can be concluded that the combined therapy concept is a promising modality to irradiate large intraocular tumours. It extends the current modalities and enables many patients to receive bulb-preserving treatment.

However, the combined therapy concept analysed in this chapter needs further adjustments to be clinically practicable. The treatment planning should be improved to maximise the target volume directly irradiated by the X-ray beams without missing the ^{106}Ru applicator. This can be achieved in many ways. The most promising is to vary the target point for each beam individually. The entry points in the pars plana can then be used for multiple beams so the beam's direction better fits the tumour's location. In the best case, the treatment plan is carefully constructed for each case individually. In addition, the divergence of the X-ray beams should be introduced after an analysis regarding the collimators. Because of the divergence, larger parts of the tumour can be irradiated while maintaining the beams size at the entry surface of the eye.

Furthermore, the ciliary body should be included in the generic eye model as it is an organ at risk. Damaging the ciliary body could enhance the risk of losing the ability to accommodate and lead to glaucoma. Therefore, the dose profile of the ciliary body should be included in future studies.

The assessment in this chapter was based on the ^{106}Ru applicator applying 100 Gy or the maximum possible value to the tumour apex calculated via the DDC. But with the combined therapy concept and the dose boost applied by the X-ray therapy, the application time of the ^{106}Ru applicator could be reduced, and the weights of the X-ray beams further increased. This might reduce the dose to OARs while maintaining sufficient tumour control. Therefore, further studies should be conducted to find the optimal combination of weights. This includes varying each beam's weight individually. In Ref. [41], this was successfully implemented by employing a differential evolutionary algorithm. Unfortunately, the minimiser did not converge in a reasonable time for the cases presented in this thesis. Increasing the efficiency of calculating the loss function or switching to a different optimiser are two approaches to overcome this problem and obtain the best possible dose profiles in both the target volume and the OARs. When utilising such an algorithm, a comprehensive study of the conditions and loss function needs to be conducted.

So far, the combined therapy concept was only analysed for very few cases. In the future, more patient data should be included, simulated and evaluated to assess the overall feasibility of this novel idea. It would be best to use data from many patients to widen the spectrum of tumour size and location to substantiate the evaluation of the combined therapy concept on a broad basis of cases.

The workflow presented in this chapter is currently adapted to analyse the effect of misplacing the ^{106}Ru applicator on the DVH and, therefore, on the outcome of the

therapy [185, 194, 195]. Further uncertainties and their impact on the applied dose can be evaluated using the workflow presented in this work. Previous studies were mainly based on the DDC of the ^{106}Ru applicator instead of the actual DVH. The dose prescription concepts might be adapted to the results from these analyses. The workflow also offers the potential to build the foundation of a novel 3D therapy planning system for the brachytherapy of intraocular tumours. This would significantly improve the quality of treatment planning on brachytherapy of ophthalmic tumours. Therefore, a future project focuses on increasing the efficiency of the MC simulation and developing a neural network that calculates the dose profiles after being trained and tested with the MC data [195, 196]. The inhomogeneity of the ^{106}Ru applicator due to local hot and cold spots is not yet implemented but currently studied [195].

8 Discussion on clinical realisation and feasibility

Chapters 5 and 7 presented results, which look promising regarding the overall suitability and the clinical benefit of the combined therapy concept. Nevertheless, many project-related approaches and concepts need to be worked out to integrate the new therapy into everyday clinical practice, which will be discussed in this chapter. Some of the discussed issues have been already addressed in Ref. [41].

X-ray therapy units are already well integrated into clinics. But for the combined therapy concept, different field sizes are necessary. Therefore, new collimators need to be produced and carefully chosen. On the one hand, small beams have the advantage of low exposure in surrounding OARs, while on the other hand, the correlated low dose rates result in extended treatment times, which may be uncomfortable for the patient. Thus, a study is needed to investigate the optimal compromise between treatment time and exposure to OARs. Using the dose rate obtained within the measurements presented in this thesis, a rough estimation of the treatment time can be given. In this example, the X-rays deposit a total dose 100 Gy in the tumour apex, which is hereby positioned with a distance of approximately 15 mm to the entry point of the beams in the pars plana. The dose rate observed in chapter 5 for 70 kV in this distance equals approximately 0.03 Gy/s. This results in a total treatment time regarding the X-ray therapy of approximately 56 min. If ten single X-ray beams would be used, this means the radiation time per beam is approximately 6 min. In the case of a fractionated plan, the treatment time would naturally be divided among the number of fractions so that the treatment time per fraction for the patient would be smaller. However, the treatment time should be significantly reduced to minimise inconvenience to the patient.

Additional X-ray beam parameters have to be measured regarding the collimator system. The lateral fall-off, reproducibility and stability need to be verified. Additional parameters that should be included are the focus skin distance, field homogeneity and collimator length. They further influence the dose rate and dose profile. All parameters must be included in the considerations and the treatment planning system to compute realistic dose profiles.

Moreover, divergent X-ray beams should be considered to enhance the tumour volume directly irradiated by the beams, as suggested in section 7.7. However, the small desired cross-sections and the divergence may lead to small distances between the exit window of the X-ray tube and the patient's eye. This could result in collisions between the

X-ray tube and the system to fixate the eye, which have to be prevented by defining restrictions to the movement of the robotic device. As stated in chapter 3, the stereotactic radiotherapy device designed by Oraya[30] already provides a good solution to fixate the patient's eye and is a verified medical product. Its suitability for the planned robotic device needs to be analysed and evaluated. Finally, measurements regarding the beam shaping have to be performed to check the feasibility of the required X-ray tube collimators in combination with the eye fixation system.

Should it become apparent during the course of this study that the desired beam parameters cannot be achieved, there is another approach that could be explored. A single standard field, for example, one with a diameter of 15 mm enters the eye frontally and is directed towards the tumour. Unlike the previous approach, this results in significant irradiation of the lens, the cornea and the ciliary body, and the risk of correlated side effects is increased. However, tumour control with simultaneous eye preservation might be preferable to these side effects and thus also indicates this approach for individual cases. Furthermore, the surgical exchange of a lens is a standard procedure in ophthalmology. However, this irradiation concept should only be considered if the previous considerations and approaches of the combined therapy concept with confocal irradiation of small fields cannot be achieved and should be carefully evaluated beforehand.

The idea of confocal irradiation needs to be evaluated for X-ray therapy units intended for the combined therapy concept. With minor improvements to the constructed phantom and the radiochromic film readout presented in chapter 5, an excellent device to verify the confocal irradiation dose profiles is already available. Confocal irradiation must be evaluated for X-ray therapy units intended for the combined therapy concept. With minor improvements to the constructed phantom and the radiochromic film readout presented in chapter 5, an excellent device to verify the confocal irradiation dose profiles is already available. The confocal irradiation can be performed with a robotic device resulting in low position uncertainties. As this system is yet to be installed, measurements can also be completed before introducing the robotic guidance to achieve early results, which are then subject to a higher position uncertainty.

A first investigation was performed regarding the robotic system as motion control. A possible solution is the UR16e designed by Universal Robots[31]. The robotic arm has a range of 900 mm and a payload of 16 kg, which fulfils the requirement to lift the X-ray therapy tube and the corresponding cooling [197, 198]. The position uncertainty of the robotic arm equals 0.05 mm [197], which is suitable for EBRT. Of course, other systems may have other advantages compared to this robotic arm. Comprehensive research and evaluation have to be performed accordingly.

A robotic arm verifies its position via the in-build joint encoders. Regarding the quality assurance, the position verification system can be derived from the CyberKnife, which is an EBRT system including a robotic motion control which is already used to treat

[30] Formerly Oraya Therapeutics Newark, California, USA. Now Carl Zeiss Meditec AG, Jena, Germany.
[31] Universal Robots (Germany) GmbH, München, Germany.

ophthalmic tumours (compare section 2.3.2). If required by clinical guidelines, external control via a camera system can be implemented additionally. With 5 to 10 cameras, it is possible to track the position and movement of the robotic arm continuously and to change or stop its activity if it does not agree with the planned movement [199, 200]. Moreover, the system might be extended to automatically turn off the irradiation of the X-ray therapy unit in those cases. Despite all safety systems, trained personnel must continuously observe the robotic system and the X-ray unit to intervene in an emergency and interrupt the therapy immediately.

Employing robotic guidance as a clinical therapeutic device needs to be carefully considered to prevent harm to the patient. Therefore, experts on this topic should be consulted for successful clinical realisation.

The final step is to evaluate all uncertainties and their propagation to the dose profile in the patient's eye. Safety margins have to be included in the treatment plan. Conventional EBRT uses the definition of the planning target volume, which comprises the tumour volume and position uncertainties. The patient-specific eye model could be improved by extending it with such clinical volume definitions.

Clinics already performing brachytherapy with ^{106}Ru applicators might also have a suitable X-ray therapy unit. In this case, upgrading this apparatus with a robotic device and the associated verification equipment represents a cost-effective approach. Otherwise, the new acquisition of an X-ray therapy unit and the robotic device may not be possible for every clinic. However, this concept might still be the most cost-effective bulb-preserving therapy for large intraocular tumours, as acquiring and maintaining a particle therapy centre entail a significant financial expense. Regarding the UKE, approximately 70 patients per year are currently treated with primary enucleation. The combined therapy concept might enable them to get a bulb-preserving treatment. Additionally, the general brachytherapy treatment of small tumours could be improved with the presented concept, resulting in a clinical benefit for approximately 300 patients per year at the UKE.

By now, no therapy planning software can combine brachytherapy and EBRT, including calculating the resulting DVHs in a reasonable amount of time. Of course, this software must be provided to efficiently plan the therapy and find the best possible parameters for the individual case. One solution would be the implementation of brachytherapy in already existing software used for particle therapy, CyberKnife or conventional external beam radiotherapies. Another approach is self-written software, which would, however, enhance the inconsistencies in clinical concepts for intraocular tumours. A current parallel project at the TU Dortmund University aims to develop a treatment planning software for brachytherapy with ^{106}Ru applicators based on the methods presented in this thesis [195].

The therapy planning software depends on the eye model. Thus, it would be best to include and combine several imaging techniques, such as computer tomography, magnetic resonance imaging and fundus photography, to calculate the 3D eye model. In addition,

the actual distance between the papilla and fovea or other scaling distances can be obtained for each patient using the Littmann-Bennett method [201–203]. With this information, the eye model can be modified to describe the patient's eye in all details.

As stated in section 7.7, the used treatment plan has to be optimised to obtain the best possible outcome. With the methods presented in this thesis, a comparative study of different strategies can be performed. In addition, an optimising algorithm can be used. With the results of Ref. [18], the minimised value can be adjusted to a complex function of different critical dose values for the various OARs to reduce the risk of side effects further while obtaining a high probability of tumour control. However, the computation time of the simulations and the optimiser is yet too high for integration into clinical practice. A current project aims, among other things, at enhancing the speed and efficiency of our simulations [195]. In addition, the composition of the material in comparison to water is investigated. If it is proven that the compositions of the eye structures can be neglected, it would be possible to derive the dose values from previously simulated 3D dose profiles instead of the generic eye simulation.

The treatment plan of the combined therapy concept and its success heavily depends on the accurate positioning of the ^{106}Ru applicator because the X-ray beams must not miss it. Verifying the position of the ^{106}Ru applicator with ultrasonic after the placement and before the X-ray therapy is recommended. To decrease the positioning uncertainty, Damato templates can be used. These transparent templates are sterile and are sewn on the eye before the ^{106}Ru applicator is applied. Due to their transparency, the overlap between the template and the tumour can be verified. After removing the template, the ^{106}Ru applicator is sewn onto the sclera using the same thread as for the template. This might result in more precise positioning of the ^{106}Ru applicator [56].

Additionally, the radiobiologic effects have not been covered in this thesis. Combining brachytherapy and EBRT requires an analysis of the impact on tissue. In this investigation, the number of fractions of the X-ray therapy and its effect on the α/β-ratio (compare section 2.7) needs to be included. Due to the reduced application time of the ^{106}Ru applicator, the number of possible fractions is limited and depends on the individual case.

At last, the clinical application is subject to guidelines and laws, which must be observed in this project's further development to avoid conflicts. The most essential DIN standards are listed in table A.10. The critical point is developing a calibration and verification process for the clinical practice under consideration of the corresponding DIN standards.

After the previous points have been sufficiently researched and developed, the project's final phase is to conduct clinical trials. At first, animal experiments have to be performed to verify the combined therapy concept. If these studies confirm the feasibility, a clinical trial with patients with highly prominent tumours should be conducted. This randomised study should focus on the gained tumour control and the risk of side effects. In addition, the combined therapy concept can also be compared with other established radiotherapy modalities.

9 Conclusion and outlook

Intraocular tumours are often treated with radiotherapeutic modalities such as brachytherapy or proton therapy. However, brachytherapy with ^{106}Ru is limited to tumour heights of less than 7 mm [16, 17] and ^{125}I brachytherapy leads to isotropically emitted low energy photons which result in irradiation of healthy tissue. Meanwhile, the availability of proton therapy for ophthalmic tumours is limited. This results in many patients undergoing an enucleation, which means a significant loss in quality of life. For example, at the UKE[32], one of the leading centres regarding ophthalmic tumours, approximately 26 % [3] of the patients are treated with a primary enucleation because no available bulb-preserving treatment option is indicated.

In this thesis, a novel concept to treat ophthalmic tumours was presented and analysed. The idea comprises brachytherapy with ^{106}Ru and external beam radiation therapy performed with low-energy X-rays. While the ^{106}Ru applicators irradiate especially the tumour base, the X-rays apply a dose boost to the tumour apex. The aim is to deploy the tumour control dose to the entire tumour volume with minimal achievable risks of side effects. The X-ray beams are planned to form confocal irradiation to protect as much healthy tissue as possible. Their entry points are located in the pars plana, a relatively insensitive eye area. One of the fundamental principles highlights the parallel execution of external beam radiation therapy and brachytherapy. This results in employing the ^{106}Ru applicator as a beam stop for the low-energy photons, which protects healthy tissue behind the tumour. Due to the angle of incidence of the X-rays, this modality is more indicated for tumours in the posterior half of the eye. A precise positioning system for the X-ray tube is indispensable. Therefore, it is intended to include a robotic device as a motorised positioning aid for the X-ray tube. This combined therapy concept could be beneficial not only for large tumours but also for small tumours and improve the general quality of the radiotherapy of intraocular tumours.

A novel water-equivalent solid phantom made from PWLR was constructed to investigate the combined therapy concept. The information and results of those measurements were presented in chapter 5. Three different detector types can be used within this phantom: self-built scintillation detectors, a soft X-ray chamber and radiochromic film. The measured uncertainties and their effect on the dose rate were in the range of 0.15 to 0.5 %. Therefore, the uncertainties are dominated by the systematic uncertainties of the de-

[32] University Hospital Essen, Essen, Germany.

tectors. In addition, the measurements presented in this thesis also showed that a ^{106}Ru applicator absorbs most of the X-rays. In relation to the dose rate in front of the applicator, the dose rate is decreased to less than 5 % due to the 1 mm thick silver plaque. Furthermore, an increased dose rate in front of the plaque is observed due to backscattering and the excitation of the silver atoms, which results in isotropic low-energy gamma radiation. These results were confirmed with Monte Carlo simulations.

The measurements were performed with two different X-ray energy spectra: 70 kV and 100 kV. The results indicate that the choice of the energy spectra for the combined therapy concept will finally be based on a compromise. On the one hand, lower energies have the advantage of an overall higher dose rate in the tumour, which results in shorter treatment times. In addition, lower energies have higher absorption rates in the ^{106}Ru applicator, which leads to lower doses in healthy tissue behind the plaque and, accordingly, lower probabilities for side effects in the corresponding structures. On the other hand, higher energies have a less steep depth dose curve. This results in less dose in healthy tissue on the path of the X-rays to the tumour. An energy spectrum of 100 kV is recommended at this point. A more detailed study regarding the choice of the energy of the X-rays should be repeated once a more dedicated treatment plan is available.

Due to the observation of fluctuations and deviations of up to 30 % in the dose profiles obtained with the radiochromic film in comparison to the other two detector types, the overall workflow to measure with radiochromic film should be improved. To obtain the best results, further investigation should be conducted into other radiochromic films made for low-energy photon irradiation. Deficits were observed in calculating dose values from the RGB scans with the commercial software FilmQA Pro. An analysis of the different parameters in this computing step could lead to more precise dose profiles. With a second cutout on the round films and a single cutout on the rectangle films, which are positioned away from axes of symmetry, the scanning direction of the film can consistently be reproduced to minimise fluctuations and deviations.

In the future, the phantom can also be used to evaluate confocal irradiation and might be suitable for quality analysis in clinical practice. Studies regarding the dose profiles of X-rays of different energy and their interaction with a ^{106}Ru applicator should be performed to find the best solution for the combined therapy concept. Additionally, the beam shaping should be analysed. Due to the shape and divergence of the beam, the treatment plan of the combined therapy concept should be adjusted and evaluated.

A novel software to obtain 3D coordinates of eye structures from a 2D fundus photo was presented in chapter 6. After the contouring of different structures is provided, the software computes a 3D eye model considering the distortion of the picture. In addition, the user can implement a distorted projection of a ^{106}Ru applicator. Stored dose profiles obtained from Monte Carlo simulations are then matched with the coordinates and used to calculate the dose profiles in the structures of interest. A slightly different version of this software was already used in an extensive retrospective analysis regarding the dose-response relationship [18]. This was the first investigation that considered not only

the treatment plan but the actual plaque position during treatment by overlapping the distorted projection with the radiation scar in the fundus photo.

The software is best employed with wide-field fundus photos to overcome problems with fundus puzzles. An extensive study on the uncertainties of this software should be performed. Especially the scaling with averaged values from studies with large cohorts may result in significant uncertainties due to the actual individual shape of each person's eye. Therefore, future versions should comprise the option to enter patient-specific measurements. These could be determined during diagnosis using modern devices to overcome individual differences. By defining a 3D model within the software and further Monte Carlo simulations, the software could be extended to obtain dose-volume histograms instead of dose-area histograms. Additional studies with this software can help to understand the dose-response relationships regarding the variety of side effects. The projections and dose profiles of COMS applicators should be included in the software. This would result in gaining more information on side-effect ratios and dose-effect curves, especially concerning large tumours that can not be treated with ^{106}Ru- but with COMS applicators.

The obtained 3D coordinates derived from the previously described software were further used with a generic eye model and a simulation workflow to evaluate the clinical benefit of the combined therapy concept. The generic eye model is built in Fusion360 and can be extended with the information on the location of the tumour and, in case of a retrospective case, of the ^{106}Ru applicator. By implementing the organs of interest and the ^{106}Ru applicator into MC simulations, dose profiles within the organs of interest can be calculated. In addition, confocal external beam radiation therapy was also implemented by including 16 X-ray beams. In total, six cases were simulated and evaluated in this thesis. The analysis showed that the combined therapy concept can be employed to treat small and large intraocular tumours with a maximum of 10 mm tumour height analysed so far. The X-rays provide the necessary dose boost to the tumour to achieve sufficient irradiation in all parts of the tumour if the target points of the beams are chosen accordingly. The therapy plan was further improved by selecting a partial set of beams that entirely hit the ^{106}Ru applicatorĊritical dose values associated with the risk of optic neuropathy, partial vision loss and retinopathy are increased by only a few percentage points compared to stand-alone brachytherapy, which is already clinical routine. Therefore, the combined therapy concept allows many patients with large intraocular tumours to preserve the eye while undergoing similar risks to other clinical approaches for smaller tumours.

Further analyses and improvements regarding the treatment plan need to be conducted. In the best case, the X-rays entry points and target points are chosen individually for each patient to maximise the irradiated tumour volume while minimising the impact on organs at risk. Implementing an optimiser to calculate the weights for each applied beam and for the ^{106}Ru applicator provides an excellent opportunity to decrease the dose in healthy structures further, reducing the risk of side effects. The presented workflow can be adapted to analyse the impact of the uncertainties of brachytherapy on the dose

profiles of both the target volume and the organs at risk. With the results from these studies, the dose prescription and planning algorithm of clinics can be evaluated and changed if necessary. Additionally, the software workflow allows the development of a novel 3D radiation treatment planning tool for brachytherapy, which would improve the quality of this modality. This is the aim of a current project [195]. In addition, the ciliary body should be implemented into the generic eye model.

Many studies are still necessary to bring the combined concept to the first radiation treatment or clinical routine. The beam collimation must be developed and evaluated, ideally parallel to the therapy plan, as these two parameters coincide. By including the robotic device, the safety concept regarding the robot-human interaction and the position uncertainty need to be developed. The eye fixation must be assessed and considered in the movement of the robotic system. A comprehensive study on all therapy uncertainties has to be conducted to estimate the benefits versus the risks of this therapy and to include safety margins into the therapy concept. This results in the definition of the planning target volume, which comprises the diagnostic visible tumour volume and the anisotropic margins to account for possible uncertainties in beam alignment, patient positioning and organ motion as it is standard for conventional radiotherapy. A radiation planning software should be developed or an existing one refined so that therapy with the combination of external beam radiation therapy and brachytherapy can be designed on a patient-specific basis. Different imaging modalities, such as fundus photos, computer tomography and magnetic resonance imaging, should be included and combined to achieve the best possible result. The clinical evaluation also comprises studies regarding the relative biologic effectiveness of the different tissues irradiated with a combination of X-rays and a brachytherapy source to define concepts for fractionation and prescribed dose values. A study comparing the combined therapy concept, brachytherapy with ^{125}I and proton therapy to treat large intraocular tumours should be conducted in the future. Even though these modalities comprise many different radiation qualities and technical limitations, the indications and contraindications should be elaborated. After clinical implementation, a prospective, double-blind study to directly compare treatment success and risks of side effects for the different modalities should be conducted.

Considering these points, the idea of combining brachytherapy and external beam radiation therapy issued in this work represents a promising new clinical modality for intraocular tumours. A clear path towards clinical implementation is sketched.

A Attachments

A.1 Construction drawings of the phantom

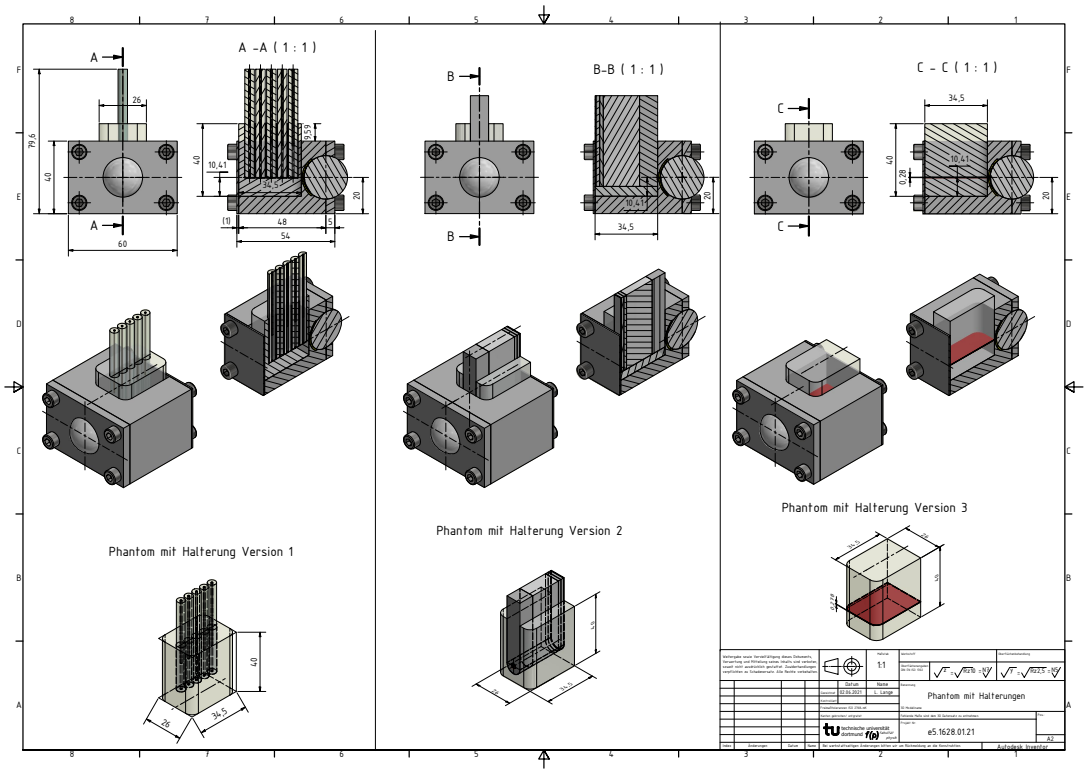

Figure A.1: Construction Drawing: Overview of the three detector setups.

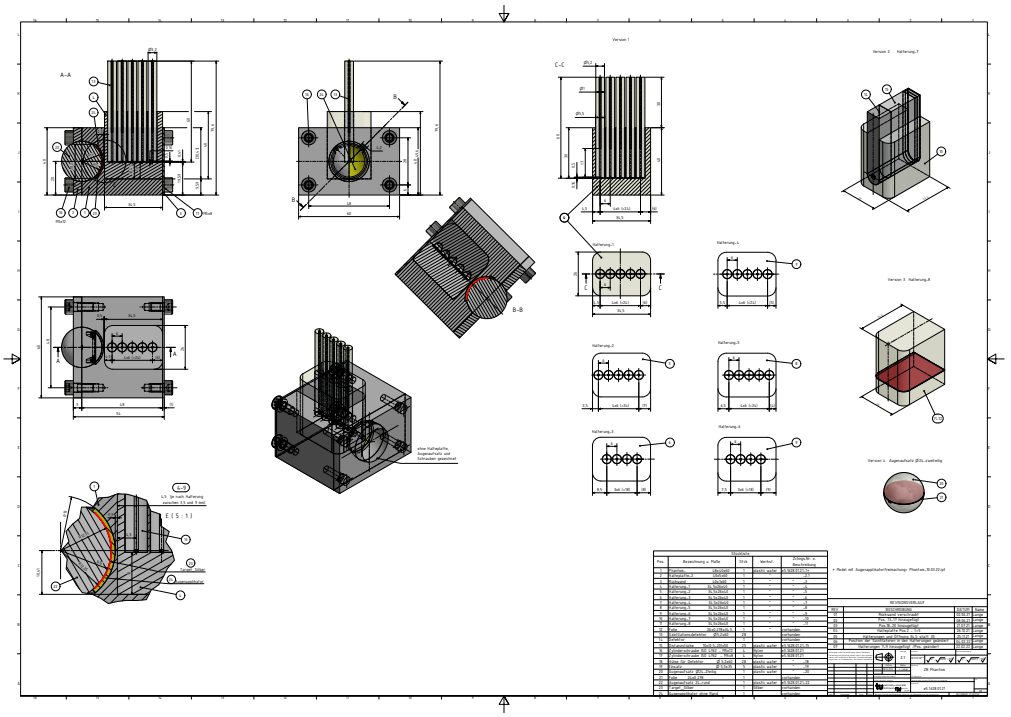

Figure A.2: Construction Drawing: Scintillation detector setup.

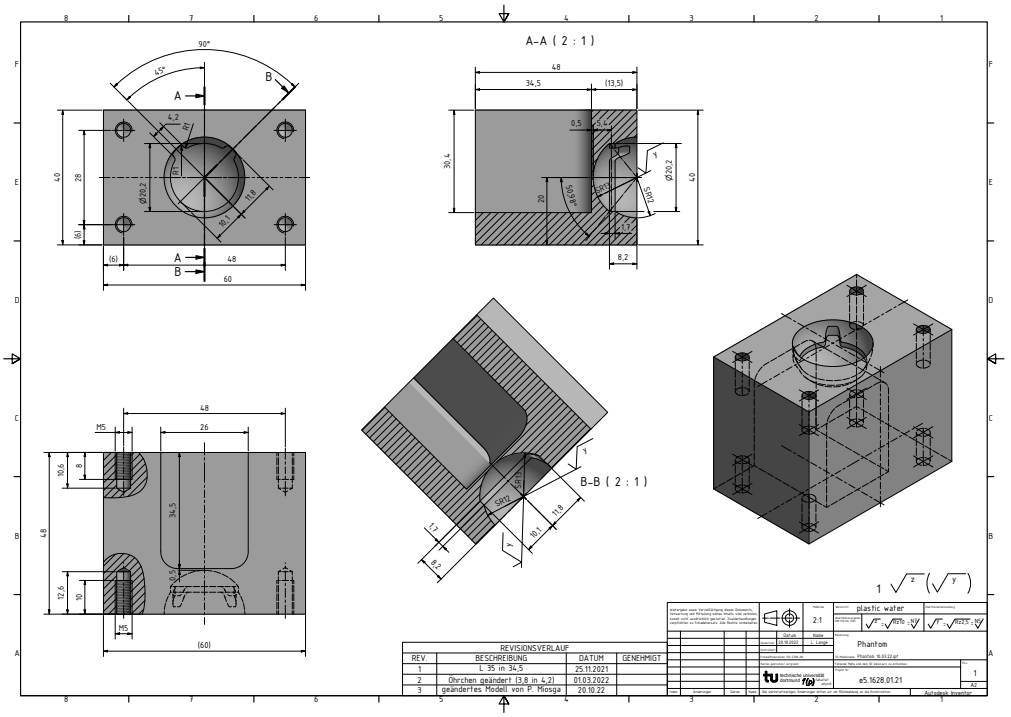

Figure A.3: Construction Drawing: Main phantom body.

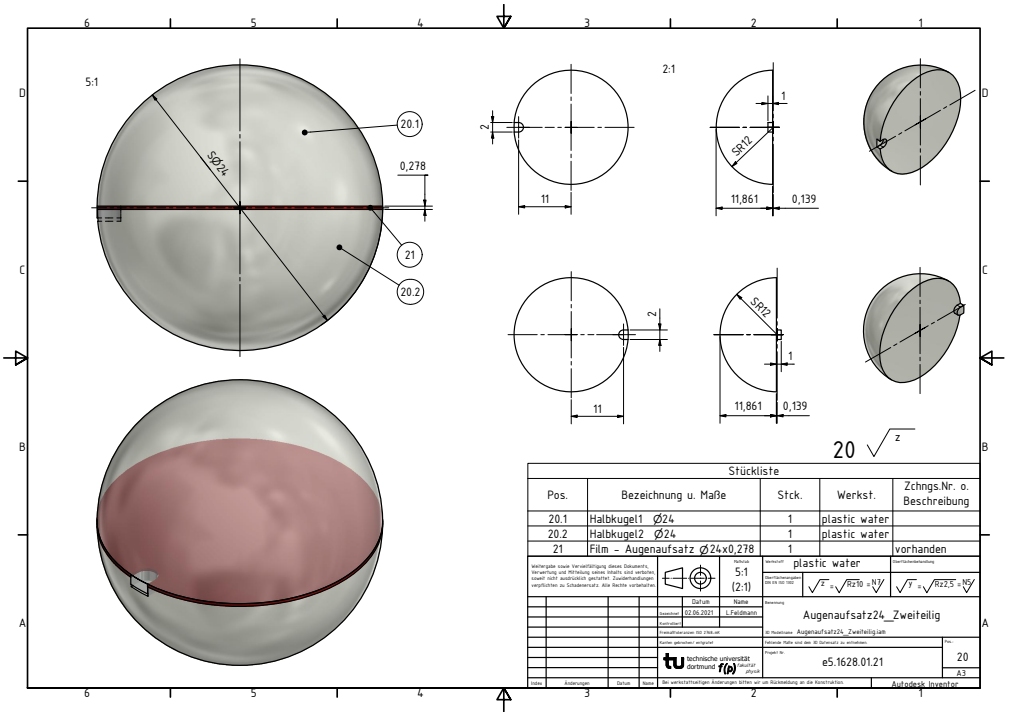

Figure A.4: Construction Drawing: Two hemispheres for the radiochromic film.

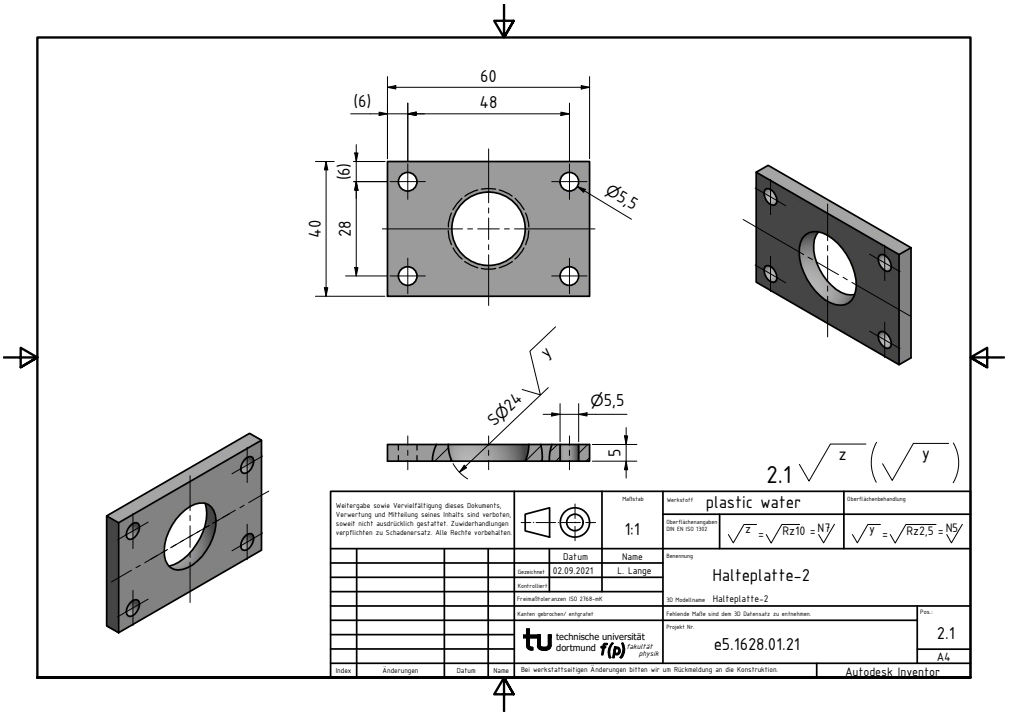

Figure A.5: Construction Drawing: front plate.

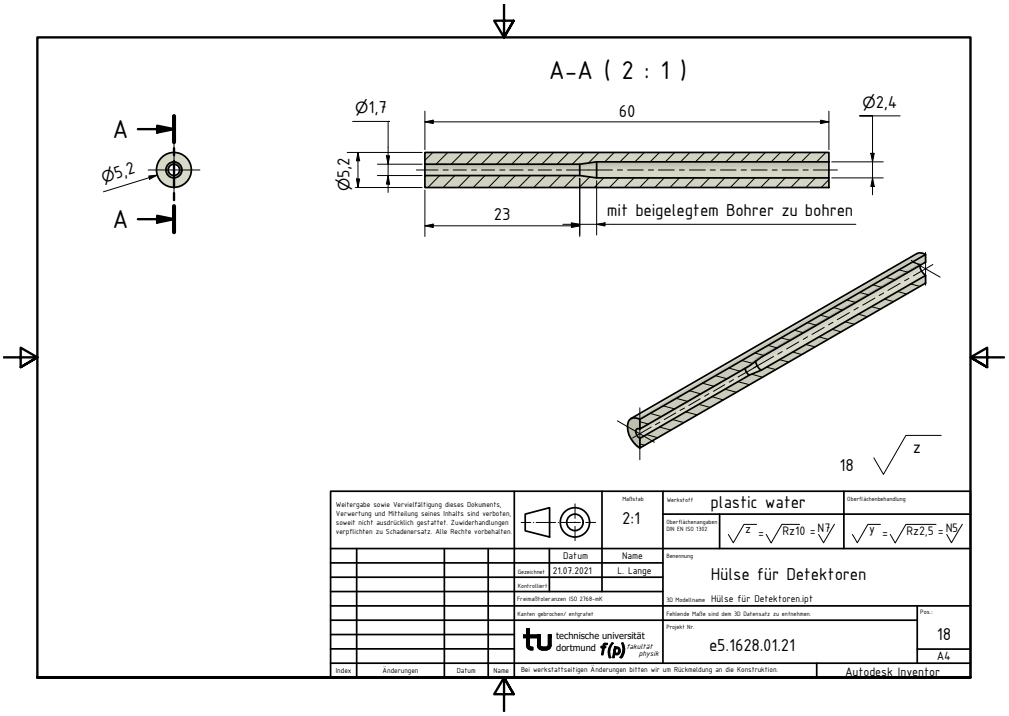

Figure A.6: Construction Drawing: scintillation detector sleeve.

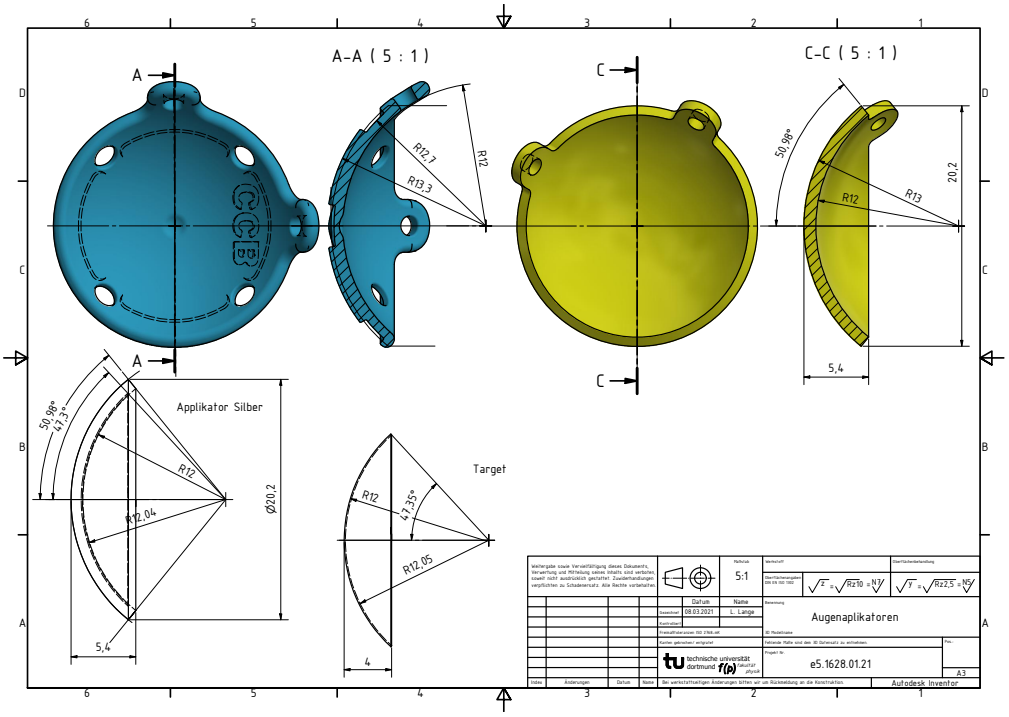

Figure A.7: Construction Drawing: dummy of a ^{106}Ru applicator of type CCB.

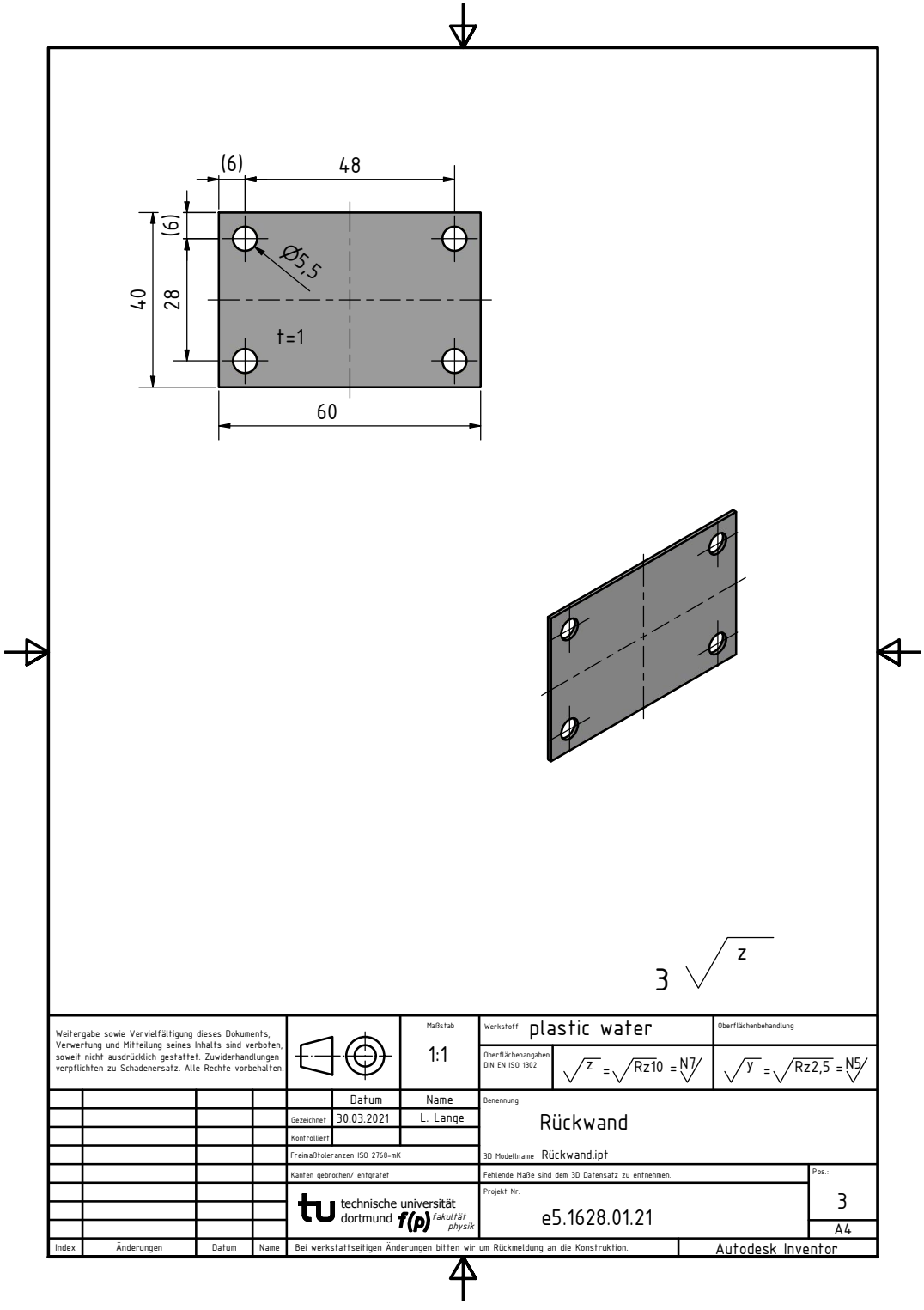

Figure A.8: Construction Drawing: front plate.

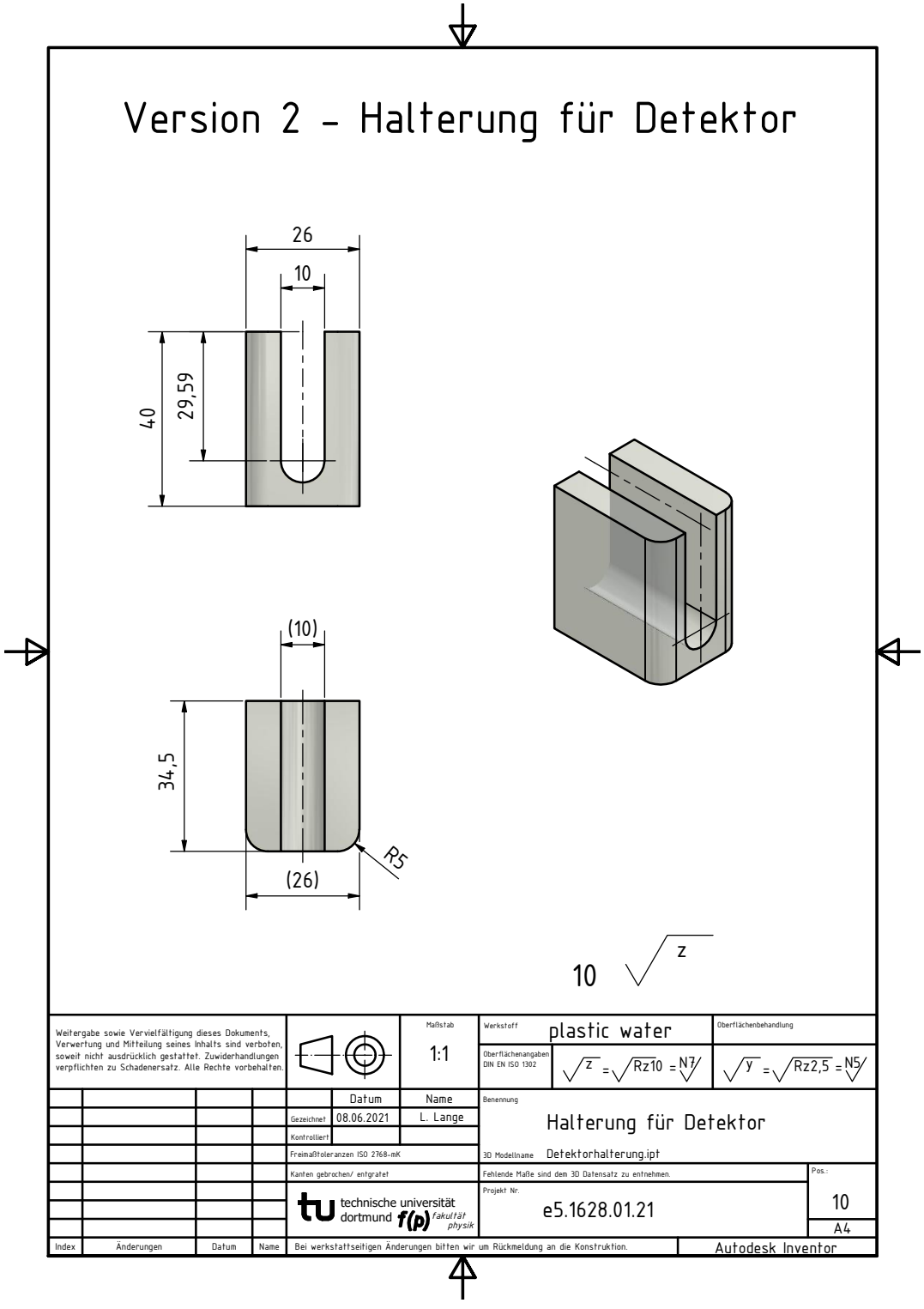

Figure A.9: Construction Drawing: bracket for the soft X-ray chamber.

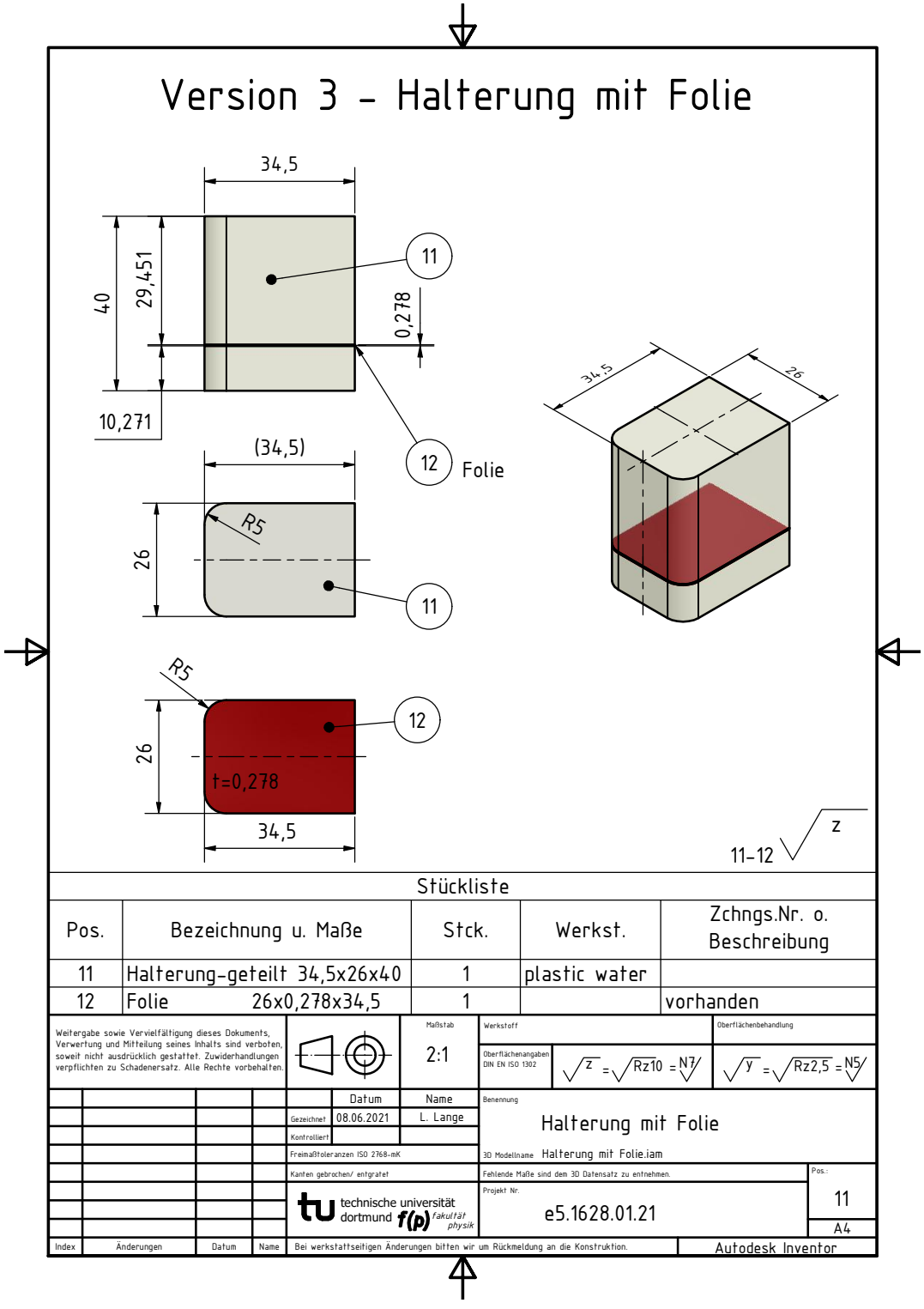

Figure A.10: Construction Drawing: bracket for radiochromic film.

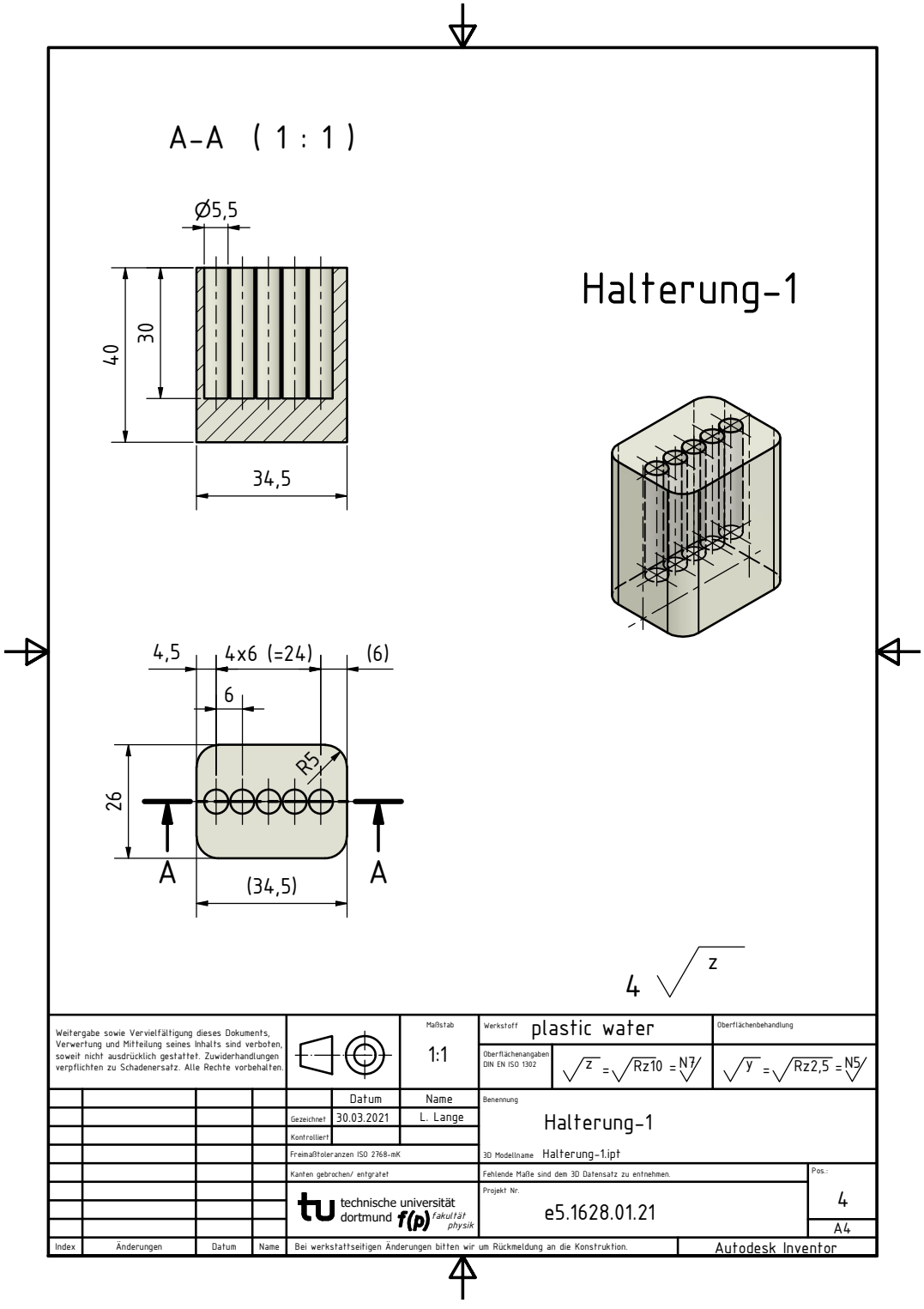

Figure A.11: Construction Drawing: bracket #1 for the scintillation detector.

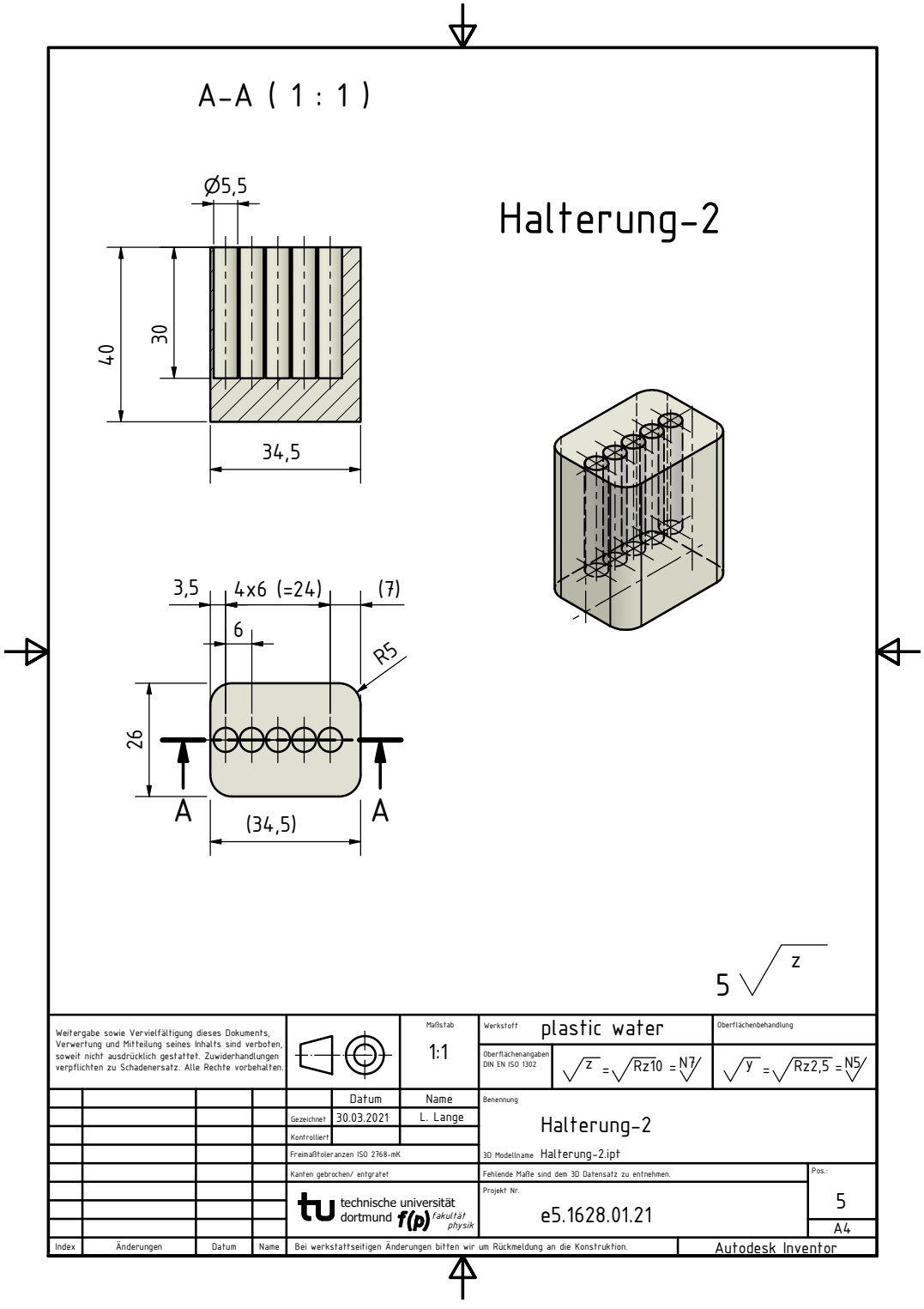

Figure A.12: Construction Drawing: bracket #2 for the scintillation detector.

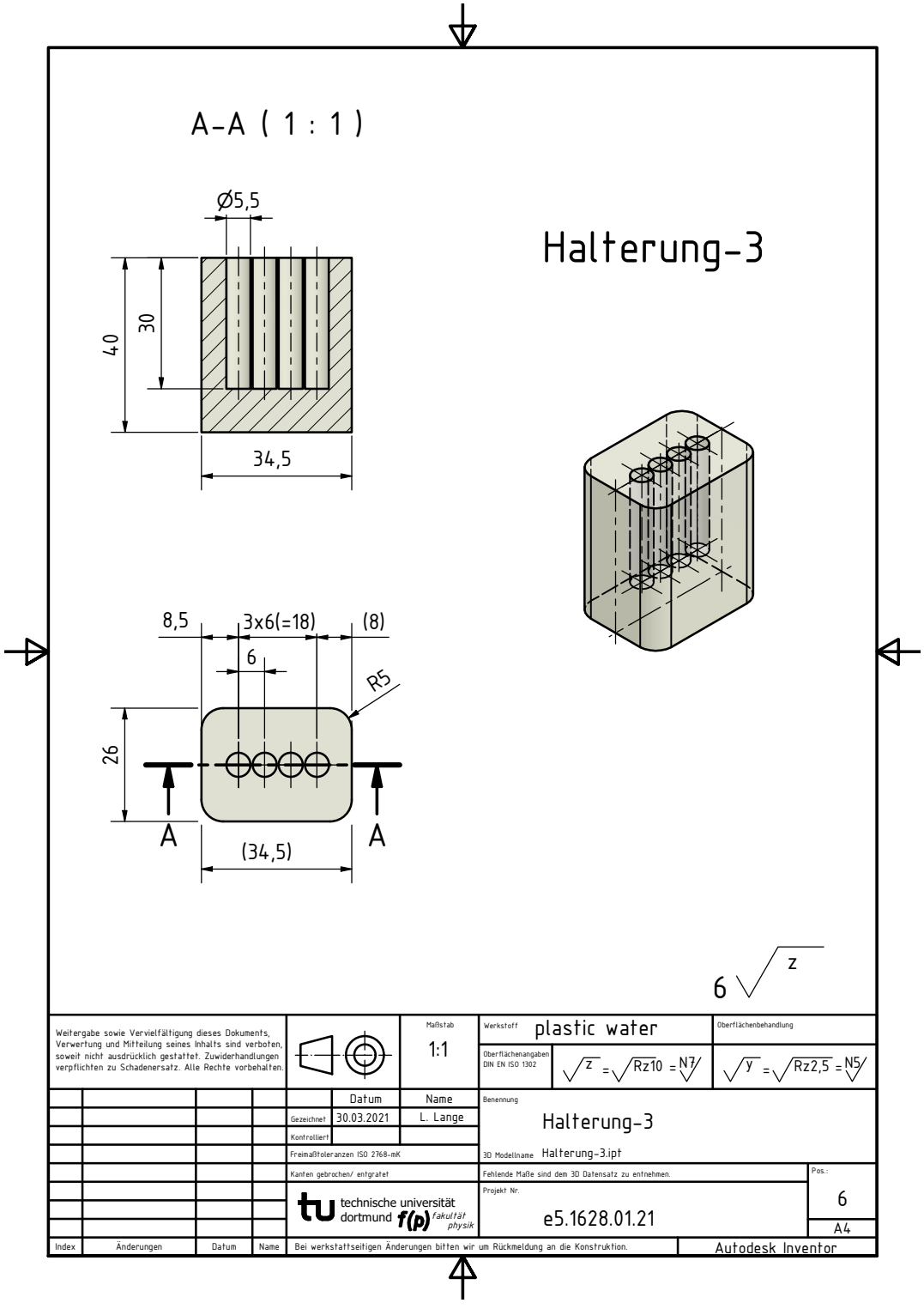

Figure A.13: Construction Drawing: bracket #3 for the scintillation detector.

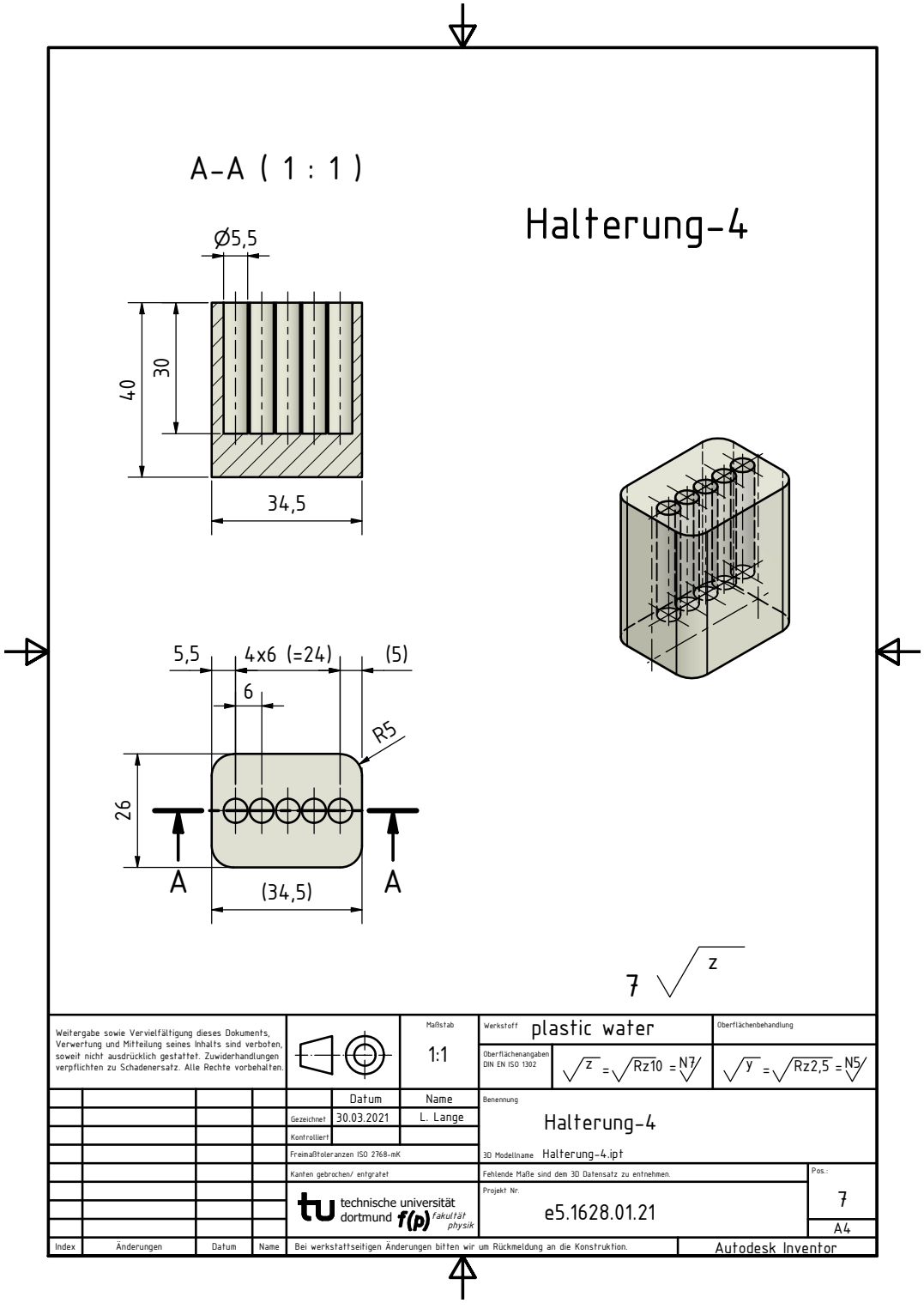

Figure A.14: Construction Drawing: bracket #4 for the scintillation detector.

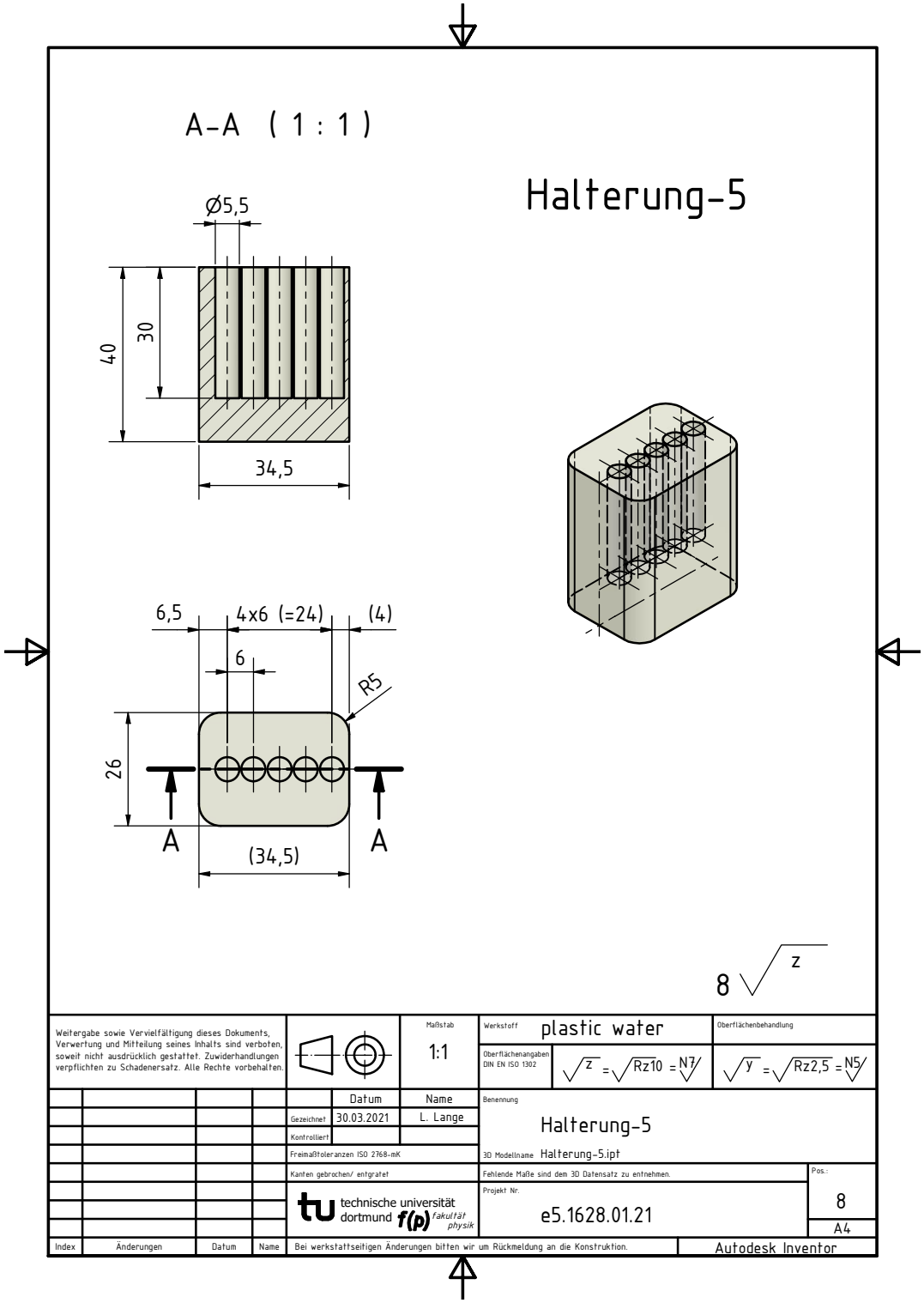

Figure A.15: Construction Drawing: bracket #5 for the scintillation detector.

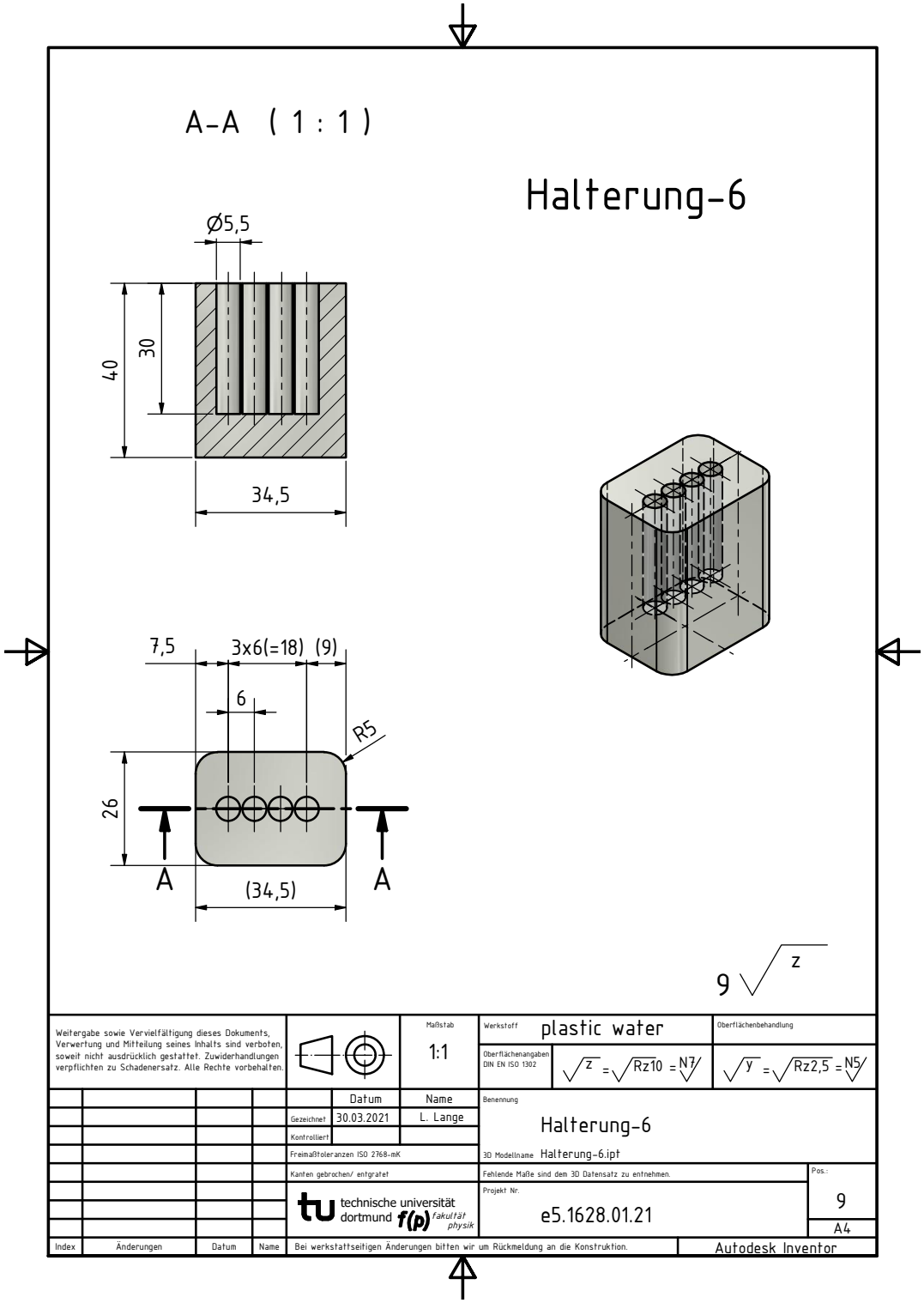

Figure A.16: Construction Drawing: bracket #6 for the scintillation detector.

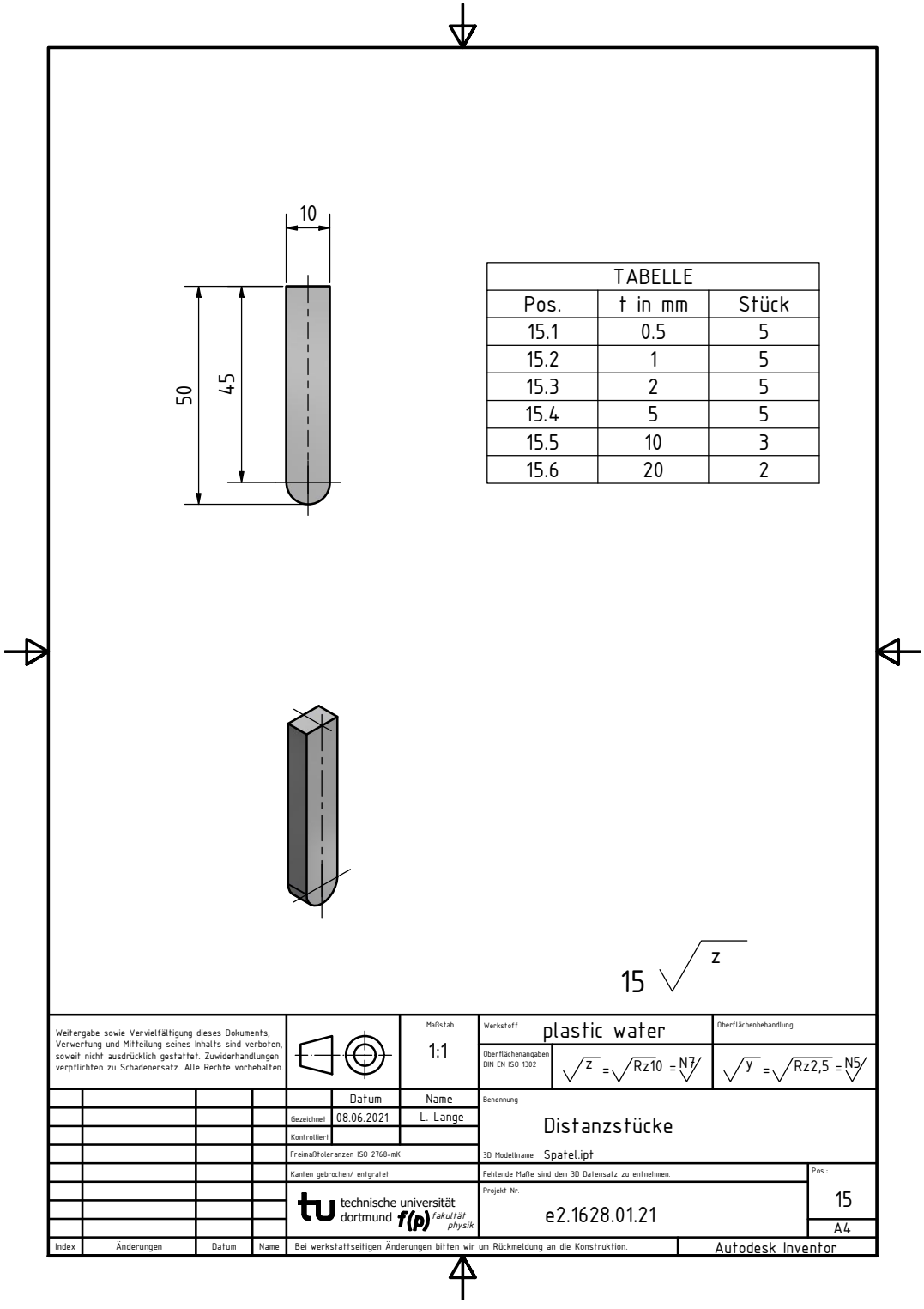

Figure A.17: Construction Drawing: filling pieces for the chamber bracket.

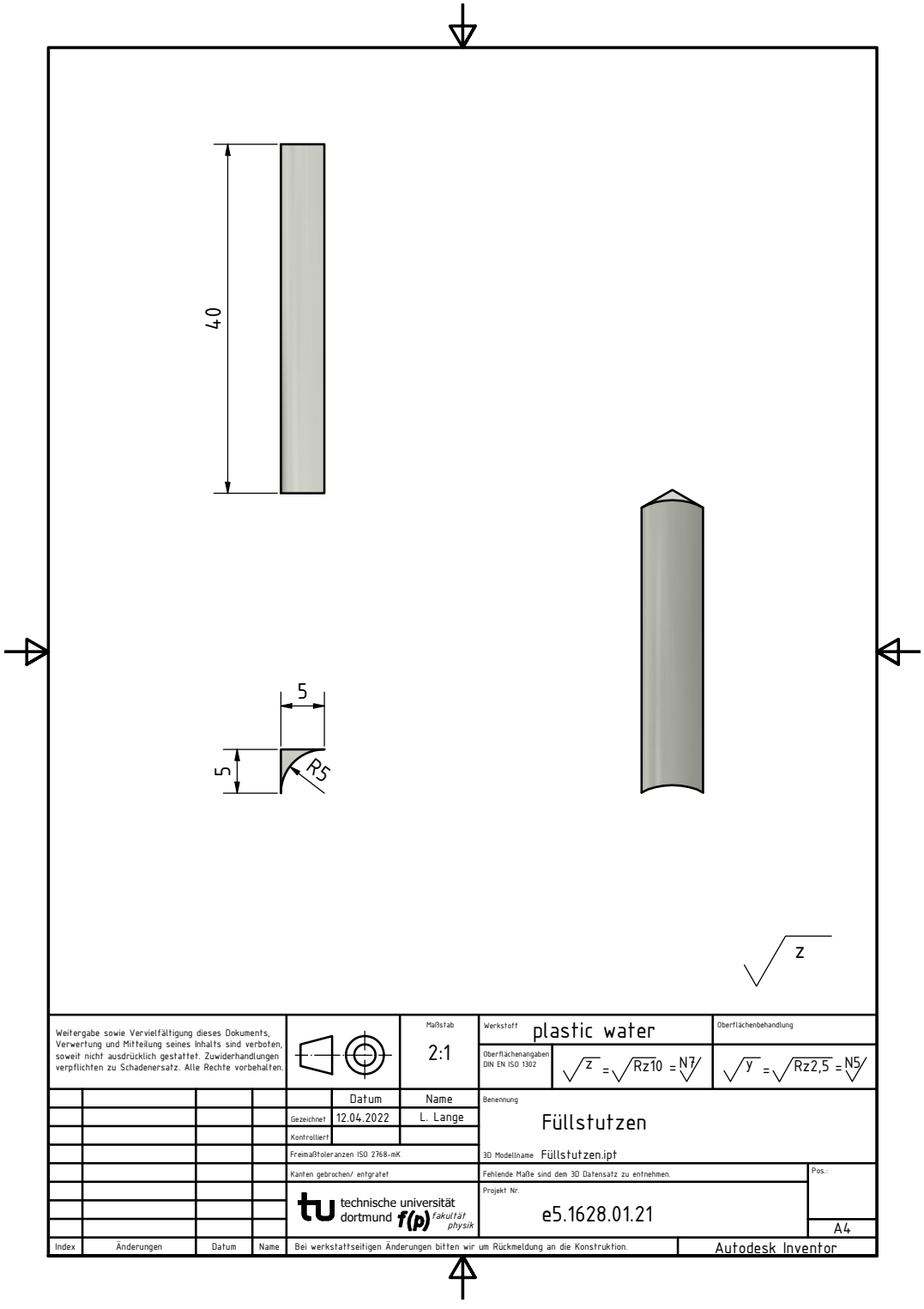

Figure A.18: Construction Drawing: general filling pieces for the brackets.

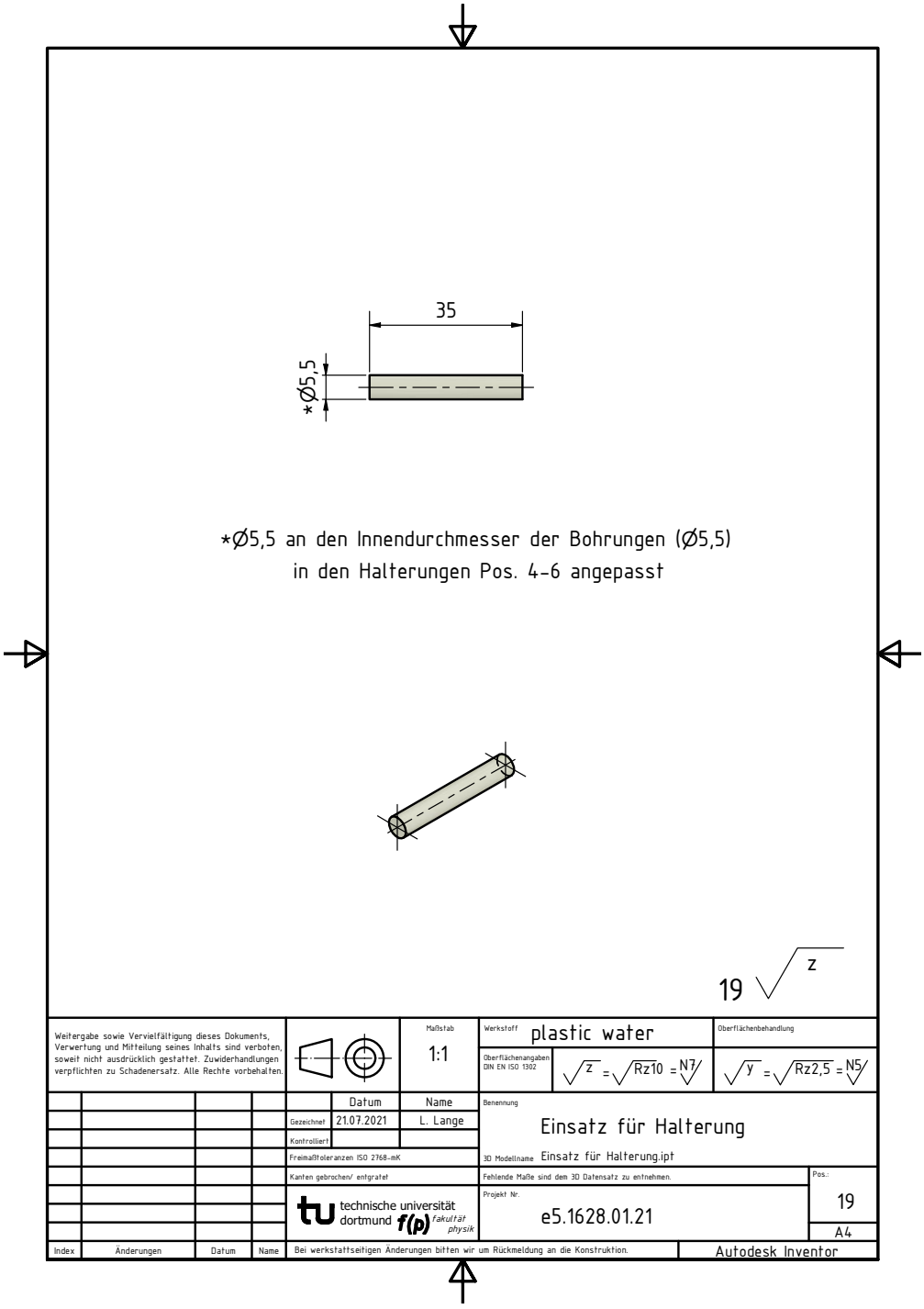

Figure A.19: Construction Drawing: filling pieces for the scintillation detector bracket.

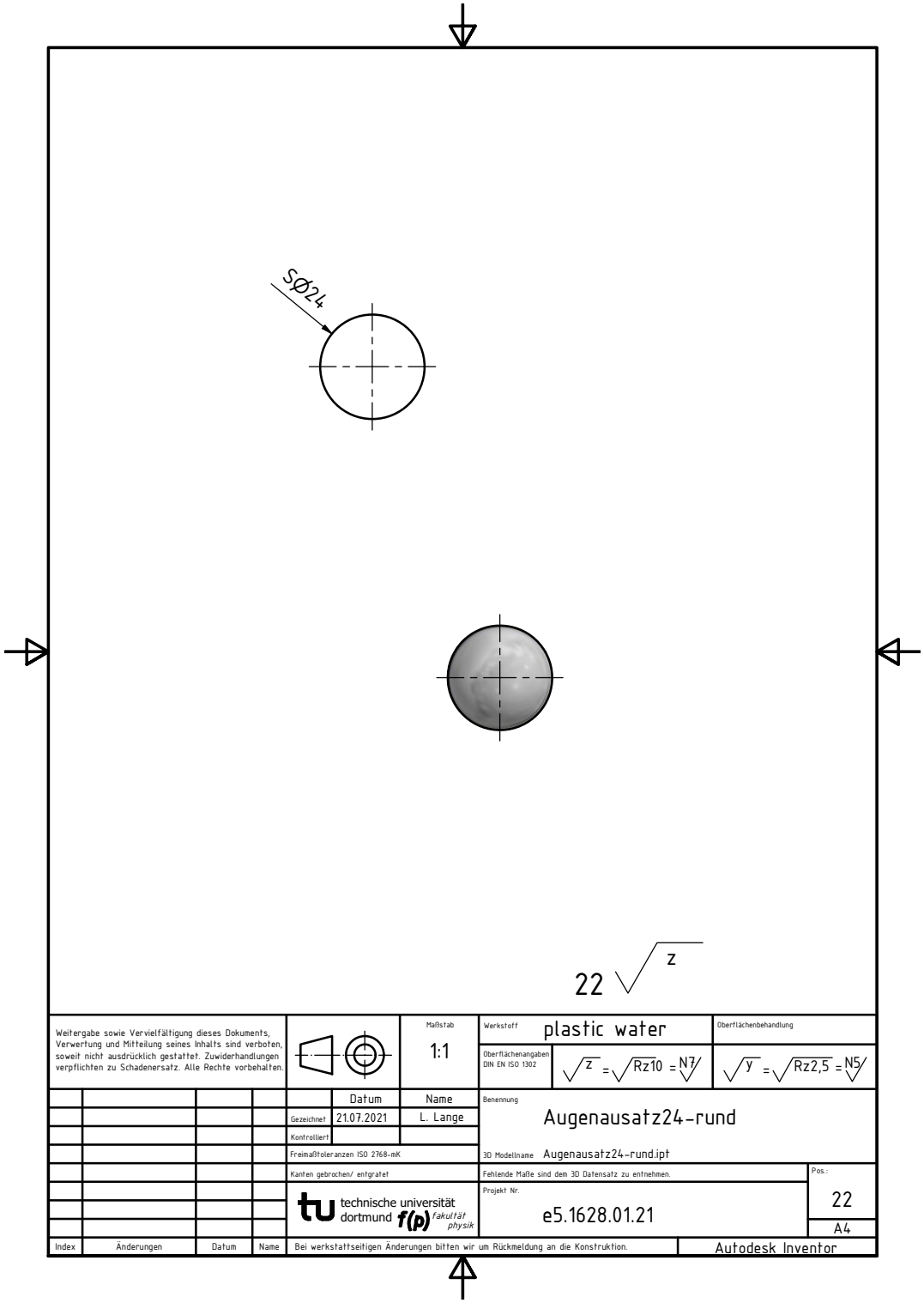

Figure A.20: Construction Drawing: sphere.

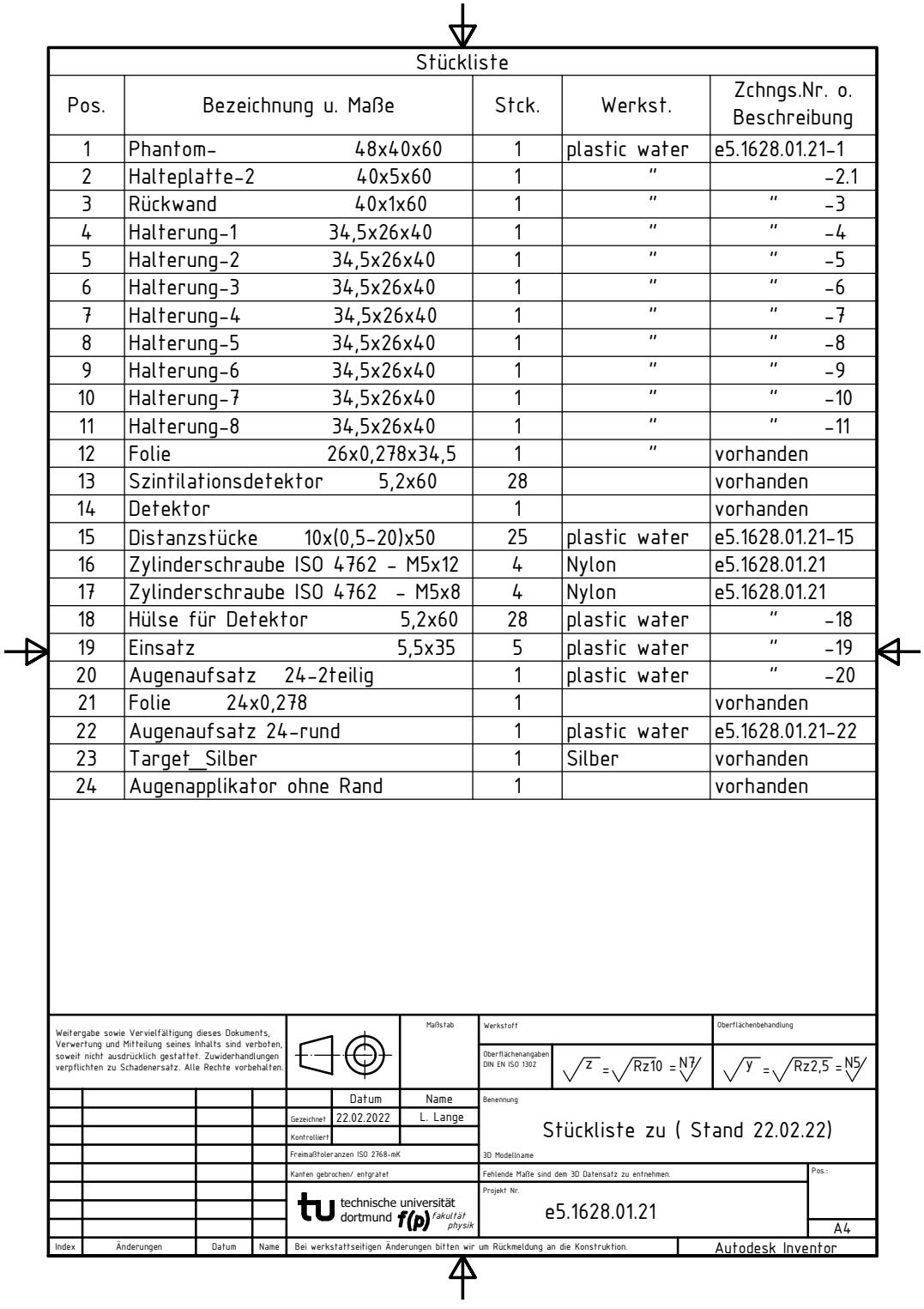

Stückliste

Pos.	Bezeichnung u. Maße	Stck.	Werkst.	Zchngs.Nr. o. Beschreibung
1	Phantom- 48x40x60	1	plastic water	e5.1628.01.21-1
2	Halteplatte-2 40x5x60	1	"	-2.1
3	Rückwand 40x1x60	1	"	" -3
4	Halterung-1 34,5x26x40	1	"	" -4
5	Halterung-2 34,5x26x40	1	"	" -5
6	Halterung-3 34,5x26x40	1	"	" -6
7	Halterung-4 34,5x26x40	1	"	" -7
8	Halterung-5 34,5x26x40	1	"	" -8
9	Halterung-6 34,5x26x40	1	"	" -9
10	Halterung-7 34,5x26x40	1	"	" -10
11	Halterung-8 34,5x26x40	1	"	" -11
12	Folie 26x0,278x34,5	1	"	vorhanden
13	Szintilationsdetektor 5,2x60	28		vorhanden
14	Detektor	1		vorhanden
15	Distanzstücke 10x(0,5-20)x50	25	plastic water	e5.1628.01.21-15
16	Zylinderschraube ISO 4762 - M5x12	4	Nylon	e5.1628.01.21
17	Zylinderschraube ISO 4762 - M5x8	4	Nylon	e5.1628.01.21
18	Hülse für Detektor 5,2x60	28	plastic water	" -18
19	Einsatz 5,5x35	5	plastic water	" -19
20	Augenaufsatz 24-2teilig	1	plastic water	" -20
21	Folie 24x0,278	1		vorhanden
22	Augenaufsatz 24-rund	1	plastic water	e5.1628.01.21-22
23	Target_Silber	1	Silber	vorhanden
24	Augenapplikator ohne Rand	1		vorhanden

Maßstab

Werkstoff

Oberflächenbehandlung

Oberflächenangaben DIN EN ISO 1302

$\sqrt{z} = \sqrt{Rz10} = \sqrt{N7}$

$\sqrt{y} = \sqrt{Rz2,5} = \sqrt{N5}$

	Datum	Name
Gezeichnet	22.02.2022	L. Lange
Kontrolliert		

Benennung

Stückliste zu (Stand 22.02.22)

Freimaßtoleranzen ISO 2768-mK

3D Modellname

Kanten gebrochen/ entgratet

Fehlende Maße sind dem 3D Datensatz zu entnehmen.

Pos.:

technische universität dortmund f(p) fakultät physik

Projekt Nr.

e5.1628.01.21

A4

Index	Änderungen	Datum	Name

Bei werkstattseitigen Änderungen bitten wir um Rückmeldung an die Konstruktion.

Autodesk Inventor

Figure A.21: Construction Drawing: List of all parts.

A.2 Light yield of scintillation detectors

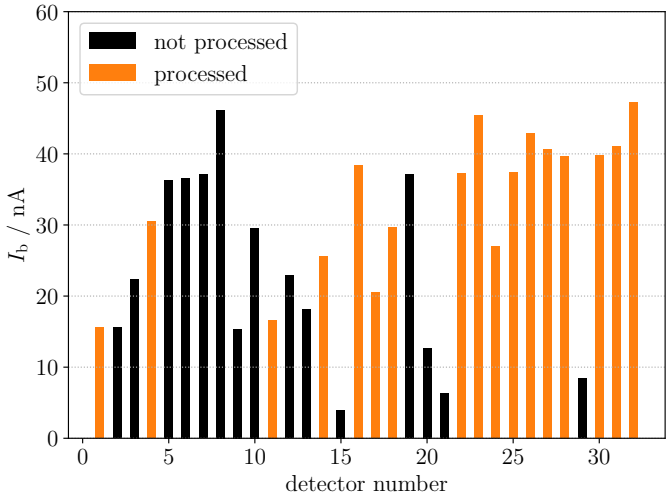

Figure A.22: Output current I_b of all scintillation detectors.

A.3 Radiochromic film calibration

Table A.1: Fit values of the calibration curves for the radiochromic film calculated with FilmQA pro™ for both photon energy spectra and each colour channel - red (r), green (g) and blue (b).

	A_r	B_r	C_r	A_g	B_g	C_g	A_b	B_b	C_b
100 kV	0.126	1.258	-2.310	0.099	2.194	-4.027	0.144	2.336	-7.266
70 kV	0.134	1.243	-2.281	0.105	2.164	-3.938	0.161	2.090	-6.685

A.4 Applicator simulation data

model	r_i / mm	θ/°	θ_T/°
CCA	12	36.05	32.49
CCB	12	50.98	47.35
CCC	13	62.34	59.18
CCD	12	43.51	39.83
CCX	12	26.50	23.11
CGD	13	52.79	49.42
CXS	12	26.50	18.55

Table A.2: Geometric data of the simulated rotational symmetrical ^{106}Ru applicators. In this table, r is the inner radius of curvature, θ is the angle of aperture of the applicator, and θ is the aperture angle of the ^{106}Ru-coated target. The data are derived from [86].

	Volume	θ / °	α_x / °	α_y / °	α_z / °
applicator	main body	50.13	0	0	0
	sub 1	15.76	38.59	0	0
	sub 2	31.50	0	66.31	−66.70
	sub 3	31.50	0	−66.31	66.70
	add 1	6.60	0	34.50	−37.50
	add 2	6.60	0	−34.50	37.50
target	main body	44.98	0	0	0
	sub 1	21.21	37.88	0	0
	sub 2	22.92	0	53.03	−63.79
	sub 3	22.92	0	−53.03	63.79
	add 1	11.1	0	34.20	−36.50
	add 2	11.1	0	−34.20	36.50

Table A.3: Parameters of the twelve different volumes to construct a ^{106}Ru applicator of type COB including its target in Geant4. α defines the rotation angle around one of the axes x, y, z. The data are derived from [84].

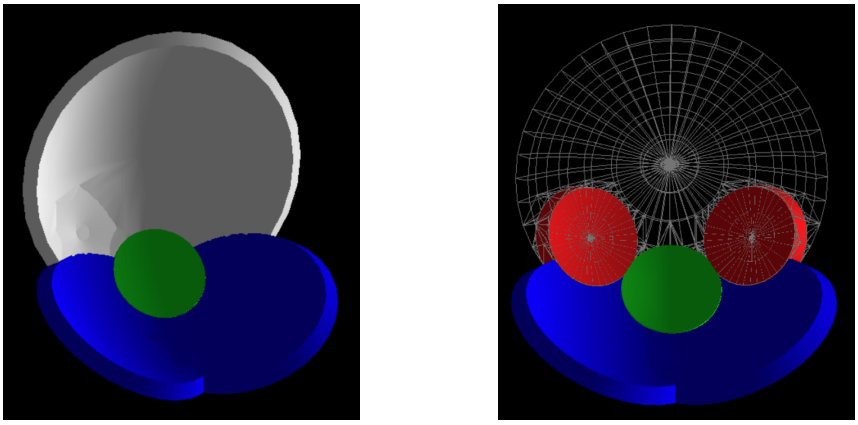

a) b)

Figure A.23: Visualisation of the construction of the COB in Geant4. It consists of several volumes which are added or subtracted to the general body in order to create the notch. The basic body is shown in grey in a) and as mesh in b), the volumes to be subtracted in green and blue, the volumes to be added afterwards in red.

A.5 Important measurements, compositions and densities of eye structures

Table A.4: The sizes of each structure used for the eye model, derived from Ref. [183].

structure	name of dimension	size / mm	Ref.
globe / bulbus oculi	sagital diameter vertical diameter	23.10 23.80	[204]
sclera	thickness at the posterior pole thickness at the equator	1.00 0.18	[204]
choroid	thickness	0.27	[204]
retina	thickness at the equator	0.18	[204]
anterior chamber	height depth	12.33 3.11	[204, 205]
cornea	peripheral thickness	0.67	[204]
lens	equatorial diameter sagital diameter	9.00 4.00	[204]
optic nerve	diameter intraocular length Intraorbital length	4.00 1.00 25.00	[204]
optic disc	horizontal diameter vertical diameter	1.76 1.92	[204]
macula lutea	diameter of the perifovea diameter of the parafovea diameter of the fovea	6.00 3.00 1.00	[206]
pars plana	nasal thickness temporal thickness	3.00 5.00	[207]

Table A.5: Chemical composition of the ocular structures used for the generic eye model. Aqueous humor is abbreviated by "a. h.", optic nerve by "o. n." and vitreous body by "v. b.", obtained from Ref. [183].

Material	mass fraction / %					
	sclera [184, 208]	cornea [184, 208, 209]	a. h. [184]	v. b. [184, 210]	lens [211]	o. n. [211]
water	68.000	78.000	98.687	99.064	-	-
Na	0.583	1.725	0.619	0.337	0.1	0.2
Cl	0.920	1.977	0.541	0.431	0.1	0.3
Ka	0.297	0.719	0.013	0.022	-	0.3
Ca	0.027	0.030	0.008	0.007	-	-
Mg	0.007	0.024	0.005	0.002	-	-
O	0.985	0.985	-	-	64.6	71.2
C	0.660	0.660	-	-	19.5	14.5
S	0.333	0.659	-	-	0.3	0.2
H	0.090	0.090	-	-	9.6	10.7
N	0.055	0.055	-	-	5.7	2.2
P	-	-	-	-	0.1	0.4
bicarbonate	-	-	0.085	-	-	-
glucose	-	-	0.014	0.054	-	-
lactate	-	-	0.015	0.036	-	-
ascorbate	-	-	0.004	-	-	-
phosphate	0.043	0.076	0.003	-	-	-
citrate	-	-	0.001	-	-	-
collagen	27.000	15.000	-	0.040	-	-
elastin	1.000	-	-	-	-	-
pyruvic acid	-	-	-	0.007	-	-
alanine	-	-	0.001	-	-	-
leucine	-	-	0.001	-	-	-
lysine	-	-	0.001	-	-	-
threonine	-	-	0.001	-	-	-
valine	-	-	0.001	-	-	-

Table A.6: Densities of the structures implemented in the generic eye model, acquired from Ref. [183].

organ	$\rho / \frac{\mathrm{g}}{\mathrm{cm}^3}$	Ref.
sclera	1.049	[187]
cornea	1.024	[187]
aqueous humour	1	[212]
vitreous body	1.0065	[213]
lens	1.07	[211]
optic nerve	1.04	[211]
retina	1.008	[187]
choroid	1.002	[187]

Table A.7: The composition of the proteins elastin and collagen. The densities are set to 1.3 $\frac{\mathrm{g}}{\mathrm{cm}^3}$ for elastin [184] and 1.343 $\frac{\mathrm{g}}{\mathrm{cm}^3}$ for collagen [214]. The data are derived from Ref. [183].

Amino acid	mass fraction / %	
	elastin [215]	collagen [184]
alanine (Ala)	17.915	9.6
arginine (Arg)	0.506	4.6
aspartic acid (Asp)	0.405	4.2
cysteine (Cys)	-	0.2
glutamine (Glu)	1.316	7.1
glycine (Gly)	36.538	35.0
hystidine (His)	0.101	0.6
hydroxylysine (Hyl)	-	0.5
hydroxyproline (Hyp)	1.923	12.5
isoleucine (Ile)	1.923	1.3
leucine (Leu)	5.061	2.2
lysine (Lys)	0.304	3.0
methionine (Met)	-	0.8
phenylalanine (Phe)	2.024	0.8
proline (Pro)	12.854	10.7
serine (Ser)	0.506	3.9
threonine (Thr)	0.709	1.3
tyrosine (Tyr)	1.113	0.3
valine (Val)	16.802	1.4

Table A.8: The compounds relevant for the definition of the used materials for the generic eye model. Information obtained from Ref. [183, 216].

composition	density/$\frac{g}{cm^3}$	structural formula
ascorbate	1.65	$C_6H_7O_6$
bicarbonate	1.67	CHO_3
pyruvic acid	1.25	$C_3H_4O_3$
citrate	1.665	$C_6H_5O_7$
glucose	1.54	$C_6H_{12}O_6$
lactate	1.209	$C_3H_5O_3$
phosphate	1.87	PO_4

Table A.9: The amino acids relevant to the definition of the different eye structures. The data are obtained from Ref. [183, 216].

amino acid	$\rho/\frac{g}{cm^3}$	structural formula
alanine (Ala)	1.432	$C_3H_7NO_2$
arginine (Arg)	1.5	$C_6H_{14}N_4O_2$
asparagine acid (Asp)	1.66	$C_4H_7NO_4$
cysteine (Cys)	1.3	$C_3H_7NO_2S$
glutamine acid (Glu)	1.525	$C_5H_9NO_4$
glycine (Gly)	1.595	$C_2H_5NO_2$
histidine (His)	1.4	$C_6H_9N_3O_2$
hydroxylysine (Hyl)	1.3	$C_6H_{14}N_2O_3$
hydroxyproline (Hyp)	1.4	$C_5H_9NO_3$
isoleucine (Ile)	1.4	$C_6H_{13}NO_2$
leucine (Leu)	1.293	$C_6H_{13}NO_2$
lysine (Lys)	1.1	$C_6H_{14}N_2O_2$
methionine (Met)	1.34	$C_5H_{11}NO_2S$
phenylalanine (Phe)	1.2	$C_9H_{11}NO_2$
proline (Pro)	1.36	$C_5H_9NO_2$
serine (Ser)	1.537	$C_3H_7NO_3$
threonine (Thr)	1.3	$C_4H_9NO_3$
tyrosine (Tyr)	1.46	$C_9H_{11}NO_3$
valine (Val)	1.23	$C_5H_{11}NO_2$

A.6 Visualisation of all cases

In the following, the individual cases are illustrated. The cube above displays the point of view with the abbreviations **L**eft, **R**ight, **F**ront, **B**ack, **T**op and **Bot**tom.

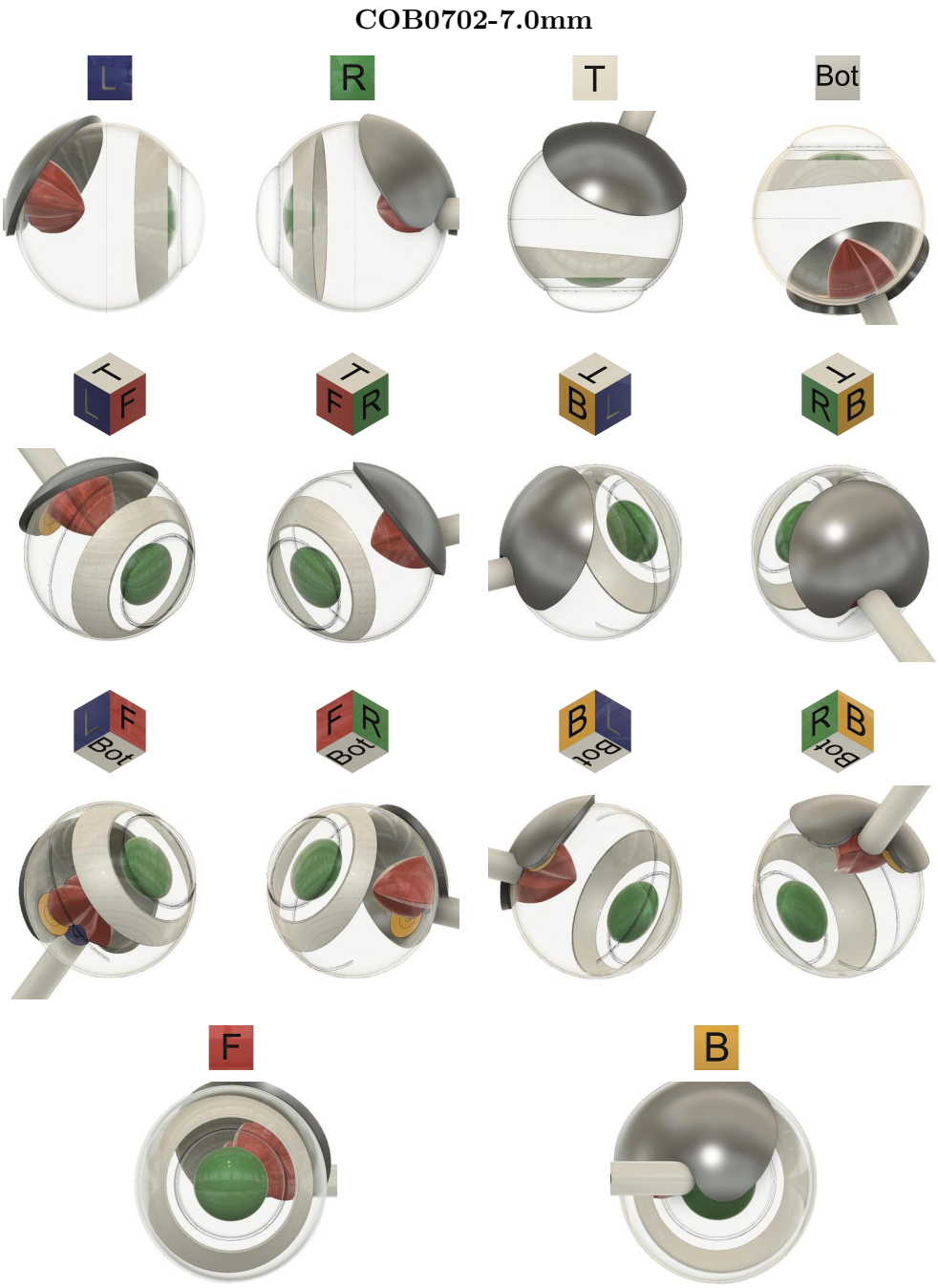

Figure A.24: Tumour shape eye model for the case COB0702-7.0mm. Each of the fourteen different views presents the tumour (red), the ^{106}Ru applicator (dark grey), the pars plana (light grey) and the lens (green) among other structures. The cube above resembles the corresponding point of view.

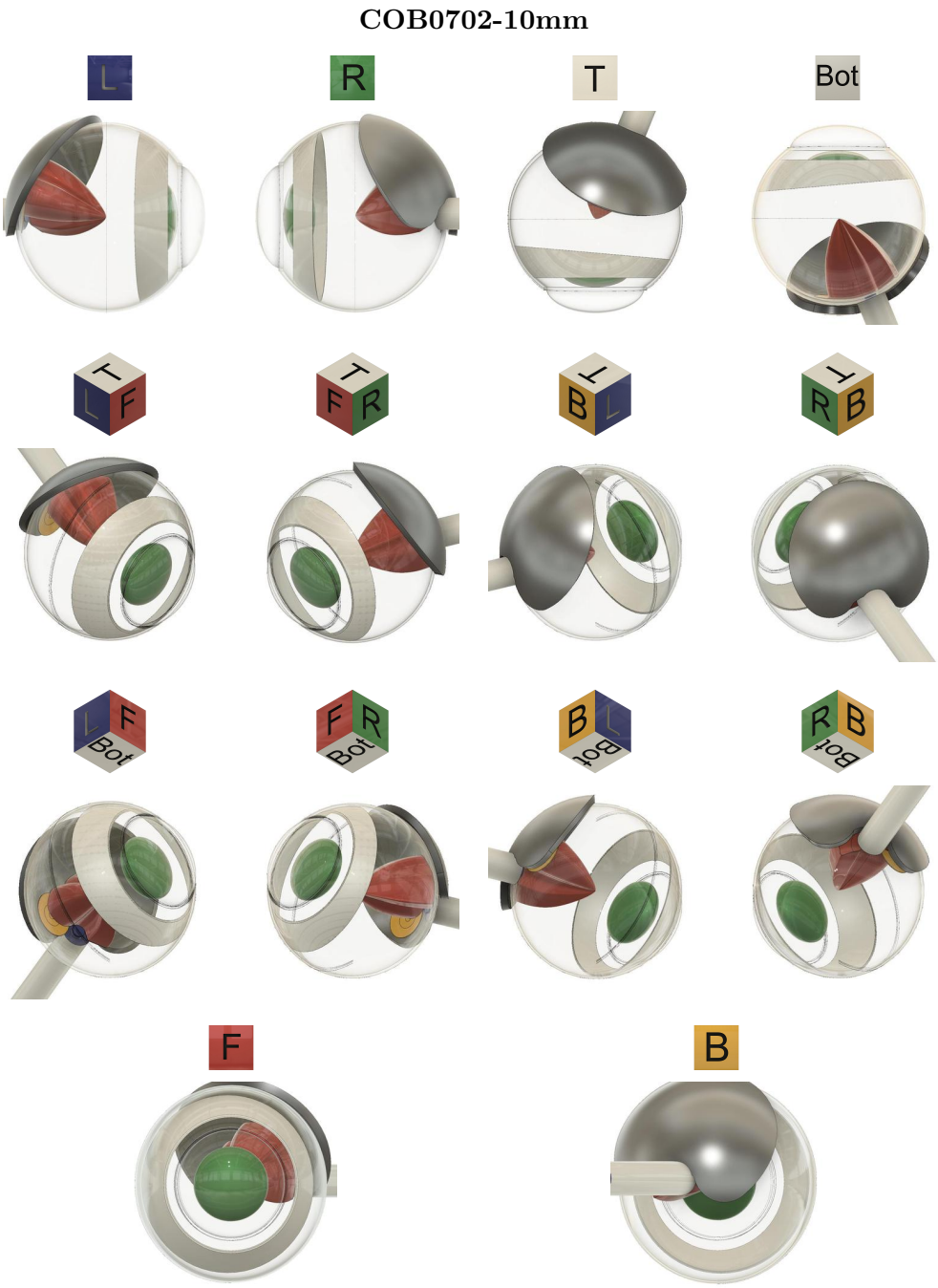

Figure A.25: Tumour shape eye model for the case COB0702-10mm. Each of the fourteen different views presents the tumour (red), the ^{106}Ru applicator (dark grey), the pars plana (light grey) and the lens (green) among other structures. The cube above resembles the corresponding point of view.

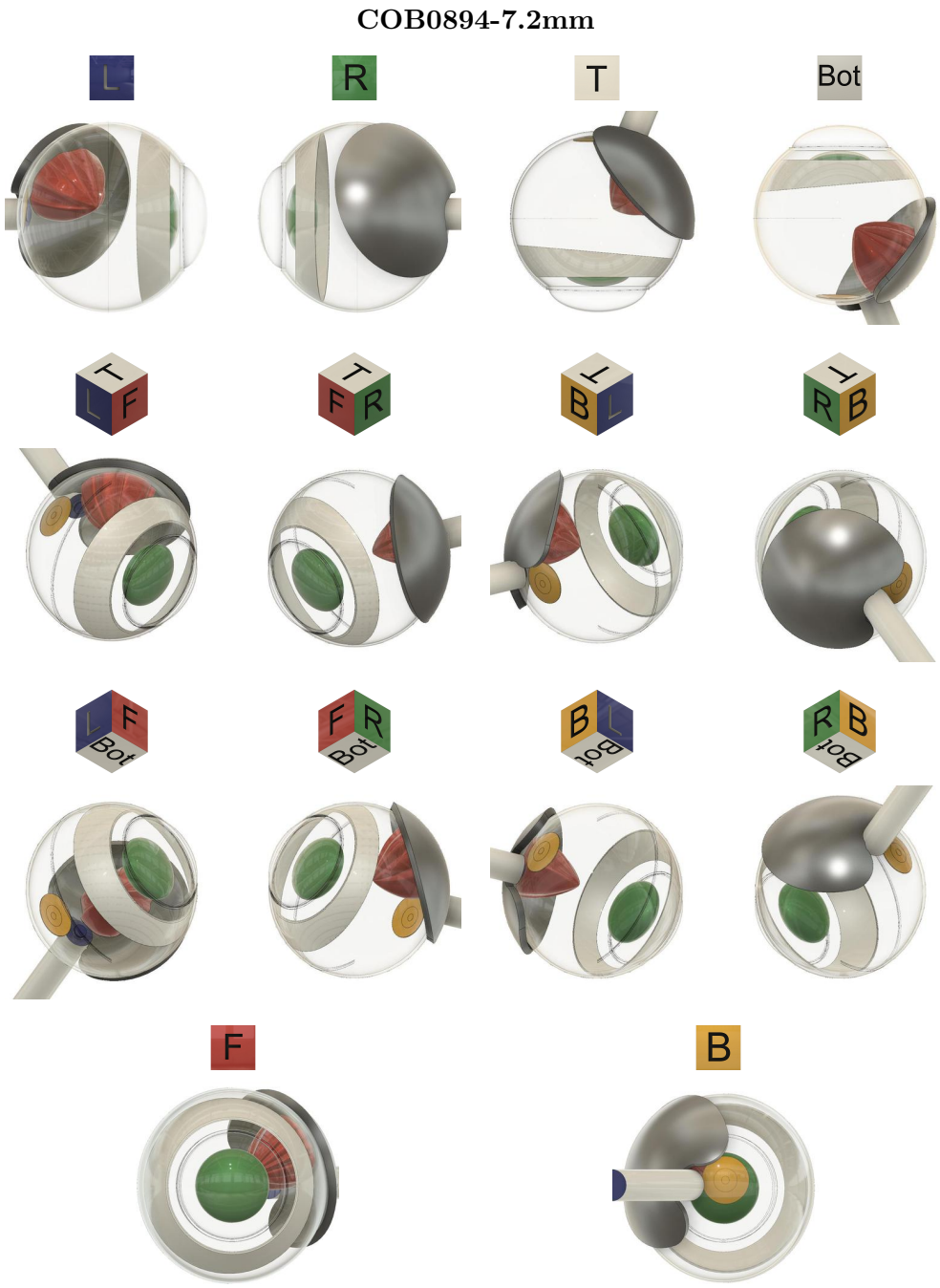

Figure A.26: Tumour shape eye model for the case COB0894-7.2mm. Each of the fourteen different views presents the tumour (red), the ^{106}Ru applicator (dark grey), the pars plana (light grey) and the lens (green) among other structures. The cube above resembles the corresponding point of view.

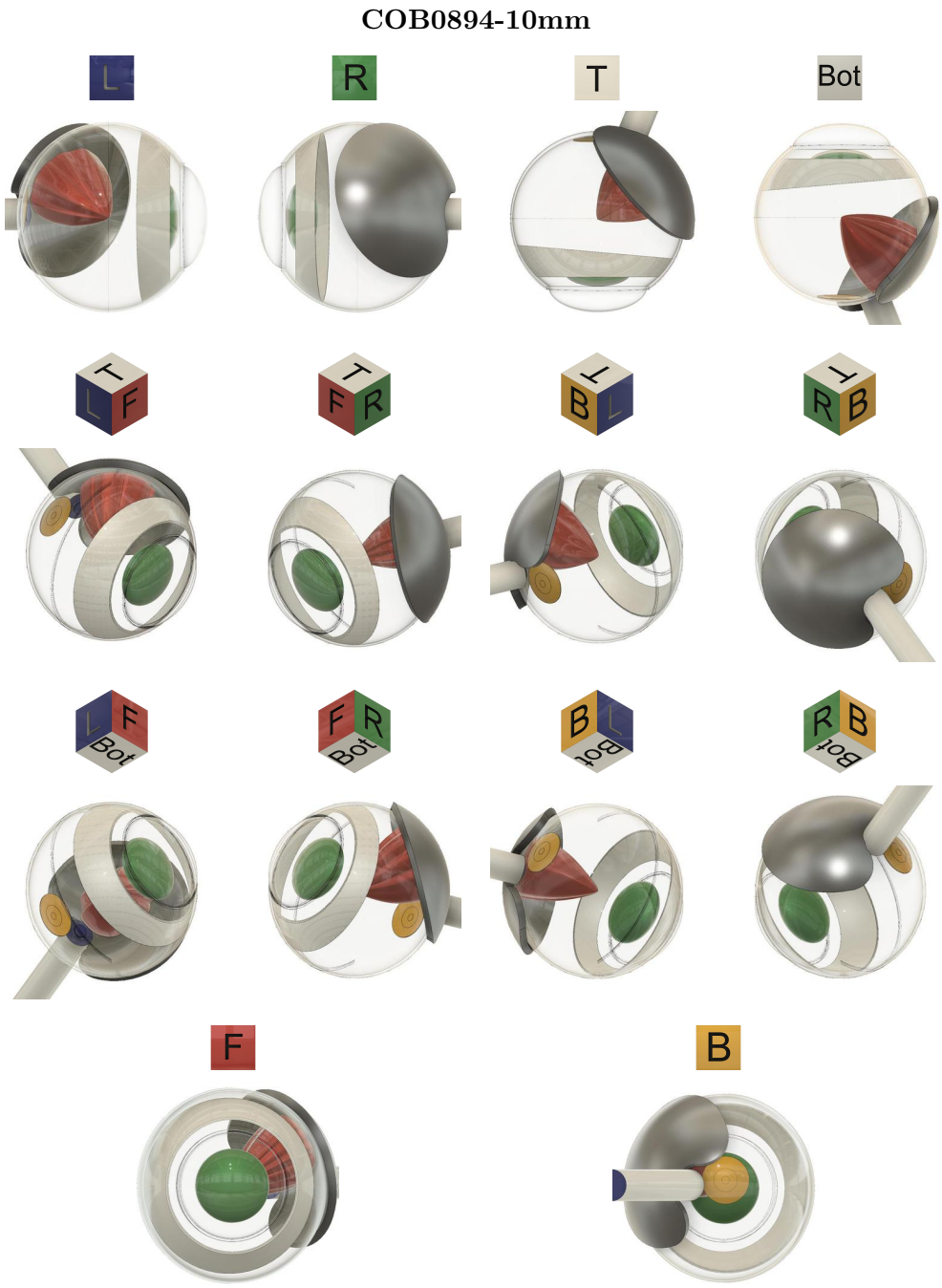

Figure A.27: Tumour shape eye model for the case COB0894-10mm. Each of the fourteen different views presents the tumour (red), the ^{106}Ru applicator (dark grey), the pars plana (light grey) and the lens (green) among other structures. The cube above resembles the corresponding point of view.

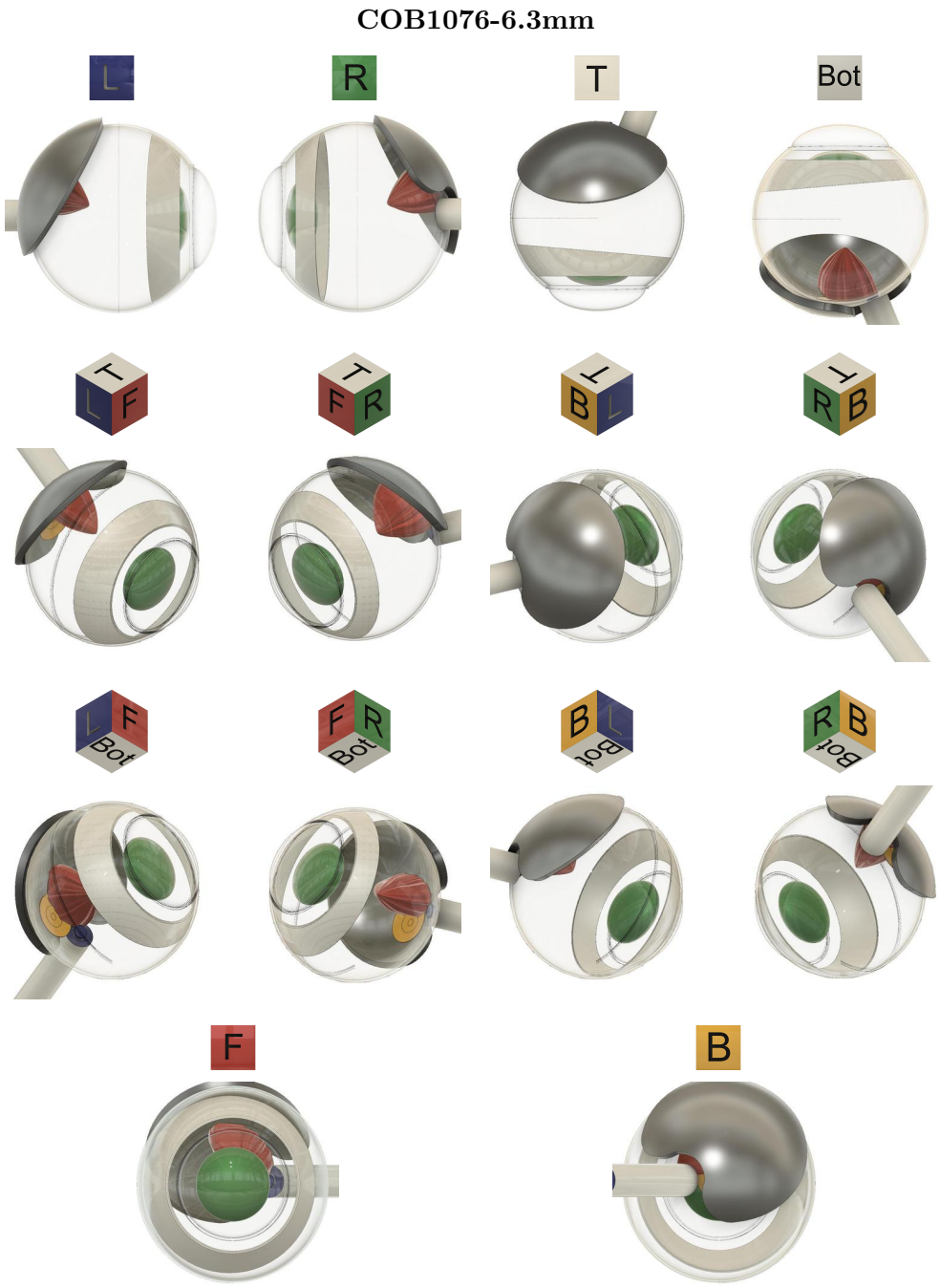

Figure A.28: Tumour shape eye model for the case COB1076-6.3mm. Each of the fourteen different views presents the tumour (red), the ^{106}Ru applicator (dark grey), the pars plana (light grey) and the lens (green) among other structures. The cube above resembles the corresponding point of view.

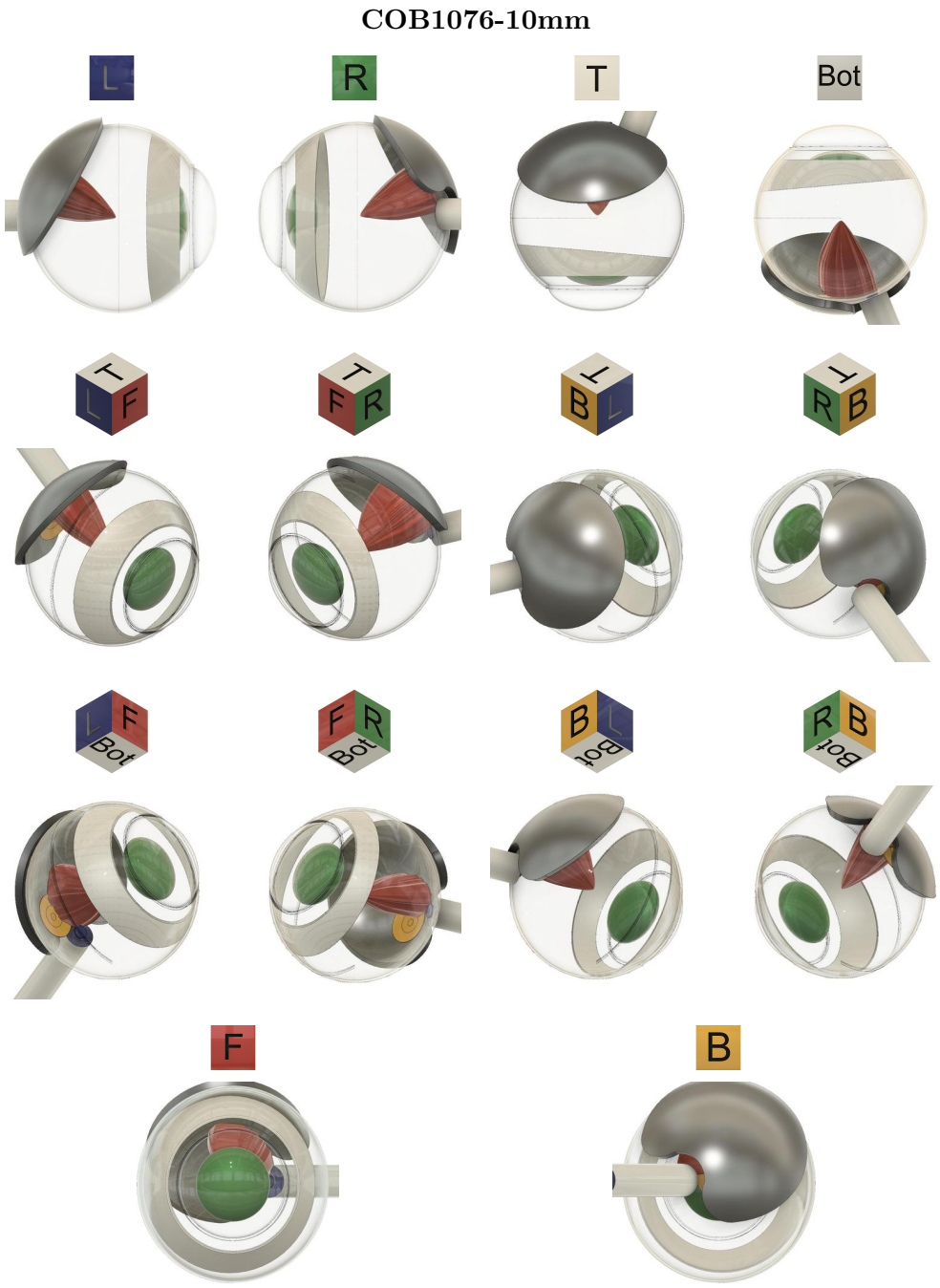

Figure A.29: Tumour shape eye model for the case COB1076-10mm. Each of the fourteen different views presents the tumour (red), the ^{106}Ru applicator (dark grey), the pars plana (light grey) and the lens (green) among other structures. The cube above resembles the corresponding point of view.

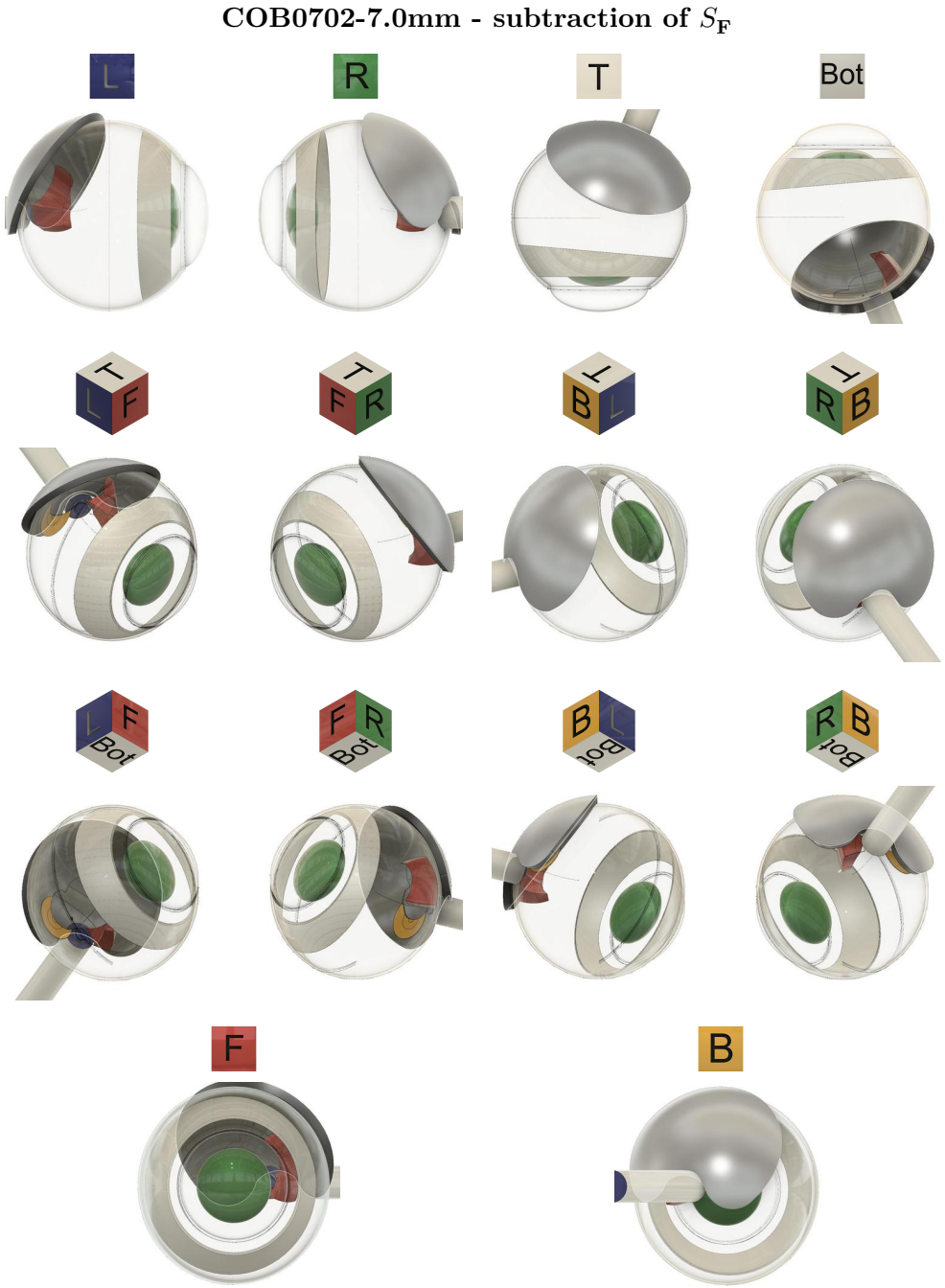

Figure A.30: Tumour shape after subtraction of the confinement with the full set of X-ray beams S_F of X-ray beams for the case COB0702-7.0mm. Each of the fourteen different views presents the tumour (red), the ^{106}Ru applicator (dark grey), the pars plana (light grey) and the lens (green) among other structures. The cube above resembles the corresponding point of view.

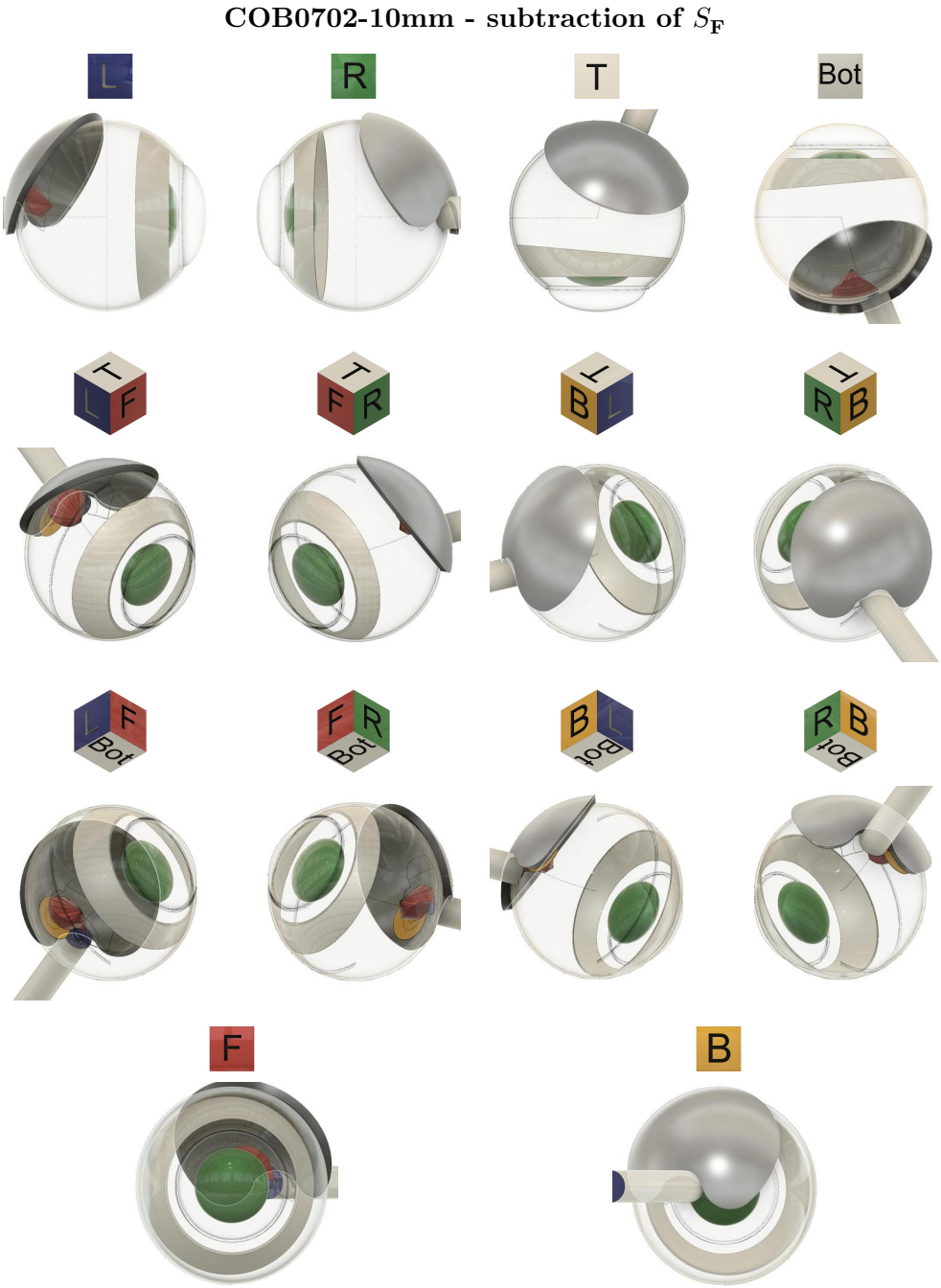

Figure A.31: Tumour shape after subtraction of the confinement with the full set of X-ray beams S_F for the case COB0702-10mm. Each of the fourteen different views presents the tumour (red), the ^{106}Ru applicator (dark grey), the pars plana (light grey) and the lens (green) among other structures. The cube above resembles the corresponding point of view.

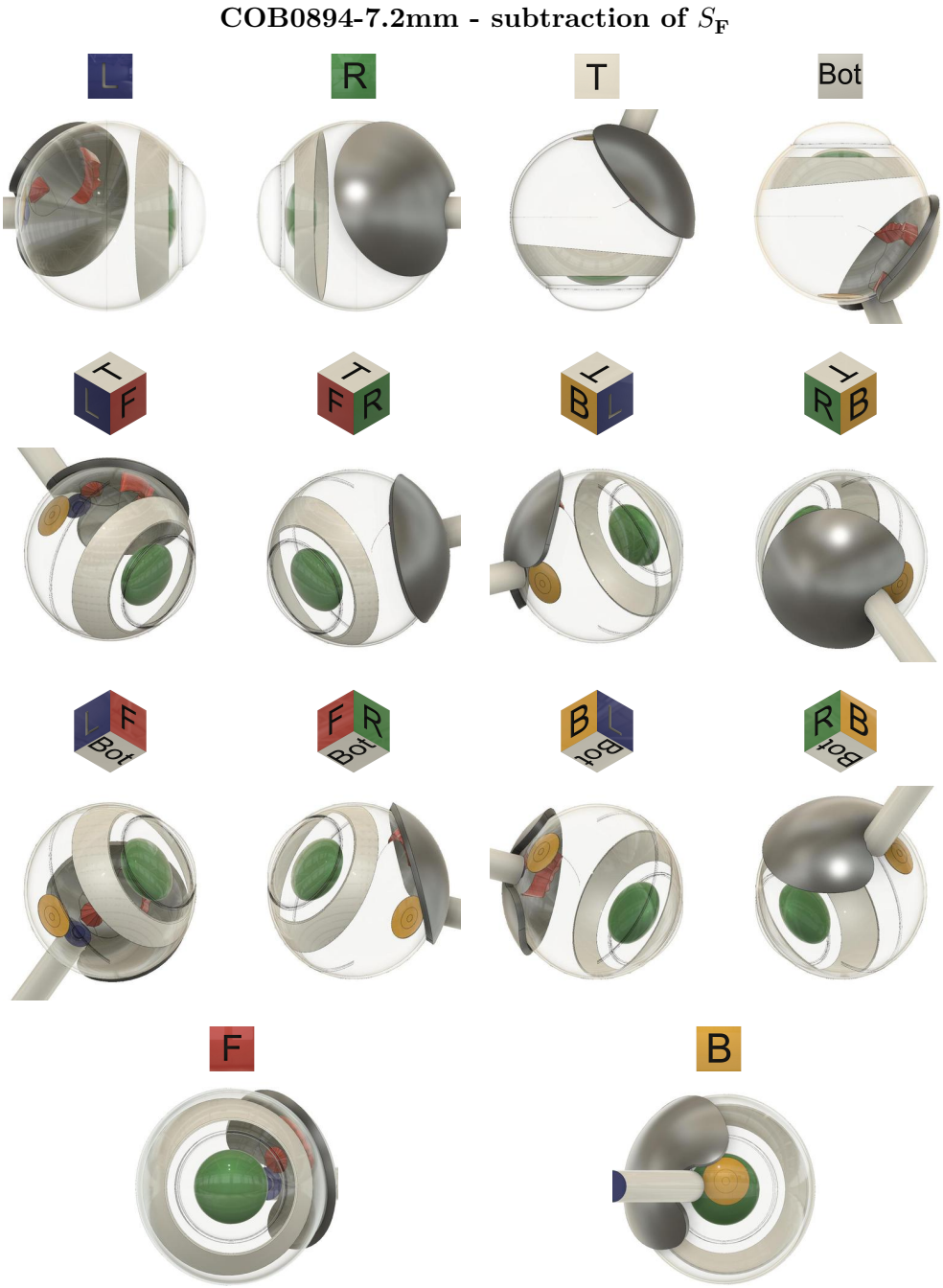

Figure A.32: Tumour shape after subtraction of the confinement with the full set of X-ray beams S_F for the case COB0894-7.2mm. Each of the fourteen different views presents the tumour (red), the ^{106}Ru applicator (dark grey), the pars plana (light grey) and the lens (green) among other structures. The cube above resembles the corresponding point of view.

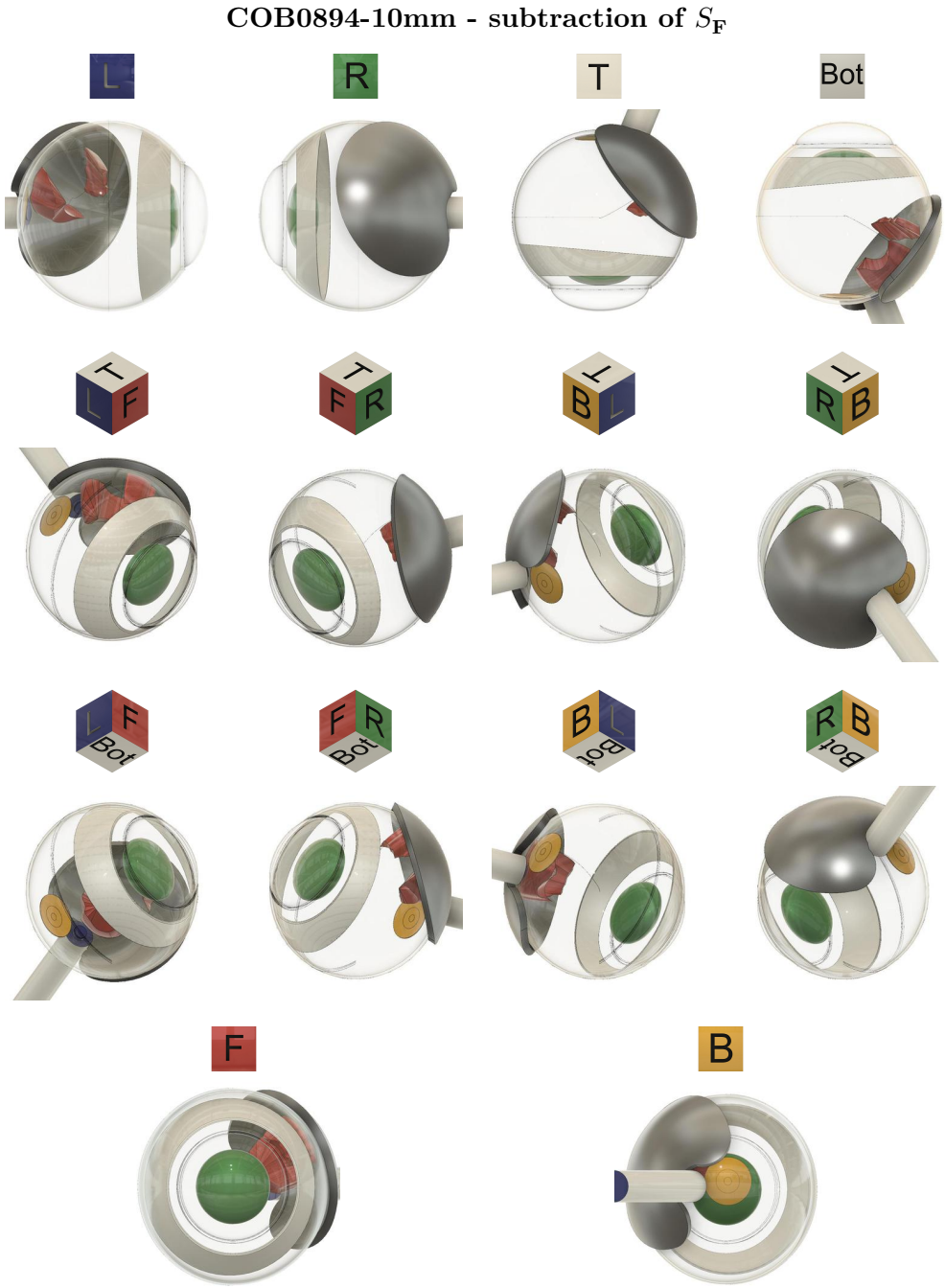

Figure A.33: Tumour shape after subtraction of the confinement with the full set of X-ray beams S_F for the case COB0894-10mm. Each of the fourteen different views presents the tumour (red), the ^{106}Ru applicator (dark grey), the pars plana (light grey) and the lens (green) among other structures. The cube above resembles the corresponding point of view.

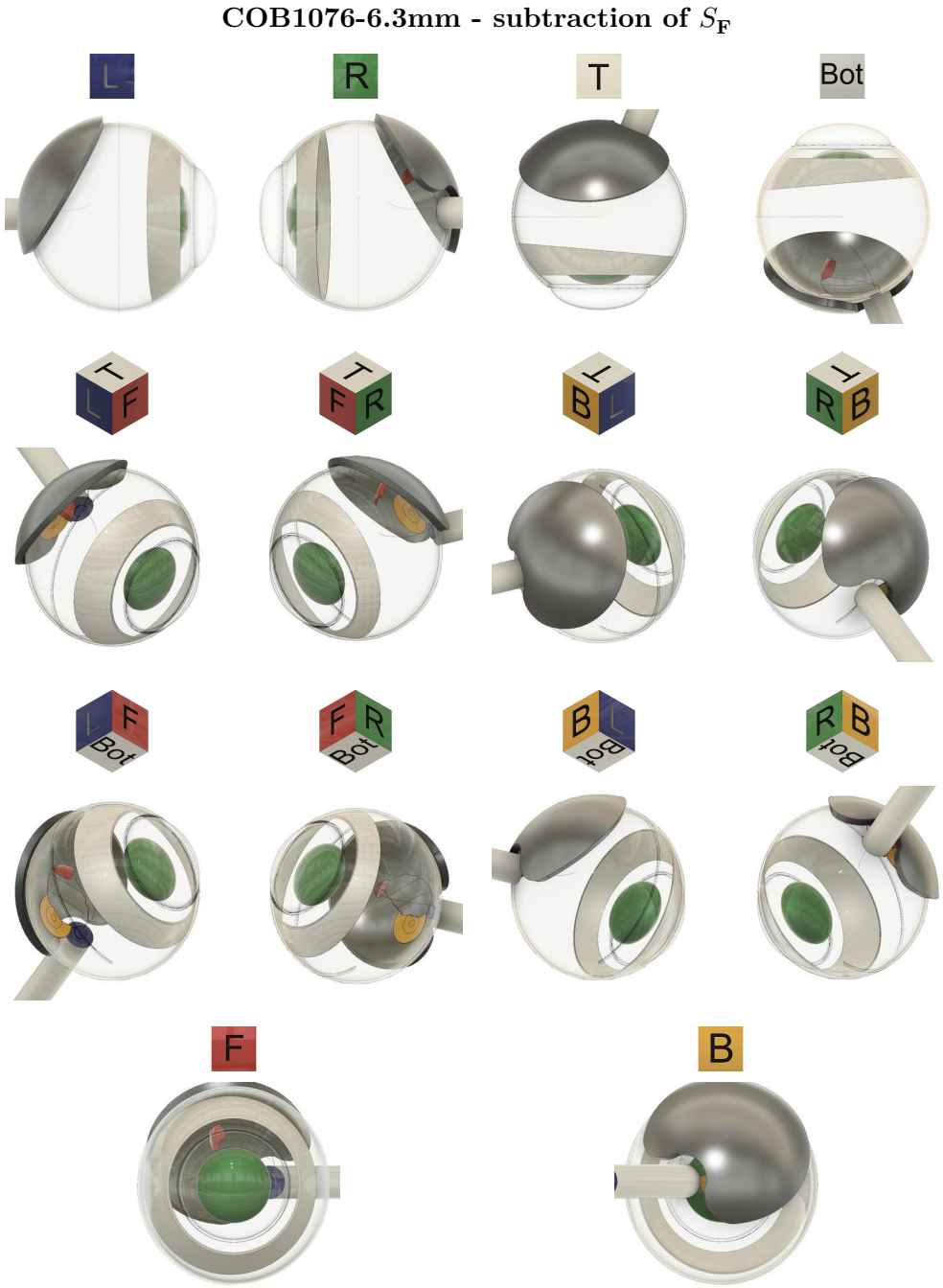

Figure A.34: Tumour shape after subtraction of the confinement with the full set of X-ray beams S_F for the case COB1076-6.3mm. Each of the fourteen different views presents the tumour (red), the ^{106}Ru applicator (dark grey), the pars plana (light grey) and the lens (green) among other structures. The cube above resembles the corresponding point of view.

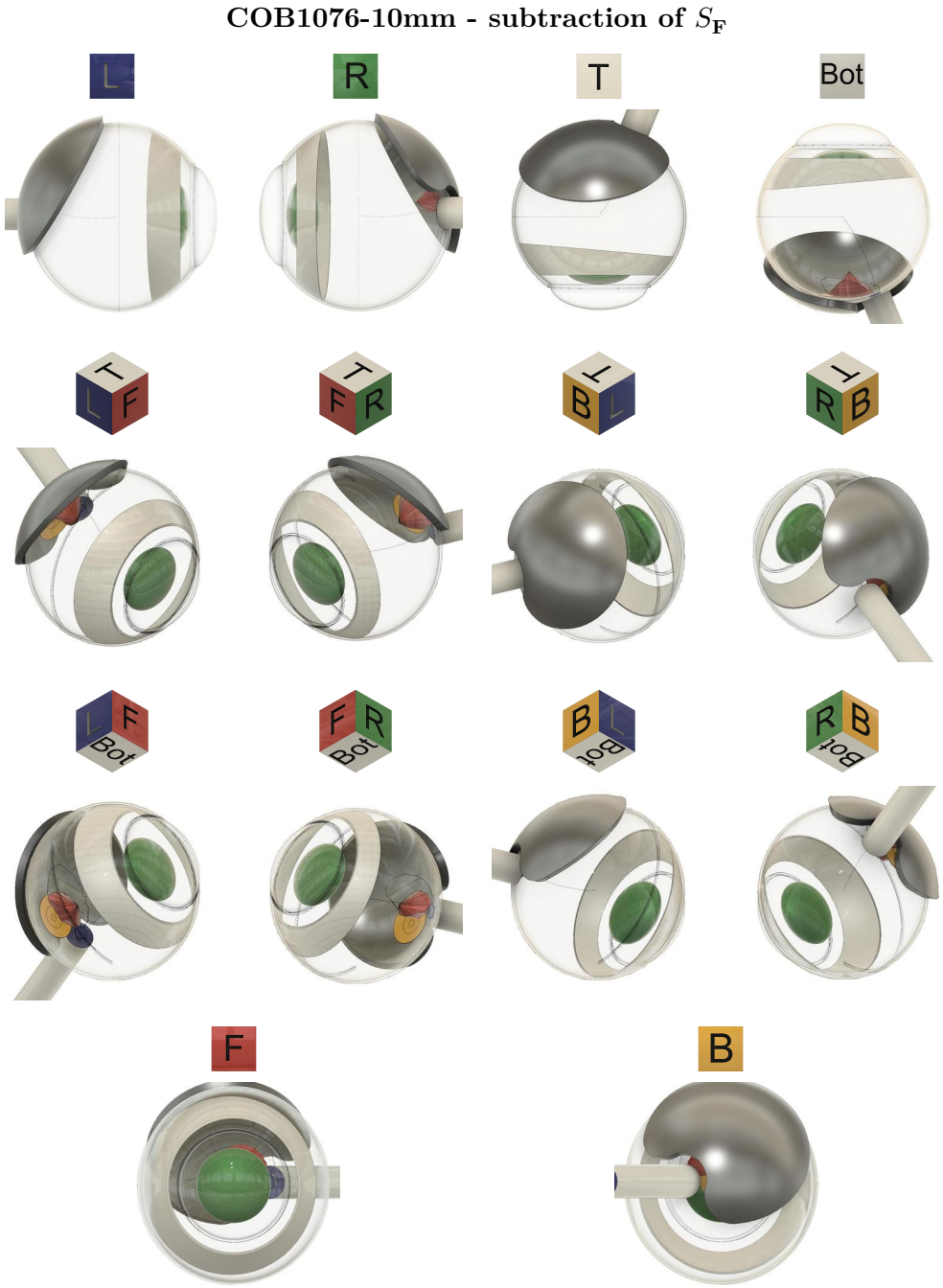

Figure A.35: Tumour shape after subtraction of the confinement with the full set of X-ray beams S_F for the case COB1076-10mm. Each of the fourteen different views presents the tumour (red), the ^{106}Ru applicator (dark grey), the pars plana (light grey) and the lens (green) among other structures. The cube above resembles the corresponding point of view.

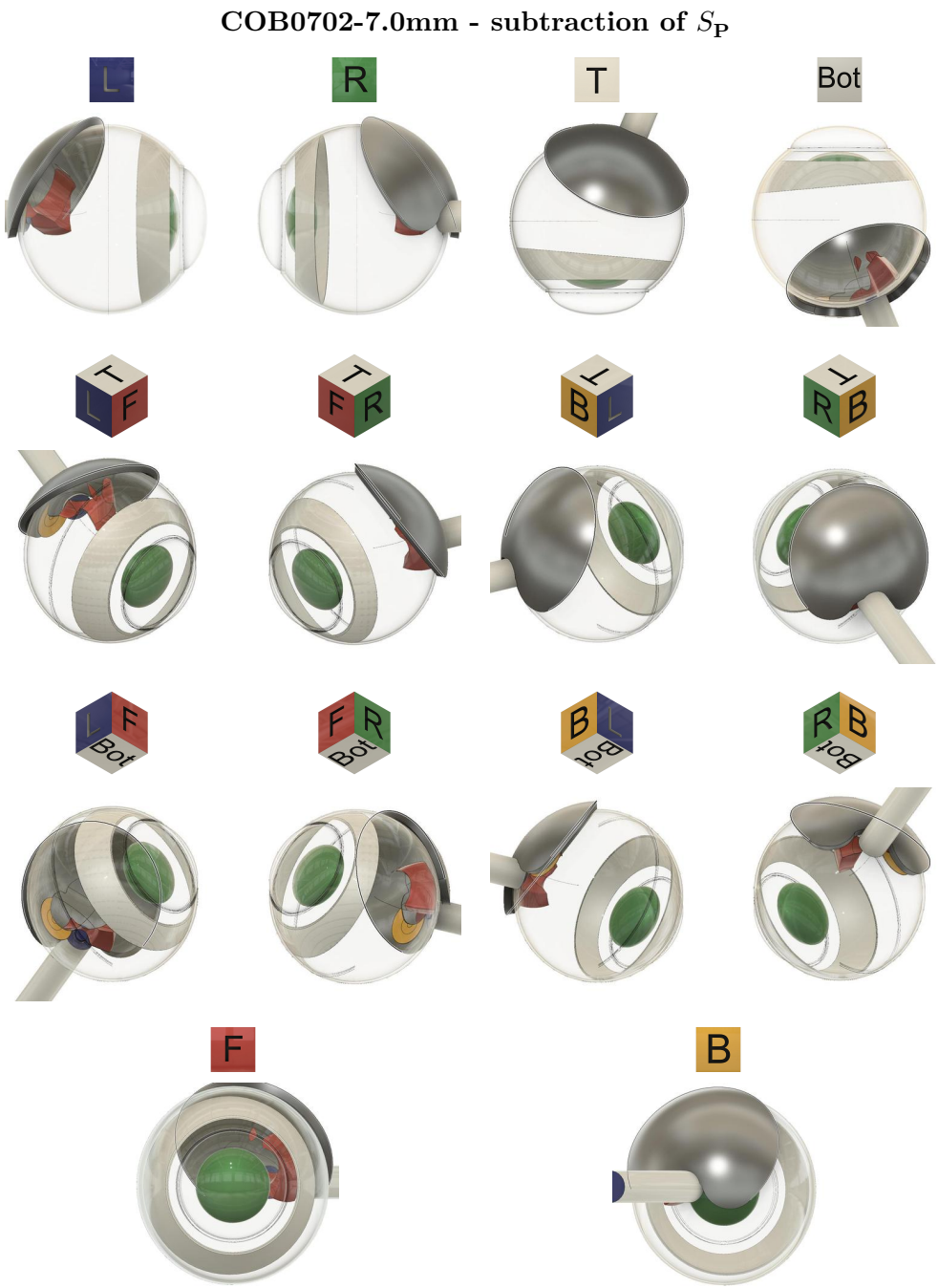

Figure A.36: Tumour shape after subtraction of the confinement with the partial set S_P of X-ray beamsfor the case COB0702-7.0mm. Each of the fourteen different views presents the tumour (red), the ^{106}Ru applicator (dark grey), the pars plana (light grey) and the lens (green) among other structures. The cube above resembles the corresponding point of view.

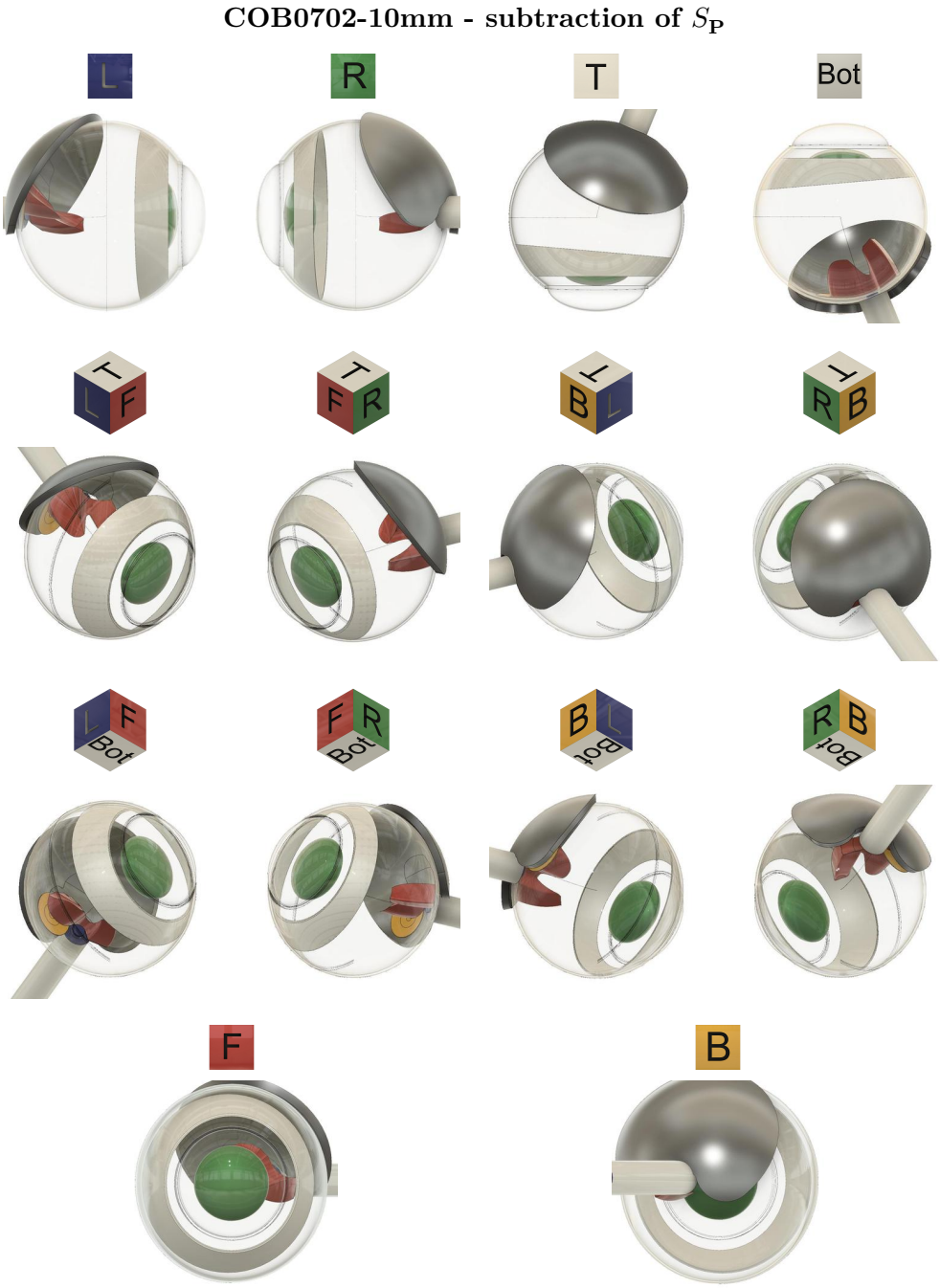

Figure A.37: Tumour shape after subtraction of the confinement with the partial set S_P of X-ray beamsfor the case COB0702-10mm. Each of the fourteen different views presents the tumour (red), the ^{106}Ru applicator (dark grey), the pars plana (light grey) and the lens (green) among other structures. The cube above resembles the corresponding point of view.

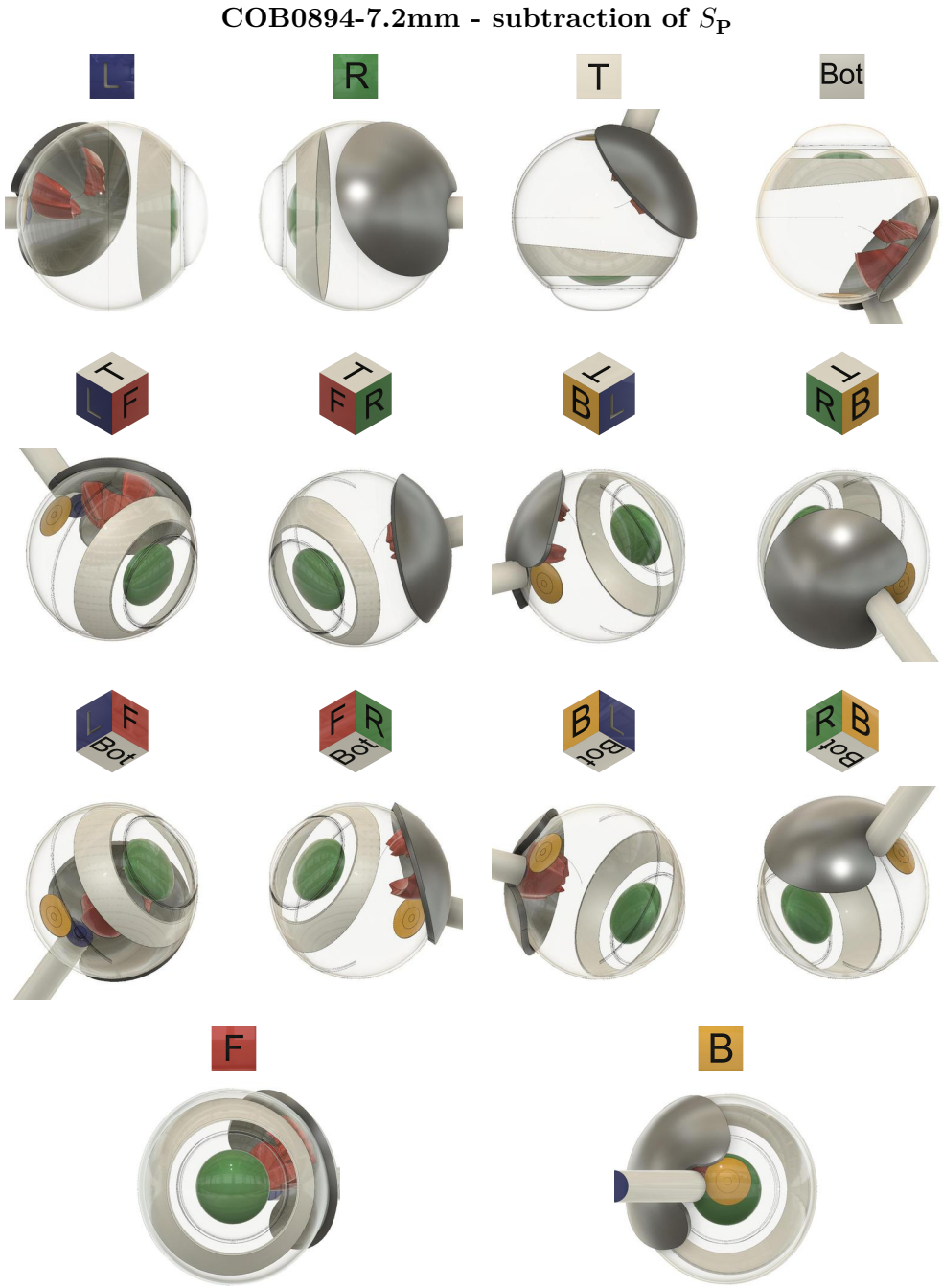

Figure A.38: Tumour shape after subtraction of the confinement with the partial set S_P of X-ray beamsfor the case COB0894-7.2mm. Each of the fourteen different views presents the tumour (red), the ^{106}Ru applicator (dark grey), the pars plana (light grey) and the lens (green) among other structures. The cube above resembles the corresponding point of view.

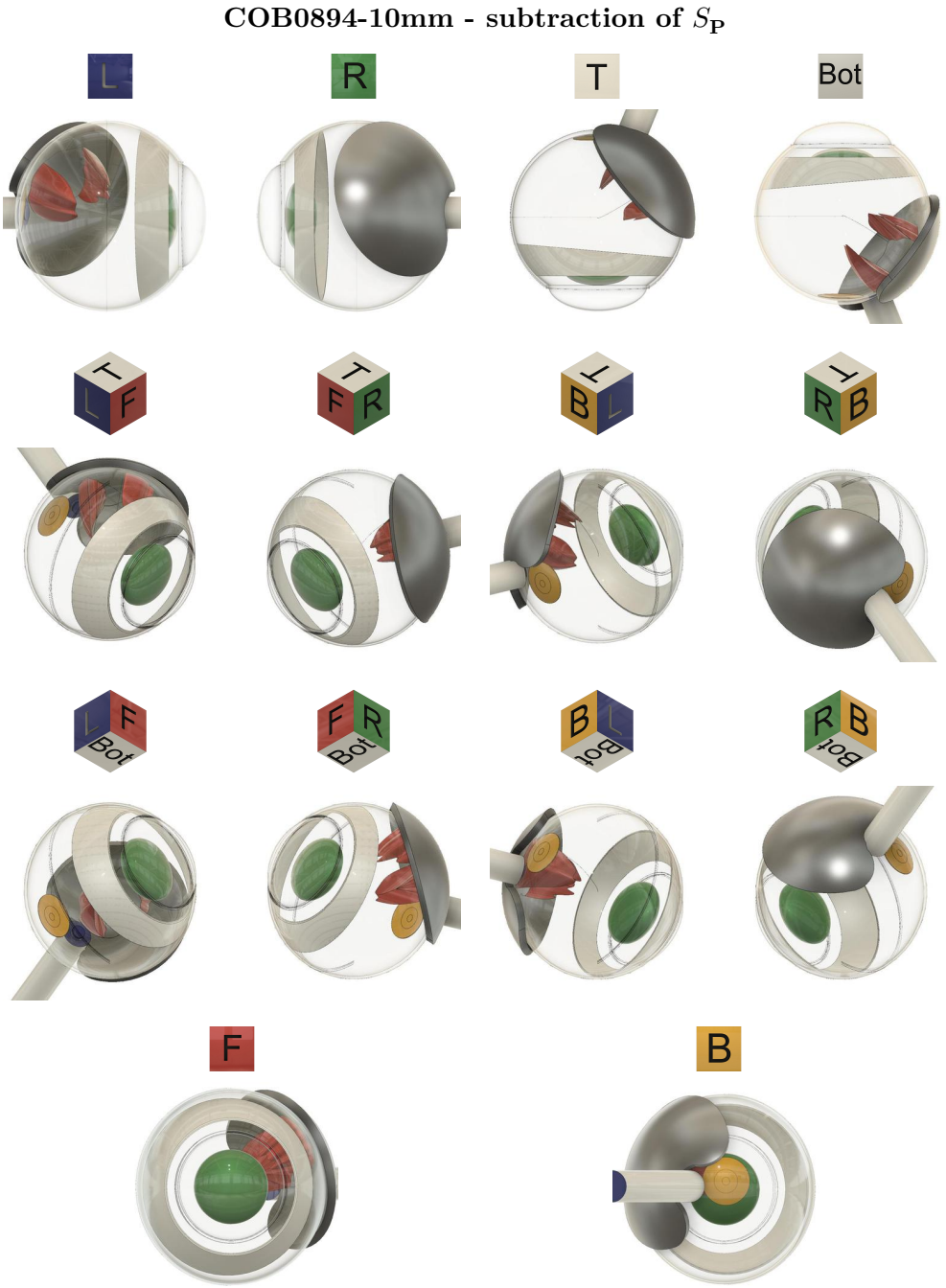

Figure A.39: Tumour shape after subtraction of the confinement with the partial set S_P of X-ray beamsfor the case COB0894-10mm. Each of the fourteen different views presents the tumour (red), the ^{106}Ru applicator (dark grey), the pars plana (light grey) and the lens (green) among other structures. The cube above resembles the corresponding point of view.

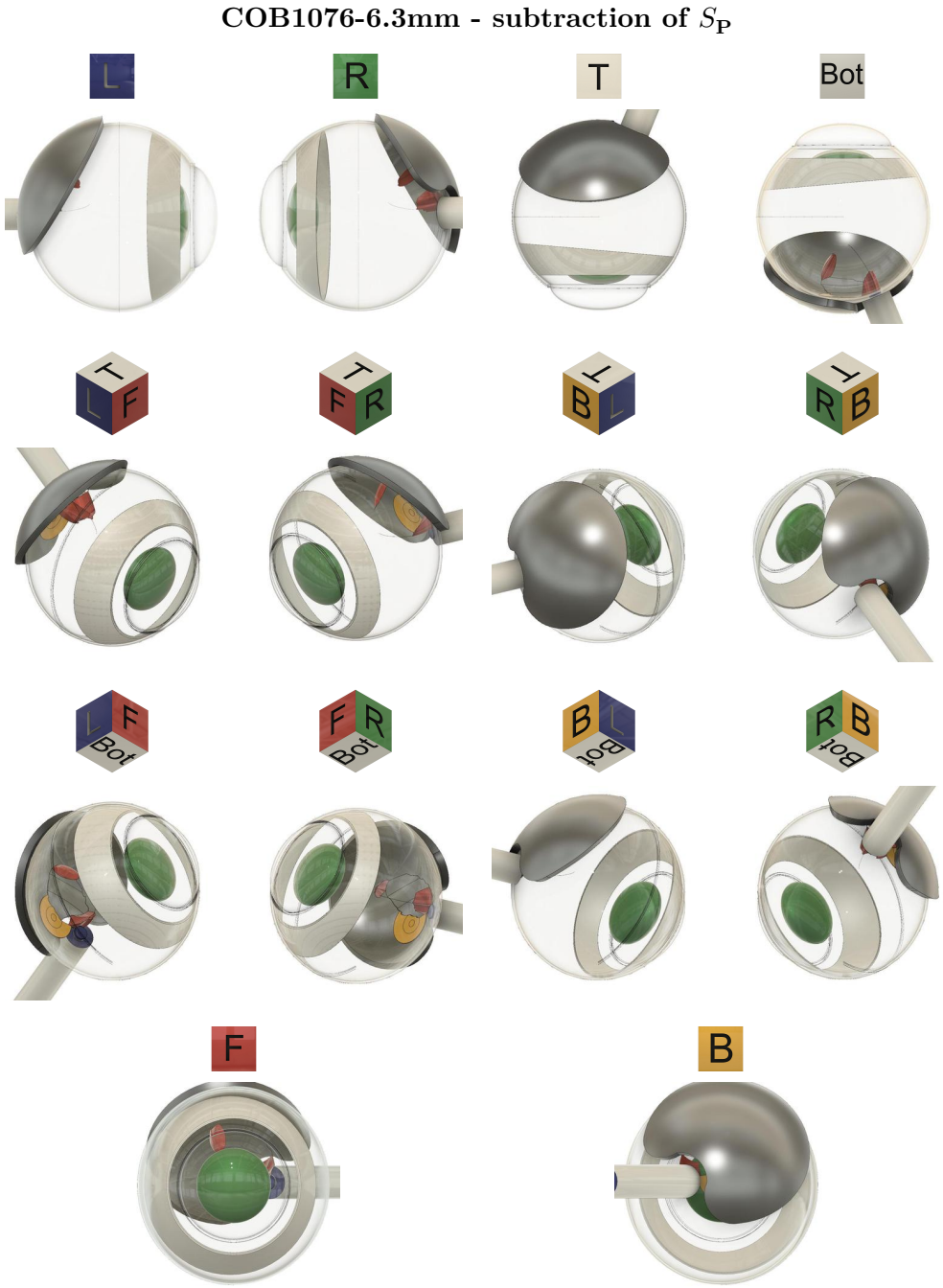

Figure A.40: Tumour shape after subtraction of the confinement with the partial set S_P of X-ray beamsfor the case COB1076-6.3mm. Each of the fourteen different views presents the tumour (red), the ^{106}Ru applicator (dark grey), the pars plana (light grey) and the lens (green) among other structures. The cube above resembles the corresponding point of view.

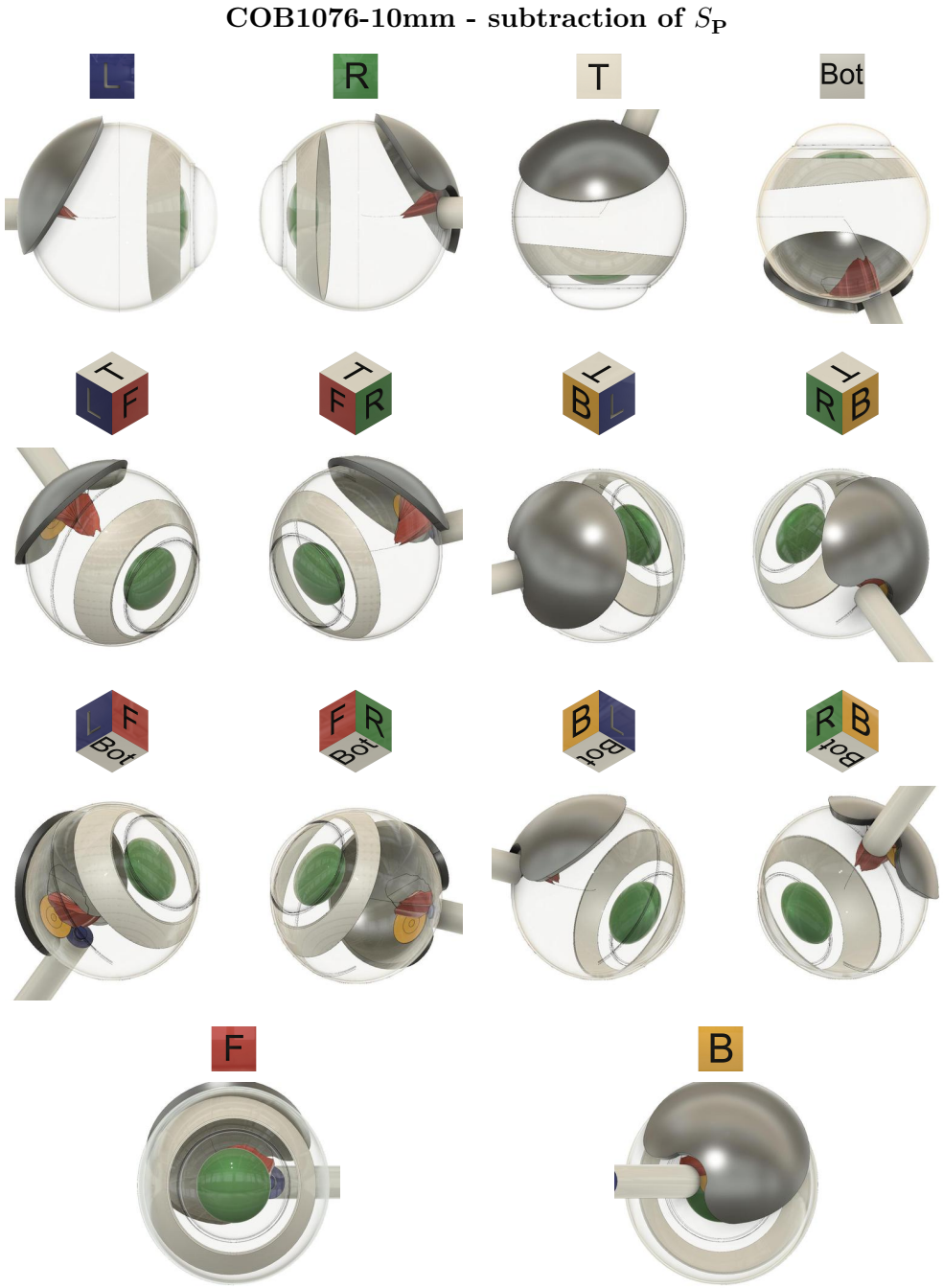

Figure A.41: Tumour shape after subtraction of the confinement with the partial set S_P of X-ray beamsfor the case COB1076-10mm. Each of the fourteen different views presents the tumour (red), the ^{106}Ru applicator (dark grey), the pars plana (light grey) and the lens (green) among other structures. The cube above resembles the corresponding point of view.

A.7 Dose volume histograms

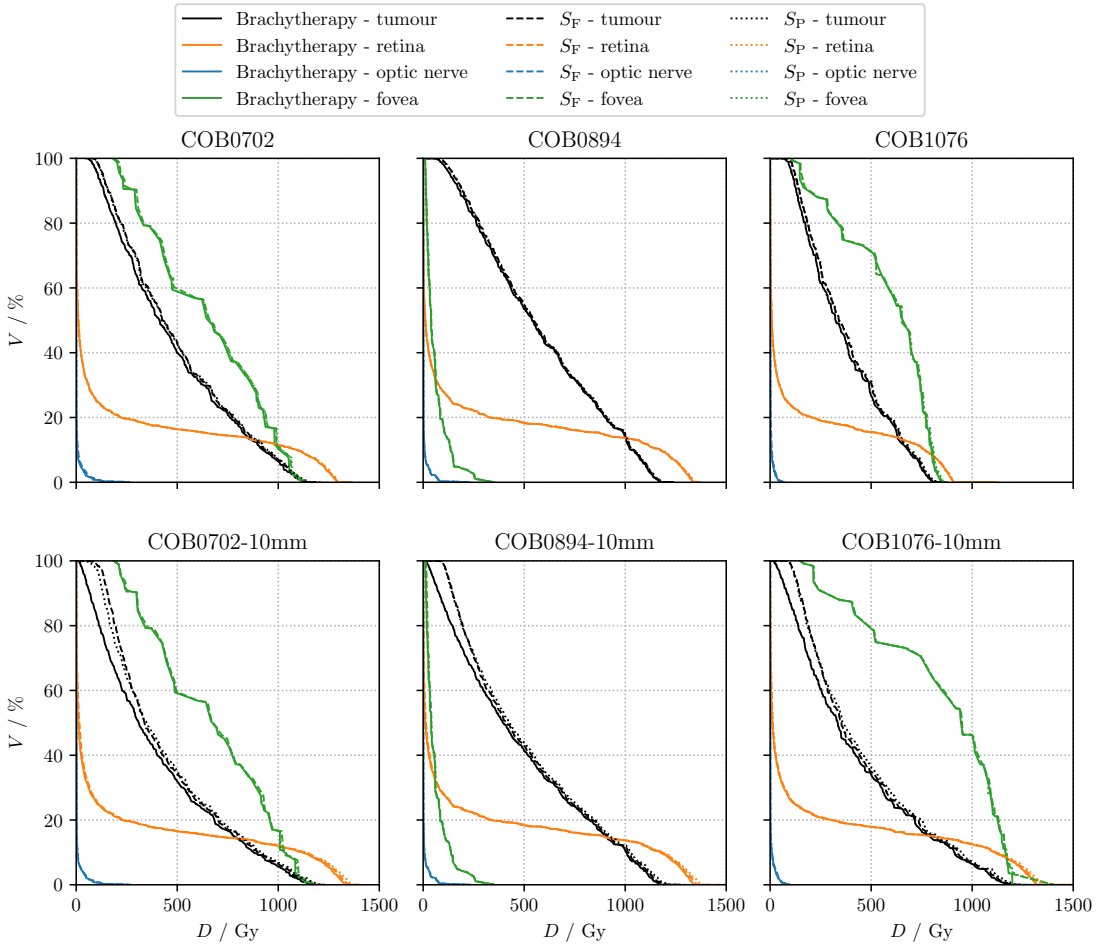

Figure A.42: DVHs of the most important structures for the combined therapy concept in comparison to stand-alone brachytherapy. The visualisation includes the results for the full sets S_F and partial sets S_P of X-ray beams. For each case, the modalities are weighted with the corresponding weights listed in tables 7.2, 7.4 and 7.5. The DVHs with a focus on the dose range of 0 to 150 Gy are presented in figure A.43 and with logarithmically scaled axes in figure 7.12.

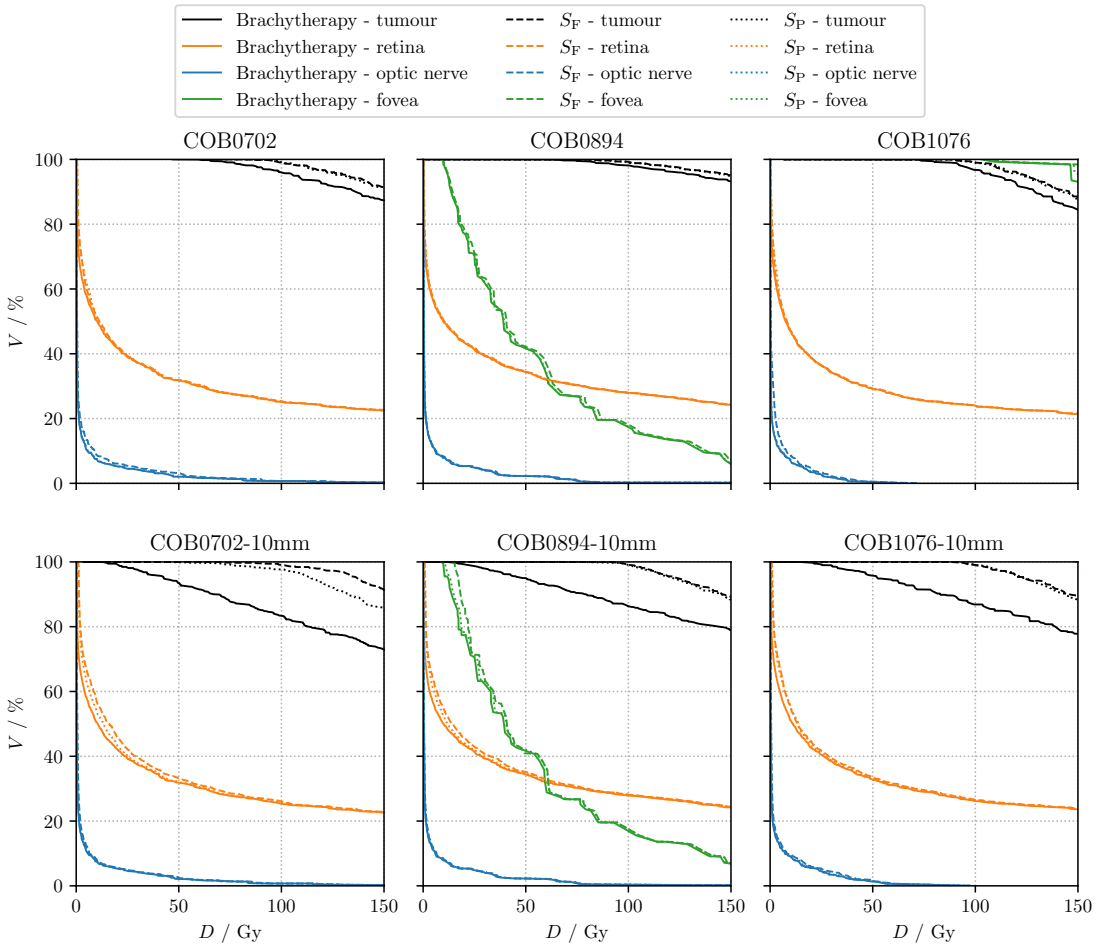

Figure A.43: DVHs of the most important structures for the combined therapy concept in comparison to stand-alone brachytherapy. The visualisation includes the results for the full sets S_F and partial sets S_P of X-rays. For each case, the modalities are weighted with the corresponding weights listed in tables 7.2, 7.4 and 7.5. The visualisation is limited to a dose of 150 Gy, refer to figure A.42 for the full range of dose.

A.8 List of DIN standards

Table A.10: List of the most important DIN standards for the combined therapy concept.

Number	Ref.	Title
DIN 54113-1	[217]	Non-destructive testing - Radiation protection rules for the technical application of X-ray equipment up to 1MV - Part 1: Technical safety requirements and testing for the manufacture, installation and operation
DIN 54113-3	[218]	Non-destructive testing - Radiation protection rules for the technical application of X-ray equipment up to 1 MV - Part 3: Formulas and diagrams for the calculation of radiation protection for X-ray equipment up to 600 kV
DIN 6814-8	[219]	Terms in the field of radiological technique - Part 8: Radiotherapy
DIN 6812	[220]	Medical X-ray equipment up to 300 kV - Rules of construction for structural radiation protection
DIN 6815	[221]	Medical X-ray equipment up to 300 kV - Rules for testing of radiation protection after installation, maintenance and essential modification
DIN 6827-1	[222]	Recording in medical application of ionizing radiation - Part 1: Therapy with electron accelerators as well as X-ray and gamma-ray therapy systems
DIN 6827-3	[223]	Recording in medical application of ionizing radiation - Part 3: Brachytherapy with enclosed radiation sources
DIN 6809-1	[224]	Clinical dosimetry - Part 1: Radiation quality of photon and electron radiation
DIN 6809-4	[225]	Clinical dosimetry - Part 4: X-ray therapy with X-ray tube voltages between 10 kV and 300 kV
DIN 6809-8	[226]	Clinical dosimetry - Part 8: Dosimetry of small photon fields
DIN 6846-2	[227]	Medical teletherapy systems with gamma-emitting sources -Part 2: Radiation safety requirements for installation
DIN 6873	[228]	Radiotherapy treatment planning systems
DIN 60601-2-8	[229]	Medical electrical equipment – Part 2-8: Particular requirements for the basic safety and essential performance of therapeutic X-ray equipment operating in the range 10 kV to 1 MV

List of Figures

List of Tables

Bibliography

[1] B. R. Straatsma et al., *Mortality after deferral of treatment or no treatment for choroidal melanoma*, 'American Journal of Ophthalmology', vol. 136, no. 1, pp. 47–54, Jul. 2003. DOI: 10.1016/S0002-9394(02)02270-5.

[2] D. Flühs et al., *The design and the dosimetry of bi-nuclide radioactive ophthalmic applicators*, 'Medical Physics', vol. 31, no. 6, pp. 1481–1488, 2004. DOI: 10.1118/1.1755471.

[3] D. Flühs and A. Förster, Universitätsklinikum Essen, Essen, Germany, *Personal communication*, 13th Jan. 2023.

[4] K. Eibl-Lindner et al., *Robotic radiosurgery for the treatment of medium and large uveal melanoma*, 'Melanoma Research', vol. 26, no. 1, pp. 51–57, Feb. 2016. DOI: 10.1097/CMR.0000000000000199.

[5] V. Schmelter et al., *Local recurrence in choroidal melanomas following robotic-assisted radiosurgery (CyberKnife)*, 'Ocular Oncology and Pathology', vol. 8, no. 4-6, pp. 221–229, 2022. DOI: 10.1159/000527915.

[6] V. Schmelter et al., *Robotic CyberKnife radiosurgery for small choroidal melanomas*, 'Melanoma Research', vol. 32, no. 3, pp. 192–199, Apr. 2022. DOI: 10.1097/CMR.0000000000000823.

[7] P. V. Foti et al., *Diagnostic methods and therapeutic options of uveal melanoma with emphasis on MR imaging—part II: Treatment indications and complications*, 'Insights into Imaging', vol. 12, no. 1, Jun. 2021. DOI: 10.1186/s13244-021-01001-w.

[8] B. Tarlan and H. Kıratlı, *Uveal melanoma: Current trends in diagnosis and management*, 'Turkish Journal for Ophtalmology', vol. 46, no. 3, pp. 123–137, 2016, PMID: 27800275. DOI: 10.4274/tjo.37431.

[9] L. Desjardins et al., 'Treatment of uveal melanoma by accelerated proton beam', in *Current Concepts in Uveal Melanoma*, S. Karger AG, Oct. 2011, pp. 41–57. DOI: 10.1159/000328257.

[10] H. Paganetti, *Proton therapy physics* (Series in medical physics and biomedical engineering). Boca Raton, FL: CRC Press, 2012, ISBN: 9781439836446.

[11] I. Seibel et al., *Local recurrence after primary proton beam therapy in uveal melanoma: Risk factors, retreatment approaches, and outcome*, 'American Journal of Ophthalmology', vol. 160, no. 4, pp. 628–636, 2015, ISSN: 0002-9394. DOI: 10.1016/j.ajo.2015.06.017.

[12] E. Fleury et al., *Improving organs-at-risk sparing for choroidal melanoma patients: A CT-based two-beam strategy in ocular proton therapy with a dedicated eyeline*, 'Radiotherapy and Oncology', vol. 171, pp. 173–181, Jun. 2022. DOI: 10.1016/j.radonc.2022.04.021.

[13] Collaborative Ocular Melanoma Study Group, *Collaborative ocular melanoma study (coms)*, NCT Number: NCT00000124. Study Sponsor: National Eye Institute (NEI)., 1986.

[14] The American Brachytherapy Society - Ophthalmic Oncology Task Force - E. Simpson et. al., *The american brachytherapy society consensus guidelines for plaque brachytherapy of uveal melanoma and retinoblastoma*, 'Brachytherapy', vol. 13, pp. 1–14, 2014. DOI: 10.1016/j.brachy.2013.11.008.

[15] M.-M. Bé et al., *Table of Radionuclides* (Monographie BIPM-5). Pavillon de Breteuil, F-92310 Sèvres, France: Bureau International des Poids et Mesures, 2016, vol. 8, ISBN: 978-92-822-2264-5.

[16] E. Stöckel et al., *Dose distributions and treatment margins in ocular brachytherapy with 106ru eye plaques*, 'Ocular Onthology and Pathology', vol. 4, pp. 122–128, 16th Sep. 2017. DOI: 10.1159/000479558.

[17] L. Tagliaferri et al., *Uveal melanoma*, 'The GEC ESTRO handbook of brachytherapy', 15th Apr. 2020.

[18] E. Sokolenko, *Retrospektive analyse einer dosisverteilung, dosisbezogene komplikationen und quantifizierung der ergebnisse einer brachytherapie mit ruthenium-applikatoren (rh-106) bei posterior gelegenen aderhautmelanomen.* Universität Duisburg-Essen, 2022. DOI: 10.17185/duepublico/76400.

[19] M. Guberina et al., *Optic neuropathy and radiation dose relationship – definition of dosethreshold values after brachytherapy for malignant eye tumors, Manuscript in preparation*, 2023.

[20] F. Grehn, *Augenheilkunde*. Springer Berlin Heidelberg, 2012. DOI: 10.1007/978-3-642-11333-8.

[21] G. K. Lang, *Augenheilkunde*. Georg Thieme Verlag, 20th Mar. 2019, ISBN: 3132426253.

[22] U. Kellner et al., *Atlas des Augenhintergrundes*. Georg Thieme Verlag, 15th Oct. 2021, 516 pp., ISBN: 313146352X. [Online]. Available: https://www.ebook.de/de/product/30014449/atlas_des_augenhintergrundes.html.

[23] G. Virgili et al., *Incidence of uveal melanoma in europe*, 'Ophthalmology', vol. 114, no. 12, pp. 2309–2315, Dec. 2007. DOI: 10.1016/j.ophtha.2007.01.032.

[24] Talos. *Anatomie des auges*. Wikimedia, Ed. (28th Jul. 2005), [Online]. Available: https://commons.wikimedia.org/wiki/File:Auge.png.

[25] R. C. Eagle, *The pathology of ocular cancer*, 'Eye', vol. 27, no. 2, pp. 128–136, Nov. 2012. DOI: 10.1038/eye.2012.237.

[26] N. Bornfeld et al., *The interdisciplinary diagnosis and treatment of intraocular tumors*, 'Deutsches Ärzteblatt international', vol. 115, no. 7, pp. 106–111, Feb. 2018. DOI: 10.3238/arztebl.2018.0106.

[27] S. Kaliki and C. L. Shields, *Uveal melanoma: Relatively rare but deadly cancer*, 'Eye', vol. 31, no. 2, pp. 241–257, Dec. 2016. DOI: 10.1038/eye.2016.275.

[28] C. L. Shields, *Metastasis of uveal melanoma millimeter-by-millimeter in 8033 consecutive eyes*, 'Archives of Ophthalmology', vol. 127, no. 8, p. 989, Aug. 2009. DOI: 10.1001/archophthalmol.2009.208.

[29] A. O. Schüler and N. Bornfeld, *Aktuelle therapieaspekte intraokularer tumoren*, 'Der Ophtalmologe', vol. 97, pp. 207–222, 2000. DOI: 10.1007/s003470050516.

[30] T. Grasbon et al., *3d-ultraschall*, 'Der Ophthalmologe', vol. 98, no. 1, pp. 88–93, Jan. 2001. DOI: 10.1007/s003470170206.

[31] B. Damato et al., *Local tumor control after 106ru brachytherapy of choroidal melanoma*, 'International Journal of Radiation Oncology - Biology - Physics', vol. 63, no. 2, pp. 385–391, 2005, ISSN: 0360-3016. DOI: 10.1016/j.ijrobp.2005.02.017.

[32] L. M. Heindl et al., *Hochdosisbrachytherapie des malignen aderhaut- und ziliarkörpermelanoms mit 106ruthenium*, 'Der Ophthalmologe', vol. 104, no. 2, pp. 149–157, Feb. 2007. DOI: 10.1007/s00347-006-1451-3.

[33] A. Böker et al., *Neoadjuvant proton beam irradiation vs. adjuvant ruthenium brachytherapy in transscleral resection of uveal melanoma*, 'Graefe's Archive for Clinical and Experimental Ophthalmology', vol. 256, no. 9, pp. 1767–1775, Jun. 2018. DOI: 10.1007/s00417-018-4032-7.

[34] L. Tarmann et al., *Ruthenium-106 plaque brachytherapy for uveal melanoma*, 'British Journal of Ophthalmology', vol. 99, no. 12, pp. 1644–1649, May 2015. DOI: 10.1136/bjophthalmol-2015-306666.

[35] B. Damato, *Progress in the management of patients with uveal melanoma. the 2012 ashton lecture*, 'Eye', vol. 26, no. 9, pp. 1157–1172, Jun. 2012. DOI: 10.1038/eye.2012.126.

[36] L. Jabbarli et al., 'Prognostic factors for surgical treatment of radiation-induced scleral necrosis after brachytherapy for uveal melanoma', Oct. 2022. DOI: 10.21203/rs.3.rs-1843226/v1.

[37] C. Espensen et al., *Predicting visual acuity deterioration and radiation-induced toxicities after brachytherapy for choroidal melanomas*, 'Cancers', vol. 11, p. 1124, Aug. 2019. DOI: 10.3390/cancers11081124.

[38] N. Kaiserman et al., *Ruthenium-106 plaque brachytherapy for thick posterior uveal melanomas*, 'British Journal of Ophthalmology', vol. 93, no. 9, pp. 1167–1171, 2009, ISSN: 0007-1161. DOI: 10.1136/bjo.2009.157701.

[39] R. Pötter et al., *Ruthenium-106 eye plaque brachytherapy in the conservative treatment of uveal melanoma: Evaluation of 175 patients treated with 150 gy from 1981-1989*, 'Frontiers of Radiation Therapy and Oncology', pp. 143–149, 1997. DOI: 10.1159/000425697.

[40] B. Emami, *Tolerance of normal tissue to therapeutic radiation*, 'Reports of radiotherapy and Oncology', vol. 1, no. 1, pp. 123–130, 2013.

[41] M. Stroth, *Untersuchungen zur Kombination von Brachy- und Röntgentherapie zur Behandlung von Augentumoren*, Supervised by Henning Manke, Masterthesis, TU Dortmund, 13th Sep. 2022.

[42] A. Takeda et al., *Late retinal complications of radiation therapy for nasal and paranasal malignancies: Relationship between irradiated-dose area and severity*, 'International Journal of Radiation Oncology∗Biology∗Physics', vol. 44, no. 3, pp. 599–605, Jun. 1999. DOI: 10.1016/S0360-3016(99)00057-7.

[43] J. M. Henk et al., *Radiation dose to the lens and cataract formation*, 'International Journal of Radiation Oncology - Biology - Physics', vol. 25, no. 5, pp. 815–820, Apr. 1993. DOI: 10.1016/0360-3016(93)90310-r.

[44] B. E. Damato, 'Local resection of uveal melanoma', in *Current Concepts in Uveal Melanoma*, S. Karger AG, Oct. 2011, pp. 66–80. DOI: 10.1159/000328261.

[45] L. Konstantinidis et al., *Trans-scleral local resection of toxic choroidal melanoma after proton beam radiotherapy*, 'British Journal of Ophthalmology', vol. 98, no. 6, pp. 775–779, 2014, ISSN: 0007-1161. DOI: 10.1136/bjophthalmol-2013-304501.

[46] K. Gündüz and N. E. Bechrakis, *Exoresection and endoresection for uveal melanoma*, 'Middle East African journal of ophthalmology', vol. 17, no. 3, pp. 210–216, Jul. 2010, PMID: 20844676. DOI: 10.4103/0974-9233.65494.

[47] J. M. Mor et al., *CyberKnife®: Eine neue therapieoption bei uvealem melanom*, 'Der Ophthalmologe', vol. 115, no. 4, pp. 302–308, Aug. 2017. DOI: 10.1007/s00347-017-0560-5.

[48] C. Mazzini et al., *Clinical outcomes and secondary glaucoma after gamma-knife radiosurgery and ruthenium-106 brachytherapy for uveal melanoma: A single institution experience*, 'Melanoma Research', vol. 31, no. 1, pp. 38–48, Aug. 2020. DOI: 10.1097/CMR.0000000000000689.

[49] Particle Therapy Co-Operative Group (PTCOG). *Particle therapy facilities in clinical operation*. (Jan. 2023), [Online]. Available: https://www.ptcog.site/index.php/facilities-in-operation-public (visited on 10th Feb. 2023).

[50] B. Damato et al., *Proton beam radiotherapy of uveal melanoma*, 'Saudi Journal of Ophthalmology', vol. 27, no. 3, pp. 151–157, 2013, ISSN: 1319-4534. DOI: 10.1016/j.sjopt.2013.06.014.

[51] K. K. Mishra et al., *Practice considerations for proton beam radiation therapy of uveal melanoma during the coronavirus disease pandemic: Particle therapy cooperative group ocular experience*, 'Advances in Radiation Oncology', vol. 5, no. 4, pp. 682–686, Jul. 2020. DOI: 10.1016/j.adro.2020.04.010.

[52] B. Damato et al., *Proton beam radiotherapy of choroidal melanoma: The liverpool-clatterbridge experience*, 'International Journal of Radiation Oncology - Biology - Physics', vol. 62, no. 5, pp. 1405–1411, Aug. 2005. DOI: 10.1016/j.ijrobp.2005.01.016.

[53] J. Hrbacek et al., *Practice patterns analysis of ocular proton therapy centers: The international optic survey*, 'International Journal of Radiation Oncology - Biology - Physics', vol. 95, no. 1, pp. 336–343, May 2016. DOI: 10.1016/j.ijrobp.2016.01.040.

[54] M. Cianchetti and M. Amichetti, *Sinonasal malignancies and charged particle radiation treatment: A systematic literature review*, 'International Journal of Otolaryngology', vol. 2012, pp. 1–15, 2012. DOI: 10.1155/2012/325891.

[55] H. Paganetti et al., *Relative biological effectiveness (RBE) values for proton beam therapy*, 'International Journal of Radiation Oncology - Biology - Physics', vol. 53, no. 2, pp. 407–421, Jun. 2002. DOI: 10.1016/S0360-3016(02)02754-2.

[56] Eckert & Ziegler BEBIG GmbH, *Damato ruthenium plaque templates*, Tech. Rep. P13D142/Rev.01, Jun. 2022.

[57] B. Damato, *Therapeutic modalities for uveal melanoma and retinoblastoma: Pros and cons*, Eckert & Ziegler BEBIG GmbH, Ed., White Paper. [Online]. Available: https://medical.ezag.com/wp-content/uploads/2023/03/White-Paper-UM-and-RB-Therapy-V4_UPLOAD.pdf (visited on 24th Apr. 2023).

[58] J. Pe'er, *Ruthenium-106 brachytherapy*, 'Developments in Ophthalmology', vol. 49, pp. 27–40, 2012, PMID: 22042011. DOI: 10.1159/000328254.

[59] M. Ebenau, *Entwicklung eines binuklidapplikators für die brachytherapie von augentumoren und untersuchungen zur dosimetrie von augenapplikatoren*, de, Ph.D. dissertation, Dec. 2017. DOI: 10.17877/DE290R-19129.

[60] M. Foerster et al., *Die behandlung von malignen melanomen der uvea mit 106-ruthenium-applikatoren. bericht über die ersten hundert essener fälle*, 'Klinische Monatsblätter für Augenheilkunde', vol. 185, no. 12, pp. 490–494, Dec. 1984. DOI: 10.1055/s-2008-1054681.

[61] P. K. Lommatzsch, C. Werschnik and E. Schuster, *Long-term follow-up of ru-106/rh-106 brachytherapy for posterior uveal melanoma*, 'Graefe's Archive for Clinical and Experimental Ophthalmology', vol. 238, no. 2, pp. 129–137, Feb. 2000, ISSN: 1435-702X. DOI: 10.1007/PL00007880.

[62] A. O. Schueler et al., *Beta-ray brachytherapy of retinoblastoma: Feasibility of a new small-sized ruthenium-106 plaque*, 'Ophthalmic Research', vol. 38, no. 1, pp. 8–12, Dec. 2005. DOI: 10.1159/000088259.

[63] H. Sommer et al., *Monte carlo simulation of ruthenium eye plaques with geant4: Influence of multiple scattering algorithms, the spectrum and the geometry on depth dose profiles*, 'Physics in Medicine and Biology', vol. 62, pp. 1848–1864, 8th Feb. 2017. DOI: 10.1088/1361-6560/aa5696.

[64] L. Tagliaferri et al., *The gec estro handbook of brachytherapy - part ii: Clinical practice, Chapter 31: Uveal melanoma*, Erik Van Limbergen, Richard Pötter, Peter Hoskin, Dimos Baltas, Ed., 15th Apr. 2020, 2nd Edition.

[65] BEBIG, *Ophthalmic brachytherapy, Ru-106 eye applicators and i-125 ophthalmic seeds*, P13D140/Rev.07, Jan. 2020. [Online]. Available: https://www.bebig.com/fileadmin/bebig_neu/user_uploads/Products/Ophthalmic_Brachytherapy/Ophthalmic_Brochure__Rev._07__English.pdf (visited on 21st Apr. 2023).

[66] A. Belaïd et al., *Brachytherapy of uveal melanomas with ruthenium-106 plaques*, 'Asian Pacific Journal of Cancer Prevention', vol. 17, no. 12, pp. 5281–5285, 2016. DOI: https://dx.doi.org/10.22034%2FAPJCP.2016.17.12.5281.

[67] P. K. Lommatzsch, *β-irradiation of choroidal melanoma with 106ru/106rh applicators*, 'Archives of Ophthalmology', vol. 101, no. 5, p. 713, May 1983. DOI: 10.1001/archopht.1983.01040010713002.

[68] P. K. Lommatzsch, *Results after beta-irradiation (106ru/106rh) of choroidal melanomas: 20 years' experience.* 'British Journal of Ophthalmology', vol. 70, no. 11, pp. 844–851, Nov. 1986. DOI: 10.1136/bjo.70.11.844.

[69] G. Heilemann et al., *Retina dose as a predictor for visual acuity loss in 106ru eye plaque brachytherapy of uveal melanomas*, 'Radiotherapy and Oncology', vol. 127, no. 3, pp. 379–384, 2018, ISSN: 0167-8140. DOI: 10.1016/j.radonc.2017.11.010.

[70] L. Tarmann et al., *Tumor parameters predict the risk of side effects after ruthenium-106 plaque brachytherapy of uveal melanomas*, 'PLOS ONE', vol. 12, no. 8, pp. 1–14, Aug. 2017. DOI: 10.1371/journal.pone.0183833.

[71] C. A. Espensen et al., *Tumour control probability after ruthenium-106 brachytherapy for choroidal melanomas*, 'Acta Oncologica', vol. 59, no. 8, pp. 918–925, 2020, PMID: 32412331. DOI: 10.1080/0284186X.2020.1762925.

[72] R.-P. Müller et al., *Results of high dose 106-ruthenium irradiation of choroidal melanomas*, 'International Journal of Radiation Oncology - Biology - Physics', vol. 12, no. 10, pp. 1749–1755, Oct. 1986. DOI: 10.1016/0360-3016(86)90315-9.

[73] R. Tjho-Heslinga et al., *Results of ruthenium irradiation of uveal melanoma*, 'Radiotherapy and Oncology', vol. 29, no. 1, pp. 33–38, Oct. 1993. DOI: 10.1016/0167-8140(93)90170-D.

[74] T. AlMahmoud et al., *Outcome analysis of visual acuity and side effect after ruthenium-106 plaque brachytherapy for medium-sized choroidal melanoma*, 'Middle East African Journal of Ophthalmology', vol. 25, no. 2, p. 103, 2018. DOI: 10.4103/meajo.MEAJO_198_16.

[75] M. A. Astrahan et al., *An interactive treatment planning system for opthalmc plaque radiotherapy*, 'International Journal of Radiation Oncology - Biology - Physics', vol. 18, no. 3, pp. 679–687, Mar. 1990. DOI: 10.1016/0360-3016(90)90077-w.

[76] Eye Physics, LLC. *Homepage plaque simulator*, [Online]. Available: http://www.eyephysics.com (visited on 10th Feb. 2023).

[77] L. Brualla, F. J. Zaragoza and W. Sauerwein, *Monte carlo simulation of the treatment of eye tumors with 106ru plaques: A study on maximum tumor height and eccentric placement*, 'Ocular Oncology and Pathology', vol. 1, pp. 2–12, 2015. DOI: 10.1159/000362560.

[78] D. Coleman et al., *Computerized ultrasonic biometry and imaging of intraocular tumors for the monitoring of therapy*, 'Transactions of the American Ophthalmological Society', vol. 85, pp. 49–81, 1987, PMID: 3328920.

[79] S. Vurgese, S. Panda-Jonas and J. B. Jonas, *Scleral thickness in human eyes*, 'PLOS ONE', vol. 7, 6th Jan. 2012, PMID: 22238635. DOI: 10.1371/journal.pone.0029692.

[80] D. Kook et al., *Variability of standardized echographic ultrasound using 10 mhz and high-resolution 20 mhz b scan in measuring intraocular melanoma*, 'Clinical

ophthalmology (Auckland, NZ)', vol. 5, p. 477, 2011, PMID: 21573095. DOI: 10.2147/OPTH.S18513.

[81] J. W. M. Beenakker et al., *High-resolution MRI of uveal melanoma using a microcoil phased array at 7 t*, 'NMR in Biomedicine', vol. 26, no. 12, pp. 1864–1869, Oct. 2013. DOI: 10.1002/nbm.3041.

[82] *Observation of various eye applicators placement at the university hostipal essen and discussions with the surgeons.* 18th Apr. 2018.

[83] J. Harbour et al., *Intraoperative echographic localization of iodine 125 episcleral radioactive plaques for posterior uveal melanoma*, 'Retina (Philadelphia, Pa.)', vol. 16, no. 2, pp. 129–134, 1996, ISSN: 0275-004X. [Online]. Available: http://europepmc.org/abstract/MED/8724957.

[84] E. Stöckel, *Das Sicherheitssaumkonzept in der okularen Brachytherapie mit Ruthenium-106 Applikatoren auf Basis von Dosisverteilungen und Unsicherheitsbetrachtungen*, Masterthesis, TU Dortmund University, 30th Sep. 2016.

[85] A. Almony et al., *Tilting of radioactive plaques after initial accurate placement for treatment of uveal melanoma*, 'Archives of Ophthalmology', vol. 126, no. 1, pp. 65–70, 2008. DOI: 10.1001/archophthalmol.2007.9.

[86] Eckert & Ziegler BEBIG GmbH, *Gebrauchsanweisung - ru-106 augenapplikatoren, Td04_000/rev.12*, Mar. 2016.

[87] Carmen Schulz, Product manager, Eckert & Ziegler BEBIG GmbH, Berlin, Germany, *Personal communication*, 25th Jul. 2023.

[88] D. Flühs, Medical physics expert, Universitätsklinikum Essen, Essen, Germany, *Personal communication*, May 2023.

[89] C. Scharmberg et al., *Mikrokollimatoren für den einsatz in der therapie hochprominenter augentumoren, Abstractband - 47. jahrestagung der deutschen physikalischen gesellschaft für medizinische physik*, L. M. Schreiber, J.-B. Hövener, Ed., Sep. 2016.

[90] C. Scharmberg et al., *Design of a precise scintillation dosimetry system for the measuring of microcollimators, Abstractband - jahrestagung der biomedizinischen technik und dreiländertagung der medizinischen physik*, O. Dössel, Ed., Walter de Gruyter GmbH, Sep. 2017. DOI: 10.1515/bmt-2017-5072.

[91] C. Scharmberg et al., *Vermessung von mikrokollimatoren mit einem hochpräzisen pen-basierten dosimetriesystem, Abstractband - 49. jahrestagung der deutschen gesellschaft für medizinische physik (dgmp) e.v*, C. Bert, M. Wucherer & F. B. Laun, Ed., Sep. 2018.

[92] C. Scharmberg, *Konstruktion und vermessung von mikrokollimatoren für die augentumor-brachytherapie, Dgmp & dpg-webinar*, 6th Jul. 2017.

[93] V. Tseng et al., *Complications from plaque versus proton beam therapy for choroidal melanoma: A qualitative systematic review*, 'Journal of Cancer Therapy', vol. 7, pp. 169–185, 2016. DOI: 10.4236/jct.2016.73018.

[94] M. H. Seegenschmiedt and O. Micke, *Strahlentherapie nichtmaligner erkrankungen*, 'Strahlentherapie und Onkologie', vol. 188, no. S3, pp. 272–290, Oct. 2012. DOI: 10.1007/s00066-012-0195-z.

[95] H. Krieger, *Strahlungsquellen für Technik und Medizin, 2. Auflage*. Springer Spektrum, 2013, ISBN: 978-3-658-00589-4. DOI: 10.1007/978-3-658-00590-0.

[96] M. Notter, *Radiotherapiebei malignen hauttumoren*, 'Schweizer Zeitschrift für Onkologie', vol. 04, 4th Dec. 2012.

[97] S. Chan, A. Dhadda and R. Swindell, *Single fraction radiotherapy for small superficial carcinoma of the skin*, 'Clinical Oncology', vol. 19, no. 4, pp. 256–259, May 2007. DOI: 10.1016/j.clon.2007.02.004.

[98] A. Pashazadeh, A. Boese and M. Friebe, *Radiation therapy techniques in the treatment of skin cancer: An overview of the current status and outlook*, 'Journal of Dermatological Treatment', vol. 30, no. 8, pp. 831–839, Mar. 2019. DOI: 10.1080/09546634.2019.1573310.

[99] H. Reich et al., *Dosimetrie ionisierender Strahlung*. Teubner Verlag, 1990, ISBN: 3519030675.

[100] H. Krieger, *Grundlagen der Strahlungsphysik und des Strahlenschutzes*. Springer Spektrum, 2017, ISBN: 9783662557594. DOI: 10.1007/978-3-662-55760-0.

[101] M. J. Berger et al., *1. introduction*, 'Reports of the International Commission on Radiation Units and Measurements', vol. os-19, no. 2, pp. 1–3, Dec. 1984. DOI: 10.1093/jicru_os19.2.1.

[102] G. Major, *Medizinische Physik*, W. Schlegel, C. P. Karger and O. Jäkel, Eds. Springer Berlin Heidelberg, 2018, pp. 89–9. DOI: 10.1007/978-3-662-54801-1.

[103] C. P. Karger, *Klinische strahlenbiologie*, in *Medizinische Physik*, W. Schlegel, C. P. Karger and O. Jäkel, Eds. Springer Berlin Heidelberg, 2018, pp. 451–472. DOI: 10.1007/978-3-662-54801-1.

[104] H. Paganetti, *Relative biological effectiveness (RBE) values for proton beam therapy. variations as a function of biological endpoint, dose, and linear energy transfer*, 'Physics in Medicine and Biology', vol. 59, no. 22, Oct. 2014. DOI: 10.1088/0031-9155/59/22/R419.

[105] S. J. McMahon, *Proton RBE models: Commonalities and differences*, 'Physics in Medicine & Biology', vol. 66, no. 4, 04NT02, Feb. 2021. DOI: 10.1088/1361-6560/abda98.

[106] H. Willers et al., *Toward a variable RBE for proton beam therapy*, 'Radiotherapy and Oncology', vol. 128, no. 1, pp. 68–75, Jul. 2018. DOI: 10.1016/j.radonc.2018.05.019.

[107] B. S. Sørensen et al., *Does the uncertainty in relative biological effectiveness affect patient treatment in proton therapy?*, 'Radiotherapy and Oncology', vol. 163, pp. 177–184, Oct. 2021. DOI: 10.1016/j.radonc.2021.08.016.

[108] J. Eulitz et al., *A monte carlo based radiation response modelling framework to assess variability of clinical RBE in proton therapy*, 'Physics in Medicine & Biology', vol. 64, no. 22, p. 225 020, Nov. 2019. DOI: 10.1088/1361-6560/ab3841.

[109] R. Drzymala et al., *Dose-volume histograms*, 'International Journal of Radiation Oncology∗Biology∗Physics', vol. 21, no. 1, pp. 71–78, May 1991. DOI: 10.1016/0360-3016(91)90168-4.

[110] R. P. Singh et al., *Evaluation of microcollimated pars plana external beam radiation in the porcine eye*, 'Journal of Clinical & Experimental Ophthalmology', vol. 02, no. 03, 2011. DOI: 10.4172/2155-9570.1000134.

[111] T. L. Jackson and J. Neffendorf, *Stereotactic radiotherapy for wet age-related macular degeneration: Current perspectives*, 'Clinical Ophthalmology', p. 1829, Sep. 2015. DOI: 10.2147/OPTH.S75638.

[112] Christoph Kaufmann, Head of R & D, WOLF-Medizintechnik GmbH, St. Gangloff, Germany, *Personal communication*, 13th Feb. 2023.

[113] Autodesk Inc., *Product documentation, Fusion 360*, Tech. Rep. [Online]. Available: https://help.autodesk.com/view/fusion360/ENU/?guid=GUID-1C665B4D-7BF7-4FDF-98B0-AA7EE12B5AC2 (visited on 13th Mar. 2023).

[114] Autodesk Inc., Ed. *Fusion 360, Planung, konstruktion, elektronik und fertigung vereint in fusion 360*, [Online]. Available: https://www.autodesk.de/products/fusion-360/ (visited on 13th Mar. 2023).

[115] Autodesk Inc., *Product documentation, Inventor 2021*, Tech. Rep. [Online]. Available: https://knowledge.autodesk.com/support/inventor (visited on 13th Mar. 2023).

[116] Autodesk Inc., Ed. *Inventor, Inventor: Leistungsstarke software für die mechanische konstruktion für ihre anspruchsvollsten ideen*, [Online]. Available: https://www.autodesk.de/products/inventor/ (visited on 13th Mar. 2023).

[117] G. G. Poludniowski and P. M. Evans, *Calculation of x-ray spectra emerging from an x-ray tube. part i. electron penetration characteristics in x-ray targets*, 'Medical Physics', vol. 34, no. 6 Part 1, pp. 2164–2174, 2007. DOI: 10.1118/1.2734725.

[118] G. G. Poludniowski, *Calculation of x-ray spectra emerging from an x-ray tube. part ii. x-ray production and filtration in x-ray targets*, 'Medical Physics', vol. 34, no. 6 Part 1, pp. 2175–2186, 2007. DOI: 10.1118/1.2734726.

[119] G. Poludniowski et al., *SpekCalc: A program to calculate photon spectra from tungsten anode x-ray tubes*, 'Physics in Medicine and Biology', vol. 54, no. 19, N433–N438, Sep. 2009. DOI: 10.1088/0031-9155/54/19/n01.

[120] S. Agostinelli et al., *Geant4 – a simulation toolkit*, 'Nuclear Instruments and Methods in Physics Research Section A: Accelerators, Spectrometers, Detectors and Associated Equipment', vol. 506, pp. 250–303, 1st Jul. 2003, changed, ISSN: 0168-9002. DOI: 10.1016/S0168-9002(03)01368-8.

[121] Geant4 Collaboration, Ed., *Geant4 - book for application developers - release 10.6*, Geneva, 6th Dec. 2019. [Online]. Available: https://geant4-userdoc.web.cern.ch/UsersGuides/ForApplicationDeveloper/BackupVersions/V10.6/fo/BookForApplicationDevelopers.pdf (visited on 9th Mar. 2023).

[122] M. Fippel and F. Nüsslin, *Grundlagen der monte-carlo-methode für die dosisberechnung in der strahlentherapie*, 'Zeitschrift für Medizinische Physik', vol. 11, pp. 73–82, 2001, ISSN: 0939-3889. DOI: 10.1016/S0939-3889(15)70493-9.

[123] D. E. Cullen, J. H. Hubbell and L. Kyssel, *Photon and electron interaction data*, U. of California Lawrence Livermore National Laboratory, Ed.

[124] H. Lewis, *Multiple scattering in an infinite medium*, 'Phys. Rev.', vol. 78, pp. 526–529, 5 1950. DOI: 10.1103/PhysRev.78.526.

[125] G. Molière, *Theorie der streuung schneller geladener teilchen ii mehrfach-und vielfachstreuung*, 'Zeitschrift für Naturforschung A', vol. 3, no. 2, pp. 78–97, 1st Feb. 1948, ISSN: 1865-7109. DOI: 10.1515/zna-1948-0203.

[126] S. Goudsmit and J. Saunderson, *Multiple scattering of electrons*, 'Physical Review', vol. 57, no. 1, pp. 24–29, 1 Jan. 1940. DOI: 10.1103/PhysRev.57.24.

[127] National Nuclear Data Center, B. N. Laboratory, Ed., Upton, NY, USA.

[128] C. M. Poole et al., *A CAD interface for GEANT4*, 'Australasian Physical & Engineering Science in Medicine', vol. 35, no. 3, pp. 329–334, Sep. 2012. DOI: 10.1007/s13246-012-0159-8.

[129] S. Müller, *Monte-Carlo-Simulationen der verschiedenen Therapieformen für intraokulare Tumore*, In progress. Supervised by Henning Manke, Masterthesis, TU Dortmund.

[130] H. Speiser, *Implementierung und Validierung von Röntgenspektren in Geant4 zur Untersuchung der Eignung der Kombination mit Brachytherapie bei Augentumoren*, Supervised by Henning Manke, Bachelorthesis, TU Dortmund, 12th Jun. 2019.

[131] E. Jasniewicz, *Geant4-Simulationen eines Phantoms als Voruntersuchung zur kombinierten Therapie von Augentumoren*, Supervised by Henning Manke, Bachelorthesis, TU Dortmund, 6th Sep. 2021.

[132] R. Hill, Z. Kuncic and C. Baldock, *The water equivalence of solid phantoms for low energy photon beams*, 'Medical Physics', vol. 37, no. 8, pp. 4355–4363, Jul. 2010. DOI: 10.1118/1.3462558.

[133] *Rw3 plattenphantom (t29672), Gebrauchsanweisung*, PTW Freiburg GmbH, Tech. Rep. D188.151.00/09 de, Mar. 2021.

[134] J. Würfel, Research Scientist, PTW Freiburg GmbH, Freiburg, Germany, *Personal communication*, 12th Jun. 2023.

[135] J. Garczyrczyk, *Entwicklung und Optimierung eines Festkörperphantoms zur systemunabhängigen Qualitätssicherung des IRay Systems*, Masterthesis, TU Dortmund University, 31st Jan. 2018.

[136] Computerized Imaging Reference Systems Inc, *Plastic water®*, Tech. Rep. PW DS 120418. [Online]. Available: http://www.cirsinc.com/wp-content/uploads/2019/04/PW-DS-120418.pdf (visited on 26th May 2023).

[137] Gammex Inc. *Certified therapy grade solid water®, Gammex 457-ctg*, [Online]. Available: http://www.bestmedicalcanada.com/pdf/Gammex.pdf (visited on 20th Feb. 2023).

[138] *Solutions for radiation medicine qa*, PTW Freiburg GmbH, Tech. Rep. D587.211.00/13 2022-12, Dec. 2022, p. 18.

[139] M. Eichmann, D. Flühs and B. Spaan, *Development of a high precision dosimetry system for the measurement of surface dose rate distribution for eye applicators*, 'Medical Physics', vol. 36, no. 10, pp. 4634–4643, 14th Sep. 2009. DOI: 10.1118/1.3218762.

[140] M. Eichmann, *Entwicklung eines hochpräzisen dosimetriesystems zur messung der oberflächendosisverteilung von augenapplikatoren*, Ph.D. dissertation, TU Dortmund, 11th Nov. 2010.

[141] M. Eichmann et al., *Development of a high-precision xyz-measuring table for the determination of the 3d dose rate distributions of brachytherapy sources*, 'Physics in Medicine and Biology', vol. 57, no. 22, pp. 421–429, 19th Oct. 2012. DOI: 10.1088/0031-9155/57/22/N421.

[142] D. Flühs et al., *Polyethylene naphthalate scintillator: A novel detector for the dosimetry of radioactive ophthalmic applicators*, 'Ocular oncology and pathology', vol. 2, no. 1, pp. 5–12, 2016. DOI: 10.1159/000381720.

[143] M. Eichmann, *Inhomogeneous surface dose distributions of 106-ru eye plaques*, 'Ocular Oncology and Pathology', vol. 4, no. 1, pp. 21–22, 23rd Jun. 2017. DOI: 10.1159/000477409.

[144] M. Bambynek et al., *A high-precision, high-resolution and fast dosimetry system for beta sources applied in cardiovascular brachytherapy*, 'Medical Physics', vol. 27, no. 4, pp. 662–667, 5th Apr. 2000. DOI: 10.1118/1.598927.

[145] M. Eichmann and B. Thomann, *Air core detectors for cerenkov-free scintillation dosimetry of brachytherapy -sources*, 'Medical Physics', vol. 44, no. 9, pp. 4900–4909, 2017. DOI: 10.1002/mp.12374.

[146] *Dosimetry media, type ebt-3*, Ashland Inc., Tech. Rep., Former Gafchromic Inc. [Online]. Available: http://www.gafchromic.com/gafchromic-film/radiotherapy-films/EBT/index.asp (visited on 20th Feb. 2023).

[147] *Efficient protocols for accurate radiochromic film calibration and dosimetry, Product specification*, Ashland Inc., Tech. Rep., Former Gafchromic Inc. [Online]. Available: http://www.gafchromic.com/gafchromic-film/radiotherapy-films/EBT/index.asp (visited on 20th Feb. 2023).

[148] Gravotech GmbH, *Lasergravierer & cutter, Ls900*, Tech. Rep. Gravotech-LS900-11-2022-de-DE, Nov. 2022. [Online]. Available: https://www.gravotech.de/sites/default/files/2022-12/Lasergravierer-Gravotech-LS900-de-DE-web.pdf (visited on 28th Feb. 2023).

[149] Open Source Vision Foundation. *Creating bounding rotated boxes and ellipses for contours*. (22nd Feb. 2023), [Online]. Available: https://docs.opencv.org/3.4/de/d62/tutorial_bounding_rotated_ellipses.html.

[150] Open Source Vision Foundation. *Hough circle transform*. (29th Dec. 2022), [Online]. Available: https://docs.opencv.org/4.x/da/d53/tutorial_py_houghcircles.html (visited on 22nd Feb. 2023).

[151] P. G. F. Watson et al., *An investigation into the INTRABEAM miniature x-ray source dosimetry using ionization chamber and radiochromic film measurements*, 'Medical Physics', vol. 45, no. 9, pp. 4274–4286, Jul. 2018. DOI: 10.1002/mp.13059.

[152] PTW Freiburg GmbH, *Detectors for ionizing radiation*, Tech. Rep. D165.229.00/14 2022-07, Jul. 2022, p. 36. [Online]. Available: https://www.ptwdosimetry.com/fileadmin/user_upload/Online_Catalog/DETECTORS_

Cat_en_16522900-14/blaetterkatalog/blaetterkatalog/pdf/complete.pdf (visited on 20th Feb. 2023).

[153] *Gebrauchsanweisung, Weichstrahlkammern typ 34013, typ 23342 und typ 23344*, PTW Freiburg GmbH, Tech. Rep. D564.151.00/005 de, Apr. 2016.

[154] *Kalibrierschein*, PTW Freiburg GmbH, Tech. Rep. 220317701, 18th Jul. 2022.

[155] *Unidos®romeo, User manual*, PTW Freiburg GmbH, Tech. Rep. D970.236.01/00 de, Jul. 2020.

[156] Hamamatsu Photonics, K. K., *H10720/h10721 series, Photosensor modules*, Tech. Rep. TPMO1062E02, Nov. 2016. [Online]. Available: https://www.hamamatsu.com/jp/en/product/optical-sensors/pmt/pmt-module/current-output-type/H10721-210.html.

[157] Hamamatsu Photonics, K. K. *H10721-210, Photomultiplier tube module.* (19th Jul. 2023), [Online]. Available: https://www.hamamatsu.com/jp/en/product/optical-sensors/pmt/pmt-module/current-output-type/H10721-210.html.

[158] Cunz GmbH & CO.KG, Ed., *Opto-elektronik.* [Online]. Available: http://www.cunz.de/documents/Cunz-POF-PMMA.pdf (visited on 7th Mar. 2023).

[159] Tektronix, Inc., Ed. *Picoamperemeter, Model 6485 specifiations.* (7th Mar. 2023), [Online]. Available: https://download.tek.com/datasheet/6485.pdf.

[160] Saint-Gobain Ceramics & Plastics, Inc., Ed., *Bc-600, Optical cement*, Jan. 2005. [Online]. Available: https://vepp2k.inp.nsk.su/~inest/halometer/SGC%20BC600%20Data%20Sheet%200105.pdf (visited on 7th Mar. 2023).

[161] B. Thomann, *AirCore-Detektoren an für die Čerenkov-freie Szintillationsdosimetrie*, Masterthesis, TU Dortmund University, 30th Sep. 2016.

[162] Physikalisch-Technische Werkstätten Dr. Pychlau GmbH (PTW), Ed., *Prüfstrahler t48010*, Freiburg. [Online]. Available: https://www.ptwdosimetry.com/fileadmin/user_upload/Online_Catalog/Radiation_Medicine_Cat_en_58721100_13/blaetterkatalog/index.html#page_1 (visited on 7th Mar. 2023).

[163] M. Ebenau et al., *Energy dependent response of plastic scintillation detectors to photon radiation of low to medium energy*, 'Medical Physics', vol. 43, no. 8, pp. 4598–4606, 15th Jul. 2016. DOI: 10.1118/1.4957348.

[164] Wolf-Medizintechnik GmbH, *T-105: Equipment for superficial x-ray therapy, Efficient applicaton for superficial x-ray therapy*, 2023. [Online]. Available: https://www.bebigmedical.com/static/upload/file/20221027/1666852967785658.pdf (visited on 28th Feb. 2023).

[165] BEBIG Medical GmbH, Ed. *X-ray therapy*, [Online]. Available: https://www.bebigmedical.com/products_24/ (visited on 8th Mar. 2023).

[166] R. D. Deslattes et al., *X-ray transition energies, nist standard reference database 128*, en, 2003, NIST, Physical Measurement Laboratory. DOI: 10.18434/T4859Z.

[167] M. J. Butson, T. Cheung and P. K. N. Yu, *Radiochromic film dosimetry in water phantoms*, 'Physics in Medicine and Biology', vol. 46, no. 1, N27–N31, Dec. 2000. DOI: 10.1088/0031-9155/46/1/405.

[168] K. N. Morris, M. D. Weil and R. Malzbender, *Radiochromic film dosimetry of contrast-enhanced radiotherapy (CERT)*, 'Physics in Medicine and Biology', vol. 51, no. 22, pp. 5915–5925, Oct. 2006. DOI: 10.1088/0031-9155/51/22/013.

[169] S. M. Vatnitsky, *Radiochromic film dosimetry for clinical proton beams*, 'Applied Radiation and Isotopes', vol. 48, no. 5, pp. 643–651, May 1997. DOI: 10.1016/s0969-8043(97)00342-4.

[170] A. Piermattei et al., *Radiochromic film dosimetry of a low energy proton beam*, 'Medical Physics', vol. 27, no. 7, pp. 1655–1660, Jul. 2000. DOI: 10.1118/1.599032.

[171] L. Zhao and I. J. Das, *Gafchromic EBT film dosimetry in proton beams*, 'Physics in Medicine and Biology', vol. 55, no. 10, Apr. 2010. DOI: 10.1088/0031-9155/55/10/n04.

[172] B. Dobler and R. Bendl, *Precise modelling of the eye for proton therapy of intraocular tumours*, 'Physics in Medicine & Biology', vol. 47, no. 4, p. 593, 2002. DOI: 10.1088/0031-9155/47/4/304.

[173] A. Lucente et al., *Widefield and ultra-widefield retinal imaging: A geometrical analysis*, 'Life', vol. 13, no. 1, p. 202, Jan. 2023. DOI: 10.3390/life13010202.

[174] B. Dobler, *Präzise modellierung von risikoorganen und zielvolumina für die protonentherapie intraocularer tumoren*, Ph.D. dissertation, Ruprechts-Karls Universität Heidelberg, 18th Oct. 2000.

[175] J. P. Snyder, *Map projections: A working manual*, Washington, D.C., U.S. Geological Survey Professional Paper 1395, 1987. DOI: 10.3133/pp1395.

[176] R. A. Jonas et al., *Optic disc - fovea distance, axial length and parapapillary zones. the beijing eye study 2011*, 'PLOS ONE', vol. 10, no. 9, pp. 1–14, Sep. 2015. DOI: 10.1371/journal.pone.0138701.

[177] J. A. Choi et al., *The foveal position relative to the optic disc and the retinal nerve fiber layer thickness profile in myopia*, 'Investigative ophthalmology & visual science', vol. 55, no. 3, pp. 1419–1426, 2014.

[178] J. Hanlon et al., *Kilovoltage stereotactic radiosurgery for age-related macular degeneration: Assessment of optic nerve dose and patient effective dose*, 'Medical Physics', vol. 36, no. 8, pp. 3671–3681, Jul. 2009. DOI: 10.1118/1.3168554.

[179] M. Ang and V. Tourassis, *Singularities of euler and roll-pitch-yaw representations*, 'IEEE Transactions on Aerospace and Electronic Systems', vol. 23, no. 3, pp. 317–324, May 1987. DOI: 10.1109/TAES.1987.310828.

[180] BEBIG, *Ru-106 eye applicators, Beta radiation for eye tumor treatment*, P13D140/Rev.06, Apr. 2021. [Online]. Available: https://www.bebig.com/fileadmin/bebig_neu/user_uploads/Products/Ophthalmic_Brachytherapy/Fact_sheet_Ru-106_Eye_Applicators__Rev.07__English_.pdf (visited on 28th Feb. 2023).

[181] D. Braden, *Repost: Cubic spline+its integral and derivatives*, 14th Nov. 2000. [Online]. Available: https://groups.google.com/g/microsoft.public.excel.programming/c/0_LpZSej644/m/H9vMDlJmKWoJ?hl=en (visited on 6th Jun. 2023).

[182] M. for Mere Mortals - Math Made Easier, Ed., *Bicubic interpolation – vba function compatible with both arrays ranges*, 14th Jul. 2013. [Online]. Available: https://mathformeremortals.wordpress.com/2013/07/14/bicubic-interpolation-vba-function-compatible-with-both-arrays-ranges/ (visited on 6th Jun. 2023).

[183] M. Stroth, *Die Implementierung eines anatomisch approximierten Augenmodells und dessen Einfluss auf die simulierten Dosisverteilungen eines 106Ru-Applikators*, Supervised by Henning Manke, Bachelorthesis, TU Dortmund, 26th Jun. 2020.

[184] Y. Kabatskiy, *The chemical compositions of eye tissues and their influence on dose deposition by low energy photons*, Bachelorthesis, TU Dortmund University, 6th Jul. 2016.

[185] A. Bennemann, *Monte-Carlo-Simulationen zur Analyse von Unsicherheiten von Dosisverteilungen bei der Brachytherapie mit Ru-106 Applikatoren*, Co-supervised by Henning Manke, Bachelorthesis, TU Dortmund, Jul. 2023.

[186] H. Bartling, P. Wanger and L. Martin, *Measurement of optic disc parameters on digital fundus photographs: Algorithm development and evaluation*, 'Acta Ophthalmologica', vol. 86, no. 8, pp. 837–841, Jun. 2008. DOI: 10.1111/j.1755-3768.2007.01146.x.

[187] J. Thijssen, H. Mol and M. Timmer, *Acoustic parameters of ocular tissues*, 'Ultrasound in Medicine & Biology', vol. 11, no. 1, pp. 157–161, Jan. 1985. DOI: 10.1016/0301-5629(85)90018-3.

[188] S. T. Awwad, *Book review*, 'American Journal of Ophthalmology', vol. 143, no. 6, 1073.e2, Jun. 2007. DOI: 10.1016/j.ajo.2007.04.032.

[189] R. A. Jonas et al., *Optic disc - fovea angle: The beijing eye study 2011*, 'PLOS ONE', vol. 10, no. 11, L. Frishman, Ed., e0141771, Nov. 2015. DOI: 10.1371/journal.pone.0141771.

[190] K. Ilavarasi and K. S. Joseph, *Variants of travelling salesman problem: A survey*, Feb. 2014. DOI: 10.1109/ICICES.2014.7033850.

[191] cameronroytaylor, *Travelling salesman in scipy*, 20th May 2017. [Online]. Available: https://stackoverflow.com/questions/25585401/travelling-salesman-in-scipy (visited on 20th May 2023).

[192] U. Ramer, *An iterative procedure for the polygonal approximation of plane curves*, 'Computer Graphics and Image Processing', vol. 1, no. 3, pp. 244–256, Nov. 1972. DOI: 10.1016/S0146-664X(72)80017-0.

[193] D. H. Douglas and T. K. Peucker, *Algorithms for the reduction of the number of points required to represent a digitized line or its caricature*, 'Cartographica: The International Journal for Geographic Information and Geovisualization', vol. 10, no. 2, pp. 112–122, Dec. 1973. DOI: 10.3138/FM57-6770-U75U-7727.

[194] P. Q. Ngo, *Untersuchung von Unsicherheiten von Dosisverteilungen auf Grundlage von Monte-Carlo-Simulationen der Brachytherapie bei Augentumoren*, Co-supervised by Henning Manke, Bachelorthesis, TU Dortmund, 23rd Aug. 2022.

[195] M. Stroth, In progress, Ph.D. dissertation, TU Dortmund.

[196] N. Oldman, *Workflowoptimierung von brachytherapie-simulationen durch anpassung der geant4-methodik*, B, TU Dortmund, Jul. 2023.

[197] Universal Robots (Germany) GmbH, München, Germany, *Ur16e, Technische daten*, Tech. Rep., May 2021.

[198] Christoph Kaufmann, Head of R & D, WOLF-Medizintechnik GmbH, St. Gangloff, Germany, *Personal communication*, 21st Apr. 2023.

[199] J. S. Furtado et al., *Comparative analysis of OptiTrack motion capture systems*, pp. 15–31, 2019. DOI: 10.1007/978-3-030-17369-2_2.

[200] H. Renz, Technische Universität Dortmund, Dortmund, Germany, *Personal communication*, 2nd May 2023.

[201] J. B. Jonas et al., *Size of the optic nerve scleral canal and comparison with intravital determination of optic disc dimensions*, 'Graefe's Archive for Clinical and Experimental Ophthalmology', vol. 226, no. 3, pp. 213–215, May 1988. DOI: 10.1007/BF02181183.

[202] H. Littmann, *Zur bestimmung der wahren größe eines objektes auf dem hintergrund des lebenden auges*, 'Klinische Monatsblätter für Augenheilkunde', vol. 180, no. 04, pp. 286–289, Apr. 1982. DOI: 10.1055/s-2008-1055068.

[203] A. Bennett, A. Rudnicka and D. Edgar, *Improvements on littmann's method of determining the size of retinal features by fundus photography*, 'Graefe's Archive for Clinical and Experimental Ophthalmology', vol. 232, no. 6, pp. 361–367, Jun. 1994. DOI: 10.1007/BF00175988.

[204] A. Bergua, *Das menschliche Auge in Zahlen*. Springer Berlin Heidelberg, 2017. DOI: 10.1007/978-3-662-47284-2.

[205] M. T. Feng et al., *Anterior chamber depth in normal subjects by rotating scheimpflug imaging*, 'Saudi Journal of Ophthalmology', vol. 25, no. 3, pp. 255–259, Jul. 2011. DOI: 10.1016/j.sjopt.2011.04.005.

[206] Z. Biró and Z. Balla, *OCT measurements on the foveal and perifoveal retinal thickness on diabetic patients after phacoemulsification and IOL implantation*, 'Eye', vol. 24, no. 4, pp. 639–647, Jul. 2009. DOI: 10.1038/eye.2009.164.

[207] A. Kampik et al., *Augenärztliche Therapie*. Georg Thieme Verlag, 2002. DOI: 10.1055/b-002-8301.

[208] H. M. Rauen, *Biochemisches Taschenbuch 2. Auflage*. Springer-Verlag GmbH, 1956, ISBN: 9783642532405.

[209] E. S. Soriano et al., *Effect of epithelial debridement on human cornea proteoglycans*, 'Brazilian Journal of Medical and Biological Research', vol. 34, pp. 325–331, 2001.

[210] J. Kokavec et al., *Biochemical analysis of the living human vitreous*, 'Clinical & Experimental Ophthalmology', vol. 44, no. 7, pp. 597–609, Apr. 2016. DOI: 10.1111/ceo.12732.

[211] D. R. White et al., *Report 44*, 'Journal of the International Commission on Radiation Units and Measurements', vol. 23, no. 1, Jan. 1989. DOI: 10.1093/jicru/os23.1.report44.

[212] J. A. Scott, *A finite element model of heat transport in the human eye*, 'Physics in Medicine and Biology', vol. 33, no. 2, pp. 227–242, Feb. 1988. DOI: 10.1088/0031-9155/33/2/003.

[213] T. V. Chirila and Y. Hong, *The vitreous humor*, pp. 125–131, 1998. DOI: 10.1007/978-1-4615-5801-9_12.

[214] I. G. Fels, *Hydration and density of collagen and gelatin*, 'Journal of Applied Polymer Science', vol. 8, no. 4, pp. 1813–1824, Jul. 1964. DOI: 10.1002/app.1964.070080430.

[215] F. W. Keeley and F. S. Labella, *Amino acid composition of elastin in the developing chick aorta*, 'Connective Tissue Research', vol. 1, no. 2, pp. 113–119, Jan. 1972. DOI: 10.3109/03008207209152064.

[216] *Chemspider, Search and share chemistry*, [Online]. Available: https://www.chemspider.com (visited on 4th May 2020).

[217] Materials Testing Standards Committee, *Din 54113-1, Non-destructive testing - radiation protection rules for the technical application of x-ray equipment up to 1mv - part 1: Technical safety requirements and testing for the manufacture, installation and operation*, DIN German Institute for Standardization, Ed., Jan. 2018.

[218] Materials Testing Standards Committee, *Din 54113-3, Non-destructive testing - radiation protection rules for the technical application of x-ray equipment up to 1 mv - part 3: Formulas and diagrams for the calculation of radiation protection for x-ray equipment up to 600 kv*, DIN German Institute for Standardization, Ed., Jul. 2020.

[219] Radiology Standards Committee, *Din 6814-8, Terms in the field of radiological technique - part 8: Radiotherapy*, DIN German Institute for Standardization, Ed., Aug. 2016.

[220] Radiology Standards Committee, *Din 6812, Medical x-ray equipment up to 300 kv - rules of construction for structural radiation protection*, DIN German Institute for Standardization, Ed., Jun. 2021.

[221] Radiology Standards Committee, *Din 6815, Medical x-ray equipment up to 300 kv - rules for testing of radiation protection after installation, maintenance and essential modification*, DIN German Institute for Standardization, Ed., Jun. 2021.

[222] Radiology Standards Committee, *Din 6827-1, Recording in medical application of ionizing radiation - part 1: Therapy with electron accelerators as well as x-ray and gamma-ray therapy systems*, DIN German Institute for Standardization, Ed., Oct. 2020.

[223] Radiology Standards Committee, *Din 6827-3, Recording in medical application of ionizing radiation - part 3: Brachytherapy with enclosed radiation sources*, DIN German Institute for Standardization, Ed., Sep. 2021.

[224] Radiology Standards Committee, *Din 6809-1, Clinical dosimetry - part 1: Radiation quality of photon and electron radiation*, DIN German Institute for Standardization, Ed., Mar. 2010.

[225] Radiology Standards Committee, *Din 6809-4, Clinical dosimetry - part 4: X-ray therapy with x-ray tube voltages between 10 kv and 300 kv*, DIN German Institute for Standardization, Ed., Apr. 2020.

[226] Radiology Standards Committee, *Din 6809-8, Clinical dosimetry - part 8: Dosimetry of small photon fields*, DIN German Institute for Standardization, Ed., Feb. 2019.

[227] Radiology Standards Committee, *Din 6846-2, Medical teletherapy systems with gamma-emitting sources -part 2: Radiation safety requirements for installation*, DIN German Institute for Standardization, Ed., Mar. 1992.

[228] Radiology Standards Committee, *Din 6873, Radiotherapy treatment planning systems*, DIN German Institute for Standardization, Ed., May 2021.

[229] Radiology Standards Committee, *Din 60601-2-8, Medical electrical equipment – particular requirements for the basic safety and essential performance of therapeutic x-ray equipment operating in the range 10 kv to 1 mv. iec 60601-2-8:2010 + a1:2015*, DIN German Institute for Standardization, Ed., 2015.

Acknowledgments

I want to take this opportunity to thank some of the many people who accompanied me on my way to the Ph.D. and who helped with this project. COVID-19 did not make it easier to finalise my work because of several scientific constraints and limited personal contacts.

Bernhard Spaan reviewed my bachelor's and master's thesis and enabled me to start with my Ph.D. Unfortunately, he died too early in the middle of this project in December 2021. The professional expertise that he provided for this analysis and the many personal pieces of advice shall not be forgotten.
Johannes Albrecht spontaneously jumped in as the first assessor. Even though his primary field of research is high-energy particle physics, and this thesis resembles his first medical physics project, he gave me a lot of advice on how to continue with my tasks and held exciting discussions with me. Not only was his door always open for scientific discussions, but he helped me a lot in my personal development.
Also, I want to acknowledge Armin Lühr for his willingness to examine this work.
This project would never have started without the expertise of Dirk Flühs. He was never tired of answering my countless questions, reviewing any abstract or presentation, or organising funding with Bernhard Spaan. Many ideas and considerations are based on his questions, comments and thoughts he expressed in one of our many meetings. I even think I would have never started my PhD without him pronouncing that I should consider continuing with an academic career.

Numerous cooperations led to the results presented in this thesis. Many thanks to Carmen Schulz from Eckert & Ziegler GmbH, Christoph Kaufmann from WOLF-Medizintechnik GmbH and Dirk Flühs from the University Hospital Essen for assisting me in many different ways and providing me with lots of information. The phantom and the detectors would have never been finalised if not Matthias Domke, Dirk Schemionek, Susanne Kralemann, Patrick Miosga, Lutz Feldmann, and Lidia Lange helped with construction, building and polishing.
I want to thank the DFG for the financial resources.

The supervised students greatly impacted the project's progress and my personal development. I want to highlight one person in particular. Michelle Stroth wrote both her bachelor's and master's thesis within this project and has since become not only a colleague but also a good friend. She accompanied me during the measurements at

Womed and did not even break one of the filling pieces (yet). Thank you for the many helpful ideas, exciting discussions and the good humour you spread.
Furthermore, I acknowledge the help of various auxiliaries assisting in building detectors, preparing data or documenting processes.

I thank the working group for countless helpful pieces of advice and the friendly atmosphere. Our admins had to endure some very shady workarounds or many simulations when I once more flooded the cluster, but they never let me down and have stood by me with recommendations and support. My office colleagues have always provided me with a pleasant working environment and patiently put up with my chaotic self. Many 'hot beverage meetings', where you could give your smoking head a time out, made my everyday life much more delightful. Not to forget some pauses in the sun with a frisbee. Some of you became very close friends over time, which I do not want to miss anymore. A special thank you to Holger, Martin and Matthias for making the pandemic much more bearable. I am very thankful for how we interacted during those hard times and how this led to our close friendships. You have helped me since the beginning of my bachelor's thesis until now in many ways. You always had time to discuss either any physical issue or personal matter.
The various discussions with the members of the graduate school have always been a help and additionally led to new friendships.
Additionally, I want to acknowledge everyone who reviewed parts or the entire thesis and helped me polish it.

A good work-life balance is sometimes hard to find when all thoughts revolve around work. I am grateful for so many wonderful friendships that have lasted since my school days or developed afterwards in university and which make my life so much more varied and beautiful. I acknowledge every single one of you.

My family has stood by me in all situations and made it possible for me to study in the first place. I want to thank you for everything you did for me. I am delighted that our contact is so close, and we support each other when it counts. Throughout the years, I have also become part of Sarah's family. Great thanks are due to them as well. They have been super welcoming to me from the beginning and have become enormously important.
I want to acknowledge my wife, Sarah, with enormous thanks. Besides the personal pieces of advice, she shared her clinical experiences with me. Long car rides were often used to compare and discuss scientific and clinical views. She strengthens my back in all situations, makes my life (literally) more colourful and joyful, is always by my side and advises me on countless things. Our relationship was not made any easier by my working on this project. Sarah has taken on a lot to help us through this time. I hope I can repay her sometime in any possible way.
Lastly, I want to thank my daughter, Ida Malou. Even when you were not born, you were the biggest motivation to work from dusk till dawn to finish this thesis. Whenever my thoughts revolved too much around this work, your little nudges brought me back to earth.